

Studies on ion acceleration in ultrashort ultra-
high intensity laser matter interaction

By
MOHAMMAD TAYYAB
PHYS 03 2014 04 003

Raja Ramanna Centre for Advanced Technology, Indore

A thesis submitted to the
Board of Studies in Physical Sciences
In partial fulfillment of requirements
for the Degree of
DOCTOR OF PHILOSOPHY
of
HOMI BHABHA NATIONAL INSTITUTE



July 2019

Homi Bhabha National Institute¹

Recommendations of the Viva Voce Committee

As members of the Viva Voce Committee, we certify that we have read the dissertation prepared by **Mohammad Tayyab** entitled “**Studies on ion acceleration in ultrashort ultra-high intensity laser matter interaction**” and recommend that it may be accepted as fulfilling the thesis requirement for the award of Degree of Doctor of Philosophy.

Chairman – Prof. S. K. Dixit, RRCAT Indore

S. K. Dixit

Guide / Convener – Prof. J. A. Chakera, RRCAT Indore

J. A. Chakera 27/7/2020

Examiner - Prof. M. Krishnamurthy, TIFR Hyderabad

M. K. Murthy

Member 1- Prof. S. R. Mishra, RRCAT Indore

S. R. Mishra
27-7-20

Member 2- Prof. S. K. Majumder, RRCAT Indore

S. K. Majumder 27/07/20

Member 3- Prof. Y. Choyal, DAVV Indore

Y. Choyal 27/07/2020

Final approval and acceptance of this thesis is contingent upon the candidate's submission of the final copies of the thesis to HBNI.

I/We hereby certify that I/we have read this thesis prepared under my/our direction and recommend that it may be accepted as fulfilling the thesis requirement.

Date: 27/07/2020

Place: Indore

J. A. Chakera

Signature: डॉ. ज. अ. चकेरा / Dr. J. A. Chakera
Guide प्रमुख, लेज़र प्लाज़्मा प्रभाग
Head, Laser Plasma Division

¹ This page is to be included only for final submission after successful completion of viva voce.

STATEMENT BY AUTHOR

This dissertation has been submitted in partial fulfillment of requirements for an advanced degree at Homi Bhabha National Institute (HBNI) and is deposited in the Library to be made available to borrowers under rules of the HBNI.

Brief quotations from this dissertation are allowable without special permission, provided that accurate acknowledgement of source is made. Requests for permission for extended quotation from or reproduction of this manuscript in whole or in part may be granted by the Competent Authority of HBNI when in his or her judgment the proposed use of the material is in the interests of scholarship. In all other instances, however, permission must be obtained from the author.

Tayyab

Mohammad Tayyab

DECLARATION

I, hereby declare that the investigation presented in the thesis has been carried out by me. The work is original and has not been submitted earlier as a whole or in part for a degree / diploma at this or any other Institution / University.

Tayyab

Mohammad Tayyab

List of Publications arising from the thesis

Journal

1. “Role of target material in proton acceleration from thin foils irradiated by ultrashort laser pulses”, **M. Tayyab**, S. Bagchi, B. Ramakrishna, T. Mandal, A. Upadhyay, R. Ramis, J. A. Chakera, P. A. Naik, and P. D. Gupta, *Physical Review E*, **2014**, 90, 023103.
2. “Filamentation control and collimation of laser accelerated MeV protons”, B. Ramakrishna, **M. Tayyab**, S. Bagchi, T. Mandal, A. Upadhyay, S. M. Weng, M. Murakami, T. E. Cowan, J. A. Chakera, P. A. Naik and P. D. Gupta, *Plasma Phys. Control. Fusion* **2015**, 57, 125013.
3. “Micrometer-sized negative-ion accelerator based on ultrashort laser pulse interaction with transparent solids” S. Bagchi, **M. Tayyab**, B. Ramakrishna, A. Upadhyay, T. Mandal, J. A. Chakera, P. A. Naik, and P. D. Gupta, *Physical Review E*, **2015**, 92, 051103(R).
4. “Effect of temporally modified ultra-short laser pulses on ion acceleration from thin foil targets” **M. Tayyab**, S. Bagchi, J. A. Chakera, R. A. Khan and P. A. Naik, *Physics of Plasmas*, **2018**, 25, 083113.
5. “Mono-energetic heavy ion acceleration from laser plasma based composite nano-accelerator”, **M. Tayyab**, S. Bagchi, J. A. Chakera, D. K. Avasthi, R. Ramis, A. Upadhyay, B. Ramakrishna, T. Mandal, and P. A. Naik, *Physics of Plasmas*, **2018**, 25, 123102.
6. “Experimental investigation on nuclear reactions using laser accelerated proton and deuteron beam”, **M. Tayyab**, S. Bagchi, A. Moorti, and J. A. Chakera, *Plasma Phys. Control. Fusion*, **2019**, 61, 115007.

Conferences

1. “Energetic negative ion generation from intense laser solid interaction”, S. Bagchi, **M. Tayyab**, B. Ramakrishna, T. Mandal, J. A. Chakera, P. A. Naik, and P. D. Gupta, DAE-BRNS National Laser Symposium-NLS-22 , Manipal, Jan 8-11, **2014**.
2. “Ion acceleration to MeV energy using 10 TW Ti:sapphire laser pulses”, **M. Tayyab**, S. Bagchi, T. Mandal, B. Ramakrishna, J. A. Chakera, P. A. Naik, and P. D. Gupta, DAE-BRNS National Laser Symposium-NLS-22 , Manipal, Jan 8-11, **2014**.
3. “Production of energetic neutrals from interaction of ultra-short laser pulses with transparent solid targets”, S. Bagchi, **M. Tayyab**, A. Upadhyay, B. Ramakrishna, T. Mandal, J. A. Chakera, P. A. Naik, and P. D. Gupta, 29th National Symposium on Plasma Science & Technology, Kottayam, Dec 8-11, **2014**.
4. “Studies on proton acceleration from layered targets”, **M. Tayyab**, S. Bagchi, B. Ramakrishna, T. Mandal, A. Upadhyay, J. A. Chakera, P. A. Naik and P. D. Gupta, 29th National Symposium on Plasma Science & Technology, Kottayam, Dec 8-11, **2014**.
5. “Initial Results On Ion Acceleration Using 150 TW, Ti:sapphire Laser at RRCAT”, **M. Tayyab**, S. Bagchi, R. A. Khan, J. A. Chakera, P. A. Naik, and P. D. Gupta, 30th National Symposium on Plasma Science & Technology , SINP, Kolkata, Dec 1-4, **2015**.
6. “Observation of proton flux enhancement in metal-dielectric double layered targets”, S. Bagchi, **M. Tayyab**, A. Upadhyay, C. Mukharjee, J. A. Chakera, P. A. Naik and P. D. Gupta, 24th DAE-BRNS National Laser Symposium , RRCAT, Indore, Dec 2-5, **2015**.

7. "Novel thin foil target for quasi-monoenergetic ion acceleration", S. Bagchi, **M. Tayyab**, A. Upadhyay, C. Mukharjee, J. A. Chakera, P. A. Naik and P. D. Gupta, 24th DAE-BRNS National Laser Symposium , RRCAT, Indore, Dec 2-5, 2015.
8. "Quasi-monoenergetic heavy ion acceleration using ultrashort high intensity laser pulses", **M. Tayyab**, S. Bagchi, A. Upadhyay, B. Ramakrishna, J. A. Chakera, P. A. Naik and P. D. Gupta, First Newton-Bhabha Workshop on High Field Science, Trivandrum, Kerala, Mar 1 - 3, 2016.
9. "Quasi Mono-Energetic Heavy Ion Acceleration From Layered Nano-Targets", **M. Tayyab**, S. Bagchi, M. Nayak , J. A. Chakera, and P. A, Naik, 32nd National Symposium on Plasma Science & Technology (PLASMA 2017), Institute for Plasma Research, Gandhinagar, Nov 07-10, 2017.
10. "Proton Acceleration with Chirped Laser Pulses", **M. Tayyab**, S. Bagchi, R. A. Khan, J. A. Chakera, and P. A, Naik, 32nd National Symposium on Plasma Science & Technology (PLASMA 2017), Institute for Plasma Research, Gandhinagar, Nov 07-10, 2017.
11. "Proton-Boron fusion reaction study using laser accelerated proton beam", **M. Tayyab**, S. Bagchi, A. Moorti, and J. A. Chakera, 27th DAE-BRNS National Laser Symposium (NLS-27), RRCAT Indore, Dec 03-06, 2018.
12. "Short lived radioisotope production using protons accelerated by high intensity laser pulses", S. Bagchi, **M. Tayyab**, A. Moorti, and J. A. Chakera, 27th DAE-BRNS National Laser Symposium (NLS-27), RRCAT Indore, Dec 03-06, 2018.

Tayyab

MOHAMMAD TAYYAB

Name & Signature

of the student

To My beloved Parents

ACKNOWLEDGEMENTS

It is my great pleasure to express my gratitude to all who have helped me directly or indirectly during the course of this thesis work.

First and foremost, I owe deep sense of gratitude to my thesis guide Dr. J. A. Chakera for his kind supervision, advice, guidance and warm hearted support from the very beginning of this work. I am greatly benefited from his experience in laser plasma physics and especially in experimental handling. He has been very kind to find time to critically go through to my draft manuscripts and provide his invaluable suggestion.

The experiments reported in the thesis would not have been successful without active support and involvement of my friend and colleague Dr. Suman Bagchi. I sincerely thank him for his constant encouragement and providing ideas during experiments and invaluable help in writing the manuscripts.

I am thankful to Dr. P. A. Naik former Head, Laser Plasma Division, and former director RRCAT for his kind guidance and encouragement during the course of this work. I am thankful to my Doctoral committee members for their important and useful suggestions from time to time for improvement during the yearly reviews of my thesis work. I am thankful to Dr. Ajit Upadhyay for providing simulation support in some of the results. I thank Mr. Tirtha Mondal, Dr. Bhuvanesh Ramakrishna for his invaluable help during the experiment and manuscript preparation. I am thankful to Mr. R. A. Khan, Mr. R. K. Bhat, Mr. R. A. Joshi, Mr. A. Singla and Mr. S. K. Meena for providing laser support. I am greatly thankful to Mr. R. P. Kushwaha, Mr. S. Sebastin, Mr. D. Karmakar and Mr. K. C. Parmar for providing mechanical support.

Finally, I am very much thankful to my wife for her continuous support. She has taken great pain in taking care of the family during all these years.

CONTENTS

	Page No.
SUMMARY	xi
LIST OF FIGURES	xiii
LIST OF TABLES	xxiv
CHAPTER 1 Introduction to laser driven ion acceleration	1
1.1 Overview of laser driven ion acceleration	2
1.2 Laser energy absorption and hot electron generation	5
1.2.1 Collisional absorption (Inverse Bremsstrahlung)	6
1.2.2 Resonance absorption	9
1.2.3 Vacuum/Brunel absorption	12
1.2.4 $j \times B$ heating	14
1.2.5 Direct Laser Acceleration	15
1.3 Laser Ion acceleration mechanism	16
1.3.1 Target Normal Sheath Acceleration	20
1.3.2 Radiation Pressure Acceleration	26
1.3.3 Laser ion acceleration in relativistic transparency regimes (Break-out afterburner (BOA))	28
1.4 Scope of the present Thesis work	29
CHAPTER 2 Lasers, Experimental setups, diagnostics, and detectors	33
2.1 Laser systems	34
2.1.1 The 10 TW Ti:Sapphire Laser	35
2.1.2 The 150 TW Ti:Sapphire Laser	37
2.2 Laser Pulse Characterization	40

2.2.1	Pulse duration measurement	41
2.2.2	Pre-pulse contrast measurement	42
2.2.3	Laser focal spot measurement	46
2.3	Ion Beam Diagnostics	48
2.3.1	Ion detectors (CR-39, MCP, and RCF)	49
2.3.2	Thomson Parabola Ion Spectrometer	54
2.4	Target Preparation and mounting	68
CHAPTER 3	Studies on proton/lighter ion acceleration using moderate contrast 10 TW, 45fs Laser system	71
3.1	Experimental details	72
3.2	Effect of foil thickness and foil material on proton acceleration	73
3.3	Proton beam collimation using sandwich targets	82
3.4	Conclusion	86
CHAPTER 4	Studies on proton/lighter ion acceleration using high contrast 150 TW, 25fs Laser system	87
4.1	Multi MeV proton and carbon ion acceleration with high contrast laser pulses	87
4.2	Effect of laser temporal shape on ion acceleration	89
4.3	Effect of laser pre-pulse on ion acceleration from thin Mylar foils coated with high Z material	104
4.4	Quasi monoenergetic proton acceleration	108
4.5	Conclusion	114
CHAPTER 5	Quasi mono energetic heavy ion acceleration	116
5.1	Quasi-monoenergetic heavy ions from <i>nano composite</i> targets	116
5.2	Quasi-monoenergetic heavy ions from <i>multilayer</i> targets	130

5.3	Conclusion	139
CHAPTER 6 Negative ion (H⁻) acceleration		141
6.1	H- acceleration from hydrogen containing transparent solid target	143
6.2	H- acceleration from thin foil targets	150
6.3	Conclusion	152
CHAPTER 7 Applications of laser accelerated ion beam		153
7.1	Experimental set up	155
7.2	Short lived ¹¹ C isotope production	157
7.2.1	¹¹ B(p,n) ¹¹ C and ¹⁰ B(d,n) ¹¹ C reaction cross section	157
7.2.2	Experimental Results on ¹¹ C production	158
7.2.3	Discussion	163
7.3	Proton-B fusion Reaction; B ¹¹ (p, 3 ⁻), (Q= 8.7 MeV)	166
7.4	Conclusion	169
CHAPTER 8 Summary and future outlook		171
8.1	Summary	171
8.2	Future Outlook	175
REFERENCES		178

LIST OF FIGURES

Chapter 1

- 1.1 Resonance excitation of electron plasma wave by obliquely incident electromagnetic radiation 11
- 1.2 Illustration of main mechanism of ion acceleration in overdense opaque target including TNSA at back surface, RPA due to hole boring at the laser focus and front surface expansion in blow off plasma 20
- 1.3 Schematic description of RPA. Ion (Red), piled up electron layer (Blue) and generated electric field. Ion in the electron compressed area are accelerated with same velocity 26

Chapter 2

- 2.1 Layout of the 10 TW Ti:sapphire laser system 35
- 2.2 Layout of Pulsar 150 TW laser system 38
- 2.3 Single Shot autocorrelation set up 40
- 2.4 Screen shot of image grabbing and analysis software of SSA *Bonsai* 42
- 2.5 ASE measurement using fast photo diode 45
- 2.6 General scheme of third order cross correlation *Sequoia* 46
- 2.7 The contrast of 10 TW and Pulsar 150 TW laser systems 46
- 2.8 Typical focal spot measured using focal spot imaging setup. (b) 3D plot of focal spot showing the intensity distribution of the focused beam 47
- 2.9 Focal spot/target imaging set up 48
- 2.10 Image of the target rear surface. As the target is placed at 30° angle, therefore right part is slightly blurred 48
- 2.11 Proton beam profile recorded on RCF stacks. Proton energy cut-off is 50

	mentioned with respective layer	
2.12	(a-f) Evolution of the ion signal on CR-39 with etching time. Ion parabola traces of different species were recorded on CR-39 detector used in TPIS	51
2.13	Carbon (a-d) and proton (e and f) tracks/pits of around 1 MeV after different etching time at 50x magnification	52
2.14	Thomson Parabola working principle	55
2.15	Parabola traces of Carbon and H ⁺ and intersecting two constant velocity lines corresponding to 0.5 MeV and 0.2 MeV respectively. The spacing between the intersection points along the particular line is constant for given set of parabolas of an element (here Carbon)	56
2.16	Real image of the developed Thomson Parabola Ion spectrometer connected to main plasma chamber	58
2.17	Magnetic field profile along the length and width of the developed magnet	59
2.18	TPIS resolution	61
2.19	General experimental set up of ion acceleration. Both thin foils and bulk solid material have been used as a target for different experimental investigations. In case of thin foils TPIS was placed along rear surface normal direction whereas for bulk solid target it is placed along front surface normal direction	62
2.20	(a) Parabolic of different species recorded using TPIS. (b) Theoretical parabola fitting using the developed algorithm to identify and reconstruct the ion energy spectrum	63
2.21	Background subtraction in raw TPIS image	64

2.22	Dynamical Noise correction using a parallel shifted parabola for ion traces recorded using Al (a) and Mylar (b) targets. The counts from the parallel shifted parabola are subtracted from real fitted parabola counts for noise reduction (b and c). The blue curves in (b) and (d) represent net counts due to proton signal only. A small hump in green curves is an artefact due to damage in MCP	66
2.21	Energy spectra of different ionic species	67
2.22	(a) Parabolic traces recorded on CR-39 detector. (b) Microscopic view showing individual proton tracks when 250 μm pinhole was used in TPIS. (c) with 100 μm pinhole in TPIS. (d) Calibration of proton spectrum obtained using MCP against absolute CR39 counts	68
2.23	Prepared CD_2 film of thickness around 8 μm	69
2.24	Thin foil mounting holder. Very small holes are due to laser shots	70

Chapter 3

3.1	Experimental set up for proton acceleration from thin foil targets with 10 TW laser system	73
3.2	(a) Ion traces recorded using TPIS from 6.5 μm Al foil and (d) derived energy spectrum	74
3.3	(a) Energy spectra of protons obtained from different Al foils. Variation of proton cut-off energy as a function of thickness is shown in inset. (b) Simulation result from hydrodynamic code Multi 1D showing density evolution of Al foils of varying thicknesses when subjected 1.5 ns ASE pulse with intensity $2 \times 10^{12} \text{W/cm}^2$	75
3.4	Proton energy spectrum obtained using 6.5 μm Al target at different ASE pre-pulse condition. Inset shows the pre-pulse profile at different	77

- opening time of Pockels cell
- 3.5 (a) Hydrodynamic simulation using Multi 1D code showing density evolution of Ni foils of different thicknesses when subjected 1.5 ns ASE pulse with intensity $2 \times 10^{12} \text{W/cm}^2$. The numbers next to line indicate the foil thickness in microns. The symbol (+) on each curve designate the initial position of targets rear surfaces. (a) Comparison of proton energy spectra from Al and Ni foils of 1.5 and 5 μm thickness 78
- 3.6 Proton energy spectrum obtained from (a) 12.5 μm and (b) 25 μm foil of different of different materials 79
- 3.7 Maximum proton energy obtained from different foil materials and thicknesses. The red line is the proton cut-off energy estimated using Mora's model. Other lines (black, blue and magenta) are guide to eye 80
- 3.8 Proton energy spectrum recoded from Al/CH/Al, CH/Al/CH and simple Al foil (a). Proton beam imprint ($>1\text{MeV}$) recorded on RCF from 5 μm thick Al/CH/Al and CH/Al/CH targets and simple 6.5 μm thick Al foil (b) 83
- 3.9 Measured proton beam divergence using the RCF from different targets 84
- 3.10 The phase space distribution of laser accelerated protons from sandwich targets (a) CH/Al/CH and (b) Al/CH/Al at time = $150 /c$ obtained by 2D PIC simulations. The rear surface electrostatic sheath field distribution for (c) CH/Al/CH and (d) Al/CH/Al targets at time = $150 /c$ 85

Chapter 4

- 4.1 Contrast of 150 TW laser in case of single SA and double SA measured 88

	with (a) third order cross-correlator <i>sequoia</i> and (b) fast photo diode coupled with 1GH oscilloscope	
4.2	The ion traces recorded with TPIS using 0.75 μm Al foil (a) without and (b) with second saturable absorber (SA2). The corresponding ion beam profiles are also shown. The proton energy spectra for two cases are shown in (c)	89
4.3	(a) The experimental set up for ion acceleration from thin foils with 150 TW system. (b) The electron trace recorded on DRZ phosphor screen using electron spectrograph along laser forward direction	92
4.4	Laser pulse duration at various detuning positions of compressor grating	93
4.5	Ion traces recorded using TPIS at various pulse duration and chirp, (a) shortest 25 fs pulse, (b) +316 and (c) -316 fs. (d) Derived proton energy spectra	95
4.6	Observed proton cut-off energies at various laser pulse duration and chirp using (a) 0.75 μm Al, 0.4 μm Al and (b) for 1.5 μm Ni foils. Laser intensity variation due to change in pulse duration is shown in top horizontal axis. The circled data points are at shortest (25fs) and unchirped pulse. The blue and red curve are connecting lines for guiding the eye	96
4.7	Full electron beam recoded on DRZ phosphor screen in the laser forward direction at (a) shortest and unchirp 25 fs , (b) +354 fs and (c) -354 fs pulse durations. (d) Measured energy spectra of hot electrons	98
4.8	(a) Third order cross correlation trace of temporally stretched pulses. (b) Estimation of pre-plasma density scale length using HELIOS code	101
4.9	Effect of high Z coating on transparent Mylar foil. (a) Ion traces	106

- recorded with TPIS along with proton beam profile (> 1.4 MeV) recorded on RCF are shown for different condition: (a) laser facing only plain $5\ \mu\text{m}$ Mylar, (b) Au coating front side and (c) Au coating at back side. The proton energy spectra for each case are plotted in (d)
- 4.10 (a) The pre-pulse passes through the transparent Mylar foil. The pre-pulse forms the pre-plasma in high Z material at target front (b) and at target rear side (c) 106
- 4.11 Effect of high Z coating on opaque Al foil. (a) Ion traces recorded with TPIS along with proton beam profile (> 1.4 MeV) recorded on RCF are shown for different condition: (a) laser facing Au coating and (b) laser facing Al and Au coating backside side 108
- 4.12 Schematic of the experimental setup 109
- 4.13 Typical ion signal recorded using TPIS showing different case (a) extended plateau (c) plateau plus hump at high energy side and (e) clean proton bunch. The corresponding proton energy spectrum is shown in (b), (d) and (f) 110
- 4.14 Contrast of 150 system 112
- 4.15 (a) Pinhole imaging by the $100\ \mu\text{m}$ diameter lead aperture. Two different laser shot from $0.75\ \mu\text{m}$ thick Al target showing (b) a clean quasi monoenergetic proton bunch and (c) protons with continuous energy distribution. The zoomed images of neutral spot are shown below the respective shots 114

Chapter 5

- 5.1 TEM image of the nano composite target showing randomly distributed Au nano particles 118

- 5.2 Schematic of experimental set-up representing two separate 119
experiments performed with 45 fs, 10 TW and 25 fs 150 TW Ti:
Sapphire lasers. The ion emission was characterized by Thomson
parabola spectrograph (TPIS) placed along front surface normal
direction
- 5.3 (a) Ion signal recorded from nano-composite target coated on 20 μm 120
thick Al substrate employing 10 TW system. The green dashed curves
are simulated Au ion parabolas. The image part inscribed by white
dotted square is zoomed and contrast enhanced. (b) Energy spectra
calculated from TPIS image showing mono-energetic behaviour of the
Au ions, with all the charge states having the same kinetic energy. (c)
The proton and carbon ion energy spectra exhibiting broad energy
distribution
- 5.4 (a) Characteristic of ion traces recorded using TPIS from plain Au 121
coated target (20 nm Au coating on 20 micron thick Al substrate) using
10 TW laser system and corresponding energy spectra is plotted in (b)
- 5.5 (a) Ion signal recorded from AuNP-Carbon nano-composite targets 123
deposited on 1mm thick Si and (b) corresponding Gold ion energy
spectra. (c) Double mono-energetic heavy Au ion bunches and
corresponding ion energy spectra (d). The green dashed line in (c) is
guide to eye for visualization of two bunched on Au⁴⁺ parabola
- 5.6 (a) Different ASE pre-pulse level. b) Proton energy spectrum at various 125
pre-pulse conditions (c) Au ion spectrum at different levels of ASE
pre-pulse, (d) Influence of laser polarization on Au ion spectrum. It is
evident that in case of horizontal (i.e. p-polarization), the gold ion and

- the proton traces are visible (inset of (d))
- 5.7 Variation of mono-energetic heavy gold ion energy at different fluence 127
level for three different laser pulse durations performed using both 45 fs, 10 TW laser as well as 25 fs, 150 TW laser. In (a) the variation is plotted with respect to laser intensity and in (b) the data is plotted as a function of laser fluence. The black solid line is fit to the data points showing Au ion energy scaling with respect to laser fluence
- 5.8 Schematic experimental diagram showing the geometry of intense, 131
ultra-short laser pulse interaction with layered targets. Simple illustrations showing the target structures; (1) only Au layer on Si of thickness 5, 10 and 20 nm, (2) “Single Layer” target comprises single layers of C and Au (5nm) coated on Si substrate and (3) “Double Layer” target consists of TWO such independent Au and C layers on Si substrate
- 5.9 Typical continuous heavy Au ion spectra obtained with pure Au targets 133
of thicknesses 5 nm and 20 nm. There are no Carbon coatings on these targets. Yellow line drawn from the origin is constant velocity line indicating that maximum energy of lower branch is same for all the charge states. Corresponding Au ion energy spectra for different charges states are shown in (d) - (f)
- 5.10 Effect of Carbon layer thickness on mono-energetic behaviour of Au 135
ions. Two distinct bunches of Au ions are observed. In image (b), Au³⁺ parabola is drawn to show that the two separate bunches lie on a parabola. The similar parabola can be drawn for other charge state as well. Notably, with increase of carbon layer thickness i.e. 10 nm, 20

nm and 40 nm, the relative energy spread of the Au ion bunches reduces as revealed from TPIS images and corresponding energy spectrum

- 5.11 The energy spread of Au ion for first and second bunches with varying carbon layer thickness. The data points represent the individual shots 136
- 5.12 TPIS image recorded from double layer targets showing two sets of bunched Au ions. The corresponding spectra are plotted on right hand side. As a representation each part of the Au³⁺ ion are marked with different colour arrows and numbers to show its place in the energy domain 137
- 5.13 TPIS record with pure Au layer of thickness 5 nm. Two ion population of different characteristic can be clearly noticed. One is having a sharp energy cutoff depicted as a constant velocity line and for other the energy increase with charge states. 139

Chapter 6

- 6.1 Experimental set up used for generating H⁻ ions from PMMA target. The ion emission along the target normal is recorded by Thomson Parabola Ion Spectrograph (TPIS) 144
- 6.2 (a) Typical Thomson Parabola Images recorded on MCP from PMMA target. The presence of H⁻ is evident along with the presence of strong H⁺ trace. The charged states of carbon are also visible but appear as smeared off (see text for details). The ion energy spectra of H⁻ and H⁺ ions are shown in (b) 145
- 6.3 Ion signal recorded on CR-39 detector from PMMA target showing the presence H⁻ of parabola trace along with other positive species. (b) 146

	Tracks formed on CR-39 detector due to the impact of individual H ⁻ ions	
6.4	Microscopic view of neutral spot on CR-39 showing individual tracks/pits formed due to neutral atoms	146
6.5	H ⁻ ions signal at various focal positions of the laser beam. Here “Z = 0” defines the front surface of the sample. Positive Z position indicates that the target has been displaced towards incoming laser direction by a specified distance	147
6.6	Variation of laser intensity with the target position with respective best focus position	147
6.7	Laser pre-pulse effect on negative ion generation	148
6.8	Thomson Parabola image recorded using 25 μm thick Al foil showing clear traces of H ⁻ and H ⁺ . (b) H ⁻ energy spectrum observed from Al foils of different thicknesses	151

Chapter 7

7.1	Outline of experimental set up. After optimization of ion signal the Boron pellet was moved into the beam path for the nuclear reaction to happen. A sheet of CR-39 covered with Al filters of varying thicknesses was placed for alpha particle detection is also shown.	157
7.2	Reaction cross-section for the $^{10}\text{B}(\text{d},\text{n})^{11}\text{C}$ and $^{11}\text{B}(\text{p}, \text{n})^{11}\text{C}$. taken from references [156]	158
7.3	(a) Proton energy spectrum recorded using 1 μm thick Cu foil. (b) Proton beam profile recorded on different RCF layers with respective layer cut-off energies.	159
7.4	(a) Photon energy spectrum recorded with HPGe detector. The	166

measured ^{11}C activity at definite time intervals is shown in (b). The grey line is the theoretical fit.

- 7.5 TPIS images showing ion signal recorded using (a) $1.5\ \mu\text{m}$ Ni/CD₂ 162 target and (b) from $1.5\ \mu\text{m}$ Ni targets. (c) Microscope view of $q/m=0.5$ parabola trace recorded on CR-39 detector depicting individual D⁺ and C⁶⁺ ion tracks. (d) Plotted proton (H⁺) and deuteron (D⁺) ion energy spectrum for both the targets
- 7.6 Recorded ion signal from (a) from $8\ \mu\text{m}$ CD₂ and (b) $8\ \mu\text{m}$ Mylar 163 targets. Plotted proton (H⁺) and deuterium (D⁺) ion energy spectrum for both the targets (c)
- 7.7 Alpha particles track observed on CR-39 detector covered with (a) $6.5\ \mu\text{m}$ 168 Al filter and (b) $12.5\ \mu\text{m}$ Al filter. Very small tracks are due to scattered protons
- 7.8 Extracted alpha particle energy spectrum (alpha particles count are 169 given for a scan area of 1mm^2 on CR-39). Inset shows fusion cross section data [156]

List of Tables

2.1	Parameters of 10 TW and 150 TW laser systems	34
2.2	TPIS design parameters	59
7.1	List of isotopes used for PET application	154
7.2	Range of protons and alpha particles (in microns) in solid Boron	168

CHAPTER 8

Summary and future outlook

In the present thesis research work, detailed experimental investigations on ion acceleration were carried out over a wide range of laser and target parameters. The experiments have been performed using moderate contrast ($\sim 10^{-6}$) 10 TW, 45 fs laser and high contrast ($\sim 10^{-10}$), high peak power 150 TW, 25 fs Ti: Sapphire lasers systems. Several important aspects related to ion acceleration using high intensity ultra-short laser pulses from thin foil target as well as from thick solid targets have been addressed. This includes exploration of different foil material and thicknesses for efficient proton acceleration in TNSA regime, use of multilayer targets for low divergent proton beam, laser temporal pulse shaping for enhancing the accelerated ion energy, quasi monoenergetic proton bunches from collisionless shock acceleration, generation of high flux H^+ ions from hydrogen containing transparent solid targets and first time demonstration of quasi monoenergetic Au ion bunches from nano composite and multilayered targets and finally, application of laser plasma accelerated proton beam in short lived radio-isotope generation and $p - {}^{11}B$ fusion reaction on a table top. The summary and future outlook based on the work reported in this thesis is discussed below.

8.1 Summary

First the optimization of the laser irradiation condition for 10 TW, 45 fs Ti:Sa laser for efficient proton acceleration was performed. An extensive study on the effect of foil thickness and the laser pre-pulse parameters were carried out. Experimental observations on optimum foil thickness for Al and Ni foil targets matches very well

with hydrodynamic simulations. The role of foil atomic number (Z) on proton acceleration has also been investigated. The results show that the judicious choice of the foil material with appropriate thickness can further enhance the ion acceleration efficiency for a given laser system parameters. It was also found that the simple scaling law based on laser intensity and laser pulse parameters are inadequate in predicting the maximum proton energy. In addition we have also observed that a suitable combination of high- Z and low- Z layered targets can give rise to low divergence proton beam.

Next, with 150 TW Ti: Sapphire system, the laser pulse and target parameters were optimized for efficient ion acceleration. In particular, the effect of laser pulse duration and temporal pulse asymmetry on ion acceleration has been studied in detail. It was found that the ion acceleration is not optimum at shortest pulse duration and highest intensity as suggested by the previous intensity scaling laws. Instead temporally stretched pulses are better for efficient ion acceleration. More importantly, we found a contrasting difference with respect to the sign of the laser pulse chirp for almost the same laser pulse duration. We found 60-70% enhancement in maximum ion energy (from 6 MeV to 10 MeV) and more than one order enhancement in flux at that energy with positively chirped 250 - 350 fs stretched pulses. Whereas negatively chirped stretched pulses show monotonic reduction in ion energy and flux. Correlated electron signal measurement also shows similar behaviour as observed for ions. The temporal pulse skewness arising due to change in grating separation of laser compressor was found to be responsible for this asymmetric behaviour.

A contrasting difference of laser pulse contrast on ion acceleration was observed from double layer targets consisting of transparent Mylar foil one side coated high- Z (Au) material. Enhancement of ion energy and flux was observed when

Au coating side was facing the laser. However a drastic reduction in ion energy and flux was observed when the Au coating was at back side. It was established that efficient pre-plasma formation by the laser pre-pulse either on target front (when Au coating at front) or on target rear side (when Au coating back side) is responsible for the contrasting difference on observed ion signal.

We have demonstrated, clean quasi monoenergetic proton bunches of energy around 3 MeV with energy spread around 40%. The laser interaction condition strongly suggests that the collisionless shock wave generated by the intense laser pulse is mainly responsible for the observed plateau and peaks in proton energy spectrum.

A new scheme on energetic (> 100 keV) H^- ion acceleration from intense, femtosecond laser pulse interaction with transparent dielectric targets have been experimentally demonstrated and explored. The method, counterintuitive to conventional H^- production mechanisms, offers low debris, high repetition rate, and consistent production of H^- ions from high density, high temperature plasma. The dependence of H^- production on the external laser focusing conditions and laser pre-pulse level indicates that H^- ions are formed due to the recombination of protons which are accelerated by the sheath field at the target surface. The accelerated H^+ while coming out of the ambient PMMA medium captures extra electrons from the co-propagating electron population to produce H^- ion. The total H^- flux estimated from CR-39 detector was found to be $\sim 10^{11}$ per shot in 4 sr. In addition H^- generation from rear surface of the thin foil was also demonstrated. The observation of H^- from thin foil targets strongly suggest that the protons (H^+) accelerated by TNSA mechanism, capture extra electrons from co-propagating electron population and become H^- .

Quasi monoenergetic heavy Au ion acceleration with different charge states of Au accelerated to the same energy using nano-composite and multilayer targets have been demonstrated for the first time. This is completely a new way to produce monoenergetic bunches of heavy ions from freely expanding laser produced plasmas. It was established that the presence of low-Z carbon layer is necessary for obtaining quasi monoenergetic features in Au ion energy spectrum. The experimental observations suggest that the Au ions are mainly accelerated by the piston effect of the hydrodynamically expanding hot plasma. The Au ions being confined in a narrow region feels the same accelerating forces. During the expansion they also feel the tamping force due to the background plasma corona. All this ultimately leads to quasi monoenergetic features in Au ion energy spectrum with all the charge states having identical energies. The present technique employs a nano-composite thin film (consisting of AuNPs embedded in C matrix) and Au-Carbon multilayer on Si or Al substrates. The target fabrication is quite simple, reliable, and produces consistent quasi monoenergetic Au ions accelerated to ~ 400 keV energy using sub 100 TW laser. Furthermore, the present approach does not require any complicated alignment or very advanced target engineering and hence can easily be operated at higher repetition rates.

Finally, application of laser accelerated ion beams viz. proton and deuteron in nuclear reactions has been demonstrated. The ^{11}C radio-isotope generation utilizing laser produced deuterons and protons beams was studied via $^{10}\text{B}(\text{d}, \text{n})^{11}\text{C}$ and $^{11}\text{B}(\text{p}, \text{n})^{11}\text{C}$ reactions respectively. We observed maximum activity of 5.2 kBq of ^{11}C in single laser shot employing $^{11}\text{B}(\text{p}, \text{n})^{11}\text{C}$ reaction that corresponds to $\sim 9 \times 10^6$ atoms of radioactive isotopes. It was also established that foil targets loaded with deuterium can increase the radio isotope production. In this regards around 30% increase in ^{11}C

production was demonstrated employing 1.5 μm Ni/CD₂ target as compared to bare 1.5 μm Ni target. It was estimated that a high peak power laser operating at 100 Hz repetition rate, can generate around 1 GBq activity in \sim 15 minutes. This looks possible once the laser systems with high repetition rate and high peak power become commercially available. The α -particles produced in fusion reaction involving proton and boron were also characterized. More than 10^7 α particles in single laser shot have been observed. The present work shows that laser driven proton beam can be useful in studying many important reactions such as p-B fusion reaction which is quite promising for futuristic power generation.

8.2 Future Outlook

Laser driven ion acceleration research aiming for compact and cost effective ion source possessing unique characteristics have been actively pursued since last two decades. During this period, continuous improvement in the accelerated ion beam qualities and better understanding of the underlying acceleration physics have been achieved. Proof of principle applications of laser plasma driven ion beam have been demonstrated and several new applications have been proposed. However, for practical applications on a routine basis, still there is a long way to go. Therefore, a continuous and sustained effort is very much required in order to have better control over different ion beam parameters like maximum accelerated ion energy and overall energy spectrum, total beam charge, conversion efficiency, accelerated species and shot to shot repeatability and stability. In this regards, several experimental studies performed in the present thesis work motivates for further studies including both theoretical as well experimental.

Effect of laser temporal pulse shape on ion acceleration from thin foils in TNSA regime can be investigated in more detail. This will include the generation and full characterization of temporally skewed pulses. We believe that such studies can be very important for modern ultra-short pulse high power lasers. The observation of clean quasi monoenergetic proton bunches through collisionless shock wave in a simple experimental geometry is an important outcome which can be further investigated. As the quasi monoenergetic signature in proton energy spectrum was not observed in every shot possibly due to the shot to shot fluctuations in pre-pulse condition, on target intensity and in accurate target positioning. Therefore, PIC simulations can be carried out to correctly model the experimental conditions with slight variation in the mentioned parameters, and pin point the exact interaction geometry for obtaining quasi monoenergetic proton bunches. This will provide deeper understanding and may help to achieve high repeatability and scope for further optimization. Further, it would be interesting to perform similar ion acceleration experiments with 1 PW Ti: Sapphire laser with further higher laser intensity which is currently under installation in laboratory.

One of the most important outcomes of the present thesis work is the demonstration of quasi monoenergetic Au ion acceleration using nano composite and multilayer targets. The work is not only interesting for ion source point view but it also contains interesting physics behind the multi species hot plasma expansion. Theoretical and simulation studies can be performed to model the multispecies hot plasma expansion including the background fictional forces and charge recombination. This work can be extended for other heavy materials as well. Effort can be made to accelerate few MeV ions using slightly high energy lasers at few hundred fs pulse duration. In this

case it might be interesting to see the competition between different acceleration mechanism at higher laser fluence and intensity.

The work on negative H^- ion production from hydrogen containing transparent solid targets can be extended with high repetition rate laser to increase the overall H^- flux which may be useful for immediate applications. The deuteron acceleration can be further optimized by controlling the surface contaminants. As the energy threshold for ^{11}C isotope production is quite low, therefore efforts can be made to get the useful isotope production through deuteron acceleration and using ^{10}B enriched targets.

SUMMARY

The present thesis work primarily deals with proton/ion acceleration from solids, thin foils and specialized nano structured targets using 10 TW, 45 fs and 150 TW, 25 fs Ti:Sapphire laser systems at RRCAT. The major findings of the thesis include the acceleration of quasi monoenergetic heavy ions which have been demonstrated for the first time. The dependence of lighter ion (H^+ and C^{1-6+}) acceleration on various laser and target parameters have been investigated. The important roles played by foil material and laser temporal shape on proton acceleration are identified. Quasi monoenergetic proton bunches with mean energy about 3 MeV and energy spread around 40% was demonstrated. By controlling the laser irradiation parameters, generation of negative H^- ion from solid targets have been demonstrated. Application of laser accelerated proton and deuteron beam in short lived positron emitting radioisotope isotope production and proton-boron fusion studies are demonstrated.

Initial ion acceleration studies were started on 10 TW Ti: Sapphire laser system to optimize the experimental parameters related to laser-foil interaction. Foils of different materials and thicknesses have been used to achieve maximum H^+ /proton energy. In particular, it was also found that a wise selection of foil material or atomic number Z can improve the proton acceleration efficiency, thereby increasing the accelerated proton/ion energy. By suitably adjusting the laser irradiation parameters, H^- ions of more than 100 keV energy was observed from solid targets. Later the ion acceleration studies were carried out at higher laser intensities using 25 fs, 150 TW laser system. Maximum recorded H^+ ion energy was around 10-11 MeV while C^{5+} ion yielded a maximum energy of 14.5 MeV. Effect of laser intensity, pulse contrast and pulse duration/ laser chirp have been studied in details. In particular, significant enhancement of ion energy from thin foil targets was observed by adjusting the laser

temporal characteristics. Remarkably, in certain laser pre-pulse conditions and highest laser intensities $\sim 10^{20}$ W/cm², quasi-monoenergetic proton bunches with total energy spread less than 40% were also observed. In a typical laser ion acceleration experiment protons (H⁺) having highest q/m ratio are the most dominant species. In general they have broad energy distribution. Contrary to the conventional observation, acceleration of quasi mono-energetic heavy gold ions to sub MeV energies have been demonstrated for the first time from gold-carbon nano-composite and multilayer targets irradiated at moderate laser intensities of 10^{18} - 10^{19} W/cm². Next, applications of laser driven proton beam were explored by employing 150TW Ti:sa laser system. In this regard an experimental study on p-Boron fusion reaction was carried out and the accompanying alpha particle flux and energy distribution have been characterized. Short lived ¹¹C (positron emitter) radioisotope generation employing laser produced deuteron and proton beam utilizing ¹⁰B(d,n)¹¹C and ¹¹B(p,n)¹¹C reactions have also been studied. About 5.2 kBq activity of ¹¹C radio-isotope was produced in a single laser shot through ¹¹B(p, n)¹¹C reaction. This represents $\sim 9 \times 10^6$ atoms of ¹¹C radio-isotopes. The relative effectiveness of laser produced deuteron and proton beam in producing ¹¹C radio-isotope are also investigated.

CHAPTER 1

INTRODUCTION TO LASER DRIVEN ION ACCELERATION

Particle accelerators have immense contribution in the exploration of fundamental structure of matter. The human curiosity about the subatomic world was the main driving force behind the development of large scale accelerator facilities. Although, initially developed for performing nuclear and particle physics experiments, in recent years accelerators have found applications in other branches of scientific research, industry and medical field [1, 2]. In high energy accelerators charged particles gain energy from longitudinal electric field set up in RF cavities. To increase the energy charge particle are made to pass through the acceleration gap many times resulting in two different accelerator configuration which are classified as linear (LINAC, RFQ) and cyclic accelerators (cyclotron, synchrotrons). These accelerators are very large and expensive devices limited to only large laboratories, industries and hospitals. Therefore, to take full advantage of particle accelerators particularly for societal benefits a path breaking improvement in size and the cost of accelerators are required. Recently, a new scheme of particle acceleration based on high intensity ultra-short laser pulses has attracted considerable attention worldwide [3], [4]. The laser driven ion accelerators have the potential to be a compact and cheaper alternative because of very high accelerating field gradient \sim TV/m (about 10^6 times higher than convention RF fields). Some unique characteristics like ultra-short pulse duration (\sim ps), high peak current (\sim kA), small source size (\sim few microns) and very small transverse emittance have opened new set of applications like ultrafast proton radiography [5], [6], probing highly transient field inside the plasma [7], [8] and study of warm dense matter [9]. The other potential applications includes ion beam cancer therapy [10]–[13], short

lived isotopes production for medical diagnosis [14], nuclear and particle physics and ion beam fast ignition [15], [16]. Although, the potential is enormous, very substantial improvements is still necessary for laser driven ion source to be successfully applied in various applications envisaged above. For example, ion beam more than 100MeV/nucleon and beyond with few percent energy spread and flux $>10^{10}$ particles/second is required for ion beam cancer therapy. A significant improvement in average ion beam power is required for most of the potential applications. Therefore a thorough understanding and control of the ion acceleration process coupled with progress in high peak power laser development is very much essential. Much experimental and theoretical work needs to be done with the aim to increase the accelerated ion energy and conversion efficiency, reduction in energy spread and spectrum control employing some advanced acceleration mechanism and target engineering. In the following section, a brief background of the earlier works on ion acceleration is presented.

1.1 Overview of laser driven ion acceleration

The generation of fast ions with nano second Nd: glass and CO₂ lasers in the intensity range of 10^{14} to 10^{16} W/cm² have been performed in early 70's [17]. The accelerated proton or ion energy was in the range of several 10's to 100's of keV range emitted in large cone angle ($> 45^\circ$) in the blow off plasma direction. These studies were mainly carried out in the context of direct drive laser fusion scheme in which generated ions contains a significant amount of absorbed laser energy. With the implementations of mode-locking [18] along with Chirped Pulse Amplification technique given by D. Strickland and G. Mourou in 1985 [19], high power laser systems having picoseconds and femtosecond pulse duration were available. In 1990's, ions with several MeV energies had been observed in many high intensity laser matter interaction

experiments for different types of targets including thick solid target [20], gas targets [21] and nano-meter sized clusters [22]. In case of solid targets, protons and heavier ion were mostly detected from target front surface (laser backward direction). The emitted ions have broad angular distribution and their origin was interpreted in terms of acceleration associated with fast electron driven plasma expansion into vacuum. Similarly the accelerated ions in gas jet and cluster targets are produced by the Coulomb explosion of plasma channel created by the high intensity laser pulse with characteristic isotropic ion emission. Low brilliance and rather isotropic ion emission common to these experiments, makes these configuration unattractive as an ion source for various application.

Laser driven ion acceleration has attracted considerable attention after three different groups [23]–[25] independently observed intense, collimated multi-MeV proton beam from micrometer thick solid foils irradiated by high intensity laser pulses in the year 2000. More than 10^{13} protons with maximum energy up to 58 MeV were observed. The resulting proton beam was detected at the target rear side i.e. along the forward direction of the laser propagation. The source of these protons was hydrocarbon contamination which is normally present on target surface under normal experimental conditions. Proton are accelerated by the space charge field formed at target rear surface generated by high energy electrons accelerated at target front surface, propagating through the target and escaping in vacuum from rear surface of the thin foil target. This process is referred to as Target Normal Sheath Acceleration (TNSA) [26] and will be described in more detail in coming section. Since then, many experiments have been performed under different experimental conditions which have helped in deeper understanding of laser driven ion acceleration physics. These studies also showed that these sources possess a extremely interesting characteristics [3], [4]:

- ❖ Extremely high acceleration field \sim TV/m as compared to \sim few 10's MV/m for RF cavities, hence the acceleration process is intrinsically compact (few MeV acceleration over few microns)
- ❖ Relatively low, energy dependent divergence ($<10^\circ$ for tense of MeV protons) that can be further modulated using specialized targets.
- ❖ High particle flux per bunch ($>10^{13}$).
- ❖ Extremely short duration (\sim ps), useful for high resolution pump probe experiments.
- ❖ Low transverse emittance <0.004 mm mrad (100 times better than conventional RF based accelerators).
- ❖ Smaller source size, characteristic equivalent to laminarity that allows achieving excellent spatial resolution for radiographic applications.
- ❖ Very high peak current at the source (\sim kA).
- ❖ Broad energy distribution (but can be modulated using advanced target engineering).

Many applications of laser driven ion beam have been proposed which include ion beam cancer therapy, radioisotope production for PET applications, fast ignition of inertial confinement fusion targets, as an injector to conventional accelerators, proton radiography and production of warm dense matter for astrophysical studies. Among the applications, which have been already demonstrated are, the proton radiography of compressed fusion target and transient electric field detection in plasmas and isochoric heating.

The TNSA accelerated proton/ion beam usually exhibit broad energy distribution and accelerated energy is not sufficiently high. By in-situ target engineering quasi-monoenergetic spectra have been generated but with low energy and flux which is not

adequate for various applications [27], [28]. The maximum proton energy reported so far through TNSA is about 85 MeV using 0.5 ps and 200 J laser pulses [29]. To further improve the maximum ion energy, ion flux, and conversion efficiency, other ion acceleration mechanisms have been proposed such as Radiation Pressure Acceleration (RPA) [30], [31] and Collision-less Shock Acceleration [32], [33]. One more proposed scheme is Break -Out Afterburner (BOA) [34] regime in which there is a strong volumetric heating of relativistically transparent thin target by the ultra-intense laser pulse leading to stronger accelerating field for ions. The basic physics of these acceleration mechanisms and related work will be discussed in later sections. Although there are many ion acceleration regimes as mentioned above, however the present thesis research work is mostly confined to TNSA regime only. In a typical laser ion acceleration experiment involving TNSA proceeds via laser energy absorption and hot electron generation at target front, propagation of hot electrons through the foil material and escaping of the hot electrons at the rear leading to sheath field formation at the target rear surface. Therefore, in the following sections laser energy absorption and hot electron generation process will be discussed.

1.2 Laser energy absorption and hot electron generation

After plasma formation by laser through various ionization mechanisms, the subsequent laser energy is absorbed into the plasma through different absorption mechanisms leading to generation of high energy electrons. The laser field accelerated electrons have much higher temperature than the bulk plasma temperature and are referred to “hot electrons”. It plays a very important role in ion acceleration process. The laser energy absorption and hot electron generation is very complex process which depends on several laser and target parameters like laser intensity, polarization, pulse duration, wavelength, laser pulse contrast, density scale length, initial target

structure and laser incidence angle. In this section, some important process of laser energy absorptions and hot electron generation by various processes will be briefly discussed.

1.2.1 Collisional absorption (Inverse Bremsstrahlung)

The collisional absorption is more effective for laser intensities 10^{12} - 10^{14} W/cm² and for long plasma density scale length $L/\lambda \gg 1$. For high intensity $> 10^{17}$ W/cm² and femtosecond laser pulses it hardly plays any role. However, the absorption of nano second Amplified Spontaneous Pre-pulse (ASE) preceding the main fs pulse is mostly absorbed by collisional process.

When an intense laser pulse interacts with matter, instantaneous ionization of the material takes place by various processes such as, multi-photon ionization (MPI), tunnelling ionization (TI), over the barrier ionization (OTBI) etc. and leading to generation of electrons and ions. These electrons can further interact with the laser pulse and subsequently transfer laser energy in to the materials via collisions. The liberated electrons oscillate with the laser field. The uniform oscillatory velocity is randomized through collisions with ions which lead to heating. This process is repetitive, and thus rapid plasma formation is takes place through avalanche mechanisms. Thus the laser pulse energy is getting absorbed by the electron-ion collisions and leading to rise in the bulk plasma temperature. This process is also called Inverse bremsstrahlung which is opposite of bremsstrahlung radiation emission process where charge particle energy converted into high energy photons. To visualize the role of these collisions in coupling of laser energy to plasma, we consider a simple model. We consider i) plasma is infinite and homogeneous ii) ions are immobile, iii) no static external electric and magnetic field is present. Under these

assumptions, the equation of motion for the electrons can be written as $\frac{dv}{dt} = -\frac{eE}{m} - \frac{v}{\tau_c}$.

Here $\tau_c (= \nu_{ei}^{-1})$ is the effective time between the electron-ion collisions and ν_{ei} is the electron ion collision frequency. τ_c can be expressed as [35]

$$\tau_c = \frac{1}{\nu_{ei}} = \frac{3}{4} \frac{(k_B T_e)^{3/2} m_e^{1/2}}{(2\pi)^{1/2} Z_i^2 e^4 n_i \ln \Lambda} \cong 3.44 \times 10^5 \frac{T_e (eV)^{3/2}}{Z_i^2 n_i \ln \Lambda} \text{ s}; \quad (4)$$

where, n_i is the ion density, Z_i is the degree of plasma ionization, T_e is the electron temperature, $\ln \Lambda$ is the Coulomb logarithm defined as $\ln \Lambda = \ln (b_{\max}/b_{\min})$ and evaluated from the integration over the whole range of scattering angles and λ_D is the Debye length. The impact parameter b is defined using characteristic length in plasma, and in the classical approximation $b_{\min} = \lambda_{ia}$ (interatomic distance) and $b_{\max} = \lambda_D$. Now to derive the dispersion relation in the simple plasma model including effect of collisions, one has to solve Maxwell's equations in free space containing the electric charge and the electric current. After solving, the dispersion relation for transverse waves yields:

$$k^2 = \frac{\omega^2}{c^2} - \frac{\omega_p^2}{\omega^2 + i \nu_{ei}} \quad (5)$$

Now for low density plasma, $\nu_{ei} \ll \tilde{\omega}_L$ a first order Taylor expansion yields:

$$k^2 \cong \frac{\omega^2}{c^2} \left(1 - \frac{\omega_p^2}{\omega^2} + \frac{i \nu_{ei} \omega_p^2}{\omega^3} \right) \quad (6)$$

Further simplification of this equation leads to:

$$k \cong \pm \frac{\omega}{c} \left(1 - \frac{\omega_p^2}{\omega^2} \right)^{1/2} \left\{ 1 + i \left(\frac{\nu_{ei}}{2\omega} \right) \left(\frac{\omega_p^2}{\omega^2} \right) \frac{1}{1 - \omega_p^2/\omega^2} \right\} \quad (7)$$

For an electromagnetic wave, $E = E_0 \exp(ikz)$, using the value of k vector derived above one can write

$$E = E_0 \exp(ik_{real}z) \exp(-k_{imaginary}z)$$

or

$$I = I_0 \exp(-2k_{imaginary}z)$$

i.e. light is absorbed in the plasma as it propagates inside the plasma. Therefore, the inverse bremsstrahlung coefficient or the spatial damping rate of the laser energy by collisional absorption, k_{ib} , can be expressed as:

$$k_{ib} = 2k_{imaginary} = \left(\frac{\nu_{ei}}{c} \right) \left(\frac{\frac{2}{2}}{\frac{2}{L}} \right) \left(1 - \frac{\frac{2}{2}}{\frac{2}{L}} \right)^{-1/2} \quad (8)$$

Now using the definition of critical density,

$$n_{cr} = \frac{m_e}{4\pi e^2} \frac{\omega^2}{\mu} \cong \frac{1.1 \times 10^{21}}{2} \text{ cm}^{-3}$$

the laser energy damping rate can be written as:

$$k_{ib} = \frac{\nu_{ei}(n_{cr})}{c} \left(\frac{n_e}{n_{cr}} \right) \left(1 - \frac{n_e}{n_{cr}} \right)^{-1/2} \quad (9)$$

Note that the dependence of k_{ib} on n_e/n_{cr} signifies that a significant fraction of absorption takes place in the vicinity of critical density, $n_e/n_{cr} \approx 1$. Now consider the change in laser intensity I , as it passes through a slab of plasma in z direction (laser propagation). The change in laser intensity can be expressed as $\frac{dI}{dz} = -k_{ib}I$. For a

plasma slab of length L , the absorption coefficient α_{abs} can be written as

$$\alpha_{abs} = \frac{I_{in} - I_{out}}{I_{in}} = 1 - \exp\left(-\int_0^L k_{ib} dz\right)$$

(10)

Where, I_{in} and I_{out} are the incident and outgoing laser intensities respectively. Therefore, in case of weak absorption ($k_{ib}L \ll 1$), $\alpha_{abs} \approx k_{ib}L$ and for strong absorption case $\alpha_{abs} \approx 1$.

Please note that for inhomogeneous plasmas, the expression for rate of energy deposition is far more complicated, as it not only depends on the electron density, but also on plasma temperature, and time evolution of the expanding plasmas. Now for a linear plasma density profile,

$$n_e = n_{cr} \left(1 - \frac{z}{L} \right); 0 \leq z \leq L;$$

the absorption coefficient can be expressed as[35]

$$_{abs} = 1 - \exp \left\{ - \frac{32}{15} \frac{_{ei}(n_{cr})L}{c} \right\}$$

Similarly for an exponential density profile of

$$n_e = n_{cr} \exp \left(- \frac{z}{L} \right);$$

the absorption coefficient can be expressed as

$$_{abs} = 1 - \exp \left\{ - \frac{8}{3} \frac{_{ei}(n_{cr})L}{c} \right\}$$

At higher intensities ($I > 10^{15}$ W/cm²), the oscillatory velocity of an electron becomes comparable to thermal velocity $v_{th} = \sqrt{kT_e/m_e}$. In this case an effective temperature can be defined as $T_{eff} \propto v_{th}^2 + v_{osc}^2$, accounting the total energy of the electron. Hence the increase in temperature reduces the collision frequency ($_{ei} \propto T^{-3/2}$). That means as the plasma temperature increases, collisional absorption becomes less and less effective.

1.2.2 Resonance absorption

The laser light can be absorbed via resonance absorption in the plasma. This absorption mechanism dominates for high plasma temperature i.e. high laser intensities ($>10^{15}$ W/cm²) and for short plasma density scale length. Moreover, in

contrast to collisional absorption which leads to heating of all plasma electrons, in resonance absorption the laser energy is primarily absorbed by a small fraction of plasma electrons resulting in the creation of hot electrons (with energy much higher than the background plasma electrons).

In Resonance absorption a p polarized laser pulse incident obliquely on the plasma with a density gradient. The laser pulse gets reflected at $n_R = n_{cr} \cos^2 \theta$ as illustrated in Fig. 1.1 (a). Here θ is the incident angle with respect to density gradient ($\vec{\nabla} n_e$) direction. Though the laser is totally reflected at $n_{cr} \cos^2 \theta$, but the evanescent field exists in the plasma. The evanescent field can propagate up to certain distance beyond the reflecting layer (Fig. 1.1 (b)). Since the origin of the evanescent wave is the electromagnetic wave itself, the evanescent wave also has the same angular frequency as the laser field. If this evanescent wave can reach the critical density layer, then at that point the plasma oscillation frequency equals the incident laser frequency i.e. the driver (electromagnetic wave) frequency. This matching yields a strong resonance excitation of electron plasma wave analogous to the forced harmonic oscillator scenario. The solution of the Maxwell equation in dielectric plasma medium easily shows the existence of singularity in the electric field at critical density surface

$$\vec{\nabla} \cdot \vec{D} = 0 \quad \Rightarrow \quad \vec{\nabla} \cdot \epsilon \vec{E} = \epsilon \vec{\nabla} \cdot \vec{E} + \vec{E} \cdot \vec{\nabla} \epsilon = 0$$

Therefore, one can write $\vec{\nabla} \cdot \vec{E} = -\frac{1}{\epsilon} \vec{E} \cdot \vec{\nabla} \epsilon$.

Now the dielectric constant of the plasma is related to plasma density by the relation

$$\epsilon = 1 - \frac{\omega_p^2}{\omega^2} = 1 - \frac{n_e}{n_{cr}}$$

We have $\vec{\nabla} \cdot \vec{E} = -\frac{1}{\epsilon} \vec{E} \cdot \vec{\nabla} n_e$

Hence, for excitation of electron plasma wave, one requires, $\vec{E} \cdot \vec{\nabla} n_e \neq 0$. The resonance condition is only for p polarized laser light where the electric field along the density gradient does not vanish ($\vec{E} \cdot \vec{\nabla} n_e \neq 0$) but the plasma dielectric function can be zero ($\epsilon = 0$, at $\omega = \omega_p$). At reflection point ($\theta = 90^\circ$), there is strong charge separation due to the electric field component along the density gradient and electrons oscillates resonantly with laser field. Therefore, the p-polarized radiation resonantly excites electron plasma wave at the critical density surface. Consequently, large numbers of plasma electrons are trapped in the plasma wave and get accelerated along the density gradient i.e. along the target normal direction.

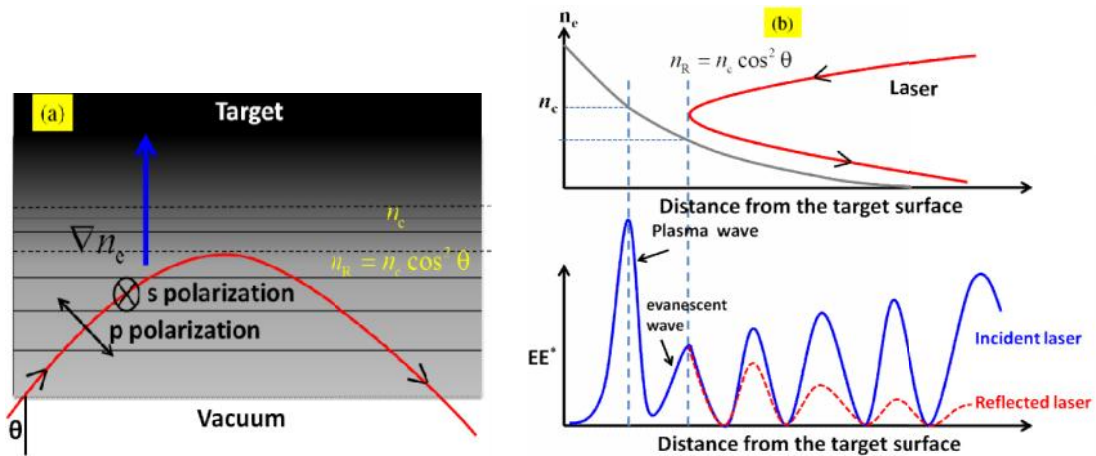


Figure 1.1: Resonance excitation of electron plasma wave by obliquely incident electromagnetic radiation.

For s-polarized incident electromagnetic wave, there is no component of the electric field along the plasma density i.e. $\vec{E} \cdot \vec{\nabla} n_e = 0$. Therefore s-polarized electromagnetic wave cannot excite electron plasma wave. From the condition of excitation of electron plasma wave $\vec{E} \cdot \vec{\nabla} n_e \neq 0$, we can see that for small angle of incidence of p-polarized electromagnetic wave, the component of the electric field along the plasma density gradient is small and hence, the resonance absorption will also be small. While for

larger angles of incidence, the total internal reflection takes place from a larger distance from the critical density layer, n_{cr} . This results in weaker coupling of evanescent wave amplitude that can reach to the critical density surface leading to excitation of electron plasma wave. So there exists an optimum angle for a given plasma density scale length where the resonance absorption maximizes. This optimum angle is given by $\sin \theta = 0.8 [c / \omega L]^{1/3}$ where L is the plasma density scale length [36]. This expression of the optimum angle of incidence can be re-written as $(k_L L)^{1/3} \sin \theta = 0.8$. So we can see that for large density scale length ($L > L_c$), the resonance absorption occurs in small range of angles around the optimum angle. On the other hand, for ($L < L_c$), the laser light can reach very close to the critical density layer. Hence the resonance absorption can occur over a broad range of angles of incidence [37].

We have seen, because of the resonance absorption mechanism a strong electron plasma wave is generated which can couple the laser energy to the plasma by collisions, collisionless mechanisms such as Landau damping, wave breaking etc. The temperature of fast (hot) electron component due to resonance absorption is observed to scale as [38]

$$T_{hot} \approx 10 \left[T_{keV} I_{15} \lambda_{\mu} \right]^{1/3} keV$$

Where T_{keV} is the background electron temperature in keV, I_{15} is the laser intensity in units of 10^{15}W/cm^2 and λ_{μ} is the laser wavelength in microns.

1.2.3 Vacuum/Brunel absorption

Resonant absorption may not be possible in the case of ultrashort laser pulse incident on a plasma having a very sharp plasma density gradient. In fact, if the density scale

length is much less than laser wavelength, a proper oscillation in the resonant field cannot be sustained. In this scenario another collisionless absorption mechanism was proposed by Brunel in 1987 [39]. The laser light non resonantly couples with plasma and a significant amount of energy can be transferred to the plasma electrons. This mechanism is also known as Brunel heating or not-so-resonant resonance absorption and is valid for ultrashort high intensity laser pulses interacting with steep plasma interface with scale length L_p smaller than quiver electron amplitude ($L < x_{osc} = eE_0/m_e \omega$).

In vacuum heating, a p -polarized laser pulse is focused under oblique incidence onto a solid target with a steep density gradient, i.e. a short scale length, L_p , of the order of the laser wave length. The electrons at the target or at critical density surface are pulled into vacuum in first half-cycle and pushed into the target in the second half-cycle by the component of laser electric field perpendicular to the target surface in every laser cycle. The electrons re-enter into the target with a velocity $v_{osc} = eE_0/m_e \omega$ which is the quiver velocity associated with the laser field in the vacuum. The electrons do not feel any restoring force during the second laser half cycle and irreversibly accelerated into the target as the laser can penetrate into the target only upto skin depth. As the electrons are accelerated in each laser cycle, hence in this case bunches of electrons are injected into the target with a frequency equal to the laser frequency. Brunel [39] empirically found that absorbed fraction of the laser energy is given by

$$f_{vh} = \frac{1}{2} \frac{v_{osc}^3}{v_d^2 c \cos \theta}$$

Where η is efficiency factor which measures the fraction of oscillatory energy converted in plasma heating and $v_d = eE_d/m_e \omega = 2v_{osc} \sin \theta$. Initially, Brunel estimated

≈ 1.75 and detailed calculation by Kato et al. [40] led the value to be $\eta \approx 1 / (1 - \omega^2 / \omega_p^2)$ emphasizing the importance of density on absorption.

1.2.4 $\mathbf{j} \times \mathbf{B}$ heating

As mentioned earlier that at lower laser intensity the electrons oscillate along the direction of the electric component, at higher laser intensity the $\vec{v} \times \vec{B}$ component of Lorentz force turn significant and electron motion will have a component along the laser propagation direction. A similar laser absorption process as reported by Brunel can occur. This mechanism is also applicable at normal incidence but here electrons are pushed through the plasma vacuum interface by the magnetic field rather by the electric field. The heating is associated with oscillating component of the pondermotive force which is for linearly polarized wave $E = E_0(x) \hat{y} \sin t$ is given as

$$f_p = -\frac{m}{4} \frac{\partial}{\partial x} v_{osc}^2(x) (1 - \cos 2t)$$

The first term on right hand side is the DC pondermotive force which pushes critical density surface inward. The second term which oscillates at twice of the laser frequency leads to heating in the same fashion as the p polarized electric field parallel to the density gradient. The $\vec{j} \times \vec{B}$ term works for any polarization apart from circular and is more effective at normal incidence and for relativistic intensities.

The heated electrons have characteristic temperature of the order of pondermotive potential.

$$T_{hot} \approx 0.511 \left(\sqrt{1 + \frac{I^2}{1.37 \times 10^{18}}} - 1 \right) \text{MeV}$$

1.2.5 Direct Laser Acceleration

Another absorption mechanism which can be effective in near critical density plasma or in high density gas jet targets and at high laser intensities is the Direct Laser Acceleration [41]. This can also be applicable in high intensity laser solid interaction where there is long density scale length pre-plasma on the solid surface [42]. The pre-plasma can be either naturally present due to undesirable laser pre-pulses preceding the main pulse or using separate low intensity laser before the main high intensity laser. In this mechanism the electrons are accelerated to energies considerably higher than the pondermotive energy which increases with the distance that laser pulse travels in the underdense medium.

When a high intensity laser pulse having frequency ω propagates in underdense plasma having plasma frequency $\omega_p (= \sqrt{n_e e^2 / \epsilon_0 m})$, it undergoes relativistic self-focussing as soon as the laser exceeds certain critical value given as $P_c(\text{GW}) \approx 0.17 (\omega / \omega_p)^2$. The self-focussing is caused by the increase in mass of the plasma electrons due to relativistic effects ($m = \gamma m_0$) as well as due to pondermotive force ($F_p = - (e^2 / 2c\epsilon_0 m \check{S}^2) \nabla I$) which expels the plasma electrons from the laser pulse axis. For a high power short pulse laser focussed to ultra-high intensity, the motion of the electrons are relativistic and the Pondermotive force is quite large due to laser intensity gradient. The increase in electron mass/inertia due to relativistic effect and decrease in electron density leads to decrease in local plasma frequency. This in turn increases the plasma refractive index $\gamma = \sqrt{1 - (\check{S}_p / \check{S})^2}$ and then the plasma acts as positive lens. The self-focussing of the laser pulse continues until it is counterbalanced by increased natural diffraction on account of reduced laser spot size.

In this way the laser pulse is self-guided in the plasma and remains tightly focussed for over several Raleigh lengths.

Laser self-focussing and guiding creates a plasma or ion channel. The characteristic feature of the formation of ion channel is the presence of self-generated strong quasi-static fields. The removal of electrons from the channel due to the laser pondermotive force generates electric field in radial direction. At the same time azimuthal magnetic field is also generated due to the electron currents in laser propagation direction because of laser $\mathbf{v} \times \mathbf{B}$ force. The relativistic electrons inside the channel experience transverse betatron oscillations at frequency $\omega = \omega_p / \sqrt{2}$ (here γ is the relativistic factor) in self-generated quasi static electric and magnetic fields [43]. The oscillating electrons are confined to the ion channel due to the net focussing force. When betatron frequency of oscillating electrons matches with laser frequency as observed in moving electron's frame of reference, an effective energy transfer from the laser to electrons can occur. The electrons resonantly gains energy from the transverse electric field of the laser. The transverse motion of the electrons gets converted into longitudinal motion by the laser magnetic field through $\mathbf{v} \times \mathbf{B}$ force. This process of laser energy absorption is known as Direct Laser Acceleration (DLA) (more details can be found in ref [42] and [44]). The DLA mechanism produces electrons with an exponential energy distribution.

1.3 Laser Ion acceleration mechanism

The electrons being the lightest particle quickly responds to the laser electric field compared to ions which are much heavier and cannot follow the laser electric /magnetic fields. Hence direct ion acceleration by the laser field is impossible. To understand this fact more clearly, let us recall the pondermotive potential (oscillatory

energy in the laser electric field) and proton mass which is lightest of all ions, one can derive approximate threshold intensity for direct laser ion acceleration to relativistic energies. The pondermotive energy of an electron

$$U_p = \frac{a_0^2}{2} m_e c^2$$

For $a_0 \sim 1$, the electrons become relativistic, which corresponds to laser intensity $\sim 10^{18}$ W/cm². For the case of proton, mass $m_p \approx 2000m_e$, the laser intensity turns out to be 4×10^{24} W/cm² ($a_0 = 2000$) to become relativistic. Such a high laser intensity is not available with existing laser technology which is currently restricted to $\sim 10^{21}$ W/cm² i.e. direct ion acceleration with currently available highest laser intensity is not possible.

As discussed in the previous section that most of the laser energy is transferred to plasma electrons through various absorption mechanisms and they are accelerated to very high energies (multi MeV). The charge separation induced by these escaping electrons generates accelerating fields in several TV/m accelerating the plasma ions to MeV energies. In other words, electrons mediate the laser energy transfer to ions and overall ion acceleration efficiency is governed by laser absorption efficiency into plasma electrons and their subsequent energy transfer to ions through sheath field formation. The idea of ion acceleration using intense laser light is almost as old as the first laser itself. But over the past two decades due to availability of ultrashort ultrahigh intensity lasers, there has been rapid progress in this field and different ion acceleration schemes have been introduced theoretically and some of them have been demonstrated experimentally. The ion acceleration processes are sensitive to various laser and target parameters like laser intensity, laser pre-pulse, polarization and target configuration and geometry. The accelerated ion characteristics viz. energy

distribution, maximum energy, charge states, directionality, pulse duration and emittance etc. depends on the laser parameters, actual geometry and interaction parameters as mentioned above. The investigations on ion acceleration with varying laser and target conditions can be categorized as follows [45].

❖ **Ion Acceleration from solid surfaces:** Ion acceleration were performed with nano second long pulses in early 1980 [46]. The laser pulses were focused on solid surfaces and ions of keV- MeV energies were detected along the target front surface normal direction. Ion acceleration is primarily driven by pressure gradient in hot plasma and ambient vacuum which causes quasineutral isothermal expansion. This configuration was later tried with short (picoseconds and sub picosecond) high intensity pulses [20], [47] which has greatly enhanced this effect. However, with short pulse laser the plasma is not in quasi-thermal equilibrium as the plasma evolution (heat transport and heat dissipation, plasma expansion) time scale is much longer than the laser pulse duration. So unlike ns long pulse lasers, here the ions are accelerated by space charge field set up by hot electrons escaping from the plasma volume. Multi MeV protons with 10^{11} - 10^{12} proton flux per sr exhibiting broad energy distribution and large angular spread (typically 40-50°) have been accelerated. Along with protons highly charged ion were also observed.

❖ **Ion acceleration from gas targets:** Plasma produced in gas jet target is an underdense plasma. As the ultra-short high intensity laser propagates through the underdense plasma, the laser beam is self-focused and channel formation takes place inside the plasma. The electrons are removed from this plasma channel by the laser pondermotive force leaving behind a highly charged positive column. The plasma channel undergoes radial Coulomb explosion ejecting ions in radial direction as observed in several experiments [21].

❖ **Ion acceleration from gas clusters:** The gas coming out from a supersonic gas jets forms clusters of gas atoms. The clusters typically consist of $10^2 - 10^5$ atoms. When these clusters are irradiated by a high intensity ultra-short laser pulse, the cluster atoms are ionized to very high charge states. The laser pulse quickly removed almost all the electrons from the cluster on a time scale much faster than the ions are able to move. The highly positively charged cluster then explodes isotropically by the strong Coulomb repulsion between the ions leading to isotropic ion emission. The emitted ions with energy in excess of 1 MeV has been reported [22]. Ditmire et al. [48] have used deuterium clusters where deuterium ions were accelerated to above 100 keV energies making the d-d fusion reaction possible. They had demonstrated the generation of neutrons in d-d fusion reaction by this technique.

❖ **Ion acceleration from thin foil targets:** The observation of few tens of MeV proton beam from thin targets with high degree of collimation and laminarity, high proton flux (up to 10^{13} per pulse), high peak current, short pulse duration and very small emittance have rejuvenated this field with promising applications both in fundamental research and practical applications. Protons were detected at rear side of the target, opposite to the laser irradiated surface along rear surface normal direction in a narrow cone angle.

Protons/Ions accelerated from gas jets and clusters have isotropic ion emission and of lower energy and hence have limited applications. Whereas, ion accelerated from thin foils have better prospect in terms of applicability both in fundamental science and practical applications. In the current PhD thesis work, I have carried out studies on ion acceleration from solid and thin foils targets (few microns to sub-micron thickness) of different material and compositions. The following section, will give an overview of

some of the most studied laser driven ion acceleration schemes in foil targets using ultrashort ultra-high intensity laser pulses.

1.3.1 Target Normal Sheath Acceleration (TNSA)

In the year 2000, three different groups [23]–[25] have reported an intense emission of multi MeV proton beam from rear surface of several micron thick foils (plastic and metallic) irradiated by high intensity laser pulses. The origin of protons was identified as the hydrocarbon contaminants present at the foil target surfaces. Initially, there was debate on the actual location of the region where the protons are accelerated and on the mechanism of acceleration. Clark et al. [25] and Maksimchuk et al. [24] had suggested that the protons are accelerated at the target front surface, crosses the foil target and detected on the rear side. Contrary to this, Snavely et al.[23] provided the evidence that protons were accelerated at the target rear surface. In order to provide an explanation for the accelerated protons detected in the experiments, Wilks et al.[26] have introduced the so called Target Normal Sheath Acceleration (TNSA) model.

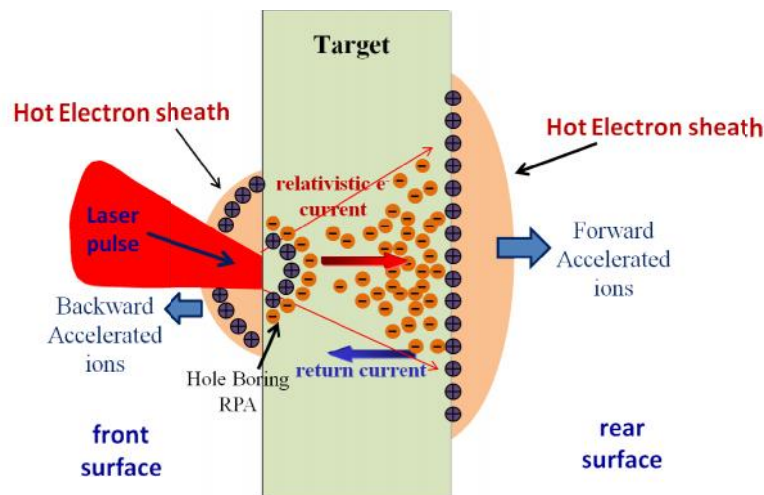


Figure 1.2: Illustration of main mechanism of ion acceleration in overdense opaque target including TNSA at back surface, RPA due to hole boring at the laser focus and front surface expansion in blow off plasma.

TNSA Physical picture:

As discussed earlier, hot electron with energy in excess of MeV, generated in the laser matter interaction at the laser focus, propagate through the thin foil target and escape from rear side. However, only a small fraction of the high energy electron population is allowed to escape before the target gets sufficiently charged. The major part of the electron population is then trapped by the electrostatic potential generated by the charge separation, forming a sheath of hot electrons. The trapped electrons circulate back and forth through the thin foil target forming the sheath field on both sides of the target. On the rear side there is no plasma to screen the sheath field and therefore the resultant induced electric field strength is in the range of few 10^{12} V/m. This field is so strong that it ionizes the atoms present at the back surface of the target and subsequently accelerated by the same field. Due to hydrocarbon contaminants which are normally present on the target surfaces, the preferentially accelerated species are protons as they have highest charge to mass ratio. If the hydrocarbon contaminants are removed prior to laser shot by target heating or laser ablation, the heavier ions can also be accelerated. The ions leave the target together with front co-propagating electrons. Since the accelerating electric field is parallel to the rear surface normal direction, therefore the mechanism is called **Target Normal Sheath Acceleration (TNSA)**. The scheme of TNSA mechanism along with other acceleration scheme (to be discussed later) is illustrated in Fig 1.2.

The physical framework underlying the TNSA mechanism i.e. the plasma expansion into vacuum has already been described in 1970's for ion acceleration with long ns pulses [49]–[51]. The major difference in modern day experiment is the use of much shorter laser pulse duration resulting in much higher electron temperature. Thus the associated temporal evolution of sheath field driving the ion acceleration is also for a

very short time (~few ps). In case of long pulse experiment, the plasma at target vacuum interface slowly expands. Due to the expansion of positive ions the electric field at the ion front is reduced during the expansion and hence the ion acceleration becomes ineffective. However, in case of short pulse experiments, the acceleration time is mainly governed by the laser pulse duration and not by the plasma expansion itself. The acceleration process stops, when the laser pulse is over.

The TNSA mechanism also works at target front surface as the high energy electrons which are accelerated along the density gradient, forms a sheath field on target front surface leading to protons/ions acceleration at the front side as well. On the front side, there is long scale length plasma due to laser pre-pulse resulting in lower electric field and therefore ions accelerated to lower energy with more angular spread. In case of very high contrast laser pulse i.e. ratio of main laser pulse intensity to pre-pulse laser intensity is very high, the pre-plasma formation would be very less. In such case the characteristics of proton accelerated from target rear surface and target front surface (laser irradiated side) are almost identical [48].

1D model plasma expansion into vacuum [53]:

Consider a pre-ionized hydrogen plasma with a step like density profile i. e. occupying the half space $x < 0$ at time $T= 0$. The ions are cold and are initially at rest with density $n_i = n_{i0}$ for $x < 0$ and $n_i = 0$ for $x > 0$. The electron temperature is T_e and they are in thermal equilibrium with the electrostatic potential generated by the charge separation, they can be described by Boltzmann distribution.

$$n_e = n_{e0} \exp\left(\frac{e \phi(x,t)}{kT_e}\right) \quad (10)$$

Where $n_{e0} = n_e(x=-\infty)$ is the unperturbed hot electron density. (x,t) is the electrostatic potential which are generated due to charge separation. The potential (x,t) obeys Poisson equation,

$$\frac{\partial^2 (x,t)}{\partial x^2} = \frac{1}{\epsilon_0} e [n_e(x,t) - n_i(x,t)] \quad (11)$$

Integrating the equation gives the initial electric field at target rear surface

$$E_{\text{TNSA}} = - \left. \frac{\partial (x,t=0)}{\partial x} \right|_{x=0} = \sqrt{\frac{2}{\epsilon_N}} \sqrt{\frac{k_B T_e n_{e0}}{\epsilon_0}} \quad (12)$$

Where $\epsilon_N = 2.71828$. The employed boundary conditions are $\frac{\partial}{\partial x} = 0$, $= 0$ at $x = -\infty$

and $\frac{\partial}{\partial x} = 0$, $= -\infty$ at $x = +\infty$. This signifies that unperturbed plasma is neutral and

there are no charges at infinity.

$$E_{\text{TNSA}} \approx \sqrt{\frac{k_B T_e n_{e0}}{\epsilon_0}} \approx \frac{k_B T_e}{e \lambda_{D0}}, \text{ where } \lambda_D = \sqrt{\frac{\epsilon_0 k_B T_e}{e^2 n_{e0}}} \text{ is Debye length.}$$

The value of the initial electric field at rear surface depends on hot electron temperature and density only. For $I_L = 10^{19} \text{ W/cm}^2$ at which the measured hot electron temperature and density are 1.5 MeV and $8.4 \times 10^{19} \text{ cm}^{-3}$ respectively, the estimated value of accelerating field would be 1.1 TV/m [54].

The step like proton distribution will expands due to the electric field generated by hot electrons expanding into vacuum. The evolution of the proton distribution driven by electron distribution is described by equation of continuity and momentum

$$\left[\frac{\partial}{\partial t} + v_1(x,t) \frac{\partial}{\partial x} \right] n_1(x,t) = -n_1(x,t) \frac{\partial v_1(x,t)}{\partial x} \quad (13)$$

$$\left[\frac{\partial}{\partial t} + v_1(x,t) \frac{\partial}{\partial x} \right] v_1(x,t) = - \frac{e}{m_i} \frac{\partial (x,t)}{\partial x} \quad (14)$$

Here v_i is the ion velocity. We must have $v_i > 0$, to describe the expansion of the plasma. Therefore, a self-similar solution of the above equation for $x+c_s t > 0$ (ahead of ion front) can be found assuming quasi-neutrality is maintained in expanding plasma; $n_e = n_i = n_{e0} \exp(-x/c_s t - 1)$. The velocity and electric field is given by [53],

$$v_i(x,t) = c_s + x/t, \quad (15)$$

$$E_{SS}(x,t) = k_B T_e / e c_s t = E_0 / \omega_{pp} t \quad (16)$$

Where $c_s = \sqrt{(Zk_B T_e + k_B T_i) / m_p} \approx \sqrt{Zk_B T_e} / m_p$ (for proton $Z=1$ and $T_i \ll T_e$).

$\omega_{pp} = \sqrt{n_{e0} e^2 / m_p}$ is the proton plasma frequency.

The self similar solution (eqn. 16) have no physical meaning as long as initial Debye

length $\lambda_{D0} = \sqrt{\frac{k_B T_e}{e^2 n_{e0}}}$ is larger than the proton density scale length $c_s t$ i.e. $\omega_{pp} t < 1$.

Further for $\omega_{pp} t \gg 1$, the self-similar solution predicts the proton (ion) distribution extends to infinity and velocity increasing without limit for $x \rightarrow \infty$. This contradicts the real situation where the protons originally situated at $x = 0$ form a well-defined ion front at the leading edge of the expanding proton distribution. The position of ion

front can be found by equating the local Debye length $\lambda_{D0} = \sqrt{\frac{k_B T_e}{e^2 n_{e0}}}$ to density scale

length, the position where the self-similarity solution becomes invalid.

$$\lambda_D = \lambda_{D0} \sqrt{\frac{n_{e0}}{n_e}} = \lambda_{D0} \exp\left[\frac{(1+x/c_s t)}{2}\right]$$

$$\lambda_{D0} \exp\left[\frac{(1+x/c_s t)}{2}\right] = c_s t$$

Putting the value of λ_{D0} and $c_s t$, we get

$$1 + x/c_s t = 2 \ln \omega_{pp} t$$

Hence, the proton velocity predicted by self-similar solution

$$v_{p,f} = 2c_s \ln \omega_{pp} t$$

The electric field at the ion front can be found can be found from acceleration.

$$E_f = \frac{m_i}{e} \frac{d}{dt} (v_{p,f})$$

$E_f = 2E_0 / \omega_{pp} t$. The apparent drawback is that the self-similar solution is not valid at initial time $t = 0$ due to singularity. This is because, initially there is charge imbalance at the plasma surface, hence the quasi neutral solution is not valid near $t=0$. Mora [53] numerically calculated the precise value of the electric field valid for any time $t > 0$.

$$E_f \approx \frac{2E_0}{\sqrt{2e_N + \omega_{pp}^2 t^2}} = \sqrt{\frac{2}{e_N}} \frac{E_0}{\sqrt{1 + \tau^2}}$$

Where $\tau = \omega_{pp} t / \sqrt{2e_N}$. This expression has the correct asymptotic behaviour for both $t = 0$ and $\omega_{pp} t \gg 1$.

One can now derive the expression for maximum ion energy using the expression for ion front velocity

$$Energy_{\max}(t) = 2Zk_B T_e \left[\ln \left(\tau(t) + \sqrt{\tau^2(t) + 1} \right) \right]^2$$

Here, the maximum ion energy diverges logarithmically with time. This drawback arises due to the isothermal assumption: the driving electron reservoir fluid have infinite energy which accelerates the ion indefinitely. Therefore, in order to make use of the formulae for maximum energy and one need to know the acceleration time $t = t_{\text{acc}}$ and unperturbed initial electron density in the sheath. The acceleration was found to be of the order of laser pulse duration or few times of it [55], [52] and the initial hot electron density was estimated by assuming the ballistic propagation of hot electrons which are generated at target front surface and reaches at target rear surface.

1.3.2 Radiation Pressure Acceleration

At higher laser intensities ($>10^{22}$ W/cm²), another mechanism of ion acceleration known as Radiation Pressure Acceleration (RPA) starts to dominate over TNSA regime. The laser transfers momentum to the target while it gets reflected at critical density surface. The Radiation pressure for plane electromagnetic wave impinging at normal incidence is given as

$$P_{\text{rad}} = (1+R)I/c$$

Where I is laser intensity and R is the target reflectivity and for $R=1$ maximum momentum transfer takes place. The radiation pressure of an intense laser pulse is associated with steady pondermotive force and indeed it is the pondermotive force which transmits the light pressure to the overdense plasma. The Pondermotive force is inversely proportional to the particle mass, hence the electrons of overdense plasma slab are pushed inwards and pile up in compressed layer whereas during the initial phase ions are immobile. This inward push continues until charge separation field balances the radiation pressure. The electric field arises because of this charge separation accelerates the ion to relativistic velocities. The process is also known as hole boring phase of RPA and is schematically depicted in Fig. 1.3

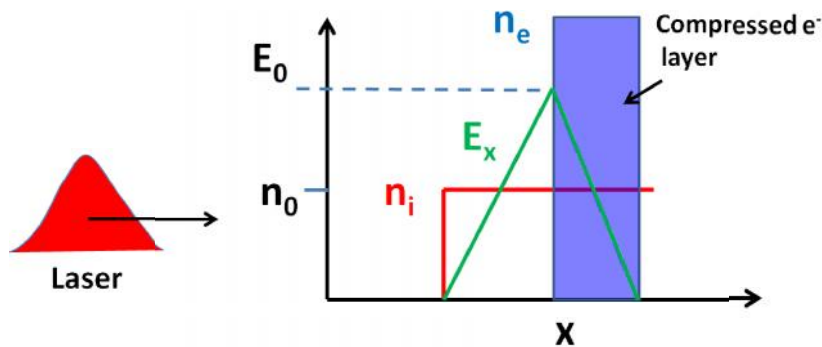


Figure 1.3: Schematic description of RPA. Ion (Red), piled up electron layer (Blue) and generated electric field. Ions in the electron compressed area are accelerated with same velocity.

Ions in the compressed layer reach at the end of compression layer at same time and with same velocity as the electric field is a linear function of x . The accelerated ions cross the compressed electron layer and travel inside the target. Electrons which have much lower inertia as compared to ions, compressed electron layer adjusted its position and propagate forward due to laser pressure. This cyclic process continues until the compressed layer reached at target rear side or the laser field is turned off. At this point, the whole focal volume region is accelerated as a single slab of plasma by laser radiation pressure. This final phase is known as “light sail” phase of RPA. The maximum ion velocity in case of RPA obtained by momentum and energy conservation is given as [57]

$$\frac{v_i}{c} = 2 \frac{v_{\text{HB}}}{c} = 2 \sqrt{\frac{I}{m_i n_i c^3}}$$

Where v_{HB} is the hole-boring velocity, I is the laser intensity, n_i and m_i are the ion density and mass. Here the ion energy scales as $\propto I$, better than TNSA scaling.

The concept of Light sail was given in 1966 by Marks [58] for spacecraft propulsion using high power lasers. The light photons reflected from moving sail/vehicle transfer a smaller fraction of their momentum and large fraction of energy to the sail. The idea was later used for thin foil targets by Esirkepov et al. [30] using very high intensity lasers ($> 10^{23}$ W/cm²). Using 3D PIC simulations, he showed that the protons gain relativistic velocities within first half cycle of the laser. Later on it was shown that RPA can be achieved at much lower intensities ($> 10^{20-21}$ W/cm²) by circularly polarized laser pulse at normal incidence [59], [60]. For circular polarization, the oscillating component of pondermotive force is absent hence the generation of hot electron is suppressed. At normal incidence, resonance absorption and vacuum heating are also suppressed. Quenching the hot electron generation process makes the

compression more effective and allows the RPA to dominate at much lower laser intensities. The experimental demonstration of RPA is quite challenging due to very stringent requirement on laser and target parameters. Recently, there are few reports which show signatures of RPA in ion energy spectrum [61]–[63]. For example Kim et al. [63] have reported 93 MeV proton beams using circularly polarized pulses with laser intensity $\sim 6 \times 10^{20}$ W/cm² from 15 nm thick polymer targets. However, the observed ion energy spectrum is still relatively broad due to the transverse inhomogeneity and heating effects.

1.3.3 Laser ion acceleration in relativistic transparency regimes (Breakout Afterburner)

The thin foil targets that are classically overdense may become relativistically transparent for laser light at ultrahigh laser intensity. The expression for critical density for relativistic case is given as;

$$n_{cr} = \frac{1.1 \times 10^{21}}{\mu^2} \text{ cm}^{-3}$$

where μ is the laser wave length in micron and γ is the relativistic factor. Hence the effective density at which the light is reflected is increased by factor γ^2 in case of relativistic plasma formed by ultrahigh intensity laser. The onset of relativistic transparency leads to strong volumetric heating of target electrons which creates a strong field that accelerates ions. This mechanism is known as Breakout Afterburner (BOA) and is more efficient as compared to TNSA. The BOA mechanism was proposed by Yin et al [34], [64]. Using 3D PIC simulation he identifies two different stages after the initial TNSA. First is the enhanced TNSA in which all the background cold electrons entirely converted to hot electrons and the second, when the laser

penetrate to the target rear side where a localized longitudinal electric field is generated with peak field location co-moving with ions. The main challenge here is to use a target which remains overdense when the peak of laser pulse arrives and at the same time thin enough for dynamics of acceleration process to proceed. Hegelich et al. [65] have obtained ~ 44 MeV/nucleon carbon ions with a 150 TW laser focussed to an intensity of 5×10^{20} W/cm². Recently Jung et al. [66] have shown 1 GeV i.e. 83 MeV/nucleon C⁶⁺ ion using same laser system from cleaned 225 nm thick diamond like carbon target. Deuteron beam upto 170 MeV was demonstrated by Roth et al. [67] through BOA mechanism.

1.4 Scope of present thesis work

The present thesis work is primarily focused on proton/ion acceleration from thin foil targets and quasi-mono energetic heavy ion acceleration from nano structured and multilayer targets using 10 TW, 45 fs and 150 TW, 25 fs Ti:sapphire laser systems at RRCAT. The work also includes generation of negative H⁻ ion from hydrogen containing transparent solid targets. Application of laser accelerated proton and deuteron beam towards short lived positron emitting radioisotope production is investigated. Proton beam have been used to induce fusion in natural Boron target ($p + {}_5\text{B}^{11} \Rightarrow 3 \text{ } + 8.7 \text{ MeV}$). The resultant fusion yield and particle energy spectrum have been measured.

Initial ion acceleration studies were started on 10 TW Ti: Sapphire laser system to optimize the experimental parameters related to laser-foil interaction. Although, there are many experimental and theoretical reports on lighter ion acceleration (H⁺/proton and carbon ions) from thin foils using similar type of lasers. But the result from one system cannot be fully generalized for other laser system because of the strong dependence on laser and target parameters as discussed above.

Slight changes in laser interaction condition viz. laser pre-pulse have significant bearing on the accelerated ion beam. Therefore for every laser system it is utmost important to determine the optimize foil thickness/material which support the pre-pulse present in the laser pulse for efficient ion acceleration. In this direction extensive work on varying laser and target parameters have been carried out. Foils of different materials and thicknesses have been used to achieve maximum H^+ /proton energy. Experimental results indicate an optimum foil thickness for a given foil material at which the proton energy maximizes. In particular, it was also found that a wise selection of foil material or atomic number Z can improve the proton acceleration efficiency, thereby increasing the accelerated proton/ion energy [68]. In continuation of this study, double-layered and multi-layered targets have been used to reduce the beam divergence and enhance the energy of the proton beam emitted from laser-foil interaction. It was observed that judicious combination of metal and dielectric foils culminates to reduced proton beam divergence as well as enhances the maximum proton energy [69]. Later the ion acceleration studies were carried out at higher laser intensities using 25 fs, 150 TW laser system operating at ~ 90 TW level. Here, the much higher contrast (ratio of pre-pulse to main pulse) $\sim 10^{-10}$ had enabled us to use the foils of submicron thickness. Maximum recorded H^+ ion energy was around 10-11 MeV while C^{5+} ion yielded a maximum energy of 14.5 MeV. Effect of laser intensity, pulse contrast and pulse duration/ laser chirp have been studied in details. In particular, significant enhancement of ion energy from thin foil targets was observed by adjusting the laser temporal characteristics with a simple adjustment of grating pair separation inside the pulse compressor. Remarkably, in certain laser pre-pulse conditions and highest laser intensities $\sim 10^{20}$ W/cm², we have also observed quasi-monoenergetic proton bunches with total energy spread less than 40%. Effect of high

z coating on CH/Mylar foil was also studied. A very interesting and contrasting effect on ion acceleration was observed when coated surface was kept at front (laser facing) and at rear.

The high intensity laser plasma interaction scenario favours the acceleration of positive ions. Although, it appears counterintuitive at first, we show that even in this adverse situation of high temperature, high density plasma, an efficient generation of negative ions (H^-) can be observed. H^- ions of more than 100 keV was observed in interaction of moderately intense (10^{17} - 10^{18} W/cm²) ultrashort laser pulses from transparent hydrogen containing solid targets [70]. The laser and target conditions for efficient H^- ion production are discussed.

Protons (H^+) having highest q/m ratio are more preferentially accelerated in space charge field (sheath field) set up by hot electrons compared to high-Z element with low q/m ratio. In general they have broad energy distribution; far from being quasi mono energetic. Using some advanced target engineering technique and ultra-high intensity lasers ($> 10^{21}$ W-cm⁻²), only few groups have demonstrated quasi monoenergetic signature in ion energy spectrum but in lighter species only [27], [28], [61]. Nevertheless, generation of quasi mono-energetic ions particularly *heavy ions* of MeV energy with high degree of reproducibility is still a challenge. In contrast to the conventional continuous ion energy spectrum, acceleration of quasi mono-energetic Au ions [71] to few hundred keV energies has been demonstrated for the first time using relatively simple nano-composite target and at moderate intensities (10^{18} - 10^{19} W/cm²). The observations are highly reproducible and replicate in all the charge states of Au ions i.e. it does not depend on charge state. The ion emission was recorded from target front surface along the target normal direction. The Au-C nano-composite target consists of Au nano-particles (AuNP) of size 3-8 nm, distributed randomly

within the 120 nm C layer. Based on above studies on Au-C nano composite target in which Au nano particles were embedded in carbon matrix, a systematic study have been carried out on well-designed multilayer targets. Quasi-monoenergetic features are observed in different charge states of Au from double layer coated targets having thin layer of Au (5 nm) and Carbon (10-60 nm). On the other hand, only plain Gold layer gives the continuous Au ion energy spectrum. The results may set the path for an easy and novel method of generating quasi mono-energetic heavy ions.

Next, experiments towards applications of laser driven proton beam were also performed. An experimental study on aneutronic fusion reaction between proton and ^{11}B target was performed using 150TW Ti:sapphire laser system. The reaction between energetic laser accelerated protons and ^{11}B produces 3 particles that releases 8.7 MeV energy. The fusion yield and particle energy spectrum have been measured. Short lived ^{11}C radioisotope (positron emitter) generation employing laser produced deuteron and proton beam utilizing $^{10}\text{B}(\text{d},\text{n})^{11}\text{C}$ and $^{11}\text{B}(\text{p},\text{n})^{11}\text{C}$ reactions have also been studied. About 5.2 kBq activity of ^{11}C radio-isotope was produced in a single laser shot through $^{11}\text{B}(\text{p}, \text{n})^{11}\text{C}$ reaction. This represents $\sim 9 \times 10^6$ atoms of ^{11}C radio-isotopes. The relative effectiveness of laser produced deuteron and proton beam in producing ^{11}C radio-isotope are also investigated. As the reaction $^{10}\text{B}(\text{d}, \text{n})^{11}\text{C}$ has energy threshold of only around 0.5 MeV, the low energy deuterons having higher flux can be efficiently utilized for ^{11}C production. Our results is an small step forward towards producing such radio-isotopes with table top moderately intense ultra-short lasers operating at higher repetition rate for the practical applications in medical applications like Positron Emission Tomography (PET).

CHAPTER 2

Lasers, Experimental setups, diagnostics, and detectors:

This chapter provides the details of the laser systems, experimental setups, ion diagnostics, detectors, targets, and different kind of lasers used for carrying out the present research studies on ion acceleration. All the experimental investigations have been carried out using two different laser systems viz. 10 TW, 45 fs, Ti:sapphire laser (Model: Alpha 10, Thales Lasers, France) and 150 TW, 25 fs, Ti:sapphire laser (Model: Pulsar 150, Amplitude Technology, France) at Laser Plasma Division, Raja Ramanna Centre for Advanced Technology (RRCAT), Indore India. The characteristic of laser accelerated ion beam depends heavily on the laser system. Therefore, it is important to give a brief description of the laser systems used during the research studies. The measurements of important laser pulse parameters like pulse duration, pre-pulse contrast and laser focal spot are also given. Generally, the high intensity laser plasma experiments are performed in evacuated vacuum chamber with base pressure typically $\sim 10^4 - 10^{-5}$ mbar. At this vacuum level a few Å thin layer of hydrocarbon and/or water vapour are always present on the target surface as a contaminants. Therefore, lighter species viz. proton and carbon ions are always present as a dominant species in accelerated ion beam irrespective of the target material used. Therefore, suitable ion diagnostics are required to have a charge and energy resolve measurement of different ionic species present in the beam. A Thomson Parabola Ion Spectrometer (TPIS) have been designed and developed for this purpose. The details of TPIS and other ion detectors are also described in this chapter. Some details of thin foil mounting and CD₂ foil preparation are also given.

More details about specialized targets specific to a particular experiment are provided wherever it is applicable.

2.1 Laser Systems

Both the 10 TW, 45 fs and the 150 TW, 25 fs Ti: sapphire laser systems are based on chirped pulsed amplification (CPA) technique [19] and uses Ti: Sapphire crystal as an active medium. In CPA technique, initially, very low energy (nJ) laser pulses of ultra-short duration are produced in a oscillator using mode-locking technique. These ultra-short laser pulses before amplifying in successive amplifiers are first temporarily stretched in a gratings based stretcher to few hundreds of ps duration to reduce the peak laser intensity in order to avoid damages of optical components during amplification. After amplifying the laser pulse in various amplifier stages it is finally compressed back in time nearly to its initial pulse duration. In this way, high power laser pulses (high energy and ultra-short pulse duration) are produced. More details about the lasers are provided in the following sections. The important parameters of both the laser systems are outlined in table 2.1.

Parameter	10 TW	150TW
Pulse duration	45 fs	25 fs
Central wavelength	800nm	800 nm
Bandwidth	20nm	70nm
Repetition rate	10 Hz	5 Hz
Pulse energy	0.45 J	3.75 J
Maximum Peak power	10 TW	150 TW
Beam Diameter	40 mm	100 mm
ASE Pre-pulse contrast (ratio of main pulse to pre-pulse)	10^{-6}	10^{-10}
Typical Focused intensity	10^{18} W/cm ²	10^{19} - 10^{20} W/cm ²

Table 2.1 Parameters of 10 TW and 150 TW laser systems

2.1.1 The 10 TW, 45 fs Ti: Sapphire laser system

The initial studies and almost half of the work of the present thesis were performed using 10 TW Ti: Sapphire laser system. It is a CPA based commercial system procured from M/s Thales, France. The block diagram of the laser system is shown in Fig. 2.1 The laser front end has a Kerr lens mode locked Ti: Sapphire oscillator which delivers few nJ, 20 fs pulses at 76 MHz repetition rate.

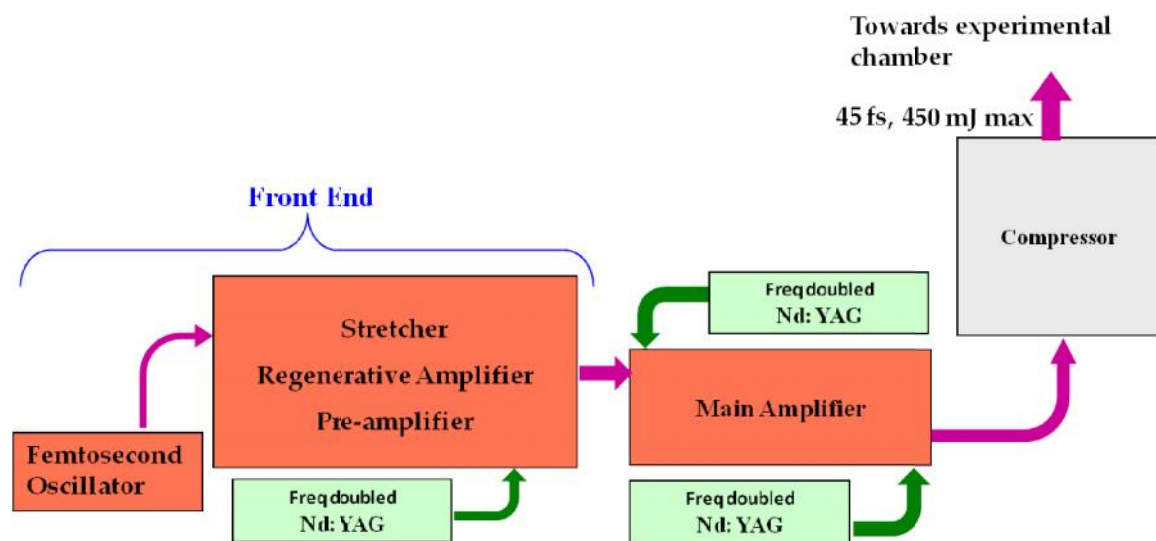


Figure 2.1: Layout of the 10 TW Ti:Sapphire laser system

The oscillator has central wavelength around 800 nm with bandwidth of ~ 50 nm. The Ti:Sa oscillator crystal is pumped by a compact frequency doubled diode pumped Nd:YVO₄ laser operating at 532 nm wavelength with output power up to 5W. The output pulses of the oscillator are then stretched to about 200 ps in an Offner type pulse stretcher [72]. The stretcher introduces positive chirp i.e. the higher wavelengths in the stretched laser pulse travel ahead of shorter wavelengths in time. The stretched pulses are then sent to amplifiers for amplification. First it is amplified in regenerative amplifier (RA) which is basically a Q-switched cavity dumped seeded oscillator. The RA is pumped by a part of green laser beam at 532 nm produced from a frequency

doubled Nd:YAG laser (Thales, model COMP). From RA onwards, the laser pulse repetition rate is reduced to 10 Hz from 76 Mz by using a Triode Valve based twin Pockels cell (using KDP crystal). This twin Pockels cell is a part of RA cavity and it is used for both pulse injection and subsequent pulse ejection at 10 Hz repetition rate from the RG amplifier. The selected pulses make 15 round trips in RA attaining overall gain of around 10^5 . After RA, the pulses are passed through a pulse cleaner set up to suppress the unwanted pre-pulses associated with main amplified pulses. The pulse cleaner is based on fast ~ 3 ns rise time Pockels cell switch. After the pulse cleaner, the pulses are then sent to multi pass pre-amplifier. The pre-amplifier is a 4 pass, bow tie amplifier which is also pumped by the remaining part of the COMP laser which was also used to pump the RA. After the pre-amplifier stage pulses of $\sim 35 - 40$ mJ at 200 ps duration are obtained. These pulses are then sent to main amplifier which is also a 4 pass bow tie amplifier based on large size Ti: Sapphire crystal (diameter 20 mm X 20 mm length). This final amplifier is also pumped by two second harmonic Nd:YAG lasers (Thales, model SAGA). The pulse energy after the main amplifier reaches to ~ 700 mJ (max). Finally, the stretched amplified pulses are compressed back in grating base pulse compressor unit consisting of two parallel gratings which introduces negative chirp in the amplified positively chirped pulse. At optimum grating separation, the positive chirp introduced by the pulse stretcher at the beginning and other optics during the amplification stages are compensated to maximum possible extent providing shorter pulse duration. During the course of amplification, spectral bandwidth of the laser pulse is reduced due to gain narrowing effect and therefore the shortest pulse duration achieved is limited to around 45 fs. During experiments one can achieve positively/negatively chirped laser pulses of longer pulse duration by reducing / increasing the grating separation of the pulse

compressor from the optimum value. The pulse compression is carried out in a vacuum chamber kept at a base pressure of around 10^{-5} mbar whereas all the laser amplifiers are kept in air. Finally, after the pulse compressor, a laser pulse energy of 450 mJ (maximum) at 45 fs pulse duration is available at maximum repetition rate of 10 Hz.

2.1.2 The 150 TW, 25 fs Ti: Sapphire laser system

This laser system delivers laser pulses of 25 fs pulse duration at a pulse energy of 3.75 J (peak power 150 TW) at 5 Hz repetition on the experimental chamber. This is also a commercial system procured from Amplitude Technologies, France (Model: Pulsar 150). The block diagram of the laser system is given in Fig 2.2. A brief description of the laser system is as follow. It starts with a Kerr lens Mode locked Ti: sapphire oscillator which delivers laser pulses of ~10 fs duration at central wavelength of 800 nm with a laser bandwidth of ~100 nm (typically 750-850 nm) at 76 MHz repetition rate. The Ti: sapphire crystal is pumped by a cw green laser beam obtained from an intra-cavity frequency doubled diode pumped Nd: YVO₄ laser. Typical average output power of the Ti:sapphire mode-locked oscillator is ~450 mW with laser energy in single pulse ~ 6 nJ.

In order to improve the laser pulse contrast ratio at earlier stage an additional Booster Amplifier Unit is used in the laser system before pulse stretcher unit. This unit consists of a compact multipass Ti:sapphire amplifier, a Pockels cell based pulse selector unit and a saturable absorber (SA1). This multi pass amplifier directly amplifies the oscillator output single laser pulse energy to micro joule level from nJ level. The saturable absorber SA1 removes residual ASE background of the laser pulses. This stage onwards a pulse selector unit select the pulses at 5 Hz repetition

rate. The output of the booster amplifier is sent to an Offner type laser pulse stretcher which temporally stretches the laser pulses to 800 ps duration.

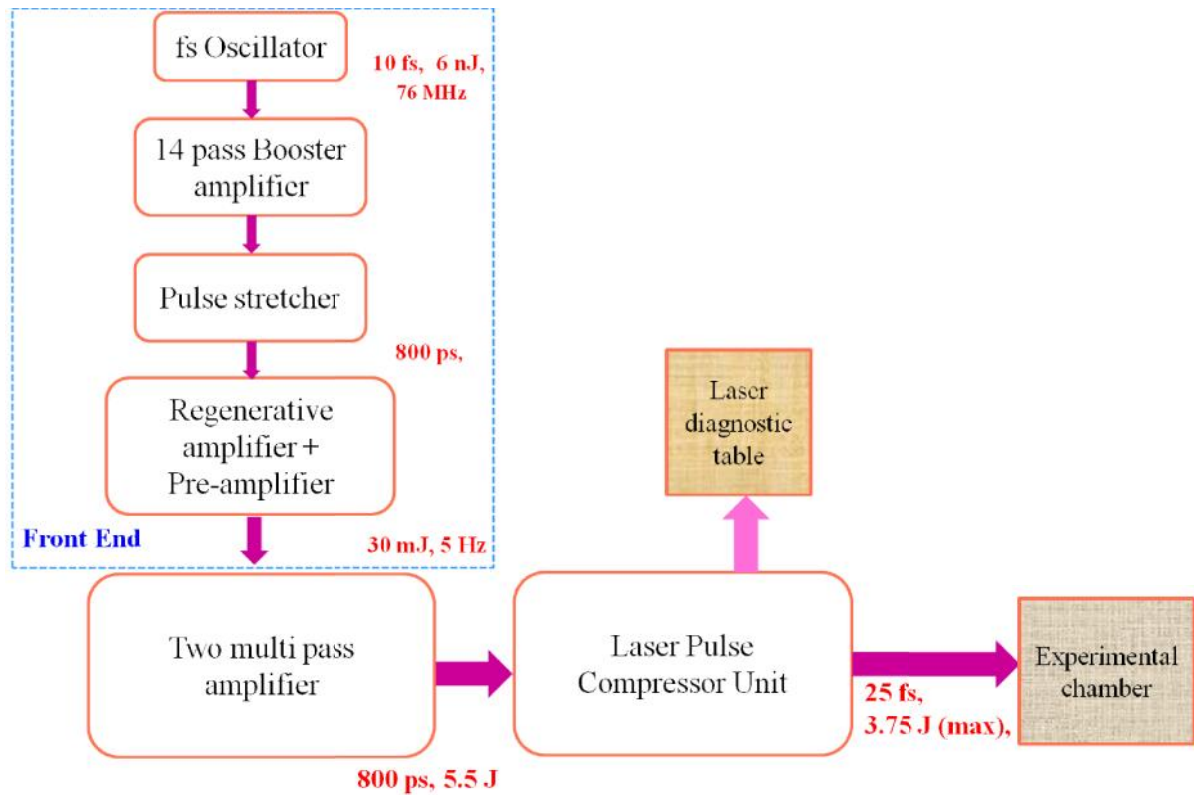


Figure 2.2: Layout of Pulsar 150 TW laser system

The stretched pulses are first amplified in regenerative amplifier to reach energy level up to 1 mJ and then they are further amplified in a bow-tie type multipass (5-pass) amplifier. The final energy reached at this stage is 25-30 mJ. A Pockels cell based pulse cleaner reduce the ASE background and pre-pulse intensity that arises mainly in to the regenerative amplifier during several round trips of the main laser pulse in the RA cavity. In order to enhance pre-pulse contrast (fs replica and ASE), one more saturable absorber (SA2) is used which is placed at output stage of the regenerative amplifier. Due to the gain narrowing in laser amplifiers, the spectral bandwidth reduces which limits the shortest achievable pulse duration at the final stage. To address this issue, an acousto-optic programmable gain control filters (*Dazzler and Mazzler*) have been used in RA cavity that efficiently prevents the gain narrowing in

the RG amplifier which otherwise resulting in reduction of the laser spectral bandwidth during amplification.

After RA and pre-amplifier, there are two multi pass Ti: Sapphire amplifiers stage. The first amplifier is pumped by second harmonic of Nd:YAG laser (model: PROPULSE) with 1.6J energy. The output laser pulse energy increases up to 250 mJ level. The final amplifier is pumped by four second harmonic Nd:YAG lasers (Model: TITAN) each providing 3.5J energy on the Ti: Sapphire amplifier crystal. This crystal of final amplifier is cryogenically cooled in order to remove heat load due to very high energy pump lasers. Laser energy after final amplifier stage is around 5.5 Joule. Before sending the amplified laser pulses in to a pulse compressor, a motorized controlled beam attenuator, based on two thin film polarizers and a half wave plate, is used in the laser beam path to vary the laser pulse energy as per user requirement. The attenuation factor can be varied from 100% to 1%. Finally, the amplified stretched pulse is compressed in a grating pair based laser pulse compressor which is kept inside a vacuum chamber (compressor chamber). The compressed laser beam this point onwards propagates in vacuum beam line up to experimental chamber kept in $\sim 10^{-5}$ mbar vacuum. At the plasma experimental chamber a laser beam of 25 fs at 3.75 J (max) pulse energy operating at 5 Hz (max) repetition rate is available. To characterize the laser pulse after compression, a part of the beam is taken out using an uncoated 1° wedge plate installed in pulse compressor chamber. The beam is taken out for measurements through a broad band AR coated window. There is a separate optical table where various diagnostics are installed for measurements of various laser parameter like laser pulse duration, pulse contrast etc. The pulse duration is measured using an standard commercial second order autocorrelator (Bonsai) or an in-house developed second order auto-correlator. The laser pulse contrast is measured with a

commercially available third order cross correlator (Make: Amplitude Technologies, Model: Sequoia) which provides laser pulse contrast up to few hundreds of ps either side of the main fs pulse. Pre-pulse contrast and ASE at ns scale level are measured using a fast photo diode and 1 GHz oscilloscope. In order to know final energy of the laser beam at the target, the laser pulse energy before compressor is measured using an energy meter (Model: Gentec QE95ELP-S-MB). The actual energy on the target is estimated by considering the overall transmission of the laser pulse compressor and other optics in the path up to target.

2.2 Laser Pulse Characterization

As the laser pulse characteristics strongly influence the laser plasma matter interaction dynamics, therefore it is important to measure and characterize some important laser parameters like pulse duration, laser pre-pulse contrast, laser intensity on the target etc. before starting the experiment. In this section, some important techniques routinely employed for laser pulse characterization are described.

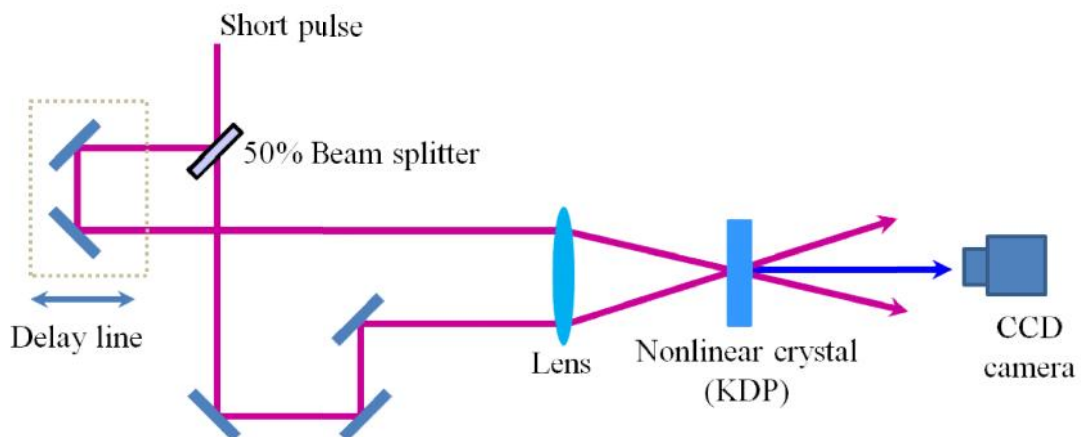


Figure 2.3: *Single Shot autocorrelation set up*

2.2.1 Laser Pulse duration

Single shot second order auto correlator has been used to measure the laser pulse duration [73]. In a second order auto correlation technique, the input beam is divided into two parts of almost equal intensity and they are made to overlap in a non-linear crystal. The generated second harmonic signal intensity is proportional to product of intensities of the overlapping beam. The measurement of second harmonic signal as function of relative time delay between the two beams gives the auto correlation function $A(\tau)$

$$A(\tau) = \int_{-\infty}^{\infty} dt I(t) I(t-\tau)$$

Experimentally, auto correlation function $A(\tau)$ is measured by introducing time delay between the two pulses using a photo diode or photo multiplier tube. The FWHM of $A(\tau)$ can be used to find out the pulse duration (FWHM) of the input laser pulse, provided the input pulse temporal profile is assumed. In contrast to multi shot scanning mode, the pulse duration can also be measured in a single shot mode. The schematic of the measurement technique is shown in Fig 2.3 In this case, the single pulse is again divided into two parts which are then sent to non-linear crystal at an angle θ . The two pulses can be made to overlap temporally and spatially inside the crystal if the beam waist in the overlapping zone is larger than c_p i.e. the pulse length. Due to this overlap, a second harmonic signal is generated which is emitted along the bisector of cross over angle of the two beams. The intensity of the second harmonic signal at each point is proportional to the product of intensities of two beams at that point. Here, the second harmonic spatial intensity distribution gives the autocorrelation function. The second harmonic signal is recorded using CCD camera.

If x is the FWHM width of the second harmonic intensity distribution (autocorrelation trace), then the pulse duration τ_p (FWHM) is given by

$$\tau_p \approx \frac{k \lambda x \sin(\theta/2)}{c}$$

Where, k is a numerical factor which depends on the laser temporal shape. For a Gaussian temporal profile k is 2 whereas for sech^2 pulse profile k is ~ 1.3 . The laser pulse duration of the 10 TW laser beam is mostly measured with in-house developed auto-correlator whereas for the 150 TW laser system we used commercial auto-correlator (*Bonsai*). A typical autocorrelation trace along with line profile of the autocorrelation signal using *Bonsai* is shown in Fig 2.4. The provided software module grabs the second harmonic signal, estimates the pulse duration as per laser temporal shape, and display the pulse duration on the screen.

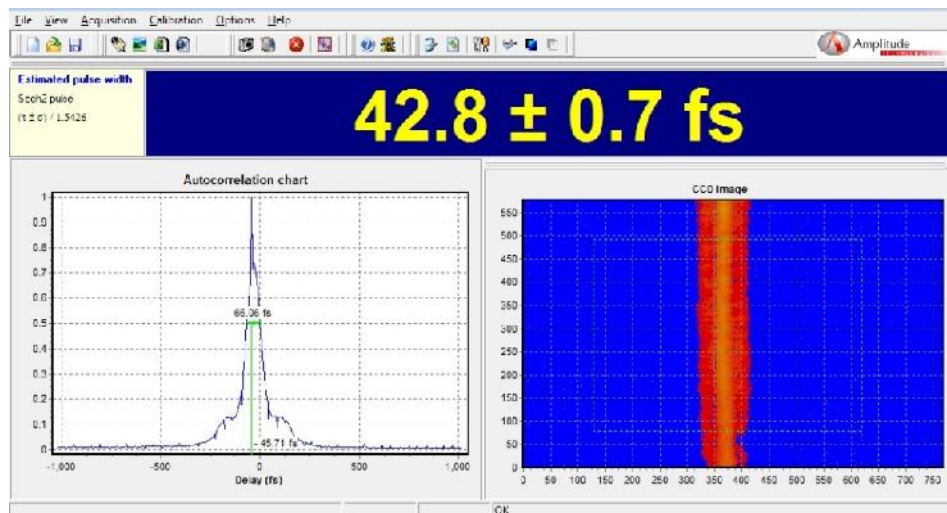


Figure 2.4 Screen shot of image grabbing and analysis software of SSA *Bonsai*.

2.2.2 Pre-pulse contrast measurement

The characterization of the pre-pulses preceding the main femtosecond pulse is very important in laser driven ion acceleration experiment. The pre-plasma formed due to pre-pulse significantly alters the laser plasma interaction dynamics of the main

femtosecond pulse. In case of thin foil target a strong pre-pulse can severely perturb the foil surface and hamper the ion acceleration process. Although, the results on the effect of laser pre-pulse on ion acceleration will be presented in later chapters, at this point the methods of characterization of the pre-pulses will be described.

In a CPA based laser system these pre-pulses arise during the amplification stage and their origin are different. The amplified spontaneous emission (ASE) in regenerative amplifier (RA) and pulse leakage due to finite extinction ratio of polarizers, Pockels cells and imperfect compression of the laser pulse constitutes different pre-pulses at varying time scales. At nano second time scale, there are primarily two types of pre-pulses. One pre-pulse (fs duration) which is basically a replica of the main fs pulse which arises due to the finite extinction ratio of Pockels switch in pulse ejection system. This replica pre-pulse appears before the main pulse at time scale equal to the round trip time of the region cavity (e.g. @ 10.6 ns in 150 TW system and @ 8.3ns in 10 TW system). Second one is the ASE, which is generated due to the amplification of spontaneously emitted photon inside the cavity. The main source of the ASE is the oscillator and the RGA. The ASE forms a low intensity background (pedestal of several ns duration) underneath the main high intensity fs pulse. To reduce the ASE, a pulse cleaner based on two cross polarizer and a fast Pockels cell is used after the RA cavity. The system works as a fast optical shutter so that it allows the main fs pulse to pass through and suppress the broad ns ASE pedestal. Some pre-pulse at ps time scale can also arise due to the spectral phase distortion during the amplification stage and imperfect compression of the stretched pulse inside the laser pulse compressor.

In the experiment the pre-pulses are monitored and characterized using fast photo diode (30 ps rise time) coupled with 1 GH oscilloscope (Lecroy Model:

WR104MXi) at ns time scale and with third order cross correlator *Sequoia* from Amplitude technology at few hundreds of ps before the pulse. The pre-pulses are characterized in terms of contrast ratio which is the intensity ratio of the pre-pulse to the main fs pulse. To measure the contrast using fast photo diode, a small part the beam is incident on the photo diode. The signal output was measured on oscilloscope. Calibrated neutral density filters were used in front of the diode so as to avoid the overexposure while measuring the high intensity main fs laser pulse. The measurements performed for 10 TW laser system is shown in Fig. 2.5 (black curves). The overall temporal resolution of fast photo diode and oscilloscope is around $\tau_s = 351$ ps. However, the measured laser pulse duration with the fast photodiode and oscilloscope combination was $\tau_s = 450 \pm 15$ ps (FWHM). This increase in the pulse width may be due to poor bandwidth of the cable used in the setup. The pulse duration of the main compressed laser pulse is $\tau_p = 45 \pm 3$ fs (FWHM) which cannot be resolved by this arrangement. Therefore, the signal height of the main laser pulse would be higher by a temporal factor $F = \tau_s / \tau_p \sim 10^4$ [74]. For the ASE measurement, neutral density filters have to be removed, but in this case the main pulse signal is saturated while the pre-pulse is now visible as pedestal at the foot of the main pulse as shown in Fig. 2.5 (red curves). It can be seen that ASE signal varies slightly on shot to shot basis. By taking account the filter attenuation and temporal correction factor and considering the temporal response of the detector, the laser pulse contrast (I_{ASE}/I_{main}) is measured to be in the range of $\sim (8 \pm 1.5) \times 10^{-7}$. During the experiment with thin foils, the ASE duration was also minimized by adjusting switching delay time of Pockels cell of pulse cleaner very close to the arrival of main pulse in the 10 TW laser. In the 150 TW laser an additional saturable absorber is used

to improve the contrast ratio which gives a pre-pulse contrast (I_{ASE}/I_{main}) better than 10^{-10} .

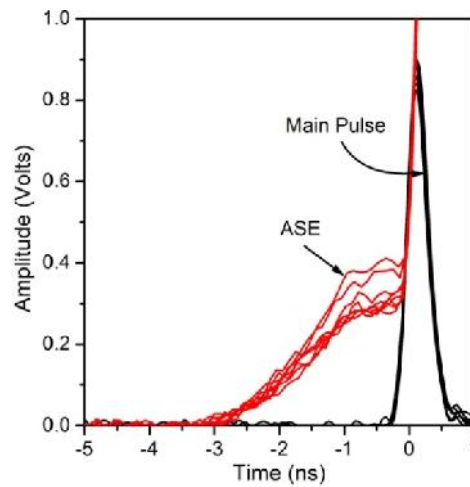


Figure 2.5: ASE measurement using fast photo diode of 10 TW Laser system. Additional filters have been used to record the main pulse.

The contrast at few 100 ps time or less cannot be measured using photo diode set up. For this we had used a third order cross correlator 'Sequoia'. The basic working principle of third order cross correlator is shown in Fig 2.6. The beam is divided into two parts. One part is used to generate second harmonic and delayed in time. The third harmonic generation inside the THG crystal is used to achieve cross correlation between second harmonic of the pulse and the pulse itself. The third harmonic signal is proportional to the temporal overlap i.e. the product of intensities of two beams inside the third harmonic crystal. The evolution of third harmonic signal with respect to time delay gives temporal profile of the pulse. The measured temporal profile of the 10 TW and the 150 TW beams are given in figure 2.7. The very high contrast in 150 TW laser is due to the use of two saturable absorbers as described earlier.

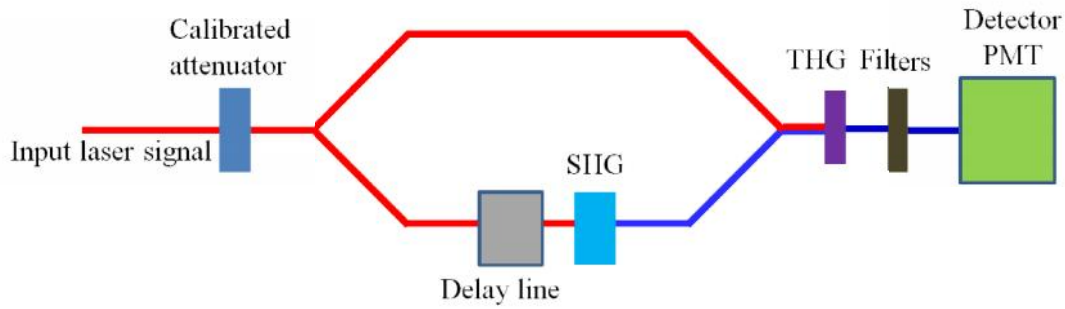


Figure 2.6: General scheme of third order cross correlation Sequoia

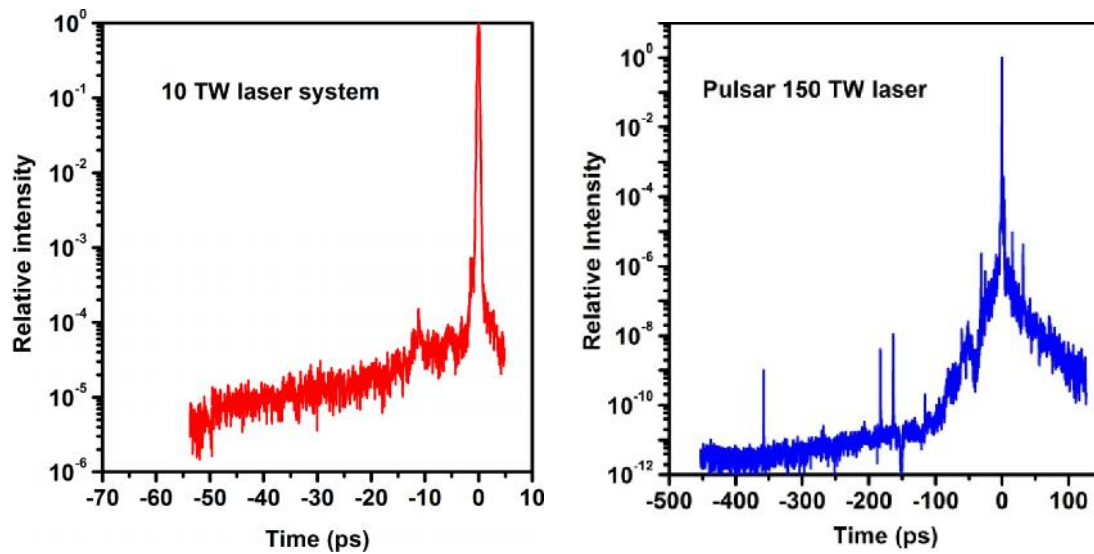


Figure 2.7: The contrast of 10 TW and Pulsar 150 TW laser systems

2.2.3. Laser focal spot measurement

The laser pulse needs to be properly focused to achieve the highest intensity at the focus. Off Axis Parabolic (OAP) mirror has been used for laser beam focussing. The OAP needs to be precisely aligned in order to achieve very small focal spot on the target. The alignment of OAP is very critical and it is optimized by imaging the focal spot on a 12 bit CCD camera (Model: PCO, Pixelfly) using 40x objective lens. The overall magnification of the setup was calibrated from the image of a mesh with known line spacing. Fig. 2.8 (a) shows the typical focal spot image of the 150 TW laser beam focused using an f/3 OAP mirror. The spot is almost circular with FWHM diameter 5 μm . The energy content within this diameter (area) was estimated to be

around 25%. Fig 2.8 (b) shows the 3D plot of the intensity distribution of focal spot. Most of the laser energy in the focal spot is concentrated within a very small area.

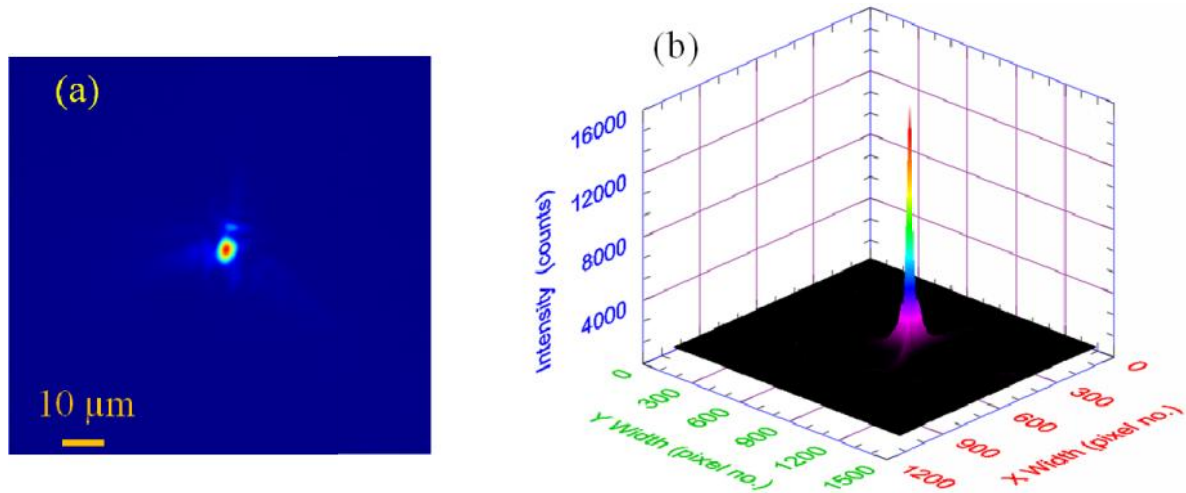


Figure 2.8: (a) Typical focal spot measured using focal spot imaging setup. (b) 3D plot of focal spot showing the intensity distribution of the focused beam.

After optimizing the focal spot by tuning the OAP mirror, the imaging set up is replaced by the target assembly. The target is kept at the laser focal plane by online monitoring the ion signal while scanning the target along the laser focus. When the target is exactly at the laser focus, the ion as well as radiation area monitor signal (kept for radiation dose measurement) are at maximum level. Later on, the imaging set up was improved with help of a long working distance (34 mm) infinity corrected objective lens. Using another imaging lens the focal spot was imaged at larger distance (outside the plasma chamber) as shown in Fig. 2.9. This imaging system was mounted on a vertical translation stage in order to remove from the beam path of laser as well as the ion during the laser shots. After optimizing the laser focal spot, the position of imaging set up was locked. Now the foil target was placed in a plane of the imaging set up so as to get the sharp target surface image on the CCD. To get the bright image on the CCD, the target surface was illuminated with the intense LED light source. Now with this imaging system the target can be placed at the best focal position with 20-30 μm accuracy of. Using the target imaging set up, the laser focal

spot was routinely monitored and the target was precisely placed at the laser focus. So rather relying on the laser focus search by monitoring the ion signal, the new target imaging set up gives absolute reference of laser focal plane. Fig. 2.10 shows the image of the Ni foil target recorded using the target imaging setup. As the target is placed at 30° angle, the left part of the image is sharper as compared to right part.

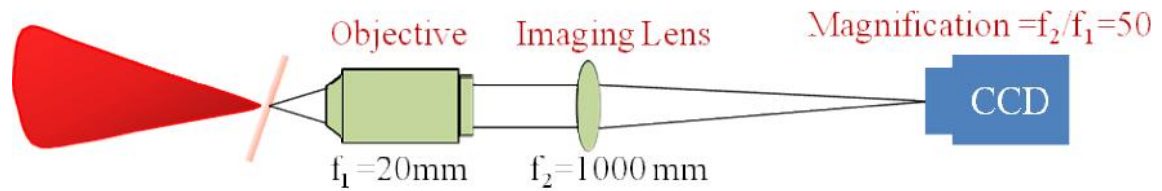


Figure 2.9: Focal spot/target imaging set up

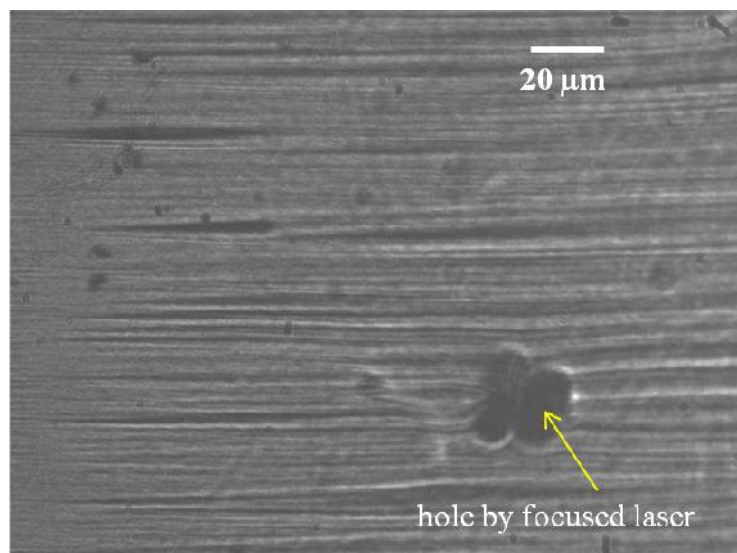


Figure 2.10: Image of the target rear surface. As the target is placed at 30° angle, therefore right part is slightly blurred.

2.3 Ion Beam Diagnostics

Different ion detectors and Thomson Parabola Ion Spectrometer (TPIS) have been used to characterize the laser accelerated ion beam. In this section first a brief introduction of various ion detectors used in the experiment will be provided later the details of main ion diagnostics i.e. TPIS will be presented.

2.3.1 Ion Detectors

Radiochromic Films (RCF):

Radiochromic Films are commonly used in medical field for radiation dosimetry of ionizing radiation. It has been also used for radiation measurement produced in high intensity laser plasma experiment. The RCF contains an organic dye which changes its colour when exposed to radiation (that's why the term radio + chromic). The film is self-developing i.e. develops in real time and requires no post exposure treatment. The change in colour is proportional to exposed radiation dose. It has a high sensitivity for highly ionizing radiations (e.g. for protons and heavy ions due to Bragg peak) and low sensitivity for less ionizing radiation like gamma-rays and electrons. The films are available with the trade name GAFCHROMIC[®] dosimetry film, manufactured by International Specialty Products (ISP Corporation). We have used GAFCHROMIC[®] HD-V2 type film in the experiments. This film consist of 8 μm thick active layer (marker dye, stabilizers etc.) coated on a clear polyester substrate of 97 μm thickness. The proton flux and energy distribution can be measured by placing a stack of RCF films in the ion beam path provided a calibration of the sensitive layer is known. In the present work the RCF has been used primarily for spatial profile characterization of the proton beam. Fig. 2.11 shows a typical image of proton beam spatial profile (for two different shots) recorded on different RCF layers having different proton cut-off energies from thin foil target using 150 TW laser.

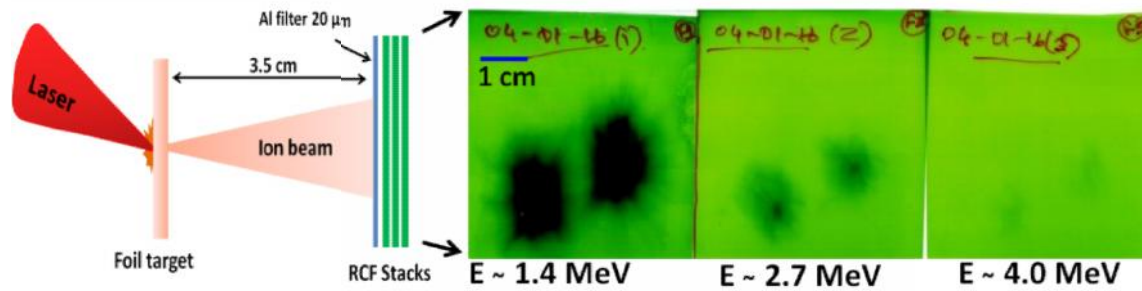


Figure 2.11: Proton beam profile recorded on RCF stacks. Proton energy cut-off is mentioned with respective layer.

CR-39 Detector:

CR-39 (or Columbia resin #39) is a solid state nuclear track detector (SSNTD) which is widely used for charge particle spectroscopy and dosimetry in different fields like medicine, space physics, nuclear physics and also in high intensity laser plasma experiments. It is a transparent plastic polymer namely polyallyl diglycol carbonate ($C_{12}H_{18}O_7$). It is sensitive only to highly ionizing radiation i.e. for protons and heavy ions but insensitive for electrons and high energy x-rays. This offers a significant advantage over other ion detectors viz. RCF film and micro channel plate (MCP) commonly employed in laser ion acceleration experiments which are sensitive to other radiations as well. The other advantage is that it is relatively cheaper and available in different sizes and thicknesses. The CR-39 sheets used in the present experiments are procured from *InterCast Europe, srl*.

When the ion passes through the polymer, it loses energy along its path by exciting and ionizing the molecules and result in chain break up. The permanent damage forms the latent track which is revealed by developing (etching) in concentrated NaOH solution at 70-80 °C for few hours. This is due the fact that the track etch rate is much faster as compared to bulk etch rate of the plastic. Accordingly a conical hole/pit is formed at the ion impact position. As the energy loss characteristics of ion depends on the energy and charge, therefore the track or pit

characteristic is also depends on ion charge and energy and it is different for different ionic species. Therefore it is possible to distinguish ionic species and their energy from the recorded track characteristics in the CR-39. The track/pit size depends on the ionic species, its energy and developing bath parameters like temperature and duration. In the present case, 6N solution of NaOH at 70° C has been used for etching the exposed CR-39 samples. The etching time was usually ranges from 1hr to 7 hr depending on the ions charge and energy. Carbon and heavy ions requires less etching time whereas protons requires relatively more time around few hours. Fig. 2.12 shows CR-39 sheet used in Thomson Parabola Ion Spectrometer (to be discussed in next section) for detecting ion signal at different etching time (a-f). Most of the tracks (parabola) are fully developed or visible in two hours etching time in case of heavy ions viz. carbon and oxygen. Whereas, the proton tracks are develop at much later time after 6-7 hours. Further, the low energy protons tracks are developed much earlier as compared to high energy protons (closer to the neutral point).

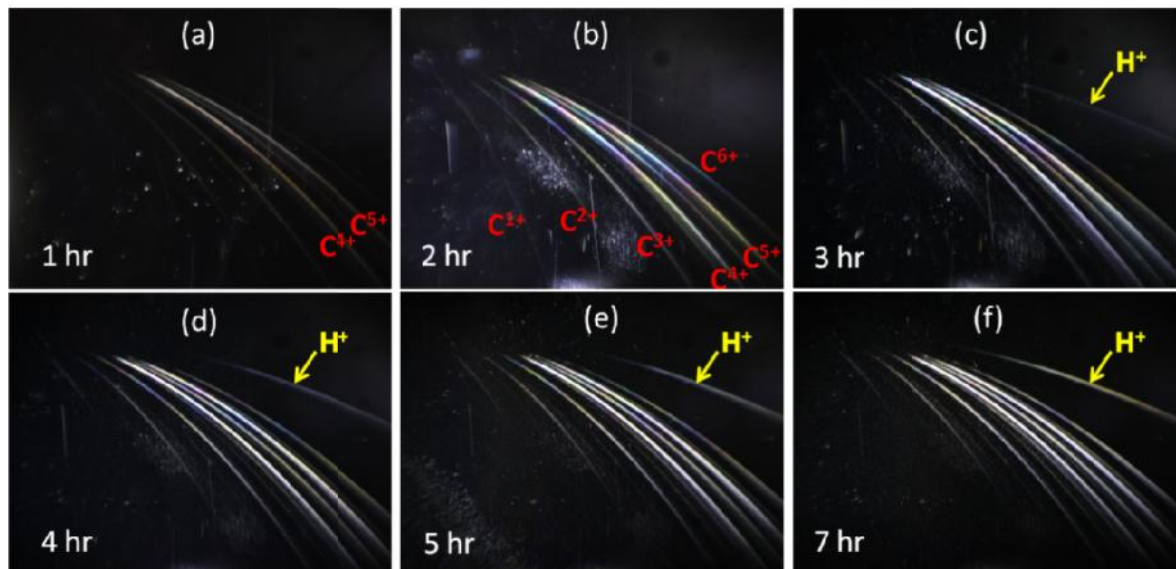


Figure 2.12: (a-f) Evolution of the ion signal on CR-39 with etching time. Ion parabola traces of different species were recorded on CR-39 detector used in TPIS.

After etching the CR-39 sheet, the tracks developed are read in an optical microscope. As the ions flux is very high, the corresponding particle track density is also very high and it becomes impossible to read the tracks manually. We have used an automated track analysis system procured from Track Analysis System Ltd. UK. The system consists of a microscope with CCD camera, motorized translation stages and pattern recognition software. The microscopic view of above images (Fig 2.10) at 50x magnification showing individual ion pits/tracks are shown in Fig 2.13. The images clearly show that, 2 hr etching is sufficient for carbon ions (Fig.2.13 (a) and (c)) after that tracks start merging (Fig.2.13 (b) and (d)). Whereas, about 6-7 hours etching time is required for the protons track to be clearly visible. As the CR-39 is sensitive to a single ion, therefore in the present work it has been used for calibration of Micro Channel Plate (MCP) detector (to be discussed in later sections). Although CR-39 has several advantages over the other detectors but the major limitation is that it is an offline diagnostic. It requires several hours processing time and hence online ion signal optimization by changing the laser irradiation parameters is not possible.

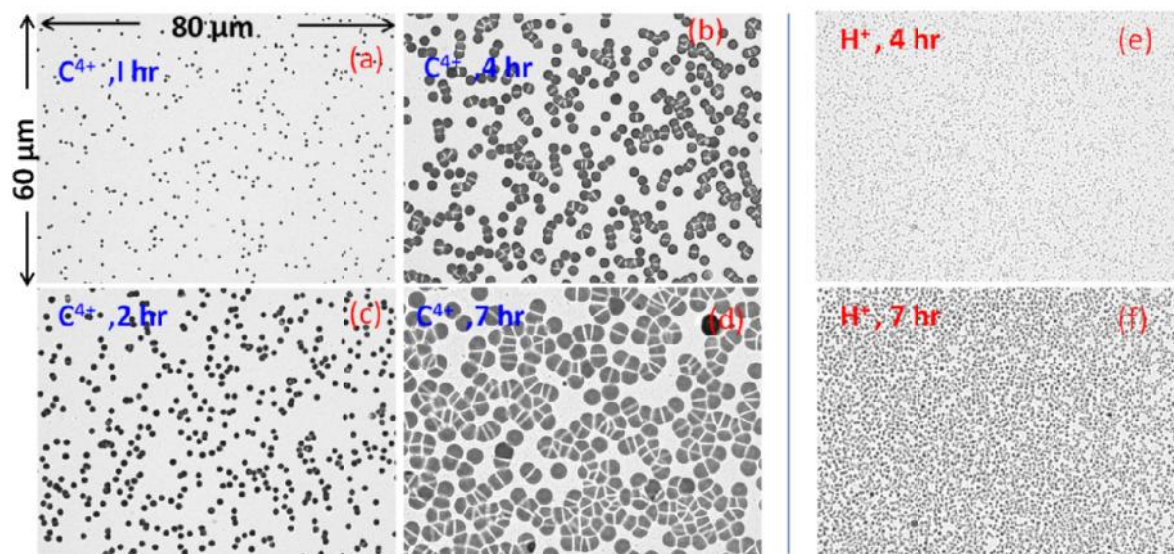


Figure 2.13: Carbon (a-d) and proton (e and f) tracks/pits of around 1 MeV after different etching time at 50x magnification.

Micro Channel Plate detector:

A Micro Channel Plate (MCP) is a two dimensional detector which is sensitive for ions, electron as well as x-ray photons. It consists of an array of large number of miniature electron multiplier channels that are arranged parallel to each other. The channel axis makes 5° - 15° angle with respect to the normal of the plate surface. The MCP channel diameter are typically in the range of 10-25 μm with aspect ratio (ratio of channel length to channel diameter) 40-60. When the incident radiation enters a channel, it produces secondary electrons from the channel wall. A high voltage $\sim 1\text{kV}$ is applied across the two faces of the MCP plate. The secondary electrons are accelerated by the electric field developed due to the applied high voltage. The accelerated electrons strike the channel wall and release more secondary electrons. This process is repetitive and finally a large number of electrons are released from the other side of the channel. In imaging mode MCP, there is Phosphor screen at the exit side which is kept at a higher potential gradient $\sim 5\text{kV}$. The electrons strikes on the phosphor screen emitting visible light. The light from the phosphor screen is image by a CCD camera. The MCP plates are used in single stage, double stage and triple stages configurations providing an electron multiplication by factor $10^4 - 10^7$ respectively. Unlike other ion detectors like CR-39, RCF and image plates, the MCP allows online measurement of the ion signal. With modern day high repetition rate laser system this offers a great advantage over the other off line detectors. Online feedback on the effect of laser irradiation parameters on ion signal gives more insight about the ion acceleration mechanism. During the present thesis work, a 40 mm size single stage MCP and 90 mm size double stage MCP had been used during different experimental campaign. The MCP-CCD detection system requires calibration for

absolute ion flux characterization. This was done by cross calibrating the MCP-CCD detector with CR-39 detector.

2.3.2 Thomson Parabola Ion Spectrometer

Thomson parabola ion spectrograph (TPIS) is a well known diagnostics for characterizing the energy spectrum of different ions and their charge states. In particular, it is a very useful diagnostics for laser plasma interaction in which a range of ion species are accelerated. Thomson parabola uses electric and magnetic fields that are applied collinearly and perpendicular to ion propagation direction. The particles enter the spectrograph through a small aperture at the front, and are dispersed by the collinear electric and magnetic fields according to their velocity and charge to mass ratio (q/m). The dispersed particles are detected at the other end of spectrograph by a two dimensional ion detector like CR-39 or a MCP detector. The ions while traveling through the two collinear fields viz. electric and magnetic fields experiences two mutually orthogonal forces due to Lorentz force and hence at a detector plane kept normal to the initial incident ion direction traces parabolic curve on the detector by each ion species. TPIS equipped with MCP as a detector enables online monitoring and recording of laser accelerated proton/ ion beam. Another advantage of using MCP is that it is not necessary to break the vacuum during the experiment (e.g. CR-39 has to be replaced after irradiation).

The Thomson parabola ion spectrometer simultaneously provides the ion energy distribution over a wide range of charge to mass ratio (q/m). The incoming particle under the action of Lorentz force ($F = q (E + v \times B)$) are deflected according to their velocity and q/m ratio by the applied fields (for non-relativistic ions) and are given by the following equations.

The deflection due to electric field;

$$x = \left(\frac{qEl}{mv^2} \right) \left(L + \frac{l}{2} \right) \quad (1)$$

The deflection due to magnetic field;

$$y = \left(\frac{qBl}{mv} \right) \left(L + \frac{l}{2} \right) \quad (2)$$

Combining these two equations, we get the equation of a parabola

$$y^2 = \left(\frac{q}{m} \right) \frac{Bl}{E} \left(L + \frac{l}{2} \right) x \quad (3)$$

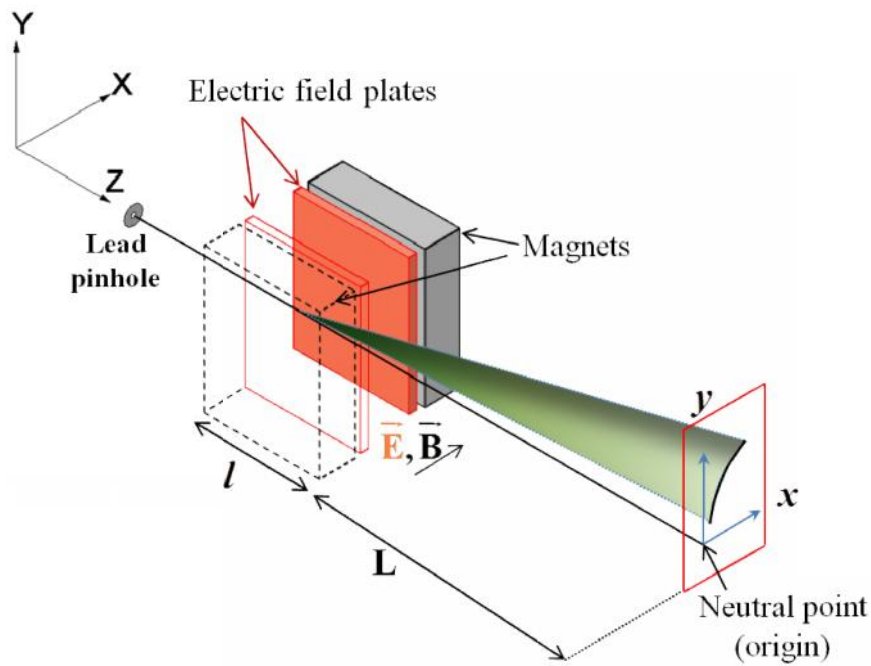


Figure 2.14: Thomson Parabola working principle

Where x and y are deflection due to E and B fields, q is the charge, m is the mass and v is the velocity of the particle. L is the drift length and l is region in which field is applied. Hence each species of different q/m ratio forms distinct parabolic traces on to the detector surface and deflection along the parabola gives the energy information. If we draw a straight line from the origin of the deflection coordinate (i.e. incident ion beam direction), we obtain a constant velocity line given by equation (4).

$$v = \frac{E}{B} \frac{y}{x} \quad (4)$$

Figure 2.15 shows theoretical parabola traces of some lighter species along with two constant velocity lines. The velocity line intersects the sets of parabolas (of Carbon) at different points. Along a velocity line the spacing between the intersections points of different carbon parabola traces is constant and they represent ions of same velocity but different energies. This holds good for any other ion species also.

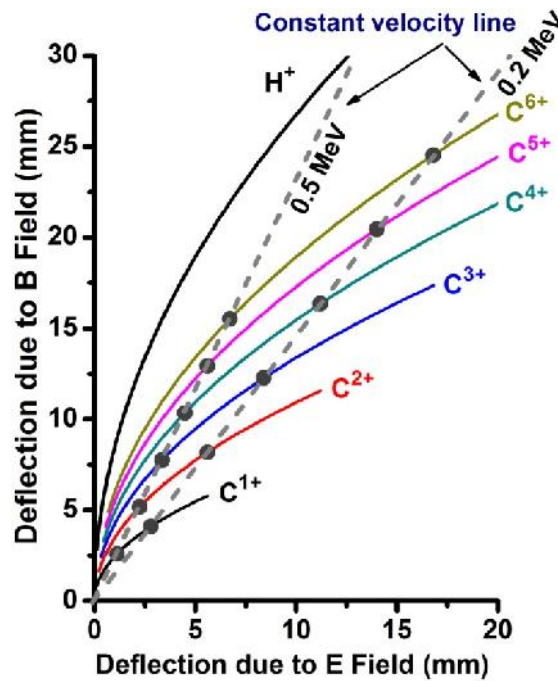


Figure 2.15: Parabola traces of Carbon and H^+ and intersecting two constant velocity lines corresponding to 0.5 MeV and 0.2 MeV respectively. The spacing between the intersection points along the particular line is constant for given set of parabolas of an element (here Carbon).

Various kinds of modifications in TPIS design have been recently reported to meet the experimental requirements [75]–[77]. High resolution and high dispersion Thomson parabola needed for high energies ions has been developed [78], [79]. In most of the system people use permanent magnets just to reduce the overall TPIS size. Normally the magnets are placed inside the vacuum chamber that basically fixes the energy range covered by the spectrometer due to finite size of the detector. Hence once the geometry and detector size are fixed, it cannot be changed without releasing the vacuum. In addition to this for online detection, MCP is preferred to have better

control on the experiment. In most of the cases the MCP is kept off centre just to use the whole area of the detector surface. Hence going for high resolution and off centre geometry one may miss the important things happening at lower energy side of the ion spectrum and particularly misses the negative species if present. Recently people have observed that along with positive ion, negative ions can also be accelerated in high temperature plasmas. This happens due to the charge exchange processes that occur while the accelerated ions traverses ambient surrounding plasma medium. The negative ions thus formed, normally have smaller energy as compared to positive ions governed by the charge exchange cross section. During the present thesis work, a versatile and compact Thomson parabola ion spectrometer has been developed. This TPIS facilitates recording of even negative ions along with MeV energy protons and carbon ions.

TPIS design and construction:

The current design is implemented by fabricating a small chamber that can be connected to main chamber. Fig. 2.16 shows the actual photograph of the in-house developed TPIS having a small parabola chamber connected to the main plasma chamber. Its input end which is rectangular in shape was connected to the main interaction chamber and at the exit end, an MCP detector was mounted. It has few additional ports, for electrical feed through, vacuum gauge and for a separate vacuum pump. Additional vacuum pump helps in achieving faster vacuum at MCP side. A Wilson seal arrangement is also provided before the MCP port to mount and insert passive detector like CR-39 during the experiment without breaking the high vacuum of the TPIS chamber. This facilitates cross calibration of MCP-EMCCD counts with the tracks recorded on the CR-39 detector for absolute measurement of ion flux. The TPIS input has a 2 cm thick lead disc with a 100 μm or 250 μm pinhole at the centre.

The thick lead shield collimates the ion beam and provides a very good shielding against high energy plasma radiation exposure to the MCP. The electric field was applied by using two rectangular copper plates of 100×50 mm size kept with a separation of 12 mm inside the rectangular pipe. The magnetic field is applied by inserting dipole magnets on the rectangular pipe from outside.

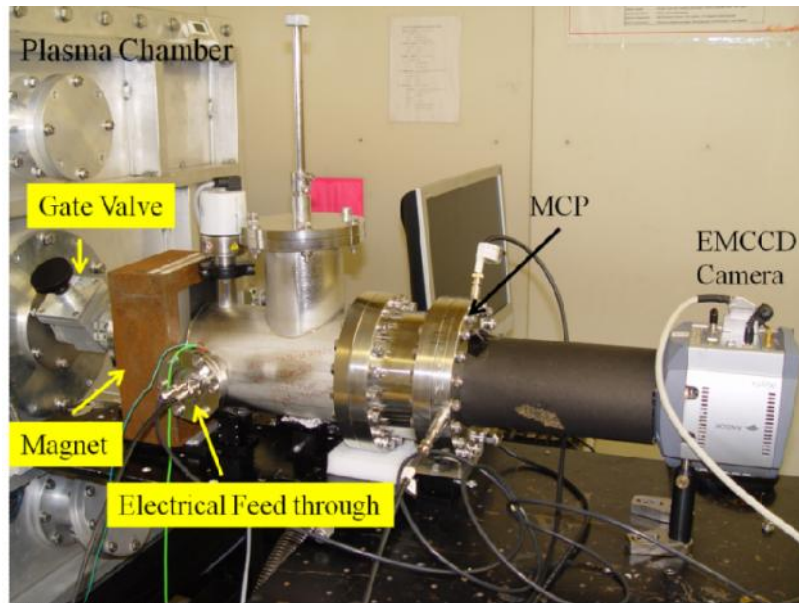


Figure 2.16: Real image of the developed Thomson Parabola Ion spectrometer connected to main plasma chamber.

Few sets of permanent dipole magnet of variable strength were designed for applying the magnetic field of different strength as per the experimental requirement. Field profile of one of such magnet is shown in Fig. 2.17. Since we are applying the magnetic field from outside, any particular region of the energy spectrum can be zoomed by proper choice of magnetic field. Also the polarity of the magnetic field can be changed during the experiment which basically changes the magnetic deflection direction. This was proved to be of great advantage and help in detecting negative ions as discussed in later chapter

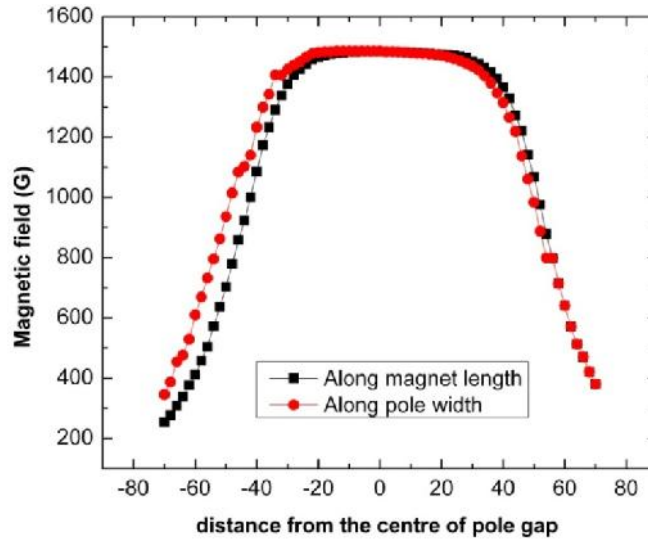


Figure 2.17: *Magnetic field profile along the length and width of the developed magnet*

Initial experiments were performed using a 40 mm diameter MCP providing a gain $\sim 10^3$. In later experiments the TPIS design was modified to increase the energy resolution and provide larger deflection area by using a double stage, high gain ($\sim 10^6$), 90 mm diameter MCP. In order to effectively use the full area of the MCP detector, The MCP port is designed off-centre from the input aperture axis of the spectrograph. The MCP phosphor screen emission / signal were imaged with a high gain Andor EMCCD camera. The camera can be externally triggered and synchronized with the laser shot to reduce the background noise. The MCP-EMCCD combination enables us online monitoring of the accelerated ion beam on a single shot basis. Various parameters of the latest TPIS are listed in table 2.2

Source to pinhole distance	745 mm
Electric filed plate length	100 mm
Field plate gap	12 mm
Field plate to detector distance	320 mm
Magnetic field to detector distance	320 mm
Magnetic field strength	1.5 kG
Magnet length	107 mm
Pinhole to detector	430 mm

Table 2.2: TPIS design parameters

Energy and Charge resolution of TPIS:

The resolution of the TPIS is primarily governed by the uncertainty in ion position on the detector surface. The primary factors contributing to the intrinsic resolution of TPIS for a given q/m ratio are the pinhole size used to collimate the incoming ion beam and the magnetic field characteristics. Higher magnetic field will result in higher dispersion and therefore higher resolution. But at the same time due to finite size of the MCP detector, higher magnetic field will limit the lower ion energy range which can be detected. Similarly, small pinhole increases the energy resolution due to the decreased spot size on the detector but this will also decrease the ion flux reaching on the detector. Hence there is a trade-off, between different parameters and choice of these parameters depends on the experimental investigation concerned. The intrinsic TPIS resolution $\Delta E/E$ can be approximated in the non-relativistic case using dispersion equation and is given by

$$\frac{\Delta E}{E} \approx \frac{2U_y}{qBl(L < 0.5l) / (2mE)^{0.5}} \quad (5)$$

Where, U_y is the ion beam spot size on the detector surface which is basically dictated by pinhole size and the distance from the source to pinhole and pinhole to detector i.e. on the magnification of the spectrograph. During the course of this work, two versions of TPIS were developed. The initial version (old TPIS) was used with 10 TW laser system where accelerated ion energy was low ($\sim 2-3$ MeV only). Later on with 150 TW laser system the TPIS design was modified to accommodate 90 mm size MCP as well as increase the drift length, electric and magnetic field values and with some more options. The energy resolutions of TPIS at different value of magnetic field and aperture sizes are plotted in Fig 2.18. The charge resolution i.e. separation of

different charge to mass ratio depends on electric field parameters together with drift lengths and the pinhole size.

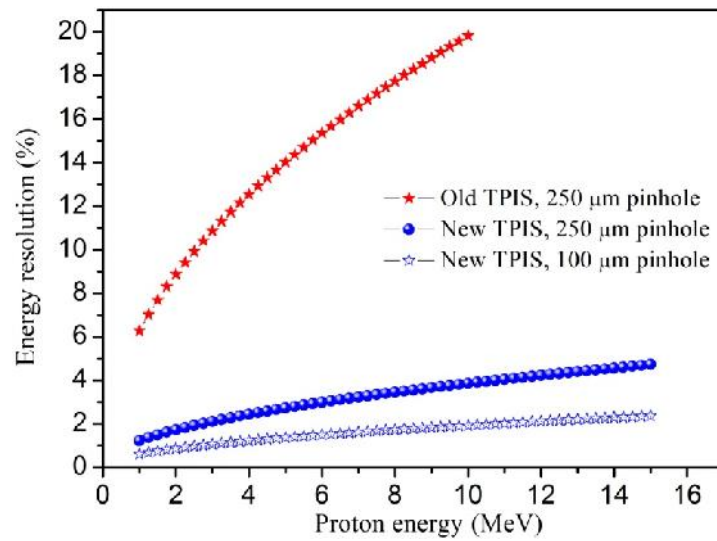


Figure 2.18: *TPIS resolution*

Performance of TPIS:

The developed TPIS has been used to characterize the energetic particle emission; positive and negative ions as well as neutrals from high intensity laser pulse with solid target. The experiments were carried out using 10 TW, 45 fs and 150 TW, 25 fs Ti:sapphire laser system at RRCAT. The general experimental setup for ion acceleration is shown in Fig. 2.15. The p-polarized laser beam was focussed using an off-axis parabolic mirror, to a peak intensity of $\sim 10^{18} - 10^{20} \text{ W/cm}^2$. The angle of incidence of the laser on the target was set to $30 - 45^\circ$. In case of thin foils the ion emission was recorded along the target rear surface normal direction (Fig. 2.19). Thick solid target was also used in few studies for recording the ions from front surface. In this the TPIS was placed along the target normal at front surface (Fig. 2.19).

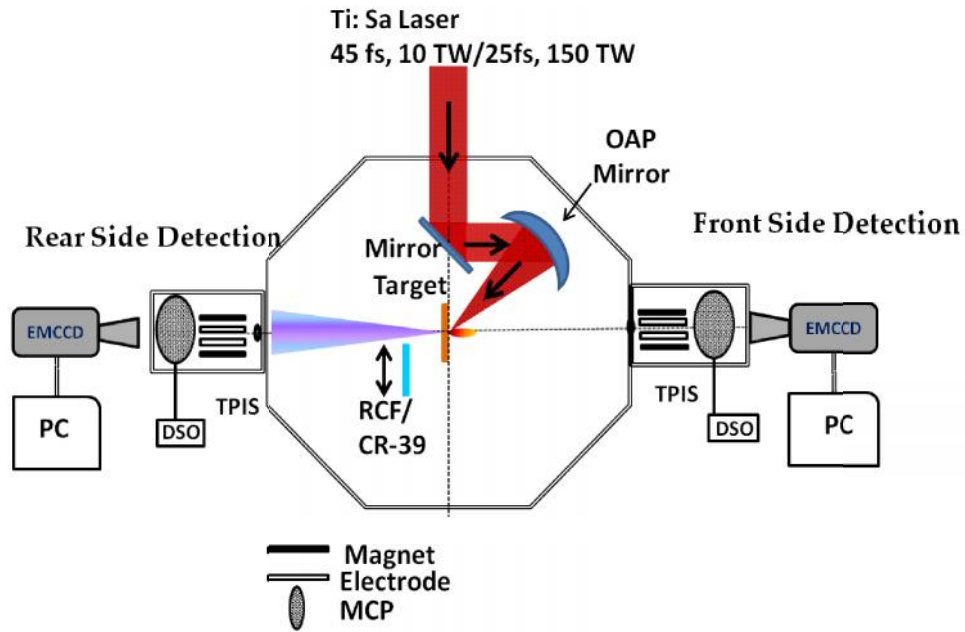


Figure 2.19: General experimental set up of ion acceleration. Both thin foils and bulk solid material have been used as a target for different experimental investigations. In case of thin foils TPIS was placed along rear surface normal direction whereas for bulk solid target it is placed along front surface normal direction.

Fig. 2.20 shows the parabolic ion traces recorded with TPIS with a 0.75 μm thick Al foil. Number of parabolic traces corresponding to different q/m ration can be seen. The parabolas are recorded as per their q/m ratio. Along a particular parabola it represents the energy information of a particular species. The points closer to the neutral spot (formed due to x-rays and neutrals) are of higher energy. Whereas low energy ions are deflected more in E and B field. Please note that irrespective of the target material, protons and carbon ions are the most dominant species. The source of protons and carbon ions is the hydrocarbon contamination which are normally present at target surface.

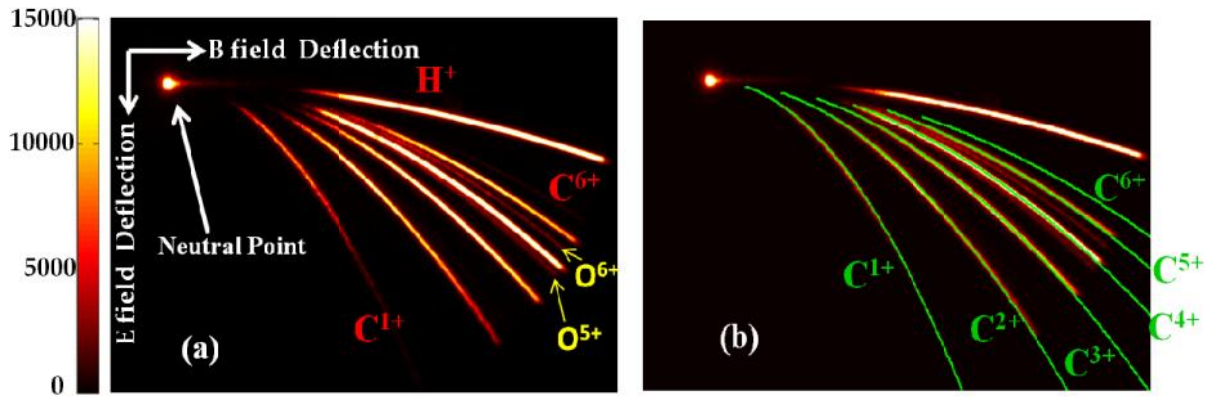


Figure 2.20: (a) Parabolic of different species recorded using TPIS. (b) Theoretical parabola fitting using the developed algorithm to identify and reconstruct the ion energy spectrum.

Data retrieval algorithm:

The captured image requires to be properly analysed to extract the information about ion charge state and their energy. According to parabola equation (eq. 3), ions of different charge to mass ratio (q/m) are separated into distinct parabolas. The parabola contains the information about ion energy with high energy ions falling close to the neutral point and those with lower energy deflected more. In the image, the deflection along x and y is given in terms of pixel coordinate i.e. spatial distance. Using the deflection equation due to E and B field, the x and y deflections is converted to energy scale. The deflection due to B field is large hence it is used for energy calculations. The neutral spot is a centre of origin for the deflection forces due to electric and magnetic fields. As the particle deflection is calculated with respect to neutral spot, hence its accurate identification is important. The centroid of the neutral spot is taken as the origin for the estimation of the ion energy for each individual TPI spectra recorded. It may also be noted that one or two pixel error in locating the origin will not introduce a significant error in energy spectrum. At maximum a proton energy of 8 MeV, one pixel width corresponds to about 100 keV energy bin. At lower proton

energy, this error would be much lower because of the non-linear dispersion due to magnetic field. The pixel intensity counts give the information about ion flux.

Hence for fast processing of the data an algorithm has been developed to theoretically reconstruct the parabolic trajectory (green line in Fig. 2.20 (b)) and read the data along line profile. Using the algorithm the observed parabolic traces are identified as marked in Fig. 2.20 (b). The parabolic trace has finite width which is basically governed by the size of pinhole used in front of the spectrometer. The full width of the trace has to be taken while counting the pixel intensity along the line profile. This was included in the algorithm by giving a slight variation of $\pm (q/m)$ about a particular q/m . The TPI ion spectra are recorded as CCD pixel intensity counts. During analysis of the ion spectra, firstly dark frame i.e. CCD camera frame recorded without firing the laser shot is subtracted from the TPIS image as depicted in Fig. 2.21. In Fig. 2.21 (c), counts/pixel along the yellow dotted line on Raw TPIS and Background image are plotted and shown in blue and black colour respectively. It is clear that camera thermal noise constitute a uniform DC background with each pixel having counts in 375- 400 range. The green line in Fig. 2.21 (c) shows counts along the same line profile after background subtraction.

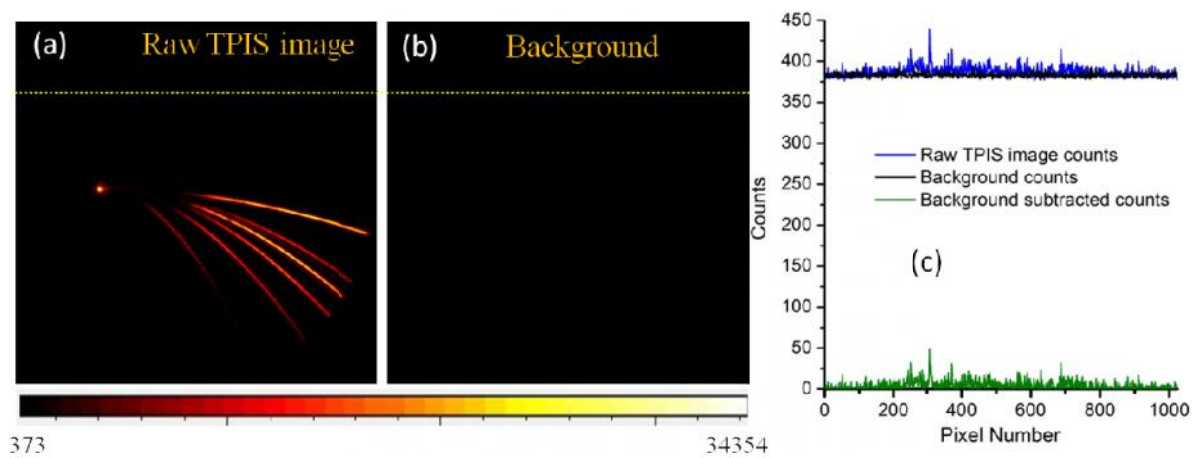


Figure 2.21: Background subtraction in raw TPIS image

One can see that, the above method of dark frame subtraction have significantly eliminated the contribution of background thermal noise signal. However, in case of ion spectra where the neutral spot is very intense i.e. having large counts, as have been observed with transparent CH foil targets and thick solid targets, the counts due to neutral spot blooming may add to the ion parabola signal close to the neutral spot. Therefore, to handle the noise (high background) generated close to the neutral point including the local background generated during the laser shot on the target, the counts along a parallel parabola taken close to the actual ion parabola signal was subtracted as shown in Fig. 2.22 (a) & (c). The width of the parabola used for noise subtraction was kept same as the actual width of the real ion parabola trace and total counts in that width involving multiple pixels is taken. In order to demonstrate the above said procedure, two different shots recorded using 0.75 μm thick Al target (Fig. 2.22 (a)) and 5 μm thick transparent Mylar target (Fig. 2.22 (c)) is taken. The proton signal count along the parabola traces and subsequent background subtraction are given in Fig. 2.22 (b) and (d) in case of 0.75 μm Al and 5 μm Mylar respectively. Red trace in Fig. 2.22 (b, d) represents $N(E)$ i.e. counts as a function of energy which is derived from respective proton parabola (blue trace in Fig. 2.22 (a, c)). It may be noted that for Al target the background is almost uniform whereas for transparent Mylar target the background counts increases as we go towards neutral spot (i.e. towards high energy side). Thus the maximum proton energy is derived after taking care of the background contribution as explained above.

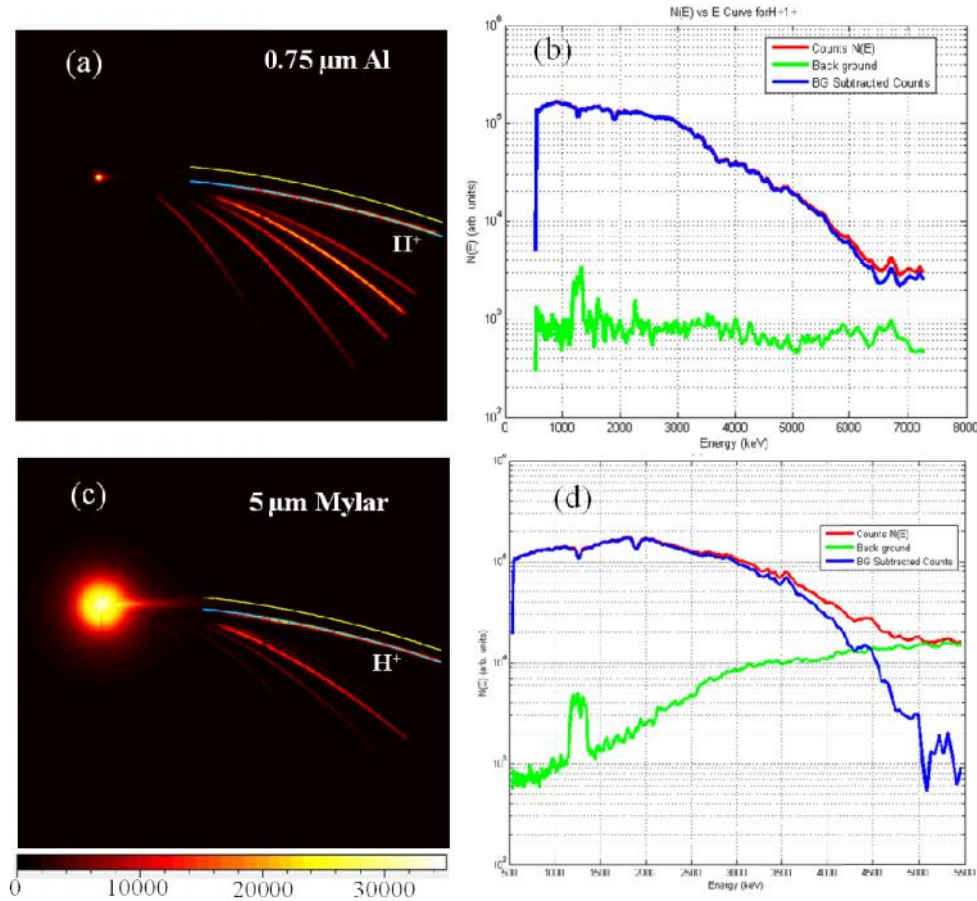


Figure 2.22: Dynamical Noise correction using a parallel shifted parabola for ion traces recorded using Al (a) and Mylar (b) targets. The counts from the parallel shifted parabola are subtracted from real fitted parabola counts for noise reduction (b and c). The blue curves in (b) and (d) represent net counts due to proton signal only. A small hump in green curves is an artefact due to damage in MCP.

Finally, the ion energy spectrum in terms of number of particles (pixel counts) as a function of energy i.e. $N(E_{kin})$ vs E_{kin} . In order to find out $dN(E_{kin})/dE_{kin}$ for a particular ion species, ion flux, N , within the energy interval E_{kin} and $E_{kin} + E_{kin}$ are taken. The constant energy width E_{kin} was taken to be 100keV. Fig. 2.23 shows the derived energy spectra of different species of the shot shown in Fig. 2.22 (a) above, using the developed data retrieval algorithm.

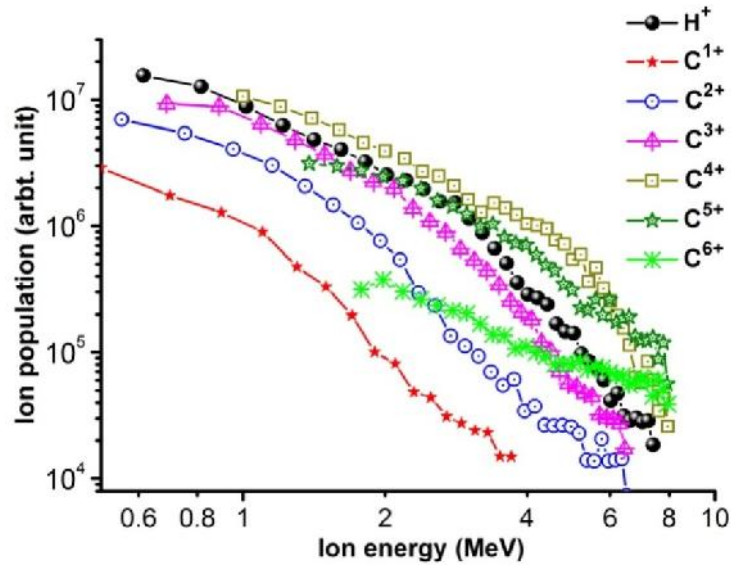


Figure 2.23: Energy spectra of different ionic species

Calibration of MCP with CR-39 Detector:

For absolute quantification of the ion population at various energies the MCP-EMCCD pixel counts requires to be calibrated with some absolute detector viz. CR-39 plate. In our recent experiment we had successfully performed the calibration. The CR-39 detector, which is sensitive to single ion has been used for this purpose. A CR-39 sheet was moved in front of the MCP in TPIS and exposed with ion beam under identical laser irradiation condition. The exposed CR-39 sheet was etched in a concentrated NaOH solution at ~ 70 °C for 7-8 hours. Fig.2.24 (a) shows the proton trace recorded on CR-39 detector. The zoomed portion shows the pits when hit by the individual proton at 50x magnification giving an idea about the proton flux density at different energies (Fig. 2.24 (b)). Initially, we had used 250 μm pinhole. The proton flux turns out to be so huge that it was difficult to count even with automatic track scanner. Therefore, later on to limit the flux we reduced the pinhole size to 100 μm (Fig. 2.24 (c)). The flux along the proton parabola was counted and energy spectrum was generated. A comparison of MCP-EMCCD and CR-39 spectra shown in Fig. 2.24 (d) yields a scaling factor. We can see that around 10^4 pixel counts correspond to 1

proton for this particular gain setting of MCP and EMCCD as well camera imaging setup. The total integrated proton flux was more 10^{12} per shot.

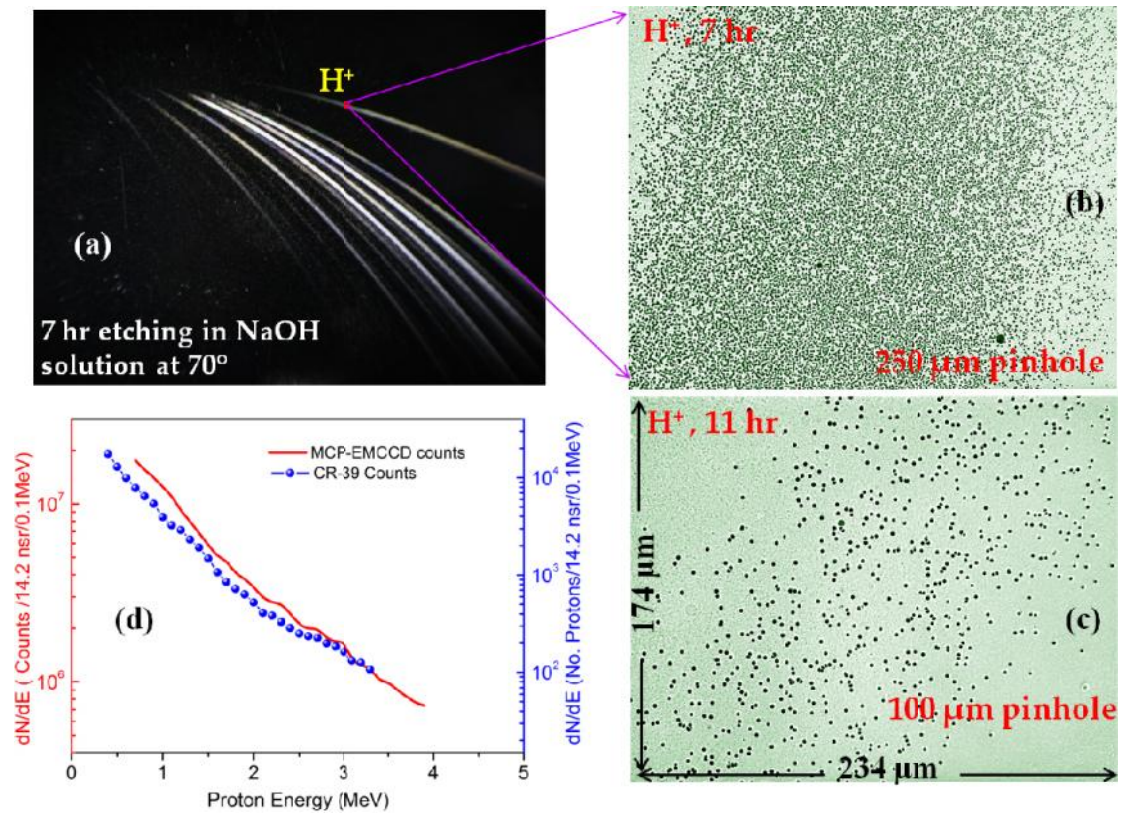


Figure 2.24: (a) Parabolic traces recorded on CR-39 detector. (b) Microscopic view showing individual proton tracks when 250 μm pinhole was used in TPIS. (c) with 100 μm pinhole in TPIS. (d) Calibration of proton spectrum obtained using MCP against absolute CR39 counts

2.4 Target Preparation and mounting

The experimental investigations presented in the current thesis are the outcome of three rounds of experimental campaign performed with 10 TW, 45 fs and Pulsar 150TW, 25fs laser systems. During this time different types of targets like thin foils of different material and thicknesses, plastic CH foils coated with high z material, sandwich target, nano structures and multilayer targets etc. have used for ion acceleration. Most of the thin foils are commercially available, however CD_2 foil (deuterated polyethylene) and deuterium coated foils were prepared in our laboratory. The CD_2 foils were prepared by the method described in ref. [80], [81]. First 99%

enriched deuterated polyethylene granules were dissolved in boiling xylene solution. The mixture is kept at boiling point for some time until all the granules have dissolved. Then the hot solution is poured onto a casting surface. The casting surface is allowed to cool, letting the xylene evaporate, leaving the CD_2 film. Using this method CD_2 film of $\sim 8 \mu\text{m}$ and $12 \mu\text{m}$ thickness depending on the CD_2 concentration with good uniformity and in large sizes were prepared as shown in Fig. 2.25. In addition to this, using dip coating method $1.5 \mu\text{m}$ thick Ni foil was coated with CD_2 at one surface. These foils have been used for deuteron acceleration. Some specialized nano structured and multilayer targets were locally fabricated at our centre. The required details of these targets will be provided in respective chapters.



Figure 2.25: Prepared CD_2 film of thickness around $8 \mu\text{m}$

Another important point of concern in case of thin foils particularly less than $2\text{-}3 \mu\text{m}$ is its mounting. It is important to hold the thin foil flat at the laser focus. For this purpose some special foil holders have been designed and fabricated. Fig. 2.26 shows one such foil mounting holder. It is made up of 0.5 mm thick spring steel sheet due to its high degree of flatness and resistance to deformation even for small thicknesses. An array of 2.5 mm holes in 11×11 format was made. The thin foils are sandwiched between two identical holders. In this configuration the laser induced

damage/perturbation is restricted to a single hole only and other parts remain unperturbed. It can accommodate quite large 121 laser shots, so that foils of different material and thickness can be mounted simultaneously for ion acceleration study in identical laser irradiation condition with quite good statistics.

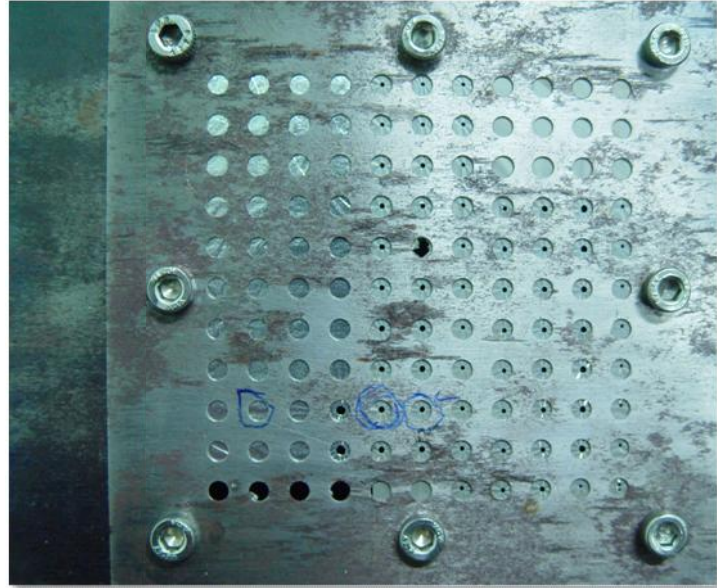


Figure 2.26: *Thin foil mounting holder. Very small holes are due to laser shots.*

CHAPTER 3

Studies on proton/ion acceleration using moderate contrast 10 TW,

45fs Laser system:

Initial studies on proton acceleration from thin foil targets were performed with 10 TW, 45 fs laser system. The important details of the laser system are given in chapter 2. One of most important point of concern in proton acceleration from thin foils is the laser pre-pulse contrast i.e. the ratio of the pre-pulse to the main pulse [56], [82], [83]. Particularly, Amplified Spontaneous Emission (ASE) pre-pulse of ns duration can significantly perturb the thin foil target by launching a shock wave and hamper the ion acceleration process. With the kind of intensities available with this laser system, ions are primarily accelerated by Target Normal Sheath Acceleration (TNSA) mechanism. The acceleration dynamics and laser pre-pulse governs an optimum foil thickness to achieve highest ion energies for a particular laser system. Although, there are many experimental studies on lighter ion acceleration (H^+ /proton and carbon ions) from thin foils using similar type of lasers, however the result from one system may not be fully generalized for other laser system due to the strong dependence on laser pre-pulse, laser focussing condition, and target parameters. Slight changes in laser interaction condition viz. laser pre-pulse and intensity have significant bearing on the accelerated ion beam. Therefore for a given laser system it is utmost important to determine the optimize foil thickness/material which support the pre-pulse present in the laser pulse for efficient ion acceleration. In this direction, we have used foils of different materials and thicknesses to optimize the proton acceleration. In particular we have shown that a judicious choice of target material can significantly enhance the accelerated proton energy. Further, use of double layer and multilayer targets

involving high z and low z combination can reduce the divergence (reduction in opening angle) of proton beam.

Several experimental studies on proton/ion acceleration from thin foils have been reported. It was observed that the accelerated proton ion energy and flux depends on various laser and target parameters like laser pulse energy, intensity, ASE contrast, foil thickness, foil material density and structural form etc. However, the ion acceleration is not fully optimized in terms of foil material or atomic number. As we have seen that the proton acceleration is intrinsically linked with hot electron transport inside the thin foil material, therefore the target foil material is expected to play important role in the acceleration mechanism. Indeed, there are reports [84] which show that hot electron propagation through the target is affected by the target resistivity. The perturbations or modulations in the beam of hot electrons current while propagating through the foil material will ultimately influence the sheath field at target rear surface and therefore the accelerated proton/ion energy spectrum. The following studies on proton acceleration from foil target are mainly motivated by the above aspect of hot electron propagation by employing targets of different foil materials.

3.1. Experimental details

The experimental set up is shown in Fig. 3.1. The p-polarized laser pulses from 10 TW, 45 fs laser system was focused using an $f/7$ off axis parabolic mirror on to foil target at an angle of 45° incidence. The maximum laser pulse energy during the experiment was in the range of 400 - 420 mJ. The laser focal spot on the target was $\sim 10 \mu\text{m}$ diameter (FWHM) which contains about 30% of the laser energy and the resultant peak intensity was $\sim 3 \times 10^{18} \text{ W-cm}^{-2}$. The main fs pulse is accompanied with a pre-pulse of 1.5 ns duration due to amplified spontaneous emission (ASE). The

contrast ratio between the main laser pulse to the ASE pre-pulse at ns scale was around 10^{-6} . The laser ASE was monitored using a fast photo diode and an oscilloscope of 1GHz bandwidth in each shot. The accelerated ion signal was recorded using a Thomson Parabola Ion Spectrometer (TPIS). The TPIS was installed along rear surface normal direction. The micro channel plate (MCP) detector and 16 bit EMCCD camera combination enables on-line ion signal monitoring. Radiochromic films (RCF) stacks have been used to record the spatial profile of the ion beam. RCF stack was wrapped in $12.5 \mu\text{m}$ thick Al foil to stop the low energy protons ($<1 \text{ MeV}$) and it was kept at 2.5 cm distance behind the foil target.

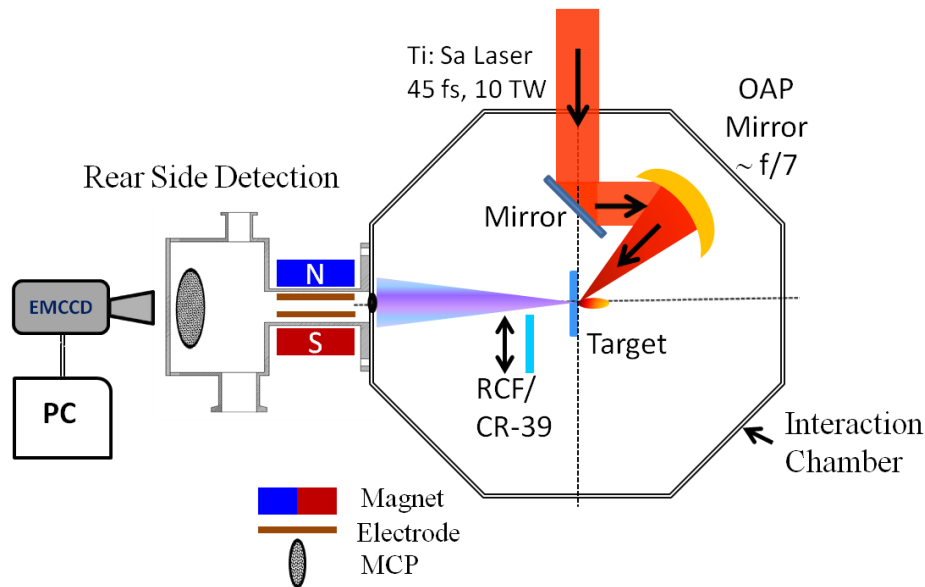


Figure 3.1: Experimental set up for proton acceleration from thin foil targets with 10 TW laser system

3.2. Effect of foil thickness and foil material on proton acceleration

Aluminum foils of different thicknesses namely 1.5, 2.5, 5, 6.5, 12.5, 25 and 50 μm were used as a target for proton acceleration. Besides these, foils of different atomic number (Z) with varying thicknesses like Ni (1.5, 5 and 25 μm), Ti (12.5 and 25 μm), Cu (12.5 μm), Ag (25 μm), and Ta (25 μm) foils were also used as a target in order to study the effect of foil material on proton acceleration. The choice of foil target of

different materials and thicknesses was based on easy commercial availability. A typical image recorded using the TPIS from 6.5 μm thick Al target is shown in Fig 3.2 (a) Protons with highest charge to mass ratio is the most dominant species. Carbon ions C^{1+} - C^{6+} are also present. The source of protons and carbon ions is the hydrocarbon contamination or impurity layers which are normally present on the target surface in typical vacuum conditions of 10^{-5} mbar inside the interaction chamber. The derived ion energy spectrum is shown in Fig 3.2 (b).

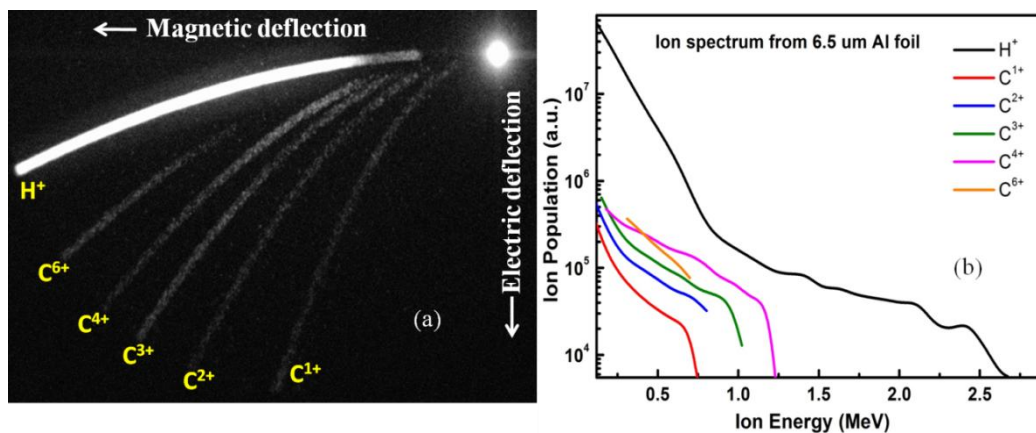


Figure 3.2: (a) Ion traces recorded using TPIS from 6.5 μm Al foil and (b) derived energy spectrum

We first studied the effect of foil thickness on proton acceleration using Al foils of different thicknesses. The proton energy spectrum from different Al foils is plotted in Fig. 3.3 (a) Variation of maximum (cut-off) proton energy with foil thickness is shown in the inset of Fig. 3.3. It is clear that as we go on reducing the foil thickness, the accelerated maximum proton energy increases. However, beyond certain thickness further reduction in foil thickness reduces the maximum proton energy. For the 10 TW laser, Al foils of around 6-7 μm thickness seems to be the optimum for achieving maximum proton acceleration. This effect has also been observed in earlier works [56], but the optimum foil thickness is different for different laser system. The reason behind this is the counter balancing effect of ASE induced foil damage/perturbation and hot electron propagation. The high energy hot electrons which is generated at target

front during the laser pulse interaction have typical divergence of 20° - 50° . The electrons traverse the foil material and reach the foil rear surface where the accelerating sheath field is formed. Therefore for thicker foils due to propagation effect, the electrons spread over a larger area on target rear surface. In addition the larger foil thickness can also stop electrons below certain energy. This result in reduction in electron density in sheath field and hence the accelerating field. As we reduce the foil thickness, the accelerating field gradient increases and hence the accelerated proton energy. However, below a certain thickness this trend changes which is due to the ASE pre-pulse arriving before the main fs pulse. The ns long ASE pre-pulse launches a shock wave in the foil material. If the shock is strong enough either it can destroy or deform the thinner foils or the shock breakout at target rear surface generates a plasma with long density gradient by target vaporization. Therefore, due to plasma formation at target rear, the sheath field is reduced to $E_{TNSA} \sim T_h/e\lambda_d \rightarrow T_h/eL$ (for plasma gradient scale length $L > \lambda_d$, the hot electron Debye length). The thinner foils are more prone to ASE induced perturbations. Hence the two counter effects give rise to optimum foil thickness.

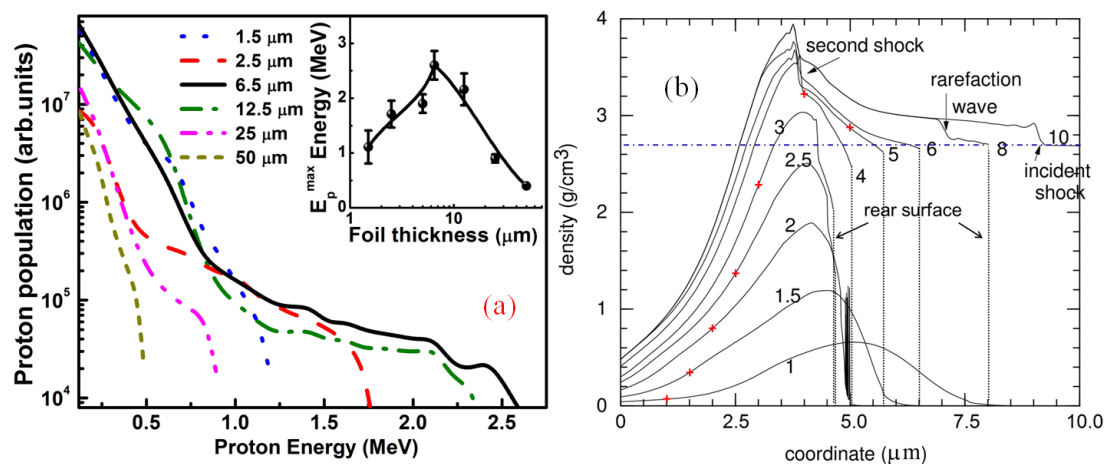


Figure 3.3: (a) Energy spectra of protons obtained from different Al foils. Variation of proton cut-off energy as a function of thickness is shown in inset. (b) Simulation result from hydrodynamic code Multi 1D showing density evolution of Al foils of varying thicknesses when subjected 1.5 ns ASE pulse with intensity $2 \times 10^{12} \text{ W/cm}^2$.

A one dimensional hydrodynamic code MULTI-1D [85] have been used to study the shock wave propagation due to the ASE pre-pulse in Al foils. Laser pre-pulse with 1.5 ns duration and 2×10^{12} W/cm² peak intensity closely matching with the measured ASE pre-pulse was used in the simulation. Fig. 3.3 (b) shows the evolution of density of Al foils with different thicknesses at the end of 1.5 ns laser pulse. The numbers next to line indicate the foil thickness in microns. The symbol (+) on each curve designate the initial position of targets rear surfaces. The foils whose rear surfaces are able to survive either in solid or solid-liquid mixed phase after 1.5 ns laser pre-pulse, for those foils the rear surfaces have been shown with a dotted vertical line. The solid Al density (2.7gm/cc) is shown by a dashed dot horizontal line. We can see that Al 1 μ m and 1.5 μ m foil are completely vaporized and no rear surface exist. In case of 2 μ m thick foil, there is region of gas-vapour mixture at rear surface. It is very much evident that for Al foil of < 2.5 μ m thickness, the foil rear surface evaporates as indicated by overall reduction in density as compared to pristine solid Al density. Up to 6 μ m thickness the rear surface appears to survive and beyond 6 μ m the rear surfaces are completely unperturbed. Therefore, the simulation clearly shows that for foil thickness less than 5- 6 μ m, the proton energy and flux decreases due to ASE induced deformation of target rear surface. For large thicknesses, it is the hot electron propagation behaviour which reduces the sheath electric field and hence reduction in proton energy. The results of hydrodynamic simulation match very well with the experimental observations.

The minimum suitable foil thickness is dictated by the laser pre-pulse strength. Therefore to further check this fact we performed the experiment with extended ASE pre-pulse duration. The ASE pre-pulse duration can be controlled by adjusting the delay time of the gate opening of Pockels cell in the pulse cleaner set up placed after

regenerative amplifier. Fig. 3.4 shows the proton energy spectrum obtained using 6.5 μm thick Al foil at various ASE pre-pulse conditions. The ASE profile at various setting of opening delay time of Pockels cell is shown in inset of fig. 3.4. With increase in ASE pre-pulse, the accelerated proton energy and flux consistently reduces. This indicates that the foil thickness that was optimum for minimum ASE pre-pulse condition does not remain so for extended pre-pulse condition. This clearly proves that the minimum suitable foil thickness giving the highest energy is governed by the laser pre-pulse condition.

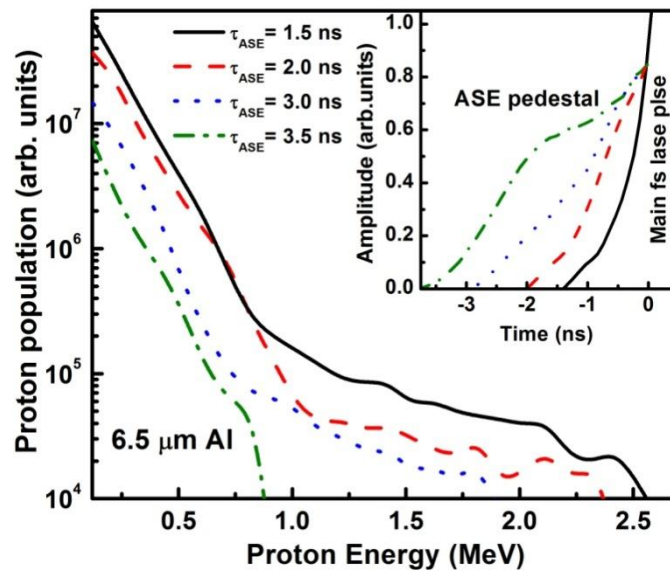


Figure 3.4: Proton energy spectrum obtained using 6.5 μm Al target at different ASE pre-pulse condition. Inset shows the pre-pulse profile at different opening time of Pockels cell.

Effect of Foil Material:

The pre-pulse induced shock pressure and the shock velocity inside the target depend on target density and atomic number. Hence to mitigate the ASE pre-pulse effect, Ni target was used. Fig. 3.5 (a) shows the results of hydrodynamic simulation showing the density evolution of Ni foils when subjected to a 1.5 ns ASE pre-pulse having intensity of $2 \times 10^{12} \text{ W/cm}^2$. Ni targets because of higher density and lower ablation rate are less affected by ASE pre-pulse as compared to Al target. For foils with

thickness more than 1 μm , the rear surface remains unperturbed (Fig. 3.5 (a)). For Ni 0.5 μm thick target, the ASE induced shock effect becomes visible (note the drop in density as compared to pristine density). Therefore, Ni foil of around 1 μm looks to be optimum thickness. Based on the simulation result, we used the Ni foil of thickness viz. 1.5 and 5 μm (available in lab) for proton acceleration studies. Proton energy spectrum from these targets is plotted in fig. 3.5 (b). For comparison, the proton energy spectrum from same thickness Al foils is also plotted. From the figure it is clear that Ni foils give significantly higher energy as compared to Al foils of same thickness. The maximum cut-off energy from Ni and Al targets of 1.5 μm thickness are 2.8 MeV and 1.2 MeV respectively. Further, it may also be noted that the observed maximum proton energy is also higher than that obtained from 6.5 μm Al foil (optimum thickness for Al) in similar experimental conditions. The lower optimum thickness for Ni foil target has resulted in less spreading of hot electrons during propagation on target rear surface. Therefore in case of Ni foil the accelerating sheath field is expected to be larger which further give rise higher energy protons.

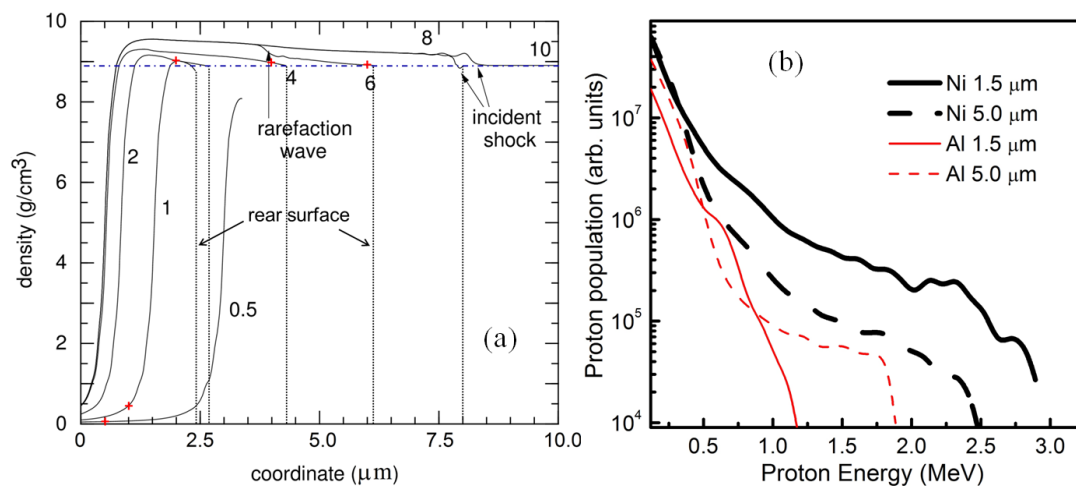


Figure 3.5: (a) Hydrodynamic simulation using Multi 1D code showing density evolution of Ni foils of different thicknesses when subjected 1.5 ns ASE pulse with intensity $2 \times 10^{12} \text{W/cm}^2$. The numbers next to line indicate the foil thickness in microns. The symbol (+) on each curve designate the initial position of targets rear surfaces. (b) Comparison of proton energy spectra from Al and Ni foils of 1.5 and 5 μm thickness.

Further, few more targets of different atomic number and densities have also been used to study the effect of foil atomic number (Z) on proton acceleration in more detail. The proton energy spectrum recorded from 12.5 μm (Al, Ti and Cu) and 25 μm (Al, Ti, Ni and Ag) thick foils are plotted in Fig 3.6 (a) and (b) respectively. The data from different foils is clubbed as per the thickness for more clarity. A 25 μm foil of Tantalum was also used but it did not give any ion signal. It can be clearly seen that the proton energy and flux decreases as the target atomic number or density increases. The maximum proton cut-off energy obtained from various targets used in the experimental campaign is summarized in Fig. 3.7.

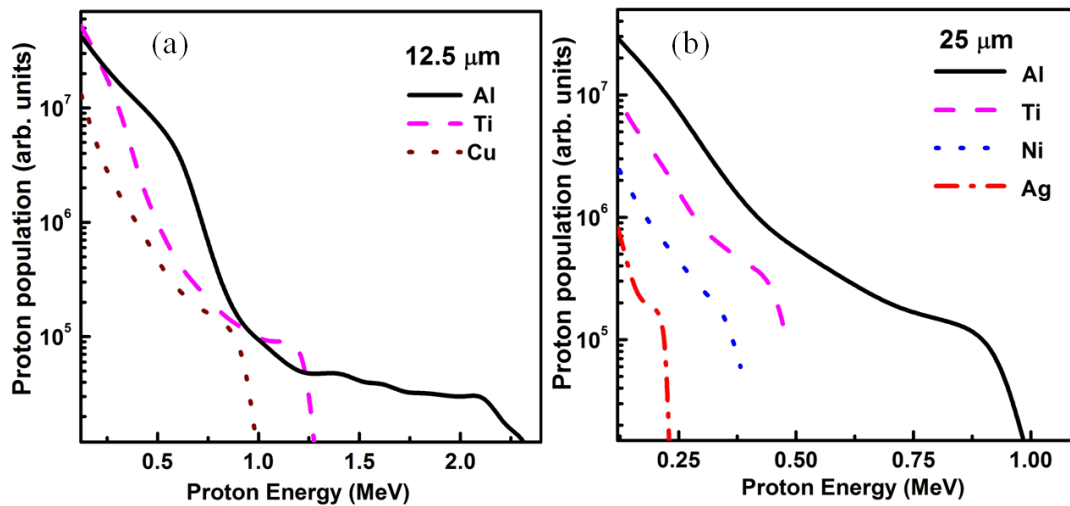


Figure 3.6: Proton energy spectrum obtained from (a) 12.5 μm and (b) 25 μm foil of different of different materials

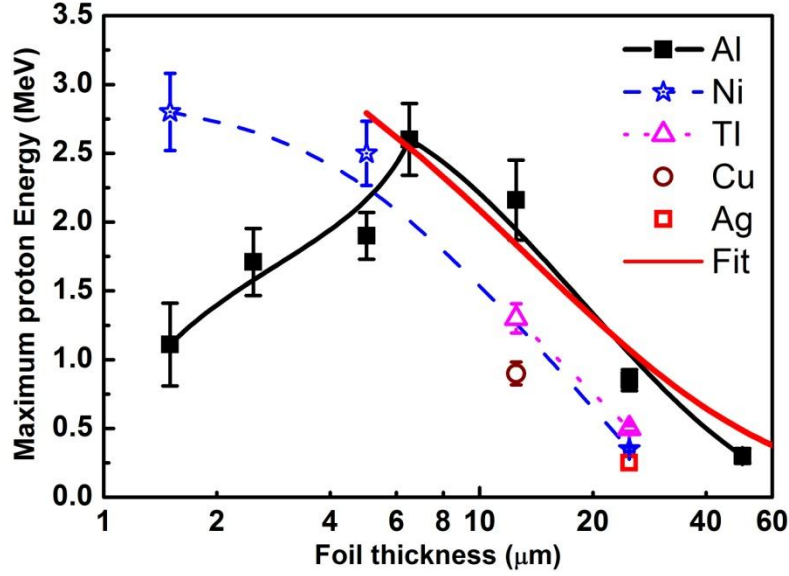


Figure 3.7: Maximum proton energy obtained from different foil materials and thicknesses. The red line is the proton cut-off energy estimated using Mora's model. Other lines (black, blue and magenta) are guide to eye.

In case of thicker foils (12.5 and 25 μm) where laser ASE pre-pulse effect is absent, the electron stopping power of the target material is playing an important role. For example, Ta 25 μm foil which did not show any ion trace can stop electrons up to 125 keV energy. In the same way, 25 μm thick targets of Ni, Ag, Ti, and Al will stop electrons up to 100keV, 100keV, 70keV and 55 keV respectively. The results clearly establish the role of hot electrons in sheath field formation at target rear surface. The thicker foils of high atomic number and density have higher electron stopping power and hence can stop the large fraction of hot electrons population in reaching target rear side. For these targets the sheath field will be weaker as reflected in lower proton energy. Using Hybrid PIC simulation, Zhou et. al. [86] have explicitly shown that by increasing the target density, the accelerated proton energy in TNSA mechanism decrease.

Finally, the observed maximum proton energies obtained from different targets was fitted using the expression based on self-similar isothermal plasma expansion model given by Mora [53] as $E_{\max} = 2T_{\text{hot}} [\ln(\tau + (\tau^2 + 1)^{1/2})]^2$. Here

$\tau = \omega_{pp} t_{acc} / \sqrt{2e}$ is the normalized acceleration time, $\omega_{pp} = (n_e e^2 / \epsilon_0 m_p)^{1/2}$ is the proton plasma frequency and t_{acc} is the acceleration time which is for ultrashort pulses can be taken as few time of the laser pulse duration [87]. n_e and T_{hot} are hot electron density and temperature that drive the rear surface expansion. One can estimate the hot electron temperature from the pondermotive scaling $T_{hot} = m_e c^2 [(1 + I \lambda^2 / 1.37 \times 10^{18})^{1/2} - 1]$, where m_e is the electron rest mass, c is the light velocity, I and λ is the intensity and wavelength of the laser light. One needs to estimate the hot electron density (n_e) in the sheath field. The total number of hot electrons that are accelerated at target front side is given as $N_e = \eta E / T_{hot}$, where E is the laser energy and η is the fraction of laser pulse energy converted into hot electrons. The value of η is typically in the range of 25 - 50% [83], [89]. The generated hot electrons propagate through the foil of thickness d and spread over an area $A_{sheath} = \pi(r_0 + d \times \tan \theta)^2$ at target rear surface. Where r_0 is hot electron source size at target front which can be taken as focal spot radius and θ is the half angle divergence of hot electrons. In similar experimental conditions we have measured the hot electron divergence to be $\sim 35^\circ$ [90]. Therefore the hot electron density in the sheath field is $n_e = N_e / c \tau_{laser} A_{sheath}$, here τ_{laser} is the laser pulse duration. Finally the maximum proton energy predicted by the plasma expansion model is compared with experimentally obtained value as shown in Fig. 3.7 (thick red line). A reasonably good agreement between experimental and theoretical values was observed. The deviation in Al for lower thicknesses is due to the destructive effect of ASE pre-pulse. The results suggest that with some constant multiplication factor, the same scaling is also valid for other foil materials as well. This further suggests that while formulating

a scaling law for proton/ion acceleration, the role of target material properties should also be considered.

3.3 Proton beam collimation using sandwich targets

In the same experimental set up used for proton acceleration in various foils, we extended the study on layered target consisting of high Z and low Z layer combination. Experimentally, we observed about 3 times reduction in proton beam divergence using multilayer (Al-CH-Al) targets. In addition, enhancement in proton energy and flux was also observed when a high Z layer was facing the laser.

Multilayer targets Al/CH/Al (2+1+2 μm), CH/Al/CH (2+1+2 μm) and double layer targets Au/Al, Al/Au on which around 0.5 μm gold (Au) was coated on 6.5 μm and 2.5 μm thick Al foil, were used in the experiment. The proton energy spectrum recorded from 5 μm Al/CH/Al and CH/Al/CH using TPIS is plotted in Fig. 3.8 (a). For comparison, proton energy spectrum from simple Al foil of 6.5 μm thicknesses is also plotted. It was found that Al/CH/Al target yielded higher proton energy and flux as compared to CH/Al/CH target. The 5 μm Al/CH/Al is found to give more or less the same energy and flux as obtained with the 6.5 μm Al foil. In general it was observed that on a pure CH foil; coating the front side (facing laser pulse) with high-Z material enhances the accelerated ion energy and flux. This is simply due to the fact that laser energy is efficiently absorbed in metallic high-Z target as compared to low-Z CH target. The proton beam profile was recorded on RCF, placed at 2.5 cm distance from the foil target and along the rear surface normal direction. The RCF was covered with 12.5 μm thick Al foil setting the energy cut-off around 1 MeV for protons and 15 MeV for carbon ions. The divergence (full emission cone angle) of the proton beam was calculated as $2\theta = 2\tan^{-1}(x/2.5)$, where θ is the half angle divergence and x is the radius of proton beam on RCF. Fig 3.8 (b) shows the proton beam profile recorded on

RCF from multilayer targets. The proton beam profile from CH/Al/CH has filamentary structures and shows large divergence as compared to Al/CH/Al target. For comparison proton beam profile recorded from 6.5 μm thick Al foil is also shown. In Fig 3.9, we plotted the divergence of the proton beam obtained from different targets. The proton beam divergence from 5 μm thick Al/CH/Al targets shows about 3 times lower divergence as compared to same thickness CH/Al/CH targets. From the graph one can also infer that whenever a high Z layer is present at target rear side, the beam divergence is lower. The overall higher divergence of Au coated Al target of 2.5 μm thickness is due to the fact that thin target are strongly perturbed because of the ASE induced shock wave as discussed in previous section.

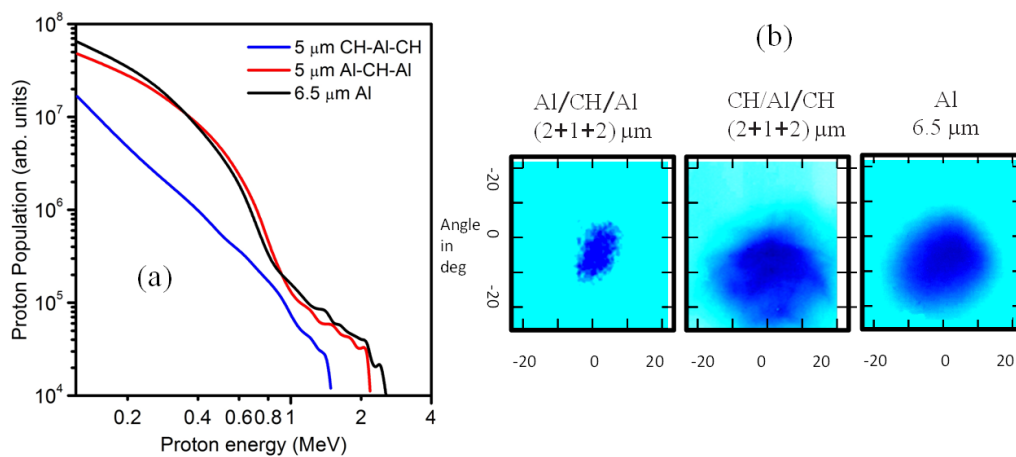


Figure 3.8: Proton energy spectrum recorded from Al/CH/Al, CH/Al/CH and simple Al foil (a). Proton beam imprint ($>1\text{MeV}$) recorded on RCF from 5 μm thick Al/CH/Al and CH/Al/CH targets and simple 6.5 μm thick Al foil (b).

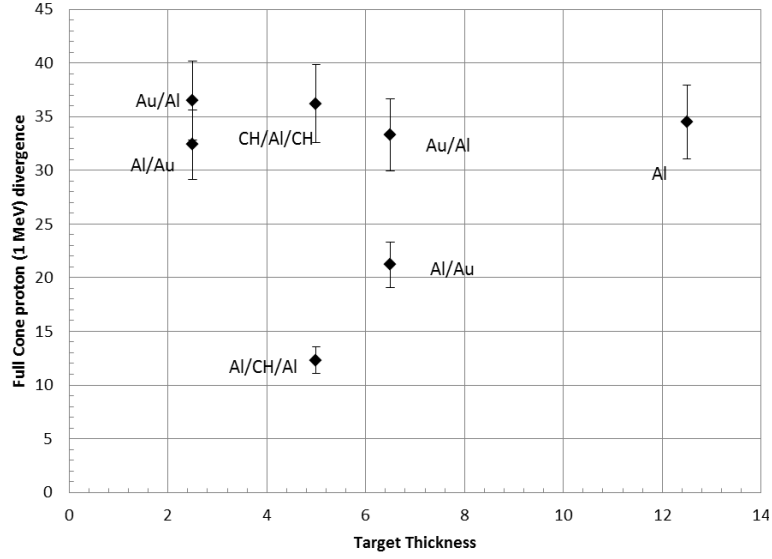


Figure 3.9: Measured proton beam divergence using the RCF from different targets.

To understand the beam collimation with multilayer targets, 2D PIC simulations have been performed using the code employed in reference [91]. In order to accommodate large density scale length, weighted particle technique was used. A p-polarized laser pulse of 800 nm wavelength and 3×10^{18} W/cm² intensity was incident from the left side of the simulation box at 45° angle. The laser transverse profile was a Gaussian with focal spot of 10 μm. The laser pulse arrives at the focus surface ($x + y = 0$) at $t = 0$ (the simulation begins from $t = -30\lambda/c$ i.e. -100 fs). In the CH/Al/CH target, CH plastic pre-plasma + 2 μm CH plastic + 1 μm Al + 2 μm CH plastic + 10 nm proton layers were used. Similarly, in Al/CH/Al target, Al pre-plasma + 2 μm Al + 1 μm CH plastic + 2 μm Al + 10 nm proton layers were employed. In the rear surface proton layer the proton density $n_H = 20n_c$ was taken. In CH plastic layer $n_H = 20n_c$, $n_{Carbon} = 10n_c$ and for Al layer $n_{Al} = 10n_c$ were taken. The pre-plasma density profile was assumed to be exponential; for CH plastic pre-plasma $n_H = 2n_{Carbon} = 20n_c \exp(-2x/\lambda)$ and Al pre-plasma $n_{Al} = 10n_c \exp(-2x/\lambda)$. The corresponding electron density n_e was taken such that to satisfy the quasi-neutrality requirement. The resolutions in x , y and t were set to be $\Delta x = \lambda/256$, $\Delta y = \lambda/64$ and Δt

$= \Delta x/c$ respectively. The proton phase space (p_x, p_y) distribution at $t = 150\lambda/c$ for CH/Al/CH and Al/CH/Al target have been compared in Fig. 3.10 (a), (b). Significantly better collimation of the accelerated proton beam from Al/CH/Al can be clearly noticed. To find out the reason for better collimation, the nature of the electrostatic field formed at target rear surface was studied for different targets. The distribution of accelerating electrostatic field E_x at $t = 150\lambda/c$ for CH/Al/CH and Al/CH/Al target is plotted in 3.10 (c) and (d). It can be seen that in case of Al/CH/Al target the electrostatic field have smooth contour line which are roughly parallel to the target rear surface over wide region. The smooth and parallel nature of electrostatic field profile gives better collimation in Al/CH/Al target as compared to CH/Al/CH targets. Similarly, the simulation results with Au/Al and Al/Au also indicates that whenever the relatively high Z layer is at target rear side, the electrostatic filed lines are relatively smooth and field lines are parallel giving better collimation or lower divergence.

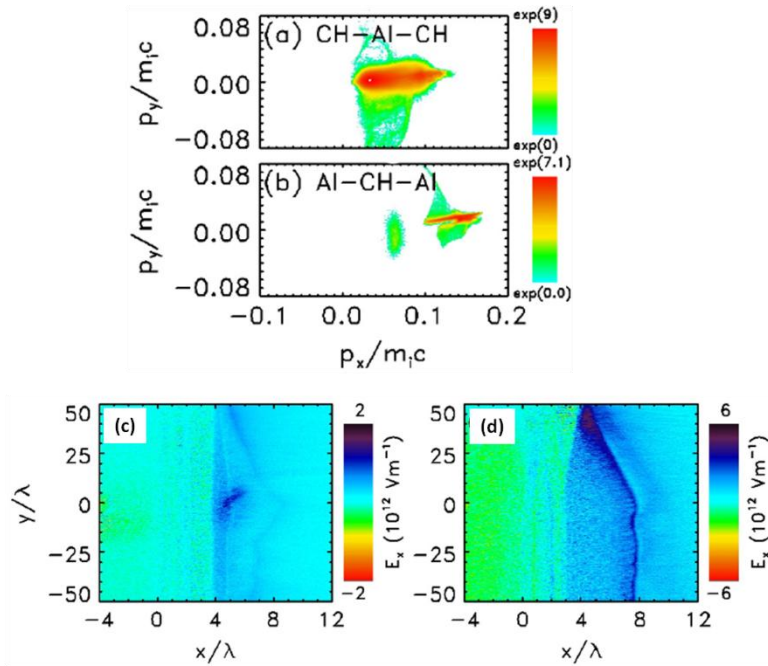


Figure 3.10: The phase space distribution of laser accelerated protons from sandwich targets (a) CH/Al/CH and (b) Al/CH/Al at time = $150\lambda/c$ obtained by 2D PIC simulations. The rear surface electrostatic sheath field distribution for (c) CH/Al/CH and (d) Al/CH/Al targets at time = $150\lambda/c$.

3.4 Conclusion

We have studied the optimization of the laser irradiation condition for 10 TW, 45 fs Ti:sapphire laser for efficient proton acceleration. An extensive study on the effect of foil thickness and the laser pre-pulse parameters was performed. Experimental observations on optimum foil thickness for Al and Ni foil targets matches very well with hydrodynamic simulations. The role of foil atomic number (Z) on proton acceleration has also been investigated. The results show that the judicious choice of the foil material with appropriate thickness can further enhance the ion acceleration efficiency for a given laser system parameters. It was also found that the simple scaling law based on laser intensity and laser pulse parameters are inadequate in predicting the maximum proton energy. In addition we have also observed that a suitable combination of high Z and low Z layered targets can give rise to low divergence proton beam.

CHAPTER 4

Studies on proton/lighter ion acceleration using high contrast 150 TW, 25fs Laser system:

Studies on ion acceleration in thin foils were extended at higher laser intensities and using higher contrast (better than 10^{-10}) beam. For this 150 TW, 25 fs Ti:sapphire laser system was used. The much higher contrast has enabled us to use foils of sub-micron thickness. With the availability of higher power laser, we explored some interesting problems by changing the laser irradiation conditions. In particular, we have demonstrated that ion acceleration from thin foils is not the optimum for shortest pulses and at highest intensity instead longer pulses with appropriate temporal shape are more promising for efficient ion acceleration. In this chapter we will discuss some of our results on monoenergetic proton bunches with energy spread ($\Delta E/E$) around 40% from 0.75 μm Al target at focused intensity $\sim 10^{20}$ W/cm². Some interesting observations on the contrasting effect of laser pre-pulse from thin transparent plastic targets coated with high Z material will also be discussed.

4.1 Multi MeV proton acceleration with high contrast laser pulses

The 150 TW, Ti: Sapphire laser system has already one saturable absorber (SA1) for improving the laser pre-pulse contrast. In initial experiment, we realised that the contrast is not sufficient for very thin foil targets. Therefore, we used an additional saturable absorber (SA2) to improve the contrast further. The details and location of these saturable absorbers are given in chapter 2, section 2.1.2. With the use of *two* saturable absorbers the pre-pulse contrast was improved to better than 10^{-10} at 100 ps time scale. The contrast of 150 TW laser system with one (only SA1) and with both

(SA1+SA2) saturable absorbers measured with third order cross correlator *sequoia* and with a fast photo diode coupled with 1GHz oscilloscope are shown in Fig. 4.1.

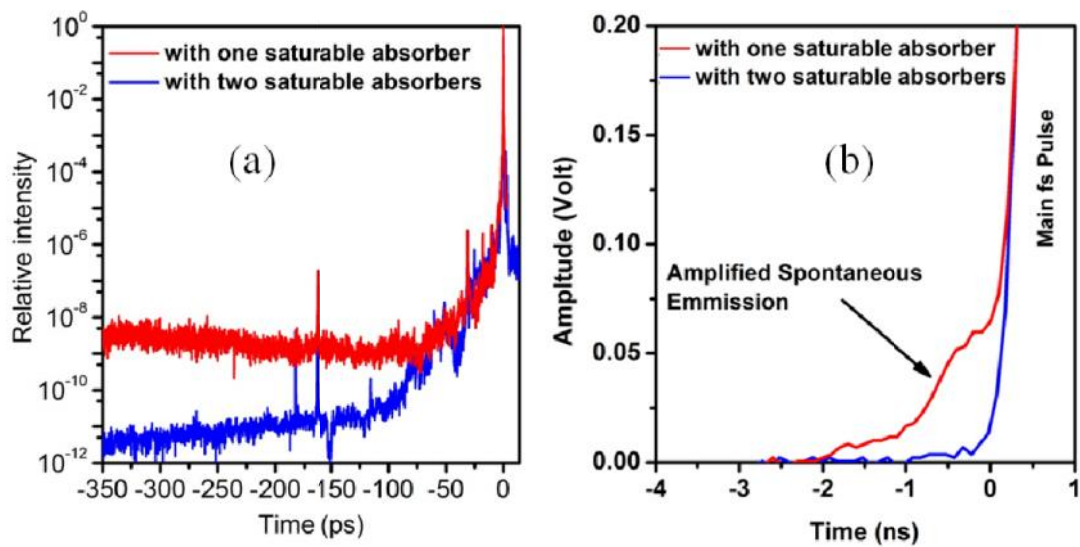


Figure 4.1: Contrast of 150 TW laser in case of single SA and double SA measured with (a) third order cross correlator *sequoia* and (b) fast photo diode coupled with 1GH oscilloscope.

The ion signal recorded using TPIS from rear surface 0.75 μm thin foil target with and without SA2 is shown in Fig. 4.2 (a), (b) in consecutive laser shots. The available laser power was around 85 TW with on target intensity $\sim 2 \times 10^{19} \text{ W/cm}^2$ at 45° angle of incidence. The proton beam profile ($> 1.4 \text{ MeV}$) recorded on RCF for the respective cases are also shown in the figure. It is very much evident from TPIS parabolic traces and from the RCF image that in case of single saturable absorber (only SA1), the foil is not able to sustain the destructive effect of the pre-pulse. The beam profile on RCF clearly shows the foil deformation due to ASE pre-pulse. The proton energy spectrum for the two cases is plotted in Fig. 4.2 (c). Significant improvement in proton energy and flux are observed in high contrast case. Please also note that with SA2 the final laser pulse energy reduces about 18-20%. Therefore, all the subsequent experiments on ion acceleration with 150 TW system were performed using extra saturable absorber i.e. with SA2. At 85-90 TW power level and focused

laser intensity $2-3 \times 10^{19}$ W/cm², the maximum accelerated proton energy was around 6-7 MeV. In next section, we will be presenting the results on ion signal optimization by modifying the temporal characteristics.

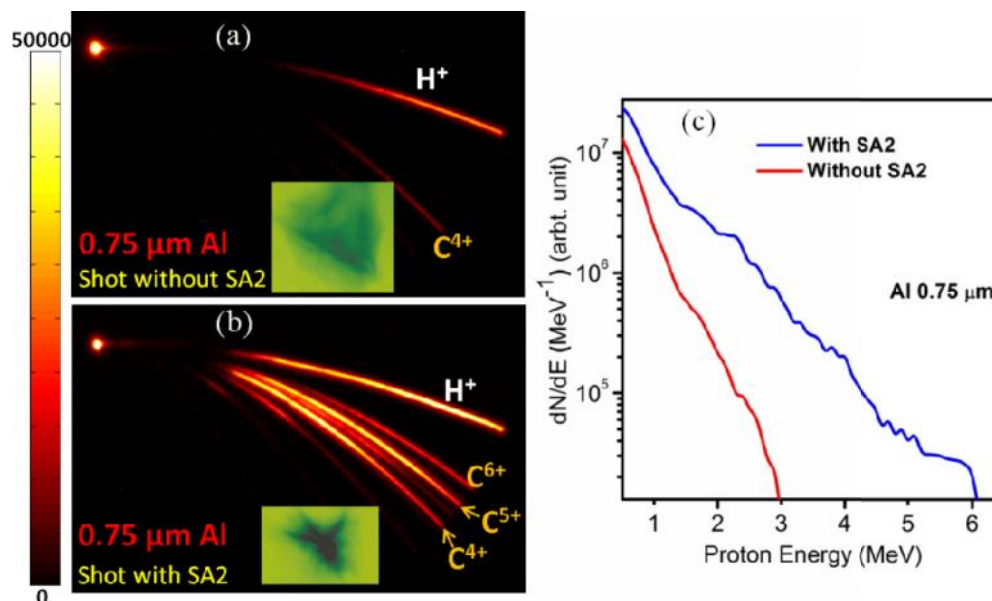


Figure 4.2: The ion traces recorded with TPIS using 0.75 μm Al foil (a) without and (b) with second saturable absorber (SA2). The corresponding ion beam profiles are also shown. The proton energy spectra for two cases are shown in (c).

4.2 Effect of laser temporal shape on ion acceleration

Now we know that, the ion acceleration efficiency depends on various laser and target parameters like laser pulse energy, intensity, pre-pulse contrast, target material, its shape, its size and thickness etc. [3], [4]. In the recent past, there has been an enormous effort for getting higher and higher ion energy and flux by optimizing these parameters [29], [92], [93]. The sheath field in TNSA which derives the ion acceleration scales as $\sqrt{n_{\text{hot}} T_{\text{hot}}}$ i.e. on the product of hot electron density and temperature in the sheath field as long as the rear surface density scale length (l) is less than hot electron Debye length λ_d . Therefore, to maximize the product $\sqrt{n_{\text{hot}} T_{\text{hot}}}$ for enhancing the accelerating field, demands efficient laser energy transfer to plasma electrons and same has been successfully demonstrated using different types nano

structured and mass limited targets [92]–[95]. Since the hot electron temperature so also the accelerated ion energy scales with laser intensity, therefore conventional wisdom guides us to maximize the laser intensity on the target by achieving minimum focal spot and using the shortest possible pulse duration. However, we observed experimentally for the first time that one can achieve higher acceleration of ions even with much longer pulse duration i.e. at much lower intensity which is counterintuitive observation. . The main reason behind this is the modification of the laser temporal shape caused by the incomplete compensation of the higher order phase terms while detuning the compressor grating separation. The detuning of the compressor grating also introduces chirp in the laser pulse. The effect of laser temporal pulse shape in enhancing the electron yield in laser wake-field acceleration [96] and in enhancement of k_x x-ray yield [97] has been demonstrated but to the best of our knowledge, this is the first experimental observation which shows the effect of laser temporal shape on ions/protons acceleration.

In this section the effect of laser pulse duration and temporal pulse asymmetry on ion acceleration with ultra-high contrast ($> 10^{-10}$) laser system has been discussed. The pulse duration was varied from minimum 25fs up to 500 fs by changing the laser pulse compressor grating separation for fixed laser pulse energy (2.1 J). It was found that the ion acceleration is not optimum at shortest pulse duration and highest intensity as suggested by the previous intensity scaling studies. Instead temporally stretched pulse is better for efficient ion acceleration. More importantly, we found a contrasting difference with respect to the sign of the laser chirp for almost same laser pulse duration. We found 60-70% enhancement in maximum ion energy (from 6 MeV to 10 MeV) and more than one order enhancement in flux at a positively chirped laser pulse of 250- 350 fs at the same laser energy. Whereas negatively chirped stretched

pulses show monotonic reduction in ion energy and flux. In order to understand the process further, we measured the hot electron energy spectrum and flux appearing at the target rear. Electron energy and flux also showed similar behaviour as observed for ions. The details of the experiments and results are discussed in the following sections.

Experimental set up:

The experiment was performed with 150 TW, 25 fs Ti: sapphire laser system. During this experiment, the available laser pulse energy was 2.1J (84 TW). The p polarized laser pulse was focused to an intensity of 3.2×10^{19} W/cm² using F/3 off axis parabolic mirror. The schematic diagram of experimental set up is shown in Fig. 4.3. Al 1.5, 0.75 and 0.4 μ m, Ta 0.5 μ m and Ni 1.5 μ m foil targets have been used in the experiment. As expected we did not see any significant difference on the performance of Al 0.4 μ m, Al 0.75 and Ta 0.5 μ m foils because fast electron propagation effect is not much important for foils of sub μ m thickness. At the same time we could not see any detrimental effect of ASE pre-pulse on the Al 0.4 μ m target which was thinnest foil used in the experiment. This signifies that there was no significant rear surface perturbation due to shock wave induced by ASE. Ion signal were recorded using the TPIS equipped with micro channel plate detector (MCP) and high gain 16 bit EMCCD camera. In order to find out the possible correlation of the hot electron signal with the ion signal, an electron magnetic spectrometer was installed along the laser forward direction for the hot electron spectrum measurement as shown in Fig. 4.3(a). Full electron beam signal was also recorded to infer the laser energy absorption and hot electron density in the sheath field. The hot electron signal was recorded on high gain DRZ phosphor screen and the light output of the phosphor was imaged onto a 14 bit CCD camera.

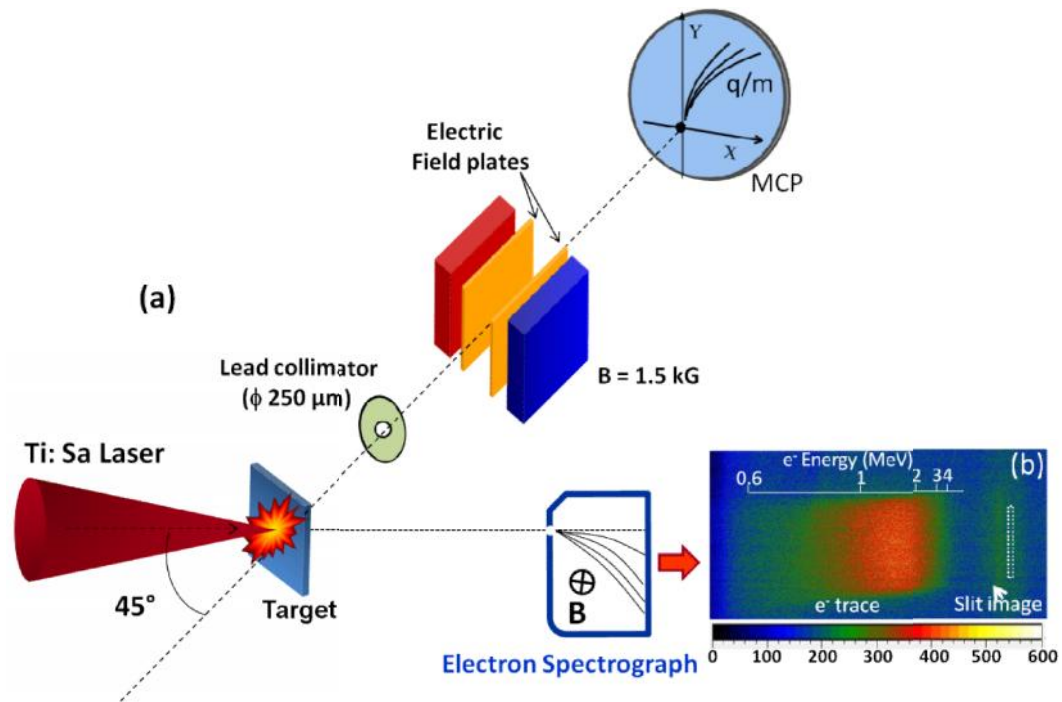


Figure 4.3: (a) The experimental set up for ion acceleration from thin foils with 150 TW system. (b) The electron trace recorded on DRZ phosphor screen using electron spectrograph along laser forward direction.

Experimental Results:

The experiments were performed at various laser pulse duration which was varied by changing the grating separation of the laser compressor. The pulse duration was measured using single shot second order autocorrelator located outside the compressor chamber. The measured and calculated* pulse duration at various grating detuning position is given in Fig. 4.4.

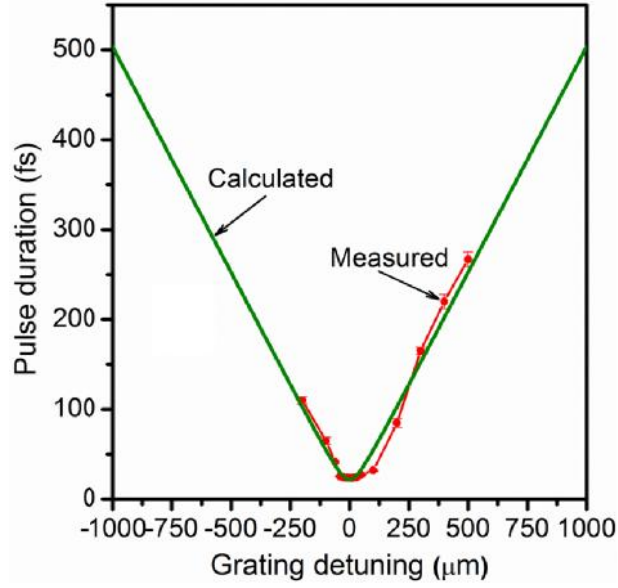


Figure 4.4: Laser pulse duration at various detuning positions of compressor grating.

* The theoretical pulse duration with grating separation for our compressor grating parameter was calculated considering second order phase using the following formula [98], [99]

$$\frac{\tau_L}{\tau_0} = \sqrt{1 + \frac{(4 \ln 2 \frac{d^2\phi}{d^2})^2}{\tau_0^4}}$$

$$\frac{d^2\phi}{d^2} = -\frac{3L_g}{2c^2\Lambda^2} \left[1 - \left(\frac{c}{\Lambda \sin i} \right)^2 \right]^{-3/2}$$

Where τ_0 is the minimum pulse duration, $\frac{d^2\phi}{d^2}$ is Group Delay Dispersion (GDD), λ is the wavelength in vacuum, L_g is separation between grating pair, c is the velocity of light in vacuum, Λ is grating period and i is the incident angle of the laser pulse to the first grating.

The grating separation providing minimum pulse duration (25 fs) was identified and from now onwards referred as “*compressor zero*”. Notably, in such studies the accurate identification of the compressor zero giving minimum pulse duration is quite important. Increasing the grating separation from the optimum (yielding shortest pulses) give rise negatively chirped pulses i.e. higher frequencies are located at the leading edge of the pulse. Similarly, decreasing the grating separation from the optimum give rise positively chirped pulses i.e. lower frequencies are located at the leading edge of the pulse. Negative and positive chirped pulses having pulse duration 25 fs to 500 fs were generated by changing the grating separation from the “*compressor zero*” to ± 1 mm. The corresponding variation in laser intensity is 3.2×10^{19} W/cm² to 1.6×10^{18} W/cm². Henceforward, “+” and “-” sign along with pulse duration will be used to designate positive and negative chirped pulses except for shortest unchirped pulse (i.e. 25 fs). Fig 3(a-c) shows the typical representative Thomson parabola ion traces obtained with 0.4 μ m Al target at two widely separated pulse duration viz. for 25 fs and for 316 fs including both positive (b) and negative (c) chirped pulses. The ion spectra clearly highlight the difference of positively and negatively chirped laser pulses in protons (H⁺) and carbon ion acceleration.

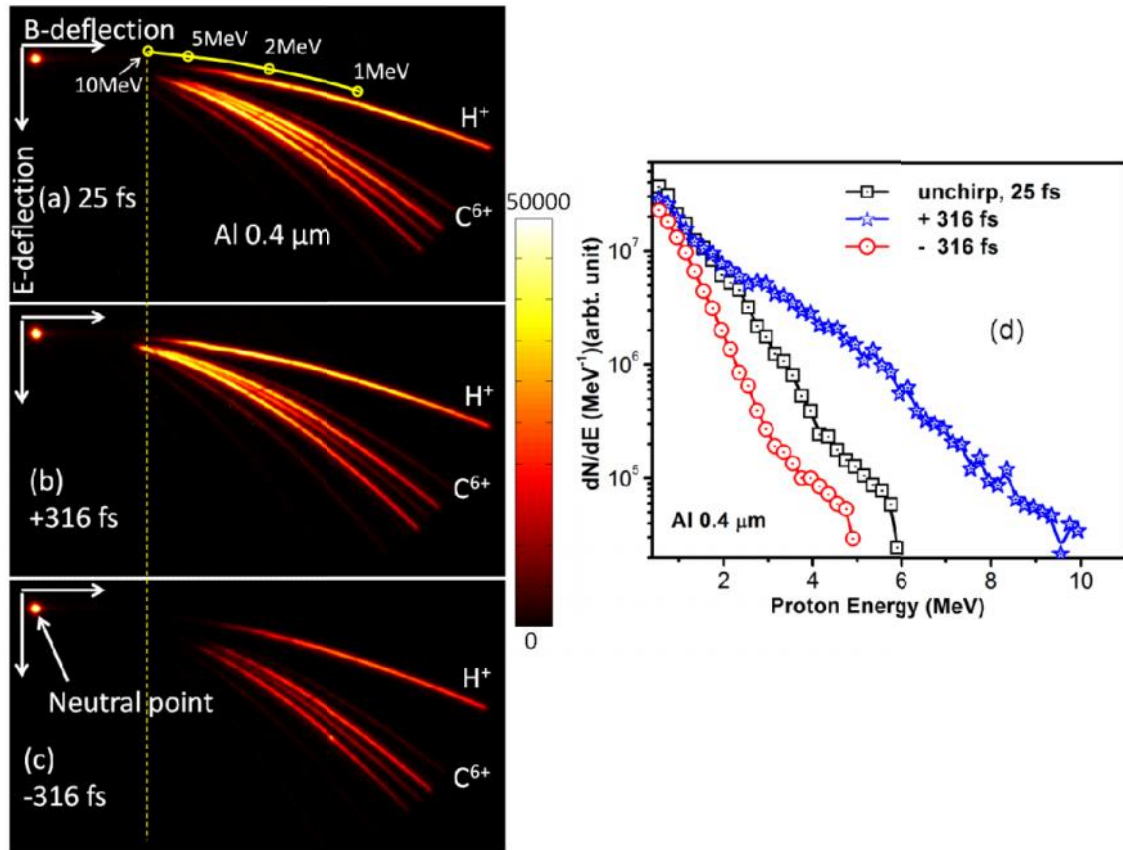


Figure 4.5: Ion traces recorded using TPIS at various pulse duration and chirp, (a) shortest 25 fs pulse, (b) +316 and (c) -316 fs. (d) Derived proton energy spectra.

For highlighting the difference, a computed (theoretical) proton parabola trace with energy marker (yellow line with small circle) is also shown parallel to the recorded proton trace. A vertical yellow dashed line is drawn for marking the 10 MeV proton deflection position with respect to neutral point position for simple comparison. The derived proton energy spectrum for these shots is plotted in Fig. 4.5 (d). Substantial enhancement in accelerated proton energy and flux were observed for longer and positive chirped pulses. As we increase the pulse duration from 25 fs to +316 fs, the maximum proton energy increases from 6 MeV to 10 MeV, whereas for -316 fs the proton energy slightly reduces to 5 MeV. A detailed study on the effect of laser pulse duration and chirp has been performed using Ni 1.5 μm, Al 0.75 μm and Al 0.4 μm targets. While varying the pulse duration, the laser energy was kept constant. A clearly visible difference on ion signal was observed in situ whenever the sign of the

laser chirp was changed at almost same pulse duration. The obtained results on maximum proton cut off energy at different pulse duration and chirp are summarized in Fig. 4.6 (a) and (b). The change in laser intensity on account of change in laser pulse duration is also shown in top horizontal axis. We can see that the obtained proton energy is not highest at minimum pulse duration i.e. at higher intensity $3.2 \times 10^{19} \text{ W/cm}^2$ rather it increases gradually as the pulse duration is increases for positively chirped pulse. The proton energy maximizes around 250 - 350 fs and decrease thereafter. About 60-70 % enhancement in proton cut-off energy was observed. However, for negatively chirped pulses, the proton energy decreases slowly with increase in pulse duration. The behavior is almost similar for Ni and Al targets. The carbon ions also show similar enhancement in energy and flux as evident from raw TPIS ion traces (Fig. 4.5 a-c). For example in case of $0.4\mu\text{m}$ Al target, the observed C^{4+} ion energy is 10 MeV for 25fs, 5.5 MeV for -316 fs and 14 MeV for +316 fs.

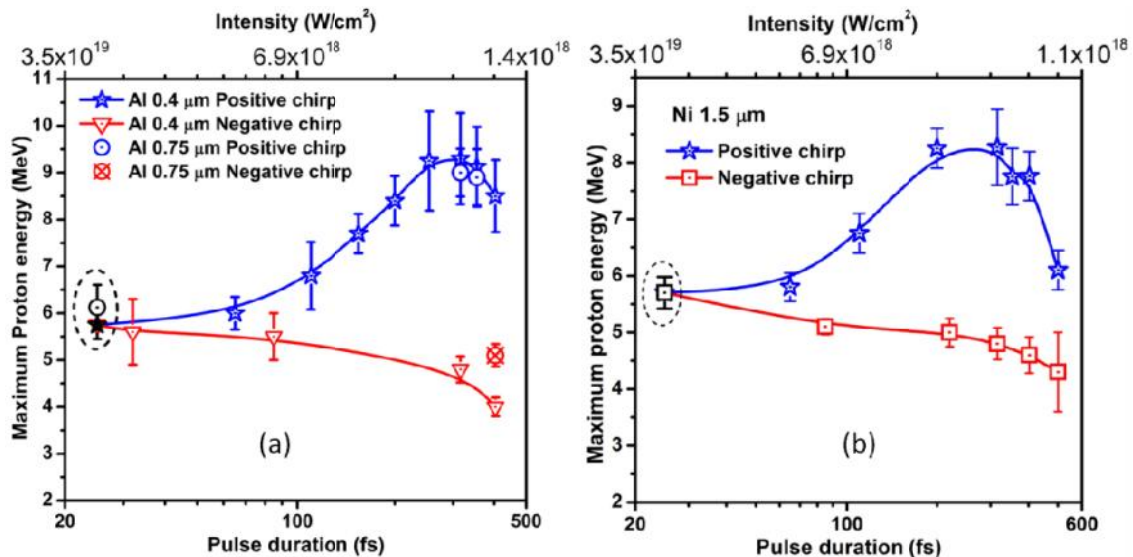


Figure 4.6: Observed proton cut-off energies at various laser pulse duration and chirp using (a) $0.75 \mu\text{m}$ Al, $0.4 \mu\text{m}$ Al and (b) for $1.5 \mu\text{m}$ Ni foils. Laser intensity variation due to change in pulse duration is shown in top horizontal axis. The circled data points are at shortest (25fs) and unchirped pulse. The blue and red curve are connecting lines for guiding the eye.

The ion acceleration is initiated by sheath field set up by hot electron population and therefore ion acceleration process is intrinsically linked with hot electron generation and laser energy absorption at target front surface. Therefore, it is interesting to find out the possible correlation of the ion signal with the hot electron signal. For this we had also recorded the hot electron spectrum of electrons populations emitted along the laser forward direction using a magnetic spectrometer. We also recorded total accumulated electron signal along the laser forward direction by using only a DRZ phosphor screen at 11.5 cm distance from the target. The beam of electrons recorded from Ni 1.5 μm target at different pulse durations, 25 fs, +354 fs and -354 fs are shown in Fig. 4.7 (a-c). The magnetic spectrometer used to measure the electron energy spectrum, consist of an entrance slit ($0.5 \times 10 \text{ mm}^2$), a dipole magnet and a DRZ phosphor screen. The distance between the source and the slit was 15 cm and between the source and DRZ phosphor screen was 21.5 cm. The measured electron energy spectrum from same 1.5 μm Ni target at 25 fs, +354 fs and -354 fs is shown in Fig 4.7 (d). In all case, the phosphor screen was covered with Al foil of 20 micron thickness setting a cut-off of 50 keV for electrons.

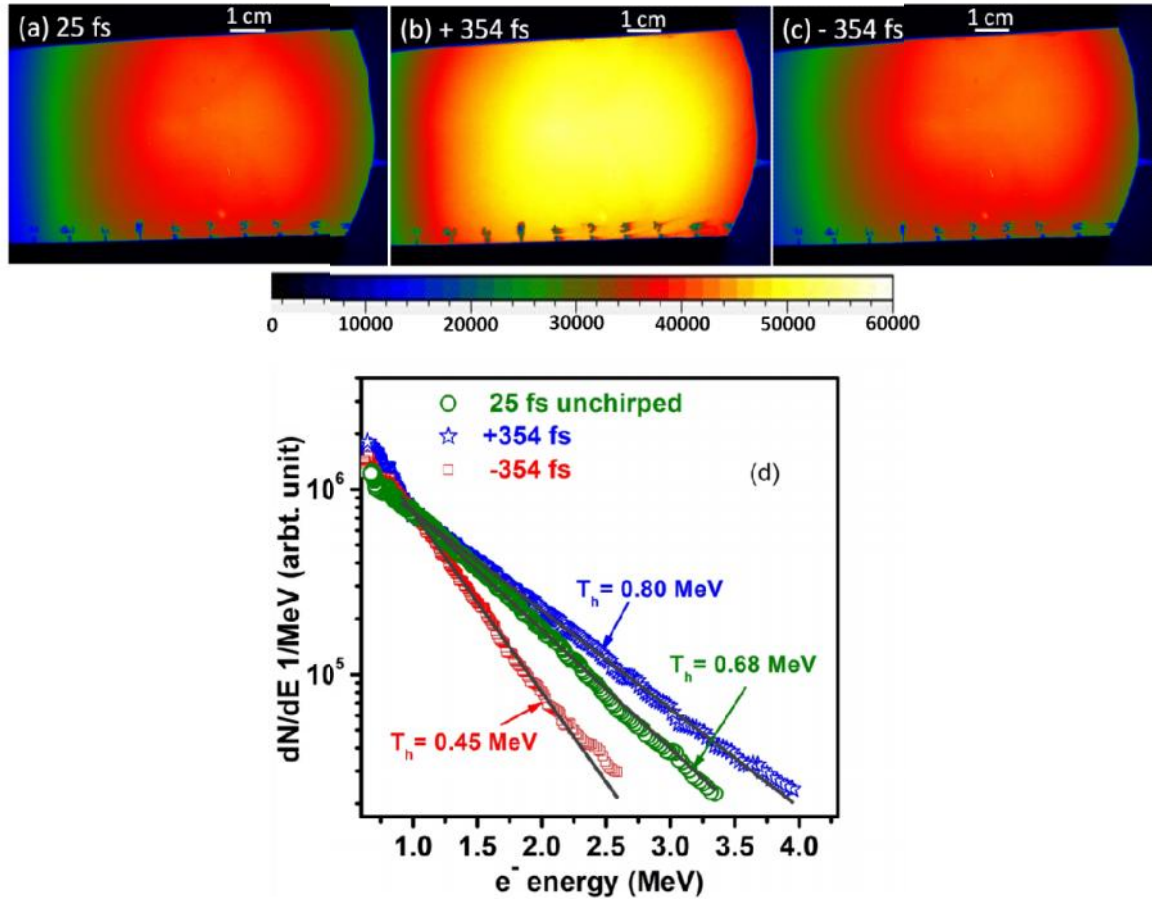


Figure 4.7: Full electron beam recorded on DRZ phosphor screen in the laser forward direction at (a) shortest and unchirp 25 fs , (b) +354 fs and (c) -354 fs pulse durations. (d) Measured energy spectra of hot electrons.

From these measurements it is evident that hot electron signal shows exact correlation with ion signal. The intense electron beam signal (Fig 4.7 b) in case of positively chirped long pulses signifies higher laser energy absorption efficiency which means higher laser to hot electron conversion as compared to negatively chirped long pulses (Fig 4.7 c) and unchirped shortest pulse of 25 fs (Fig 4.7 a). The electron beam detected in laser forward direction is basically the population of escaped electrons from the target and is a direct signature of hot electron density in the sheath. The electron spectra were fitted with Boltzmann distribution of the form $f(E) \sim \exp(-E/T_h)$, resulting the hot electron temperatures 0.68 MeV, 0.8 MeV and 0.45 MeV for 25 fs, +354 fs and -354 fs respectively. The hot electron signal measurement clearly

indicates that the product of hot electron temperature and density is higher for positively chirped long pulses which finally lead to higher accelerating field (TNSA field $\propto \sqrt{n_{\text{hot}} T_{\text{hot}}}$). The electron beam profile recorded on phosphor screen also gives beam divergence around 50° (full angle).

Discussion:

There are some previous reports which discuss the dependence of proton energy on laser pulse duration [88]. At fixed laser pulse energy the change in pulse duration triggers different competing processes which can affect the ion acceleration from thin foils. (1) According to plasma expansion model given by Mora, the maximum proton/ion energy is $E_{\text{max}} = 2T_{\text{hot}} [\ln(1 + (\omega_{\text{pp}} t_{\text{acc}})^2)]^2$. Here $\omega_{\text{pp}} = \sqrt{2} e / \sqrt{2} e$ is the normalized acceleration time and T_{hot} is hot electron temperature.

$\omega_{\text{pp}} = (n_e e^2 / \epsilon_0 m_p)^{1/2}$ is the proton plasma frequency $e = 2.71828$ is the numerical constant. t_{acc} is the characteristic acceleration time which is for ultrashort pulses can be taken as few time of the laser pulse duration and for sub pico second pulses it is approximated as $t_{\text{acc}} = 1.3 \times \tau_{\text{Laser}}$. Therefore t_{acc} is linked with laser pulse duration. (2)

At the same time, for a fixed laser pulse energy the increase in pulse duration increase the laser energy absorption as reported by many authors [88]. Carrie *et. al.* [100] have shown that the laser energy absorption increases from 20% for 30 fs pulses up to 70% for 300 fs laser pulses. More laser energy absorption means we have higher number of hot electrons albeit some reduced electron energy. (3) T_{hot} increases with increase in laser intensity and it generally goes as $T_{\text{hot}} \approx (I^2)$. Where α and β are constants that depend on laser target irradiation conditions and involved laser absorption mechanism. For example, in pondermotive scaling the hot electron

temperature is given as $T_{\text{hot}} = m_e c^2 [(1 + I \lambda^2 / 1.37 \times 10^{18})^{1/2} - 1]$. If one considers only the change in laser intensity due to change in pulse duration, T_{hot} is expected to decrease. (4) There is one more effect which can arise in case long laser pulses as discussed in Refs [82], [88] is the plasma formation on target rear surface because of electron heating which has detrimental effect on sheath field. (5) In addition, hot electron recirculation due to increased electron bunch length (\sim laser pulse length) can also effectively enhance the sheath electric field [101].

Having listed some of the possibilities, we see that the change in laser pulse duration at fixed pulse energy have resulted various complex and competing processes, such as change in laser energy absorption and hot electron temperature, ion acceleration time, formation of plasma at rear side due to electron heating and hot electron recirculation due to increased bunch length. The contravening variation of the mentioned parameters indicates relatively moderate variation in accelerated proton energy with laser pulse duration at fixed laser energy as observed in previous reported results [55], [82], [88], [102]. Still all these variations arising due to the change in laser pulse duration do not substantiate the observed experimental results. The bandwidth of the laser pulse is 70 nm at central wavelength 800 nm; hence a simple frequency rearrangement within the laser pulse (i.e. only chirp) cannot explain the observed result. There are some previous reports on electron acceleration in laser wake field acceleration scheme and enhancement of k_x x-ray yield that talks about the role of laser pulse temporal shape in altering the laser interaction condition to a significant extent. To determine any possible role of laser temporal shape, we used third order cross correlator (Sequoia) to measure the temporal profile of stretched pulses as shown in Fig. 4.8 (a). The third order cross correlation traces indeed displays asymmetric temporal pulse shape modification whilst varying the pulse duration by

changing the grating separation. The inadequate cancellation of higher order phase terms mainly the third order dispersion term [99], [102], at displaced grating position give rise to asymmetric temporal shape modification. We can see that positively chirped laser pulse has comparatively slow rise and fast fall on the other hand negatively chirped laser pulses exhibit sharp rise and slow fall. However, it should also be noted that this particular observation of pulse shape modifications may be true for the present laser compressor configuration and may not hold good for the other similar pulse compressor setup. Change in the constitutive parameters of the laser compressor may change the nature of pulse shape asymmetry [96], [99], [102] even with same sign of the laser chirp.

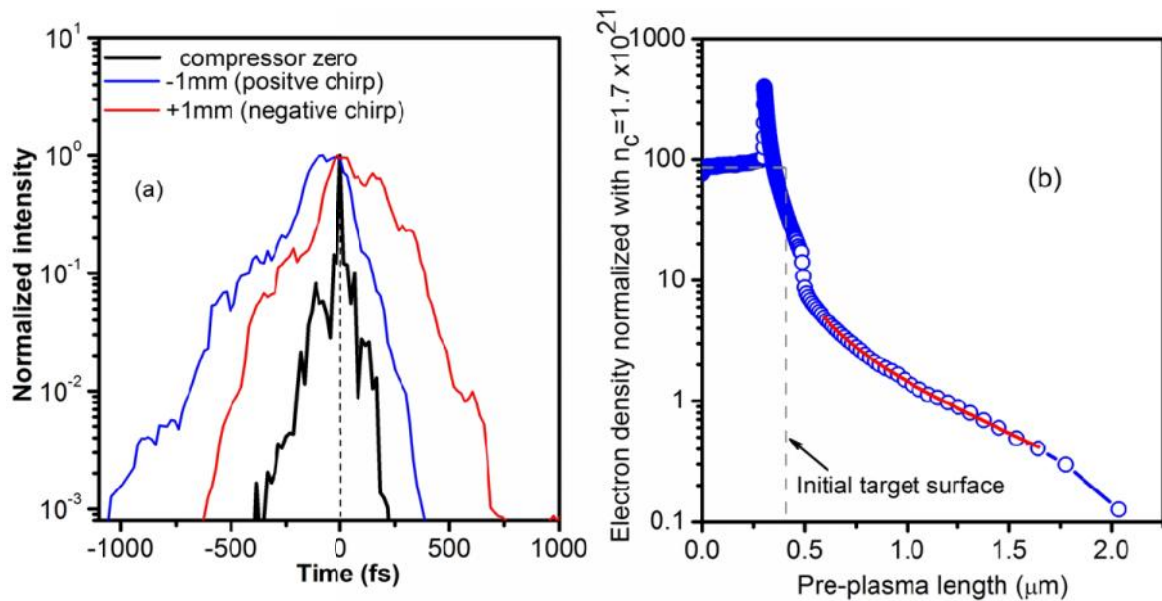


Figure 4.8: (a) Third order cross correlation trace of temporally stretched pulses. (b) Estimation of pre-plasma density scale length using HELIOS code.

The laser interaction dynamics and hence the energy absorption can be significantly different for differently modified temporally skewed pulses having same pulse duration. The primary difference lies in the formation of appropriate pre-plasma scale length that alleviates in efficient laser energy absorption [97], [103]. A suitable pre-plasma before the arrival of main pulse have been proven to be very advantageous for

effective laser energy absorption [104]–[107]. In one of the study reported by Nuter et. al. [105], it has been suggested that a low energy fs pre-pulse prior to the main pulse is useful to create a suitable density gradient which enhances the absorption of the main laser pulse and thereby to get the higher ion energy.

The hot electron signal measured in different directions has different characteristics and also hints towards the various laser absorption mechanisms. For example, in $j \times B$ absorption which dominates at relativistic intensities ($> 10^{18} \text{ W/cm}^2$), electrons are emitted along laser propagation direction. Nevertheless, experimentally it was found that for an overdense plasma (or with small pre-plasma having density scale length $\ll \lambda$), the measured temperature of fast electrons is less than anticipated by pondermotive scaling [108]. This is due to fact that in an overdense plasma, the electrons do not able to come across full pondermotive potential as the collisionless skin depth (c/ω_{pe}) is shorter than laser wavelength. At relativistic intensities the electrons traverse a distance larger than c/ω_{pe} before they could even attend one fourth of a laser wavelength. This was the reason for much lesser hot electron temperature of 0.68 MeV for 25 fs and highest intensity (3.2×10^{19}) than anticipated by $j \times B$ heating (1.4 MeV). On the contrary, a small pre-plasma with scale density length L or larger is better for laser energy absorption via $j \times B$ heating. Therefore in order to interpret the anticipated enhanced laser energy absorption leading to somewhat higher hot electron temperature for positively chirped longer pulses at lower intensity ($2 \times 10^{18} \text{ W/cm}^2$), it is helpful to know the pre-plasma condition before the main pulse arrival. The pre-plasma due to the pre-pulse (Fig. 4.1) was estimated using HELIOS a 1D hydrodynamic Code. The estimated electron density profile is shown in Fig. 4.8 (b). Even though the contrast is high, still it produces some pre-plasma of $2\mu\text{m}$ scale length. The electron distribution around the critical density is fitted with double

exponential decay function giving the scale length $L/\lambda = 0.16$ and 0.67 . The estimated density scale length L is too short (sharp) for effective laser energy absorption via $j \times B$ mechanism [109], [110].

Therefore, when positively chirped long pulses interacts with target, the initial gentle rising part of the pulse creates pre-plasma that have enough time to expand before the remaining intense part arrive at the target. These kinds of pulses are most likely providing suitable scale length L . In this case the main part of the laser pulse get absorbed in efficient manner in the plasma and the electrons are heated to high temperatures. On the contrary, if the leading edge of the laser pulse is rising fast, the intense laser part interacts with plasma having steep density gradients and hence low laser energy absorption. Similar is the case of negatively chirped pulses (sharp rise). This will also result in lower laser energy absorption because the plasma does not have sufficient time to expand. Enhancement in absorption of laser pulse energy into the plasma resulting to higher electron temperature, long acceleration time as well as hot electron recirculation for positively chirped long pulse appears to perform decisive role in efficient ion acceleration in the present case. Further increase in the laser pulse duration beyond 250-350 fs, the maximum accelerated proton energy begins to decrease. This is mainly due to the fact that the laser intensity is not sufficient enough to produce strong accelerating field to accelerate the ions.

At this point, we have discussed only about $j \times B$ absorption mechanism as experimentally the hot electron signal was measured in that direction. At the same time, few other mechanisms like vacuum heating (VH) and resonance absorption (RA) might also be applicable. The well-disposed matching of pre-plasma density scale length for enhanced laser absorption via VH and RA have been described by few authors [97], [103]. The comparative strength of the above mentioned

mechanisms in the present case requires more elaborate electron signal measurement in all relevant directions. This can be an interesting problem for future experiments.

Here, one important point to be noted is that the skewness in laser temporal shape arises by simply detuning the grating separation from “*compressor zero*”. In the current work, we have not attempted to correct the higher order phase terms by tuning the compressor gratings alignment causing pulse shape asymmetry. This needs more dedicated effort involving full temporal characterization for example employing FROG set up. We trust that more study is required to amply appraise and understand the temporally asymmetric pulse generation mechanism and its effects on laser plasma interaction dynamics and ion acceleration.

4.3 Effect of laser pre-pulse on ion acceleration from thin Mylar foils coated with high Z material

Slight pre-plasma formation on foil target front surface is helpful in efficient laser energy absorption and hence in ions acceleration. At the same time, the plasma formation at foil target rear surface is highly detrimental for ion acceleration through TNSA mechanism as discussed in previous chapters. In this section, the two contrasting situation will be investigated using double layer targets consisting of transparent Mylar foil coated with high Z (Gold) material. It will also be shown that the pre-pulses can be constructively used for this purpose as long as it is not perturbing the whole target. The Experiment was performed with 150 TW Ti: Sapphire laser system. During this experiment, the available laser pulse energy was 2.1 Joule. Positively chirped pulses with pulse duration +316 fs were used for all the shots. The laser pulse (p-polarized) was focused on to the foil target at 30° incidence angle employing an f/3 off axis parabolic mirror. The focal spot was measured to be ~ 5 μ m (FWHM) which contains around 25% of the pulse energy. Hence the resultant on

target peak intensity was $\sim 7.5 \times 10^{18}$ W/cm². Pure Mylar foil of 5 μ m thickness and Mylar foil one side coated with 30 nm Gold were used as targets. Along with this, 2.5 μ m Al foil one side coated with 30 nm Au was also used. The ion emission was recorded using TPIS placed along rear surface normal direction. The ion beam profile was recorded on radiochromic films (RCF) stacks placed at 2.5 cm distance from the foil target. The RCF stack was covered with 25 μ m Al foil setting proton energy cut-off around 1.4 MeV. The typical shots along with recorded RCF profile in different laser irradiation condition (a) only 5 μ m, (b) 5 μ m Mylar coated with 30 nm Au, with Au coating *front* side and (c) 5 μ m Mylar coated with 30 nm Au, with Au coating *back* side are shown in Fig 4.9 (a) – (c). The proton energy spectra for these shots are plotted in Fig. 4.9 (d).

We see that proton energy significantly increase (4MeV to 5.7 MeV) when Au coating is at front side (case (b)) as compared to only plain Mylar foil (case (a)). But when the Au coating is at back side, a drastic reduction in proton as well as Carbon ions signal was observed as evident from raw TPIS image (Fig. 4.9 case (c)). For example the accelerated proton energy is reduced to 1.5 MeV in case (c) from 4 MeV as observed in case (a). Surprisingly, a bare 30 nm Au coating either on *front* side or on *back* side on transparent 5 μ m thick Mylar foil have highly contrasting effect. It is also important to note that the above observation was highly repeatable and was checked for many laser shots.

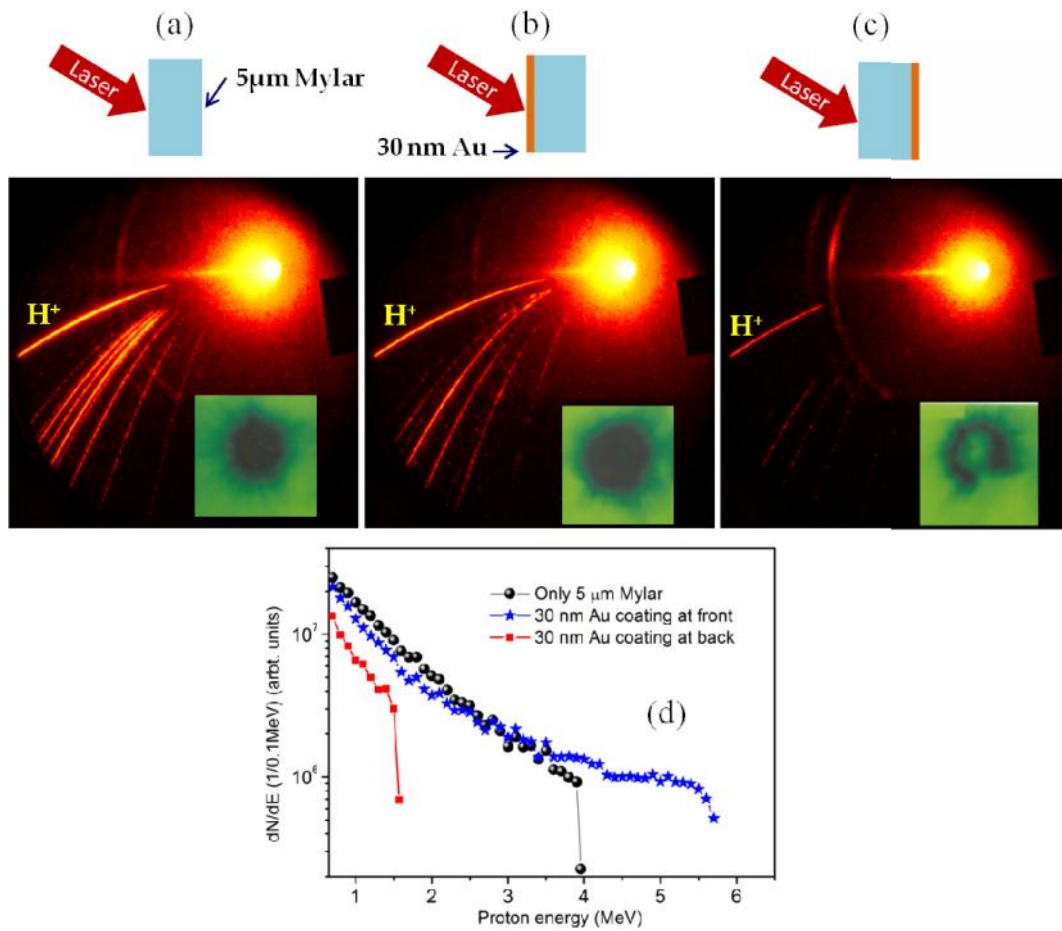


Figure 4.9: Effect of high Z coating on transparent Mylar foil. (a) Ion traces recorded with TPIS along with proton beam profile (> 1.4 MeV) recorded on RCF are shown for different condition: (a) laser facing only plain $5 \mu\text{m}$ Mylar, (b) Au coating front side and (c) Au coating at back side. The proton energy spectra for each case are plotted in (d).

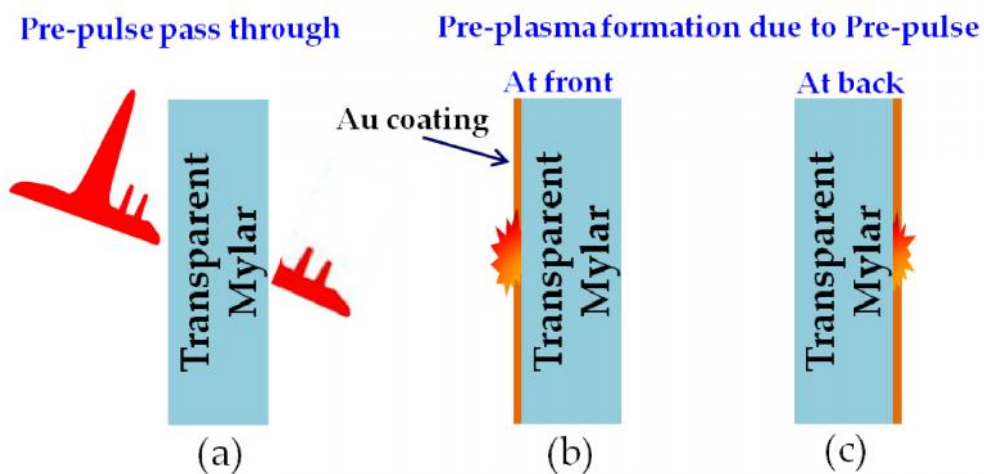


Figure 4.10: (a) The pre-pulse passes through the transparent Mylar foil. The pre-pulse forms the pre-plasma in high Z material at target front (b) and at target rear side (c).

The difference can be understood as follows. The three cases are explained through a diagram shown in Fig 4.10. Although the laser contrast is high, still the exponentially rising few hundred ps ASE pre-pulse is sufficiently intense enough to form some pre-plasma. As discussed in chapter 1 section 1.3.1, the ns long ASE pre-pulse are mainly absorbed through collisional absorption mechanism. The collisional absorption is more effective in high z targets. Therefore, the ASE pre-pulse will be more efficiently absorbed in Au coating layer. In case of only Mylar as it is a transparent foil, the ASE pre-pulse will not create plasma due to low absorption in low- Z Mylar target, and it will simply transmitted through it (Fig. 4.10(a)). So in case of Au coating is on front side, the ASE pre-pulse will be effectively absorbed in high Z Au layer leading to pre-plasma formation (Fig 4.10 case (b)). The main intense laser pulse will be efficiently absorbed in preformed plasma leading to enhanced ion acceleration. Similarly, when the Au coating is at back side, the pre-plasma will be now formed at the back side by ASE pre-pulse as depicted in Fig 4.10 case (c). It is well established fact that pre-plasma formation at target rear surface is highly detrimental for ion acceleration through TNSA mechanism. This is the reason why the Au coating at back side of Mylar strongly suppresses the ion signal. The recorded proton beam profile on RCF shown in Fig. 4.9 (a) – (c) for all three configurations, unambiguously support our arguments. The proton beam profile for case (a) and (b) was almost similar considering shot to shot fluctuations. However, for case (c) i.e. when Au coating is at back side, the proton beam is hollow (Fig 4.9 (c)). The formation of pre-plasma due to transmission of ASE pre-pulse at rear side has strongly diluted the accelerating sheath field and therefore almost no accelerated ions from the central region. In order to further check this fact, we used Al 2.5 μm thick target which is *opaque* to 800 nm laser light. The 2.5 μm thick Al target was also one sided coated with 30 nm Au. The

typical shots along with proton beam profile for the two cases i.e. (a) when coating is front side and (b) when coating is back side are shown in Fig. 4.11. Considering shot to shot fluctuations, both the target configurations exhibit similar behaviour. Here, as the target is opaque (Al) and it does not allow ASE pre-pulse to pass. Therefore, in this case the pre-pulse does not show the contrasting effect as observed in case of transparent Mylar target.

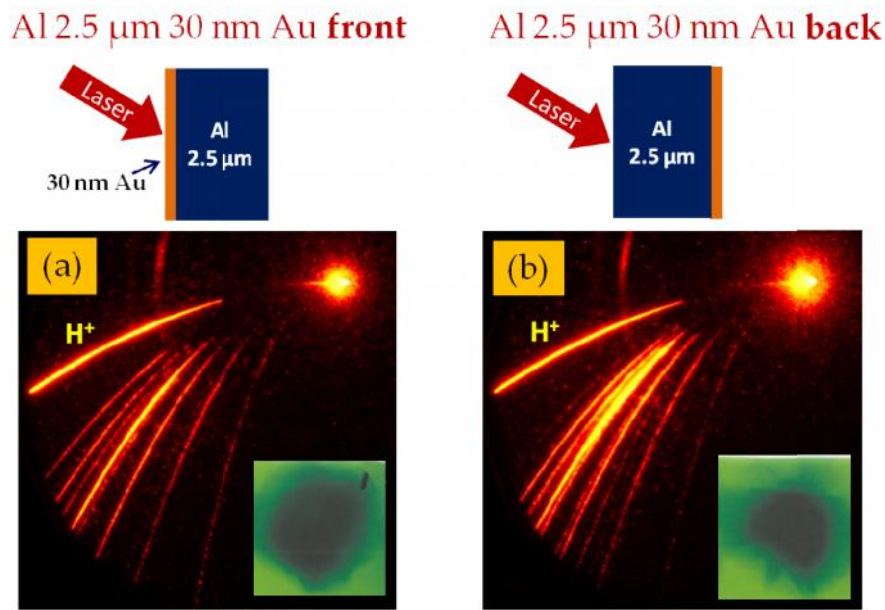


Figure 4.11: Effect of high Z coating on opaque Al foil. (a) Ion traces recorded with TPIS along with proton beam profile (> 1.4 MeV) recorded on RCF are shown for different condition: (a) laser facing Au coating and (b) laser facing Al and Au coating backside side.

4.4 Quasi monoenergetic proton acceleration

The TNSA is a most robust and relatively easily implementable ion acceleration mechanism. The ions accelerated through TNSA mechanism normally exhibit broad energy distribution. However, most of the envisaged applications require quasi monoenergetic ion beam e.g. in cancer therapy. Using very complex target engineering [27], [28] and energy selection devices [111], spectral modification of TNSA accelerated ion beam have been demonstrated. In addition, some advanced acceleration mechanism have also been proposed like Radiation Pressure Acceleration

(RPA), Collisionless Shock Acceleration (CSA) and Break out after burner (BOA) which can give rise ion beams with narrow energy spread. But, the experimental implementation of these mechanisms is quite challenging. Nevertheless, there are few successful proof of principle demonstration on quasi-monoenergetic ion acceleration with narrow energy spread using the advanced acceleration mechanism and target design. Here, we present some of our interesting results on quasi monoenergetic proton beam observed during the recent experiment with 150 TW laser system.

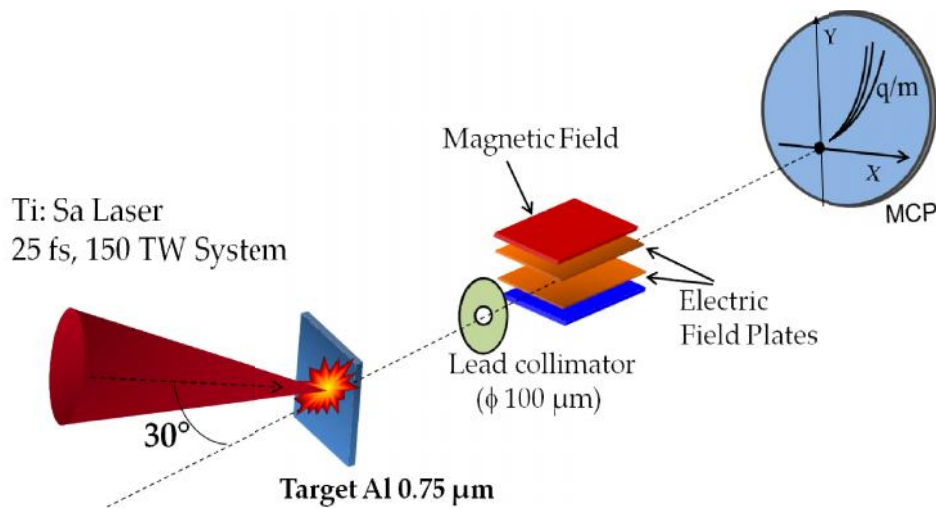


Figure 4.12: Schematic of the experimental setup.

The schematic of the set up is shown in Fig. 4.12. The p-polarized laser pulse was focused using an F/3 off axis parabolic mirror on to the foil target at 30° angle of incidence. In this experiment the available laser pulse energy was 2.2 – 2.4 J i.e. 90-95 TW laser power for 25 fs pulse duration. The on target intensity was $\sim 1 \times 10^{20}$ W/cm² which is significantly higher than in previous experiments. Al 0.75 μm foil was used as a target. The accelerated ion species was analyzed using Thomson parabola ion spectrometer (TPIS).

About 35- 40 % of the shots we observed either a plateau or plateau with a hump or a clean peak in proton energy spectrum. Few representative shots along with plotted proton energy spectrum are shown in Fig. 4.13 (a) – (f). For the shots in which a clean

proton bunch was observed, the total energy spread ($\Delta E/E$) was around 40% at central energy about 3 MeV. It is important to note that in previous experiments, we had regularly used the Al 0.75 μm target but we could observe such features in proton energy spectrum. However, at that time the peak laser intensity was lower ($\sim 3 \times 10^{19}$ W/cm^2) as compared to present case.

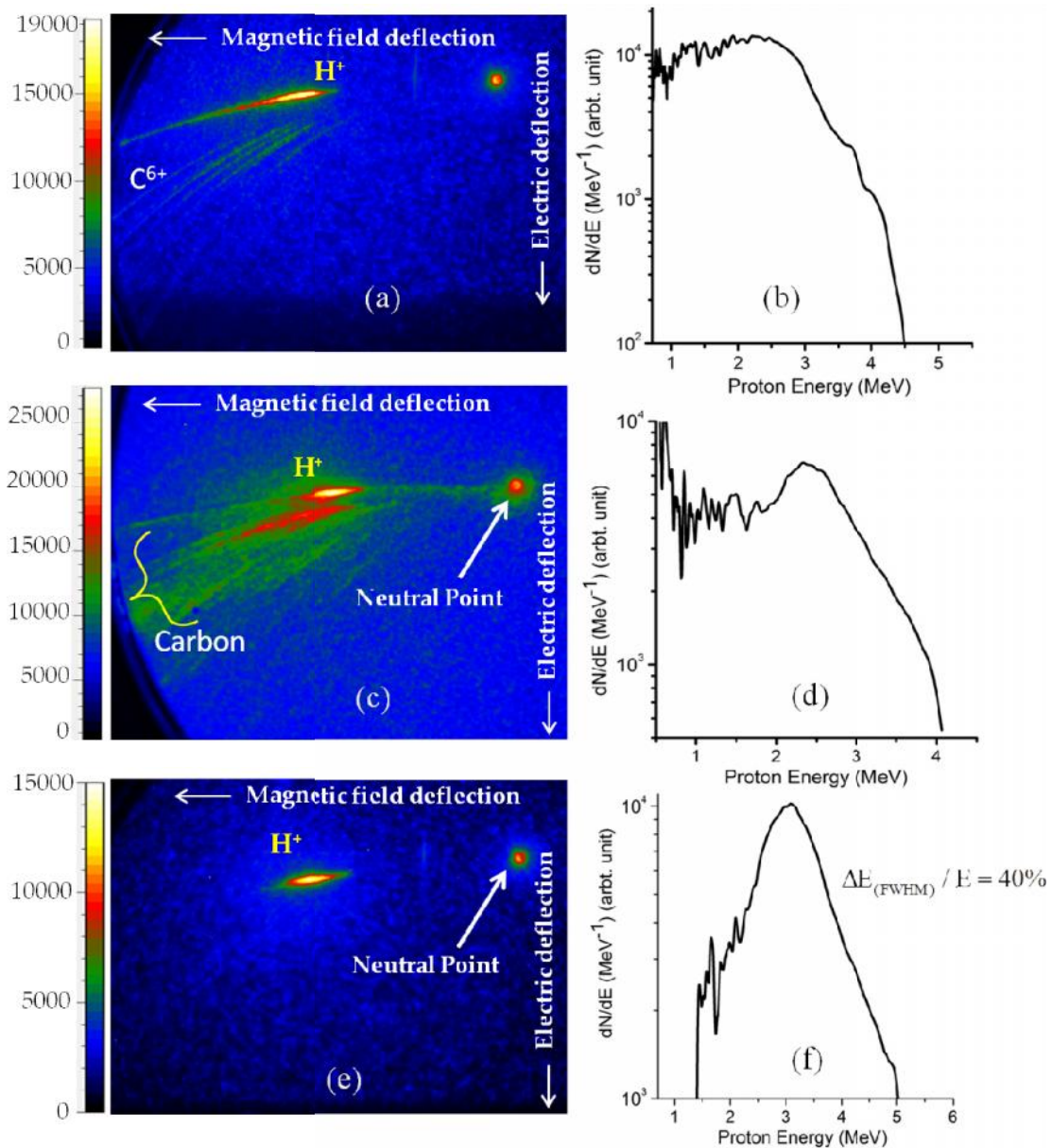


Figure 4.13: Typical ion signal recorded using TPIS showing different case (a) extended plateau (c) plateau plus hump at high energy side and (e) clean proton bunch. The corresponding proton energy spectrum is shown in (b), (d) and (f).

Discussions:

The spectral features obtained in the experiment are unlike of TNSA accelerated ion beam which normally shows a broad energy distribution with exponential decay profile similar to Boltzmann like energy distribution. Another mechanism which can be very effective in the present experimental conditions is the collision shock acceleration (CSA) driven by intense laser pulse initially proposed by L. O. Silva et. al. [32]. In PIC simulation, they have demonstrated the formation of electrostatic shock wave in overdense plasma slab, over a wide range of laser intensities and target parameters. The generated shockwave propagates inside the plasma slab and reflects the upstream ions to a velocity twice the shock wave velocity. They have explicitly shown that the characteristic feature of shock acceleration is the plateau in ion energy spectrum. Later on, in some experimental [33], [112], [113] and theoretical [114] studies it was shown that quasi monoenergetic ion can be generated by collisionless shock wave in spatially tailored near critical density plasma. First experimental demonstration of mono energetic proton beam of ~ 20 MeV energy via CSA was reported by Haberberger et. al. using powerful CO₂ laser (wavelength 10 μm) and hydrogen gas jet target [33]. There are some recent efforts which try to achieve this scheme using modern day compact lasers operating at 1 μm or 800 nm wavelength from thin foil targets [112], [113]. In these cases the plasma density was tailored using a pre-pulse before the main intense pulse so as to generate a strong collisionless shock wave. A strong collisionless shock wave is generated in near critical density plasma tailored in such a way so that it has exponentially decreasing density profile at target rear side [115]. In this case the laser energy gets efficiently absorbed in near critical density plasma leading strong heating of plasma volume. The expansion of the heated plasma volume which has exponentially decreasing profile at rear side (i.e. sudden

discontinuity in density) generates electrostatic shock that can reflect the upstream ions leading to generation of high energy, quasi monoenergetic ion beams. In such conditions, due to target expansion and rear surface density gradient, the TNSA mechanism is not much effective. In some intermediate condition both TNSA and CSA mechanism can give rise to combined ion acceleration in which ion energy spectra have plateau or a peak superimposed on the high energy side [32], [114]–[119].

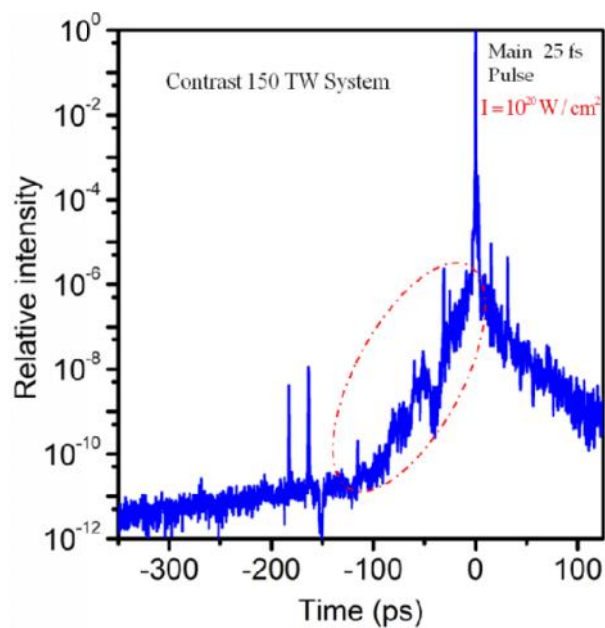


Figure 4.14: *Contrast of 150 system.*

With this background, one can easily correlate that the observed spectral features in proton energy spectrum are due to CSA. Now the question is how the favourable condition was met in the present experiment? A closure looks at the laser irradiation parameter suggest that indeed efficient collisionless shock wave can be generated in present experimental condition. The peak laser intensity was the highest $\sim 1 \times 10^{20}$ W/cm² in the present experiment as mentioned earlier. Although the contrast is quite high, but due to overall increased intensity (assuming the same focusability for pre-pulse), the closely lying 100-150 ps exponentially rising pre-pulse (shown in Fig.

4.14) is now strong enough to heat the Al 0.75 μm target. The heated Al 0.75 target together with its attached hydrocarbon contamination layer at rear side will expand reducing the target density. It is possible that it may even become a near critical density plasma. Being lighter the hydrogen layer at rear will be expanded more as compared to rest of the target. Now, when the main pulse arrives, it strongly heats the low or near critical density target. The subsequent expansion of the heated target leads to the generation of collisionless shock wave which reflects and accelerates the upstream hydrogen ions to high velocities and with quasi-monoenergetic features.

So far, we have presented a possible explanation of the observed plateau and quasi-monoenergetic features in proton in proton energy spectrum. But how one can be sure that it is really the case! To our arguments we have noticed very strong experimental evidence. We know that the small aperture (here 100 μm) used in TPIS also do the pinhole imaging as illustrated in Fig. 4.15 (a). The neutral spot thus formed is basically the target image constituted mainly by the high energy photons or x-rays. In Fig. 4.15, we present two laser shots showing in one case a clean quasi monoenergetic proton bunch and in second case a continuous proton trace was observed. The zoomed images of the neutral spot are shown below the respective shots.

Now if we focus on neutral spot images, we see that for the shot, in which a continuous proton trace was observed (Fig 4.15 (c)), the neutral spot is quite bright and more intense at the centre. This means that the target remains overdense at the arrival of the main pulse and hence larger x-ray emission from the central region. At the same time the shot in which a clean proton bunch is observed (Fig 4.15 (b)), the neutral spot is less bright and more importantly it is also hollow. This means that there is overall less x-ray emission from the laser target and even lesser from the central part of the interaction region. This is a clear signature that the target has expanded due

to heating by the pre-pulse and becomes underdense at the arrival of the main fs pulse. This is the required condition of strong collisionless shock generation by the intense laser pulse ($\sim 10^{20}$ W/cm²) in near critical density plasma as reported by several authors discussed above. However, we believe that numerical modelling of the experimental results may give more insight into the plasma interaction dynamics and collisionless shock generation and may also help to pin point the exact plasma condition to obtain good monoenergetic proton bunches with high repeatability.

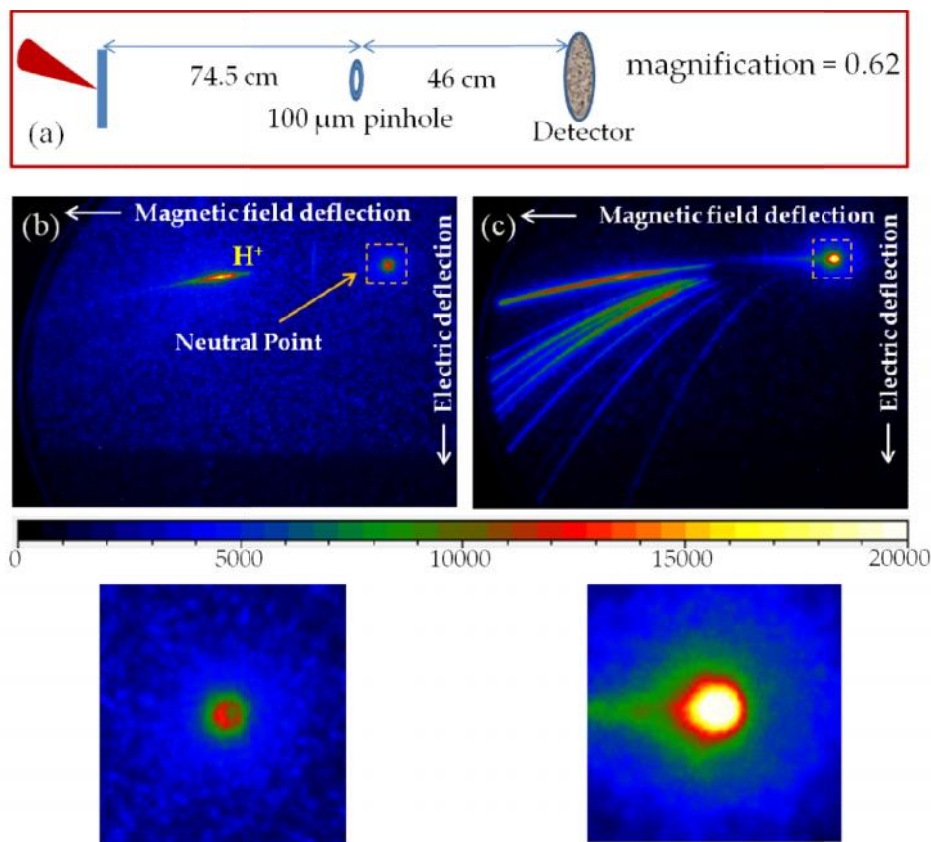


Figure 4.15: (a) Pinhole imaging by the 100 μm diameter lead aperture. Two different laser shot from 0.75 μm thick Al target showing (b) a clean quasi monoenergetic proton bunch and (c) protons with continuous energy distribution. The zoomed images of neutral spot are shown below the respective shots.

4.5 Conclusion

The 150 TW Ti: Sapphire laser and target parameters were optimized for efficient ion acceleration. The effect of laser pulse duration and temporal pulse asymmetry on ion

acceleration has been discussed. It was found that the ion acceleration is not optimum at shortest pulse duration and highest intensity as suggested by the previous intensity scaling data. Instead temporally stretched pulses are better for efficient ion acceleration. More importantly, we found a contrasting difference with respect to the sign of the laser chirp for almost the same laser pulse duration. We found 60-70% enhancement in maximum ion energy (from 6 MeV to 10 MeV) and more than one order enhancement in flux at that energy with positively chirped 250- 350 fs stretched pulses. Whereas negatively chirped stretched pulses show monotonic reduction in ion energy and flux. Correlated electron signal measurement also shows similar behaviour as observed for ions. The temporal pulse skewness was found to be responsible for this asymmetric behaviour.

A contrasting difference of laser pulse contrast on ion acceleration was observed from double layer targets consisting of transparent Mylar foil one side coated high-Z (Au) material. Enhancement of ion energy and flux was observed when Au coating side was facing the laser. However a drastic reduction in ion energy and flux was observed when the Au coating was at back side. It was established that efficient pre-plasma formation by the laser pre-pulse either on target front (when Au coating at front) or on target rear side (when Au coating back side) is responsible for the contrasting difference on observed ion signal.

We have demonstrated, clean quasi monoenergetic proton bunches of energy around 3 MeV with energy spread around 40%. The laser interaction condition strongly suggests that the collisionless shock wave generated by the intense laser pulse is mainly responsible for the observed plateau and peaks in proton energy spectrum.

CHAPTER 5

Quasi mono energetic heavy ion acceleration

5.1 Quasi-monoenergetic heavy ions from nano composite targets

Ion acceleration using high intensity, ultra-short laser pulses can be implied in various potential applications such as an injector to conventional particle accelerators [120], hadron therapy [121], proton radiography [122], study of warm dense matter [9], proton driven fast ignition [15], and astrophysical applications [33]. However, one of the major impediments towards employing these sources in practical applications lies in the inherent challenge of producing mono-energetic ions with energy control. The primary mechanism of accelerating protons and lighter ions is the highly transient and spatially non-uniform sheath field formed at the foil rear side by the escaping “hot” electrons generated by the intense laser pulse at the front. The process commonly known as Target Normal Sheath Acceleration (TNSA) [26], exhibits some unique characteristics like ultra-low transverse emittance [123], short ion bunch duration and high peak current [3] [4]. Protons (H^+) having highest q/m ratio are more preferentially accelerated in space charge field (sheath field) set up by hot electrons compared to high-Z element with low q/m ratio. In general they have broad energy distribution; far from being quasi mono energetic. Using some advanced complicated target engineering technique few groups have demonstrated quasi monoenergetic features in lighter ionic species [28] [27]. Apart from this few advance acceleration mechanisms are also proposed that can give rise to better quality ion beams in terms of narrow spectral range. For example, the RPA mechanism [30], [31] can generate quasi-monoenergetic ions employing ultra-thin foils (few 10’s of nm) and ultra-high intensity ($> 10^{21} \text{ W-cm}^{-2}$) lasers. But there are only few experimental reports showing

limited RPA signature that too in lighter ions only [61], [124]. These mechanisms put stringent condition on lasers pulse parameters and target fabrication aspects. As a result, generation of quasi mono-energetic ions particularly *heavy ions* of MeV energy with high degree of reproducibility is still a challenge. Another, mechanism which is also widely investigated is the collisionless shock acceleration (CSA) mechanism. The collisionless shock wave generated by the intense laser pulse inside the plasma can accelerate plasma ions to high energies with quasi-monoenergetic features. However, experimentally this is also quite challenging and there are only very limited reports demonstrating quasi-monoenergetic signature that too in lighter species only [33], [112]. Contrary to the scenario presented so far, we present consistent and high repeatable monoenergetic Au ion acceleration in multispecies plasma expansion in which the heavier (Au) element is present in miniscule amount. We demonstrate, for the first time quasi monoenergetic Au ion acceleration from nano-composite targets consisting of Au nano particles (AuNPs) randomly distributed in relatively thick Carbon coating using short pulse lasers focused to moderate intensities $\sim 10^{18}$ W/cm². The experiments have been performed with both 10 TW and 150TW Ti: Sapphire lasers.

Au-Carbon nano composite target:

The nano-composite thin films were synthesized using an atom beam sputtering setup, consisting of a commercial atom gun (model FAB 110) capable of delivering 2 keV neutral atom beam of 5 cm in diameter with equivalent current density of 30 μ A/cm², a sputter target, and a rotatable substrate holder housed in a vacuum chamber. The details of the setup and its use for synthesis of nano-composite thin films are available in previous works [125], [126]. Gold and Carbon was co-sputtered on Al (20 μ m thick) and Si substrate (1mm thick). The coated thin films consist of Au nano particles

(AuNPs) which are randomly distributed in thick carbon layer. The total Gold content was 2 – 4 atomic % and it was present in form of AuNPs of size 3 – 8 nm embedded in carbon matrix with total coating thickness around 120 nm. The AuNPs size distribution was found from transmission electron microscopic (TEM) measurement of the pristine samples and gold concentration with total coating thickness was determined by Rutherford backscattering measurements. The TEM image of the examined sample is shown in Fig. 5.1.

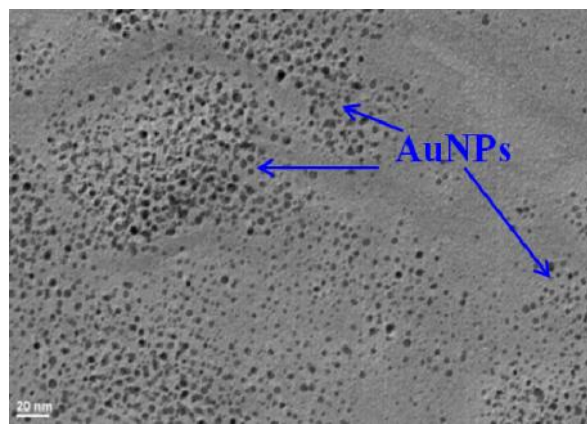


Figure 5.1: TEM image of the nano composite target showing randomly distributed Au nano particles.

Experimental set up:

The schematic of experimental set up is described in Fig. 5.2. The results presented here was obtained using both 10 TW and 150 TW lasers and verified in two different experimental campaigns. The most of the studies were carried out using 45 fs, 10 TW laser system (maximum operated power ~ 7 TW) and later on the 25 fs, 150 TW laser system (maximum operated power ~ 85 TW) was used to scale up the study at higher intensity and to re-confirm the observations. The p-polarized laser pulses were focused by the off-axis parabolic mirror onto the target. The laser incidence angle was 45° with respect to the target normal direction. The resulting laser intensity on target was ~ 10^{18} W/cm² and ~ 2×10^{19} W/cm² for 10 TW laser and 150TW laser respectively.

The laser interaction chamber was kept in a base vacuum level of 5×10^{-5} mbar. The ion emission was recorded along the *target front surface normal direction* using in-house developed Thomson Parabola Ion Spectrograph (TPIS) consisting of MCP and a 16 bit EMCCD (ANDOR iXON) camera on single shot basis. The flux of heavy Au ions was estimated using CR-39 detector.

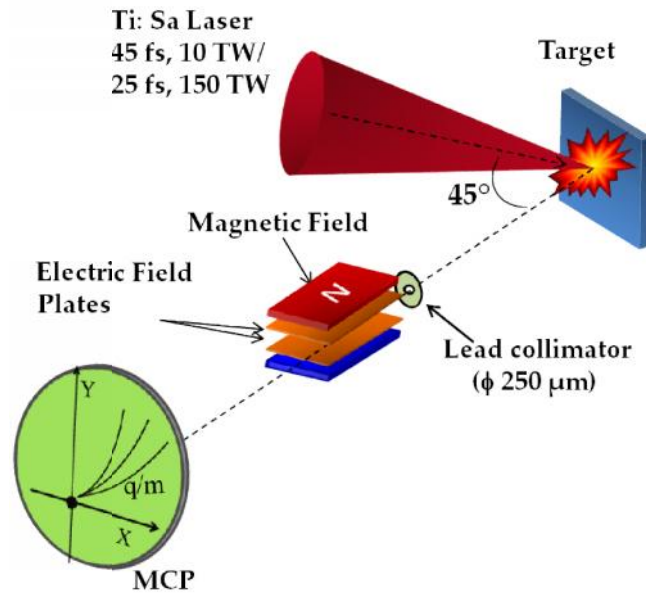


Figure 5.2: Schematic of experimental set-up representing two separate experiments performed with 45 fs, 10 TW and 25 fs 150 TW Ti: Sapphire lasers. The ion emission was characterized by Thomson parabola spectrograph (TPIS) placed along front surface normal direction.

Experimental Results:

Au ions from Nano composite film on Aluminium substrate:

Figure 5.3 (a) shows a typical (TPIS) image recorded by irradiating the nano-composite target along the front surface normal direction for an intensity of $\sim 10^{18}$ W/cm². Ion traces of two distinct natures can be clearly observed. The lighter ions namely protons and carbon ions have continuous parabolic traces (i.e. continuous energy distribution), while the heavier Au ions of different charge states (Au²⁺ to Au⁹⁺) show a very intense and clear bunches or mono-energetic peak. In this picture, the Au¹⁺ charge state position is merged in bright neutral spot. The black dot near the

neutral spot is damage portion on the MCP. The green dashed lines are the theoretically simulated Au ion parabolas. The each fitted parabola show the energy range from 20 keV to 200 keV with energy interval of 20 keV (represented by green dots on dashed green line). Now, one can notice that each bright spots falls nicely on fitted parabolas. Please also recall that any line drawn from the origin of the deflection coordinates i.e. from the neutral spot is a constant velocity line. One such line (shown by red dotted line) representing 90 keV energy is drawn in the TPIS image shown in Fig. 5.3 (a). All the bunches of different charge states of Au, falls on a constant velocity line that means all the Au charged states have the same energy.

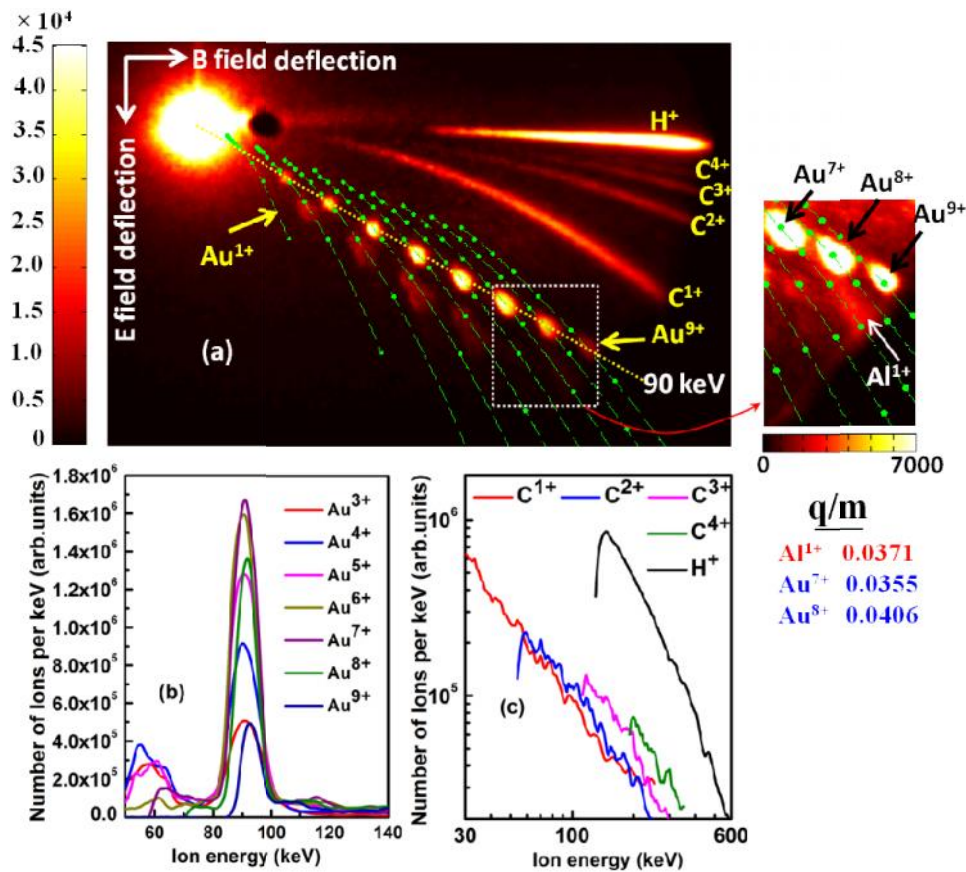


Figure 5.3: (a) Ion signal recorded from nano-composite target coated on 20 μ m thick Al substrate employing 10 TW system. The green dashed curves are simulated Au ion parabolas. The image part inscribed by white dotted square is zoomed and contrast enhanced. (b) Energy spectra calculated from TPIS image showing monoenergetic behaviour of the Au ions, with all the charge states having the same kinetic energy. (c) The proton and carbon ion energy spectra exhibiting broad energy distribution.

The energy distributions of Au ions are shown in Fig. 5.3 (b). All the charge states of Au ions exhibit the same energy (~ 92 keV) and narrow energy spread (E_{FWHM}/E) 7-9%. At the same time, lighter species namely H^+ and $C^{1+ - 4+}$ display exponential energy distribution (Fig. 5.3 (c)), such as typically observed in TNSA mechanism. Heavy Au ions having quasi mono-energetic features and with all the charge states exhibiting same energy is an altogether new and interesting observation. This is untypical to any electric field induced acceleration process. Hence, it appears that, heavy and lighter ions are accelerated via two different mechanisms. To estimate the flux of heavy Au ions, we used CR-39 detector in place of MCP. After exposure, the CR-39 sheet was etched in concentrated NaOH solution for few hours. The developed Au ion tracks were counted using an optical microscope. For Au^{2+} , the total estimated ion flux was found to be more than 10^{10} in single laser shot.

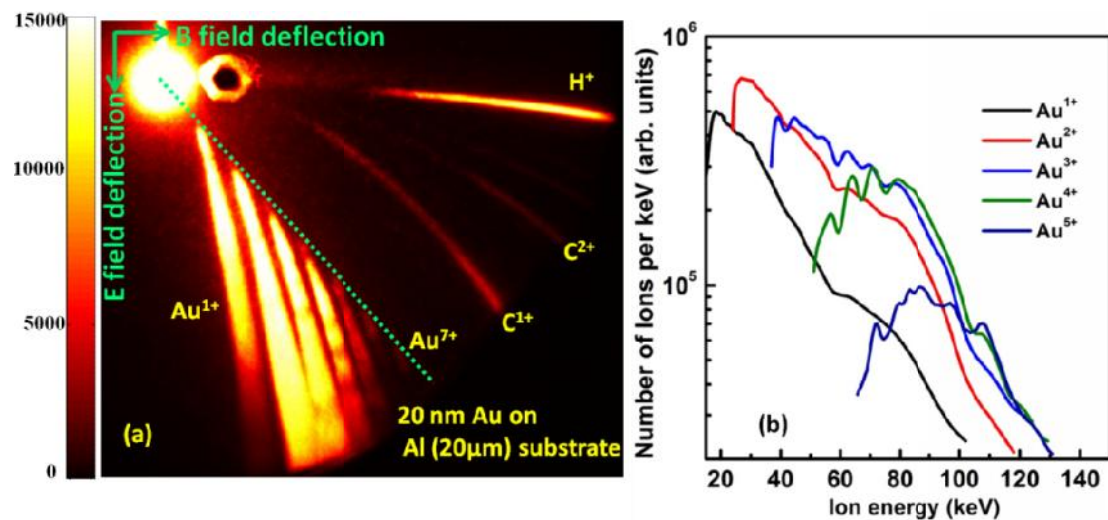


Figure 5.4: (a) Characteristic of ion traces recorded from *plain Au coated* target (20 nm Au coating on 20 micron thick Al substrate) using 10 TW laser system and corresponding energy spectra is plotted in (b).

Energy Spectrum from Pure Au film:

It is important to see how Au ion energy spectrum from pure Au film i.e. without carbon matrix looks like. Fig. 5.4 (a) shows the TPIS images recorded from only Au

coated targets (20 nm thin Au coating on 20 micron thick Al substrate). It is evident from the image that Au ion traces are continuous in nature. Fig 5.4 (b) shows the Au ion energy spectra exhibiting broad energy distribution. Therefore, we observed that with plain Au coated targets, the heavy Au ion energy spectra were always continuous. Another important point to be noticed here is that the maximum energy of all the charge state of Au are almost same (depicted by a constant velocity line drawn in green colour) which is unusual for electric field induced acceleration.

Au ions from Nano composite film on *Silicon* substrate:

The plasma expansion characteristics may also depend on substrate material. Therefore, to study the effect of substrate, similar Au-C nano composite layer was also deposited on 1 mm thick Silicon wafer. Fig. 5.5 (a) shows the ion signal recorded from Au-Carbon nano-composite target deposited on Si substrate. Clean bunches of Au ions falling nicely on a constant velocity line (shown by green dotted line) can be clearly seen in this case also. The Au ion energy spectrum is plotted in Fig. 5.5 (b). All the charge states of Au ions have the same energy and quasi monoenergetic features similar to Al substrate. Further in the ion traces shown in Fig. 5.5 (a), an intense parabolic trace of Si^{1+} with charge to mass (q/m) ratio = 0.0356 can be seen, indicating the heating of the substrate by the laser pulse. Particularly, the maximum energy of the Si^{1+} matches perfectly with the Au^{7+} (q/m = 0.0355). The same was also observed in the case of Al substrate as depicted in inset of Fig. 5.3 (a). It can be seen that Al^{1+} (q/m ratio = 0.0371) lies in between Au^{7+} (q/m ratio = 0.0355) and Au^{8+} (q/m ratio = 0.0406) according to their q/m ratio and the same has been observed in the Fig. 5.3(a) inset. Maximum substrate ion velocity matches with Au ion velocity. Now, we know that quasi mono-energetic features do not get affected by target substrate material and Au ions velocity matches with substrate ion velocity. This

provides a very important clue in understanding the mechanism responsible for heavy Au ions acceleration and will be discussed afterwards.

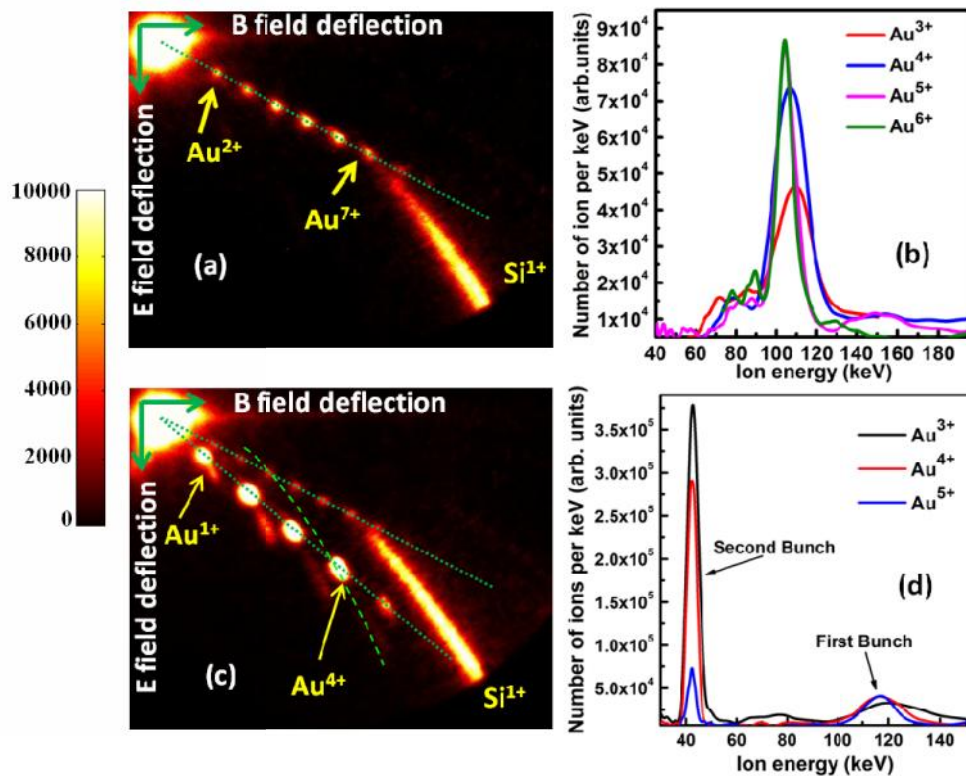


Figure 5.5: (a) Ion signal recorded from AuNP-Carbon nano-composite targets deposited on 1mm thick Si and (b) corresponding Gold ion energy spectra. (c) Double mono-energetic heavy Au ion bunches and corresponding ion energy spectra (d). The green dashed line in (c) is guide to eye for visualization of two bunched on Au⁴⁺ parabola.

The above observations on Au bunched ions are quite consistent and have high repeatability. In all 300 laser shots recorded, almost all the shots show quasi mono-energetic signature (with typical energy around hundred keV with energy spread around 6 - 8 %) irrespective of the Au charged states. This unambiguously establishes the consistency and repeatability of quasi mono-energetic heavy ion production in the present scheme. Of all the shots fired, majority of them (> 80 %) exhibit distinct single energy of Au ions where all Au ion species possess the *same* kinetic energy. Though the clear and distinct single bunching of Au ions is observed in most of the cases, however in number of shot we also observe double peaks (Fig. 5.5 (c) and

corresponding spectrum in figure Fig. 5.5 (d)) and also multiple energy-bunching of Au ion. Moreover, combinations of bunched mono-energetic Au ions with continuous traces are also recorded.

Effect of laser pulse parameters on Au ion bunching:

It was mentioned earlier that the same energy of all the charge state of Au ions signals to a mechanism which does not dictated by electric fields induced because of charge separation inside the plasma. If that had been the case, the energy of the different charge states of Gold would have been obviously different. The ion acceleration by the charge separation induced electric field or by front surface TNSA is governed by energetic electrons the so called hot electrons produced by the intense laser pulse. Hence to comprehend the applicable acceleration mechanism, it is imperative to investigate the role of hot electrons in the observed mono-energetic behaviour of heavy Au ions. We employ three simple ways to control the production of hot electrons, namely, laser ASE pre-pulse [127], laser polarization [128], and pulse duration [88]. The different ASE pre-pulse conditions used in experiments are shown in figure 5.6 (a). The change in proton energy spectrum due change in pre-pulse condition are displayed in Fig. 5.6 (b). Evidently, increase in ASE pre-pulse level definitely deters the proton energy spectrum. The response of Au ions energy spectrum to various laser ASE pre-pulse conditions is shown in Fig. 5.6 (c). Therefore, increase in the laser ASE pre-pulse level, a consistent and considerable reduction in proton energy and flux was observed. However, the quasi monoenergetic bunching feature does not show any systematic decline in mean Au ion energy. Notably the effect of laser pre-pulse on front surface accelerated ions (in laser backward direction) has been studied by Ceccotti et al [52]. The extended pre-pulse creates pre-formed plasma which dilutes the sheath field formed at the target front

surface, thereby reducing the accelerating field and hence proton energy and flux [52]. Next, we change the laser polarization from linear (P-) to circular. The energy spectrum of Au^{5+} for both polarizations is plotted in Fig. 5.6 (d). It is clear that with the change of polarization from linear (i.e. P-) polarization to circular, though the nature of heavy Au ion bunching has no noticeable change but the proton spectra is considerably reduced as expected and in fact, is not even visible within the active area of the detector for circular polarization (inset of Fig. 5.6 (d)). So both these tests imply that the hot electrons may not have a direct consequence on expansion behaviour of these bunched heavy Au ions.

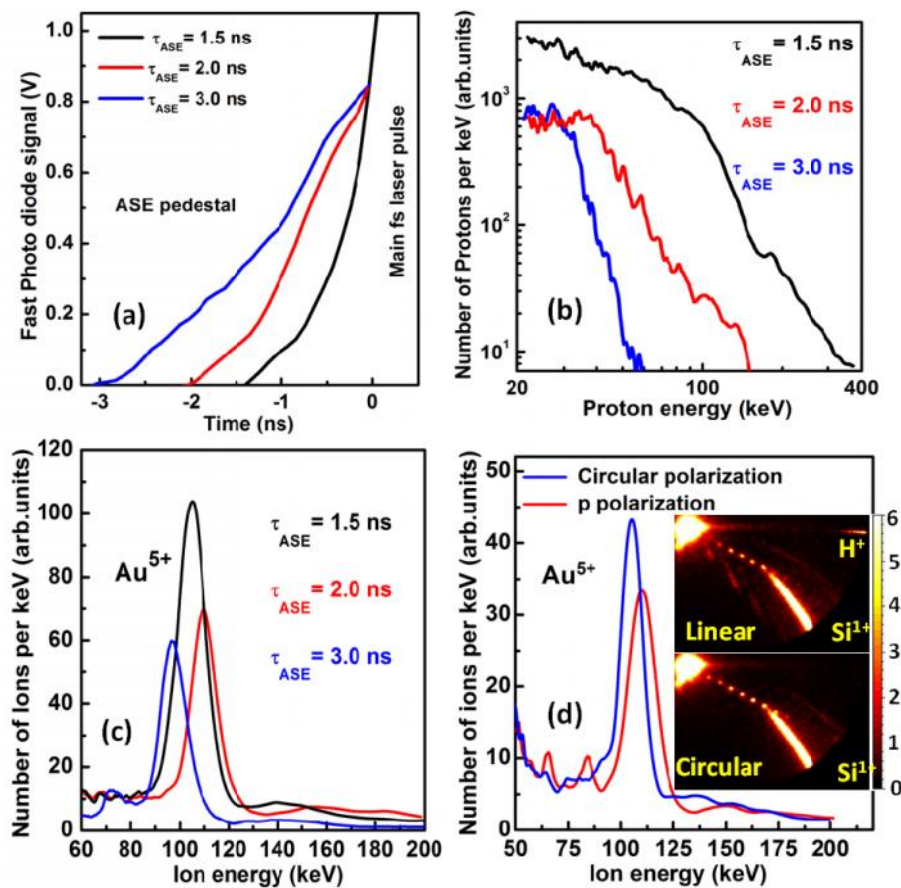


Figure 5.6: (a) Different ASE pre-pulse level. b) Proton energy spectrum at various pre-pulse conditions (c) Au ion spectrum at different levels of ASE pre-pulse, (d) Influence of laser polarization on Au ion spectrum. It is evident that in case of horizontal (i.e. p-polarization), the gold ion and the proton traces are visible (inset of (d)).

Later on, the same study was repeated at higher intensity $\sim 2.3 \times 10^{19}$ W/cm². Similar to earlier observed result with 45fs, 10 TW laser system, the lighter ionic species (proton and carbon) show broad energy distribution. However, the Au ions again show quasi monoenergetic spectrum but at higher energy around ~ 400 keV. The availability of higher power and higher laser pulse energy had enabled us to study the scaling of heavy Au ions with laser intensity. First the laser intensity was changed by increasing the pulse duration from 25 fs to 480 fs (positively chirped) by adjusting the compressor grating separation. No noticeable change in the energy spectra of Au ions was observed in spite of the fact that the peak laser intensity has decreased from 2.3×10^{19} to 1.2×10^{18} W/cm². It may also be noted here that at 480 fs pulse duration the laser intensity with 150 TW system is almost equal to the maximum laser intensity achievable by 10 TW laser system at 45fs, however the energy of Au ions is increased from 115 keV to around 400 keV. The increase in Au ion energy in the case of 480 fs pulse may be attributed to the increase in laser fluence at the laser focus by using higher peak power 150 TW laser system. To confirm the dependence of laser fluence on quasi monoenergetic Au ion energy we varied the laser pulse energy keeping the other interaction parameters unchanged. The fluence variation was done at two laser pulse durations i.e. at minimum pulse duration of 25 fs and long stretched pulse of 480 fs. The results are summarized in Fig. 5.7 (a) and (b) showing variation of Au ion energies for different laser intensities and laser fluences for both 10 TW and 150 TW laser systems. In Fig. 5.7 (a), the variation in Au ion energy is plotted as a function of laser intensity, whereas in Fig. 5.7 (b) the same data point are plotted as function of laser fluence. From figure 5.7, we can see that the quasi monoenergetic Au ions energy is not sensitive to laser intensity; instead it strongly depends on laser fluence

on the target. This kind of dependency on the laser fluence is uncharacteristic of the commonly know ion acceleration mechanism involving short laser pulses.

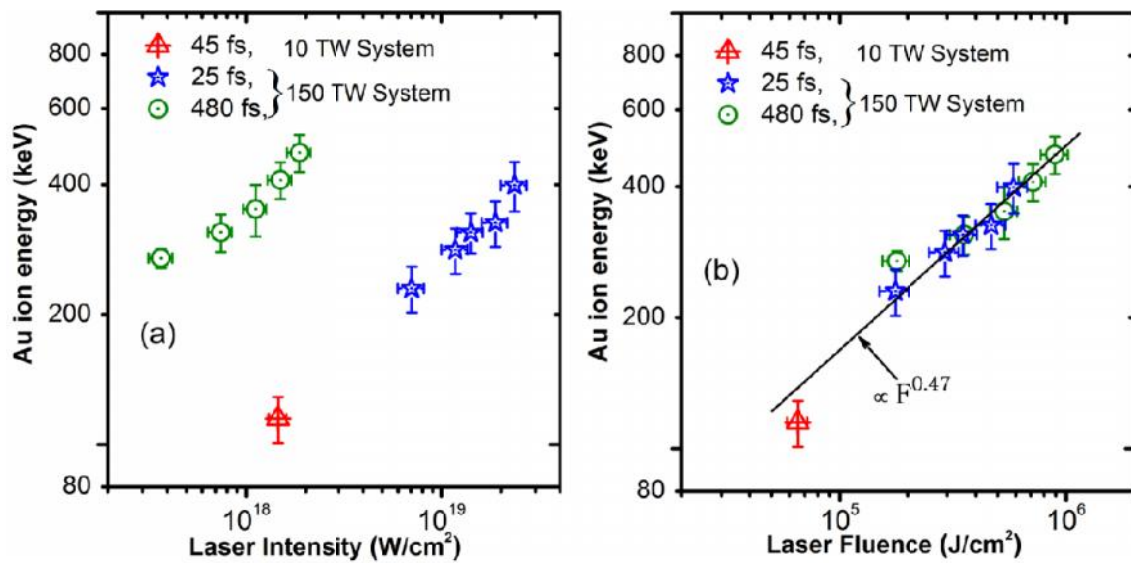


Figure 5.7: Variation of mono-energetic heavy gold ion energy at different fluence level for three different laser pulse durations performed using both 45 fs, 10 TW laser as well as 25 fs, 150 TW laser. In (a) the variation is plotted with respect to laser intensity and in (b) the data is plotted as a function of laser fluence. The black solid line is fit to the data points showing Au ion energy scaling with respect to laser fluence.

Discussions:

Therefore from the above experimental results presented so far, the following inferences can be drawn: (1) Quasi monoenergetic Au ions energy spectrum characteristics do not corroborate with lighter atomic species e.g. protons, Carbon ions, (2) Maximum energy of Au ions equals maximum substrate ion energy, (3) laser pulse properties e.g. ASE pre-pulse, laser polarization and pulse duration do not have the noticeable effect on the energy of quasi mono energetic Au ions unlike lighter protons and carbons, (4) the quasi monoenergetic Au ion acceleration does not show clear dependence on laser pulse intensity rather mainly depends on laser fluence. The above observations are *not due to* any hot electron mediated charge separation induced ion acceleration mechanism.

Furthermore, the two most important points of heavy Au ion acceleration are, (1) All the Au ions irrespective of the charge states have identical final velocity, indicating that the acceleration mechanism does not depend on charge, and (2) quasi monoenergetic features in Au ion energy distribution. The first point is quite obvious, as had it been the case, then the Au ions with different charge states would exhibit different energies. However, the second point is not so obvious.

The Au-C nano-composite target has AuNPs of 3-8 nm size with total Au concentration around 2 – 4 atomic % embedded in 120 nm thick carbon matrix. The total thickness of deposited film is less than skin depth for the 800 nm laser. Hence, the high intensity laser pulse can interact with the substrate material forming a high temperature, solid density plasma. First, lighter ions (protons and carbon) are accelerated by the sheath field set up by the hot electrons over a time scale of few times the laser pulse duration, and they take out most of the energy from the sheath field potential. During this time scale, the heavier Au ions, barely move, and hence confined in very thin layer. The thin layer of Au ions experiences the expansion of the bulk plasma produced by the femtosecond laser pulse on the target substrate. As all the Au ions face the identical push i.e. plasma pressure, due to the expanding bulk plasma, the final Au ion velocities are therefore same. That's why the observed maximum velocity of Au ions matches with substrate ion velocity. This explanation gives a feeling that the carbon matrix is just for holding the AuNPs and allowing the laser radiation penetrate through it and heat the target substrate. However, if we recall from Fig. 5.4 that only plain layer of Au yields a continuous Au ion energy distribution. Therefore, the presence of carbon layer is crucial in modifying the energy distribution of Au ions towards quasi monoenergetic behavior. The carbon layer not just only holds the nano particles in place for the main fs pulse but it also keep the

AuNPs intact from the heating effect of laser pre-pulses. As Au ions are confined to a thin layer and their initial positions are fixed, therefore they feel the same pressure by the expanding substrate plasma resulting in identical energy of Au ions irrespective of the charge states. As a proof of this argument, consider the expansion of only plain Au coated target. The pre-pulse will heat the Au layer leading to pre expansion of Au layers, hence their initial positions and velocities differ. Therefore, the spread in velocities in energy distribution of Au ions is already present to start with before they feel the push due to expanding substrate plasma. This leads to same maximum energy of all Au ions but having spread in energy distribution (Fig. 5.4 (b)).

The experimental observations clearly establish that for obtaining quasi monoenergetic Au bunches, the presence of Carbon layer is necessary. However, for same maximum energy of all the charge states, there is one more possibility which is the charge recombination in background plasma. During the interaction the Au atoms are ionized to some fixed average ionization state depending on the laser irradiation condition. The Au ions are then accelerated by the expanding plasma. Since electrons are co-moving with Au ions in the expansion stage, the Au ions because of their large size as well as moderate electron affinity of 2.31 eV, can capture electrons resulting in decrease of ionization states over the expansion. When these Au ions reaches the TPIS they possess the same maximum energy and similar spectrum but at different ionization states. The electron capture by accelerated Au ions is expected to be more prominent in case of Au-C nano composite targets as the presence of low density C pre-plasma may also help in electron capture apart from the direct Au-electron interactions.

Here, a plausible explanation of the experimental results is provided which is based on the observed characteristics of the ion emission and its dependence on the

laser pulse and target parameters. However, we believe that in depth theoretical modeling aided by simulations will bring more insight on the experimental observations. Still in order to further cross check our understanding on Au ion emission characteristic, another experiment was performed with 150 TW system in which we studied the effect of Carbon coating on Au ion bunching. The new experimental observations also clearly establish that for getting quasi monoenergetic Au bunches, the presence of Carbon layer is necessary. At the same time there is clear signature of charge recombination in background plasma. The results are presented in next section.

5.2 Quasi-monoenergetic heavy ions from *multilayer* targets

In continuation of previous experimental campaign with Gold-Carbon nano-composite (AuNP-C) targets, we have also performed experiments with layered targets. The primary difference of these new “layered targets” with the previous AuNP-C nano-composite targets lies in the method of deposition. In AuNP-C targets, the Au and C were co-sputtered while in the present scenario, they are sputtered in sequence. To elaborate further, first thin Au layer (thickness around 5 nm) and is coated on thick (0.5 mm) Si substrate which may be considered semi-infinite when compared to the thickness of the deposited layers. On top of this Au layer, carbon layers of different thicknesses (10 nm, 20 nm and 40 nm) are deposited. Please note, in the following texts, “Single Layer” target implies that there is only one layers of Au and Carbon are coated on the substrate i.e. C*/Au/Si. Here the asterisk (*) sign indicates the layer facing the laser irradiation. In continuation of this nomenclature, a double layered target implies TWO such layers of Au and C coated in sequence on Si substrate i.e. C*/Au/C/Au/Si. In Fig. 5.8, a simple illustration of the target composition is displayed.

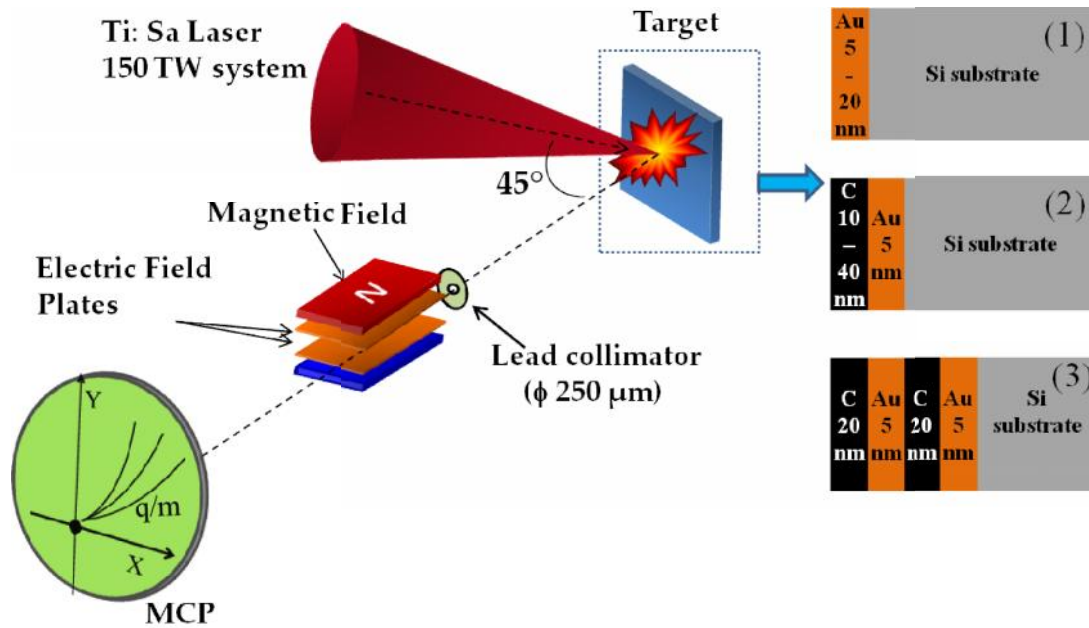


Figure 5.8: Schematic experimental diagram showing the geometry of intense, ultra-short laser pulse interaction with layered targets. Simple illustrations showing the target structures; (1) only Au layer on Si of thickness 5, 10 and 20 nm, (2) “Single Layer” target comprises single layers of C and Au (5nm) coated on Si substrate and (3) “Double Layer” target consists of TWO such independent Au and C layers on Si substrate.

Though the primary motive behind these experiments were to verify our initial hypothesis while explaining the mono-energetic expansion of heavy Au ions, but after rigorous study of these samples a lot of new results start appearing which are discussed below. The experimental set up is similar to previous experiments as shown in Fig. 5.8. The experiments have been conducted 150 TW laser system operated at **40 TW** level. The laser pulse is focussed on the layered targets at an angle of 45° with respect to front target normal direction to an intensity $\sim 1.5 \times 10^{19} \text{ W/cm}^2$. The experimental chamber has been kept at a base vacuum of 5×10^{-5} mbar. Ion emission was recorded using TPIS placed along front surface normal direction. All the data presented here are collected on single shot basis.

Au ion energy spectrum from only pure Au layer:

Now, first let us concentrate on the results of the pure gold targets i.e. complete absence of C layer. We used different Au coating thickness starting from 5nm, 10 nm and 20 nm. Like previous observation, the heavy Au ion traces are continuous in nature with a finite maximum cut-off. Although, the Au parabolic traces are mostly continuous but their fine features varies on shot to shot basis. Few typical representative shots along with energy spectrum are shown in Fig. 5.9. The Au ion energy distributions from these targets are mostly continuous or have broad energy distribution. Apart from being continuous in nature almost all the shots show **two** distinct set of ion populations having different origin (more apparent in Fig. 5.9 b and c). The two different characteristic populations or branches are distinguished by drawing a line (dotted yellow line from the origin) in Fig. 5.9 (a-c). The parts of Au ion population above and below the yellow dotted line have different characteristics. In other words each Au ions seems to be constituted by two different mechanism or sources. The corresponding energy spectra are plotted in Fig 5.9 (e-f). The red vertical arrow in Fig. 5.9 (e-f) marks two parts of the population. The 1st branch (above the yellow dotted line in raw TPIS image) consisting mostly the higher charged states and for which the maximum energies are not the same anymore. The maximum Au ion energy for this branch keeps on increasing with increasing charge states. This is typical of field acceleration process (TNSA or close to that). Also the width of the parabola and population is also small. However, apart from this, another set (below the yellow dotted line) consisting of relatively low charged states (Au^{1+} to Au^{7+}), have sharp high energy cut-off and same maximum energy and contains higher ion flux. We feel that different part of the population of Au ions arises from two different acceleration mechanisms or from two different sources. One is dominated by

hydrodynamic expansion and the other is dominated by the electric field induced acceleration.

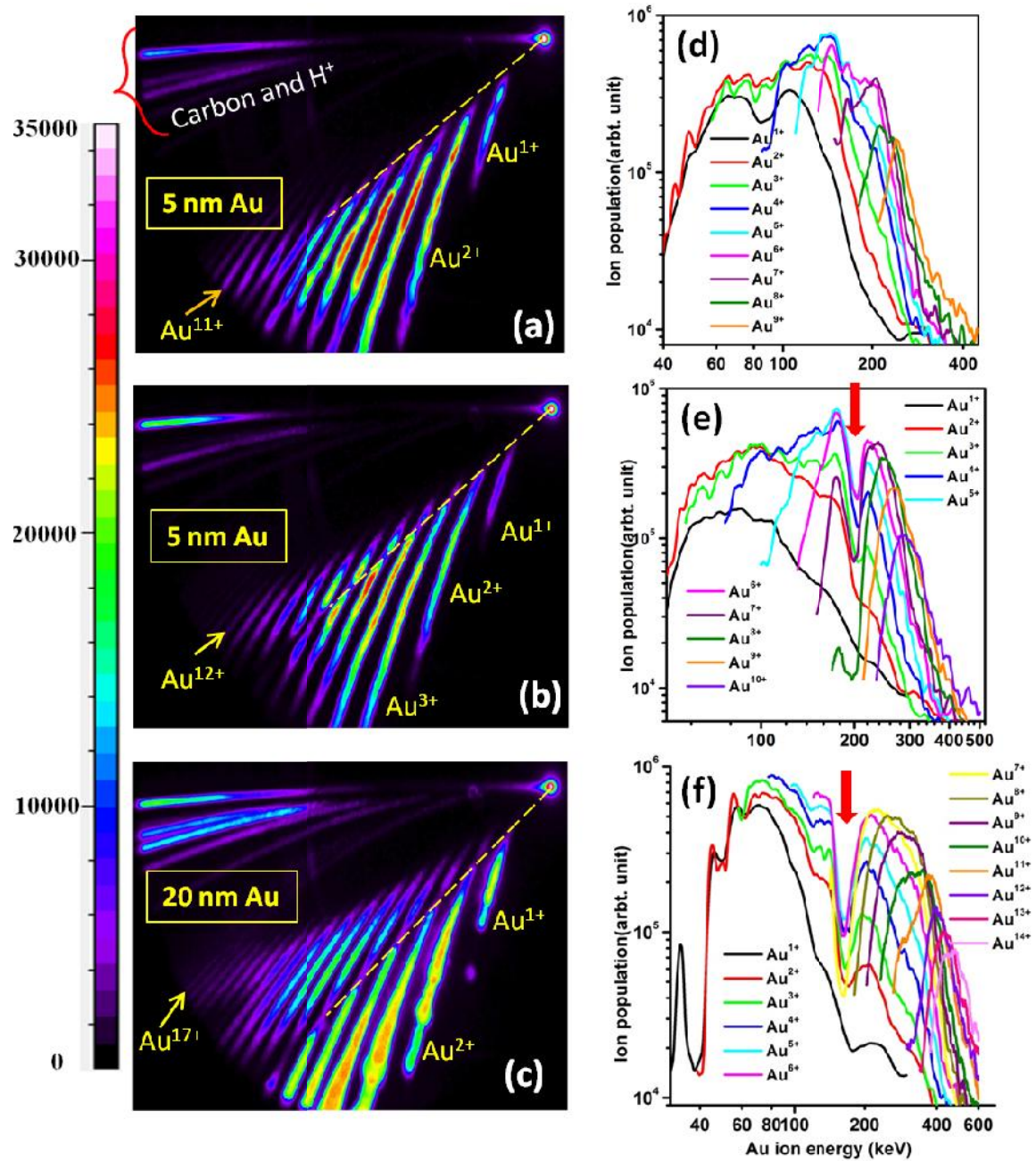


Figure 5.9: Typical continuous heavy Au ion spectra obtained with pure Au targets of thicknesses 5 nm and 20 nm. There are no Carbon coatings on these targets. Yellow line drawn from the origin is constant velocity line indicating that maximum energy of lower branch is same for all the charge states. Corresponding Au ion energy spectra for different charges states are shown in (d) - (f).

Effect of carbon layer thickness:

Now let us come to the most important part of this experimental campaign i.e. role of carbon layers on Au ion acceleration. All the laser irradiation parameters were kept identical as used for only plain Au coated target. Figure 5.10 shows the impact of carbon layer coating on top of Au layer. In the experiment, to explore the role of the carbon coating we have now varied the thickness of the carbon layer thickness to 10 nm, 20 nm and 40 nm. It is indeed astonishing to find that mere presence of 10 nm thick carbon layer considerably affects the Au ion expansion behaviour (Fig. 5.10 (a) and (d)). As expected, with further increase of the carbon layer thickness, the more prominent mono-energetic behaviour is revealed. In other words the relative energy spread decreases. The effect of carbon layer thickness on the mono-energetic behaviour of heavy Au ions is summarized in the Fig. 5.11.

Here again there are two distinct set of population, but with reduced energy spread. As depicted in Fig. 5.10 (a), the population below the constant velocity line (yellow dotted line) will be called as first bunch and above this line will be called as second bunch. It is clear that increasing the carbon layer thickness, reduces the Au ion energy spread. First set of ion bunches as indicated in Fig. 5.10 and 5.11 appears to be more sensitive to carbon layer thickness. At the same time, the second set of ion bunches shows less sensitivity towards Carbon coating thickness (when increases from 10 to 40 nm). In addition, in first bunch all the charge states have sharply same energy whereas for second bunch, the energy slightly increases with charge states as can be seen in Fig. 5.10. Please also note that with C*/Au/Si target the observed ionization state is limited to Au⁴⁺ to Au⁵⁺, whereas with Au/Si i.e. with only Au coated targets it was normally more than Au¹⁵⁺. Therefore, Au ion energy spectrum from both the targets; Au/Si and C*/Au/Si, have one to one correspondence except

that in the later case i.e. with addition of carbon layer, the Au ion energy spread as well as the observed charge states reduces.

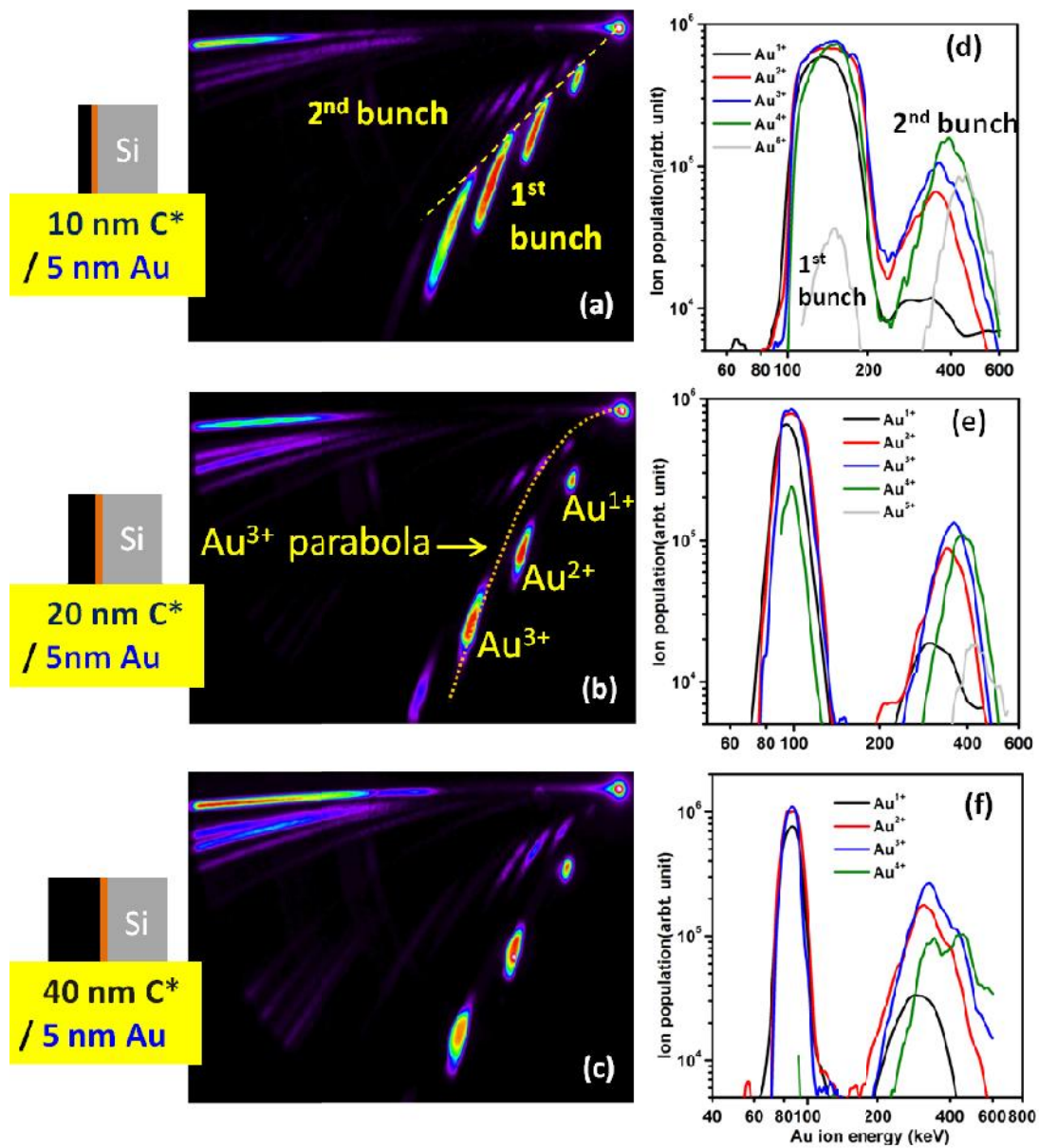


Figure 5.10: Effect of Carbon layer thickness on mono-energetic behaviour of Au ions. Two distinct bunches of Au ions are observed. In image (b), Au^{3+} parabola is drawn to show that the two separate bunches lie on a parabola. The similar parabola can be drawn for other charge state as well. Notably, with increase of carbon layer thickness i.e. 10 nm, 20 nm and 40 nm, the relative energy spread of the Au ion bunches reduces as revealed from TPIS images and corresponding energy spectrum.

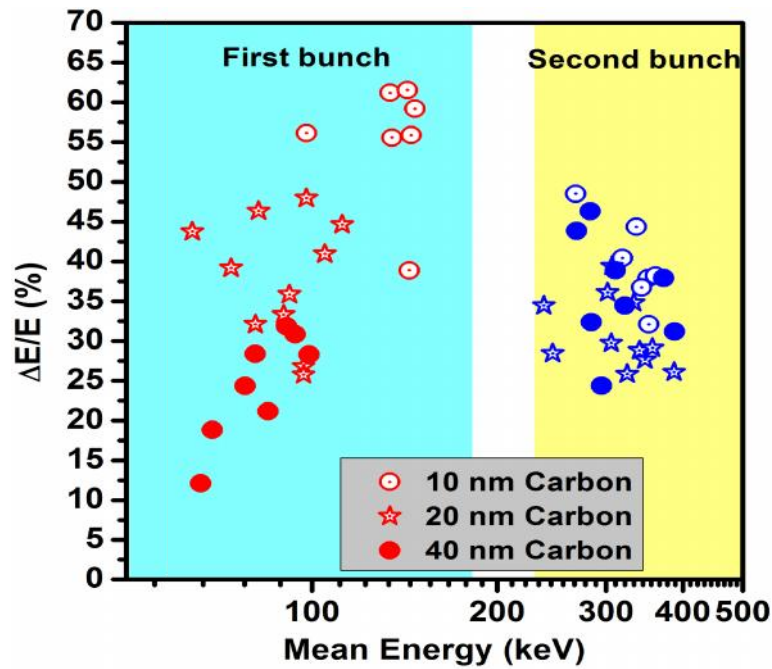
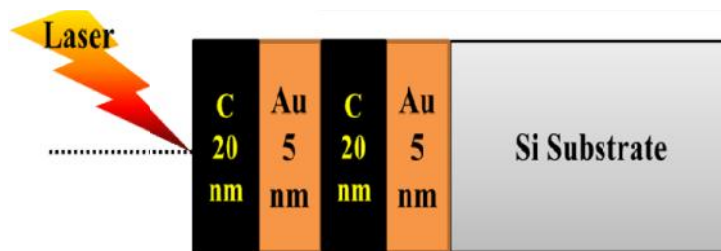


Figure 5.11: The energy spread of Au ion for first and second bunches with varying carbon layer thickness. The data points represent the individual shots

Result of from Double layer target



Similar to single layer of Au and carbon C*/Au/Si, we have also used double layer C*/Au/C/Au/Si targets. The shots from multilayer target also shows clear signature of energy bunching. Surprisingly in many shots similar to single layer of Au and carbon (C*/Au/Si), in many shots of double layer of (C*/Au/C/Au/Si) also shows two separate bunch. Fig. 5.12 (a) shows the Au ion emission recorded using multilayer targets. The Au ion energy spectrum plotted in Fig. 5.12 (b). A parabolic trace on the TPIS image is drawn (for Au³⁺) as a representation to show and identify different part of Au³⁺ ion. Also each parts of the Au³⁺ ion parabolic trace are marked with different colour arrow and numbers to show which part of the trace constitute which part of the

spectrum. The same is applicable to other charge state as well. Therefore, it is very much clear that the Au layers which are buried at different depth definitely show its effect on overall energy spectrum.

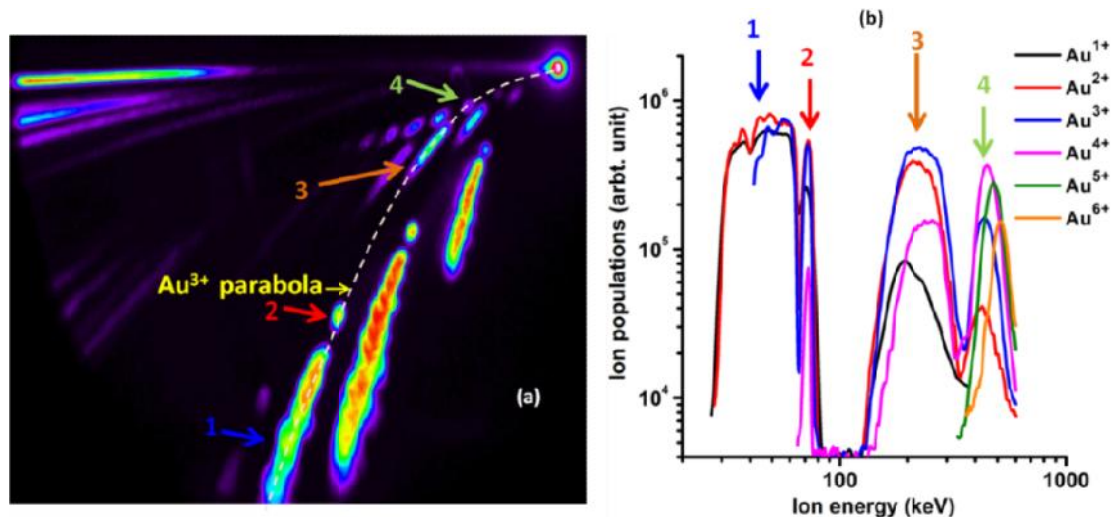


Figure 5.12: TPIS image recorded from double layer targets showing two sets of bunched Au ions. The corresponding spectra are plotted on right hand side. As a representation each part of the Au^{3+} ion are marked with different colour arrows and numbers to show its place in the energy domain.

Discussions:

First let us compare these results with the results obtained with Au-Carbon nano-composite target used in the previous experiment. The present experiments clearly establish the role of low Z carbon layer in obtaining quasi-monoenergetic Au ions. However, here in addition, few new interesting features are also observed. With introduction of the carbon layer, *two distinct bunches of quasi monoenergetic* Au ions appear unlike the case of pure Au coating which mainly shows broad energy distribution. Although there are relative variation; in the energy of the observed bunches but overall they belong to two distinct energy regions. This is quite different from previous experimental campaign with AuNP-C nano-composite targets. There the Au nano-particles predominantly yielded single bunches (80 % of total number of shots taken) while two or multiple bunching were observed for relatively small

number of shots. However, in the *present case with layered targets*, it is the double bunching that is dominating for most of the shots. In addition the two bunches seems to be accelerated by two different mechanisms (all the charge states in first bunch have exactly the same energy whereas in second bunch the energy slightly increase with the charge states). Therefore, the new features can be a *consequence of 2D effects of the thin films as well due to high contrast of the laser pulse*. Also note that earlier nano-composite target was co-sputtered but here in layered target the coating is sequential.

Now let's come to the energy characteristic of two bunches. As mentioned earlier, the close inspection of the observed ion traces in TPIS and their energy spectrum from Au/Si and *C/Au/Si targets shows a strong correlation. In other words, the observation of two bunches from *C/Au/Si layered target seems to be linked with the observation of two different populations from plain Au coated targets presented earlier. In order to elaborate further, let us go back to the case of *pure Au film* case once again. Fig. 5.13 below shows one such case. The two distinct features, like previous ones (Fig. 5.9), are clearly noticed. It seems that in presence of the carbon layer, the higher charge states recombine and as a result they override on the parabolas of lower charge states and become a part of that parabola. This may explain the origin of two bunches with the layered targets. So what is basically happening is that the Au layer expansion is significantly inhibited by the exterior carbon corona giving rise to narrow-band features in Au ion energy spectrum. Therefore, the confinement of the Au layer in narrow region, tamping action of the exterior carbon corona as well charge recombination in background plasma seems to be the main reason behind quasi mono energetic Au ions with same energy for different charge states, in the present case.

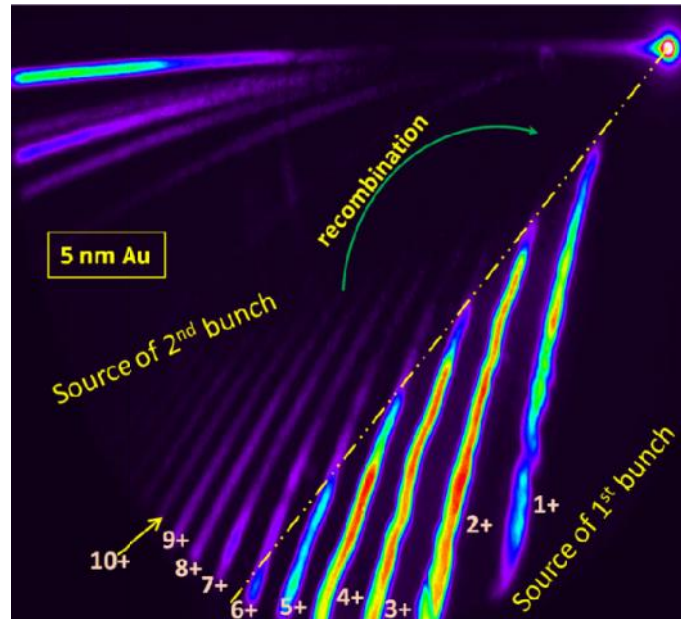


Figure 5.13: TPIS record with pure Au layer of thickness 5 nm. Two ion population of different characteristic can be clearly noticed. One is having a sharp energy cutoff depicted as a constant velocity line and for other the energy increase with charge states.

5.3 Conclusion

Quasi monoenergetic heavy Au ion acceleration with different charge states of Au accelerated to the same energy using nano-composite and multilayer targets have been demonstrated for the first time. This is completely a new way to produce monoenergetic bunches of heavy ions from freely expanding laser produced plasmas. It was established that the presence of low Z carbon layer is necessary for getting quasi monoenergetic features in Au ion energy spectrum. The experimental observations suggest that the Au ions are mainly accelerated by the piston effect of the hydrodynamically expanding hot plasma. The Au ions being confined in a narrow region feels the same accelerating forces. During the expansion they also feel the tamping force due to the background plasma corona. All this ultimately leads to quasi monoenergetic features in Au ion energy spectrum with all the charge states having identical energies. However, at higher laser intensity and high contrast laser pulse the

effect of electric field induced acceleration also starts visible (as clearly observed with layered targets). It was also noticed that the charge recombination in the background plasma can also give Au ion with identical energies.

The present technique employs a nano-composite thin film (consisting of AuNPs embedded in C matrix) and Au-Carbon multilayer on Si or Al substrates. The target fabrication is quite simple, reliable, and produces consistent quasi monoenergetic Au ions accelerated to ~ 400 keV energy using sub 100 TW laser. Furthermore, the present approach does not require any complicated alignment or very advanced target engineering and hence can easily be operated at higher repetition rates.

CHAPTER 6

Negative ion (H^-) acceleration:

High energy negative ions (H^-) and neutral atoms have important applications in different areas of science and technology. Heating of tokamak fusion plasma [129], as an excellent charge exchange injector to conventional high energy circular accelerators as well as electrostatic tandem accelerators [130], [131], ICF related research [132] and ion beam lithography [133] etc. are some of the applications where the negative ions and neutrals have significant advantages over the positive ions. The conventional negative ion (H^-/D^-) sources are based on charge exchange processes and are basically two types [134]. One is the plasma volume source in which H^-/D^- are formed by dissociative electron attachment to a vibrationally excited molecule ($e + H_2^* \rightarrow H^- + H$). Another is the plasma surface sources in which H^-/D^- are formed when hydrogen or deuterium plasma interacts with low work function surfaces like Cs and other alkali metals. The negative ions thus formed are extracted by applying the external electric field. As the electron affinity of Hydrogen is only 0.75eV, therefore for survival of negative H^- ions, the plasma temperature in such devices is kept quite low around 1eV.

Contrary to the conventional approach, recently a new way of producing negative ions using high intensity short pulse laser has emerged [135]–[138]. Generally high intensity laser based ion accelerator favours the acceleration of highly charged positive ions. However, in some recent experiments few groups have demonstrated generation of negative ions and neutrals from gases, clusters and water spray targets. The main idea is to tailor the interaction condition in such a way so as to provide a sufficient neutralizing medium for the accelerated positive ions to become

neutral and negative ions. Therefore, the efficiency of the scheme depends on the efficiency of neutralization. For example Rajeev et. al. [137], [139] have demonstrated upto MeV energy neutral and negative ions of Ar with near 100 % particle conversion efficiency due to the enhanced charge transfer of positive ions from Rydberg excited atomic clusters formed around laser focal volume. S. Ter-Avetisyan et. al. [135] have reported negative oxygen ion (O^-) production in the interaction of high intensity ($\sim 5 \times 10^{19} \text{ W/cm}^2$) laser pulse with water spray target. More than 10^9 O^- ions per steradian up to MeV energy were reported. The acceleration of negative ions were explained by the recombination or electron capture process occurring in the surrounding water spray while the positive ions accelerated in the plasma channel traverses through it. The inherent disadvantage of the above high intensity laser based scheme to real life implementation is the low repetition rate of such systems as well as almost isotropic ion emission which limits the overall available flux for a particular application.

In the present work we demonstrate, energetic H^- ion generation from ultra-short laser pulse interaction with easily commercially available transparent solid targets of low atomic number [70]. The negative ions produced by laser interaction with solid target offer high brightness and consistent production with reliable control over the flux and energy. It was shown that by using transparent solid targets containing Hydrogen e.g. Polymethyl methacrylate (PMMA, $(C_5H_8O_2)_n$), a directed energetic H^- ion beam can be obtained. The use of solid targets also offers a higher repetition rate operation of such sources. The experimental results on H^- generation from thick solid targets are discussed in section 6.1.

In addition to H^- generation from hydrogen containing thick solid targets, H^- ions were also observed from thin foil targets. We show that in appropriate condition,

protons accelerated at rear side through TNSA mechanism can be converted to H^- ions by recombination with copropagating electron populations. The results on H^- generation from thin foil targets will be discussed in section 6.2.

6.1 H^- acceleration from hydrogen containing transparent solid target

Experimental details:

The experimental set up is shown in Fig 6.1. The experiments have been performed with a 45 fs, 10 TW Ti: Sapphire laser system. The laser pulse was focussed by an f/7 off-axis parabolic mirror (OAP) to a focal spot diameter of 10 μm (FWHM) resulting to an intensity of $3 \times 10^{18} \text{ Wcm}^{-2}$. The target was 5 mm thick sheet of PMMA and the laser incidence angle with respect to target normal was 45° . Some other targets like thick glass and solid metals were also used. The vacuum inside the plasma chamber was in the range of $\sim 5 \times 10^{-5}$ mbar. For analyzing the accelerated charge particles, a Thomson Parabola Ion Spectrograph (TPIS) equipped with Micro Channel Plate (MCP) was used. The output of the MCP phosphor screen was imaged by a 16 bit EMCCD camera (ANDOR iXon). The reflected beam from the target in the specular direction was collected by a lens to an energy meter. Part of this reflected beam was fed to a spectrograph recording the reflected beam spectrum. In this configuration, the spectrometer also records super-continuum emission (SCE) generated as a consequence of ultra-short laser pulse propagation inside the transparent solid targets used in the experiment.

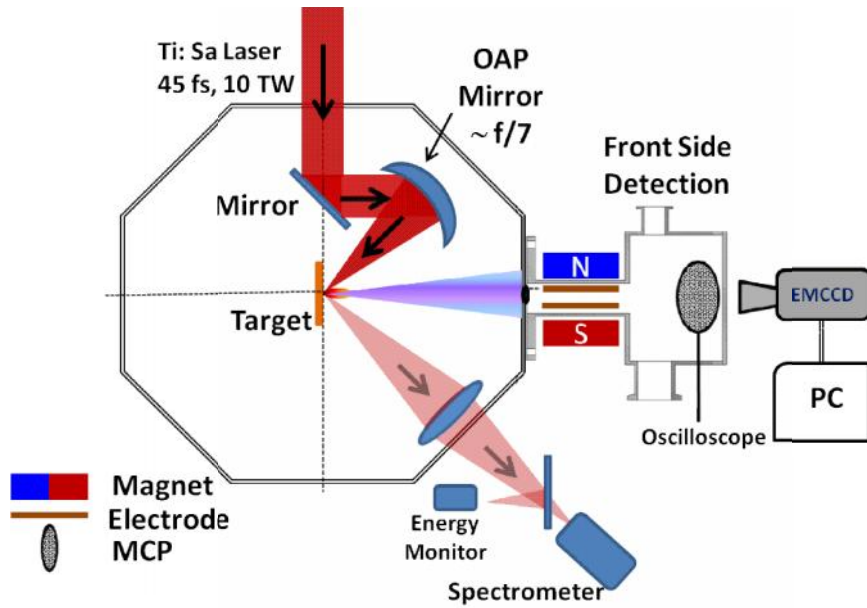


Figure 6.1: *Experimental set up used for generating H ions from PMMA target. The ion emission along the target normal is recorded by Thomson Parabola Ion Spectrograph (TPIS).*

Experimental Results:

Figure 6.2 (a) shows a typical ion traces recorded by TPIS. The appearance of the H⁻ along with H⁺ and carbon ions is evident. Although the population of H⁻ compared to H⁺ is small, as expected, a consistent generation of H⁻ ions on every single laser irradiation was observed. The derived ion energy spectrum from the TPIS picture is shown in Fig 6.2 (b). Energetic H⁻ ions with energy up to 120 keV was observed. In contradiction to commonly observed TPIS traces, in this case, we observe smearing of the nearby ion parabola traces particularly for carbon ions. In order to investigate further, we have scanned the sample across the geometrical focal position of the laser, similar to z-scan. It was observed that when the target (front) surface coincides with the laser focal position, the proton energy is maximized and the carbon traces (C^{1+ - 6+}) are distinct. Notably, in this position (“Z = 0”, say) hardly any H⁻ ion was detected. But as the target is shifted from the focus (on both sides), the H⁻ ion traces starts appearing along with reduction in H⁺ energy and smudging of carbon ion traces. Even

with the change of the externally applied electric and magnetic field this remains unaffected. The smearing of the parabolic traces and appearance of the H^- ions at defocused positions indicates an elongated laser focussing inside the transparent target.

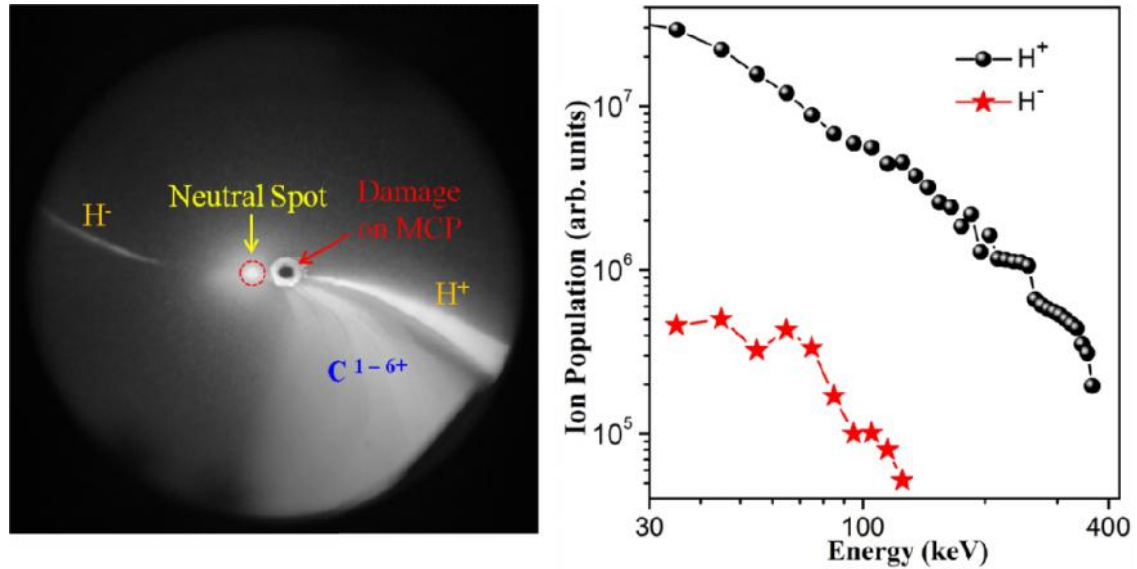


Figure 6.2: (a) Typical Thomson Parabola Images recorded on MCP from PMMA target. The presence of H^- is evident along with the presence of strong H^+ trace. The charged states of carbon are also visible but appear as smeared off (see text for details). The ion energy spectra of H^- and H^+ ions are shown in (b).

Later on, to find out the actual H^- ion flux we also used a CR-39 sheet in place of MCP detector. The ion parabolic traces recorded on CR-39 detector are shown in Fig 6.3(a). By switching the polarity of the electric field two set of traces were recorded as depicted in the picture (Fig 6.3 (a)). Almost similar characteristic ion traces as recorded with MCP detector can be seen in CR-39 also. The carbon traces are smeared. The microscopic view of the H^- ion parabola trace is shown in Fig. 6.3 (b) showing individual H^- tracks/pits. The total H^- ion flux was estimated by counting tracks recorded and it was found to be $\sim 10^{11}$ per shot in 4 sr assuming similar divergence as of proton beam. The abundance of negative ions also suggests the formation of neutrals. Analysing the neutral spot formed on CR-39 sheet indeed show

the presence of neutral atoms (Fig. 6.4). It is clear from Fig. 6.4 that the neutral spot consist of pits of different sizes. The small pits are due to hydrogen (H^0), and bigger pits are due to neutral carbon or oxygen.

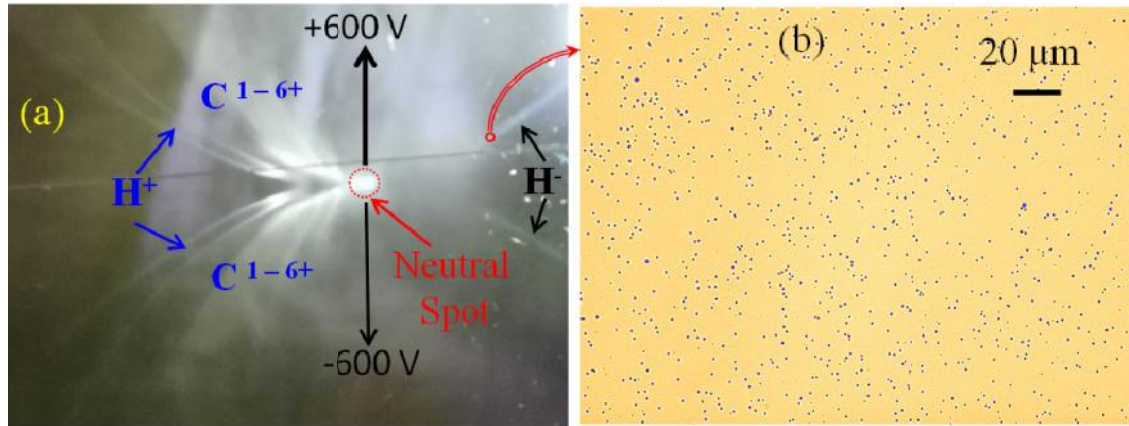


Figure 6.3: Ion signal recorded on CR-39 detector from PMMA target showing the presence H^+ of parabola trace along with other positive species. (b) Tracks formed on CR-39 detector due to the impact of individual H^+ ions.

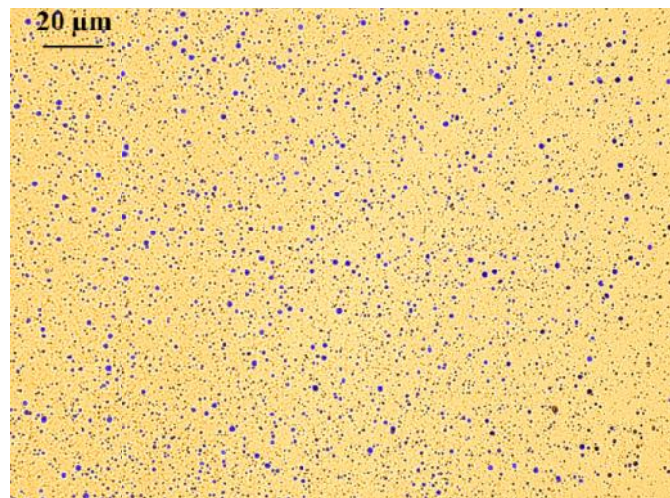


Figure 6.4: Microscopic view of neutral spot on CR-39 showing individual tracks/pits formed due to neutral atoms

Effect of laser Defocusing:

The variation of H^+ ion spectra with focal position is depicted in figure 6.5 (a). A representative picture explaining the effect of target scanning across the laser focus is also shown in Fig. 6.5 (b). In the figure, “ $Z = 0$ ” implies that the laser focus is at the front surface of the target. A positive value of z ; implies that the target is being moved

towards the laser direction or laser geometrical focus is inside the target. Evidently, when the laser focuses exactly on the front surface of the target, the appearance of H^- is negligible. But as the target is moved towards laser implying that the geometrical focal position of the laser lies within the target, a strong appearance of H^- is observed. However, as the target is moved considerably off from the “Z=0” position, the H^- ion flux and energy start to decrease. The laser intensity variation on account of laser defocusing assuming an ideal Gaussian beam is shown in Fig. 6.6.

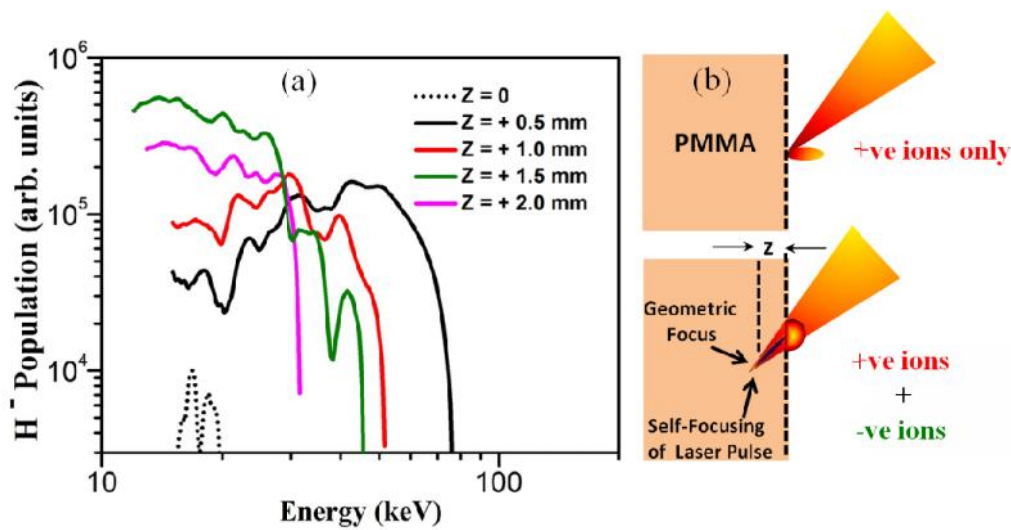


Figure 6.5: H^- ions signal at various focal positions of the laser beam. Here “Z = 0” defines the front surface of the sample. Positive Z position indicates that the target has been displaced towards incoming laser direction by a specified distance.

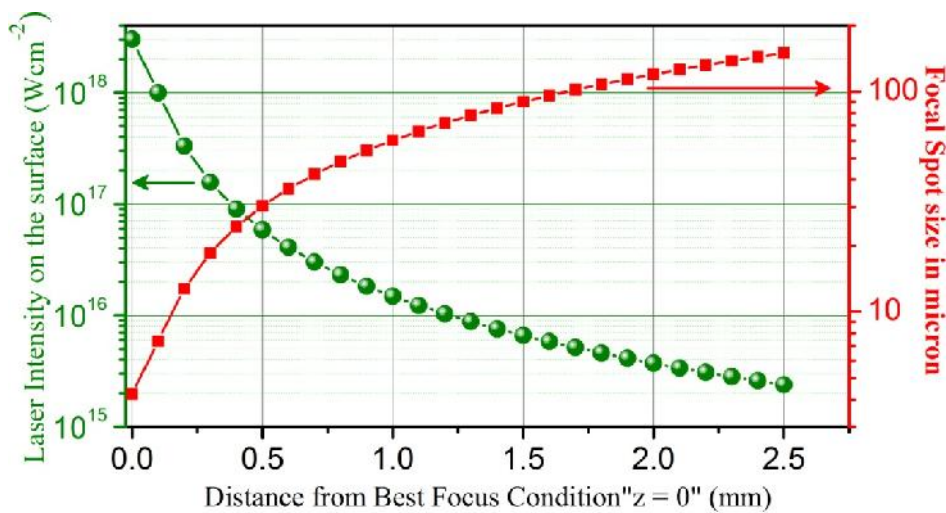


Figure 6.6: Variation of laser intensity with the target position with respective best focus position

Effect of laser pre-pulse:

It is well established that increasing laser pre-pulse (ASE) reduces the accelerated proton (H^+) signal. In order to understand the H^- ion generation process we also studied the effect of laser ASE pre-pulse on H^- ion generation. Fig 6.7 shows the H^- ion energy spectra with increasing level of ASE pre-pulse. It is observed that that an increase of the laser pre-pulse substantially reduces the H^- ion generation.

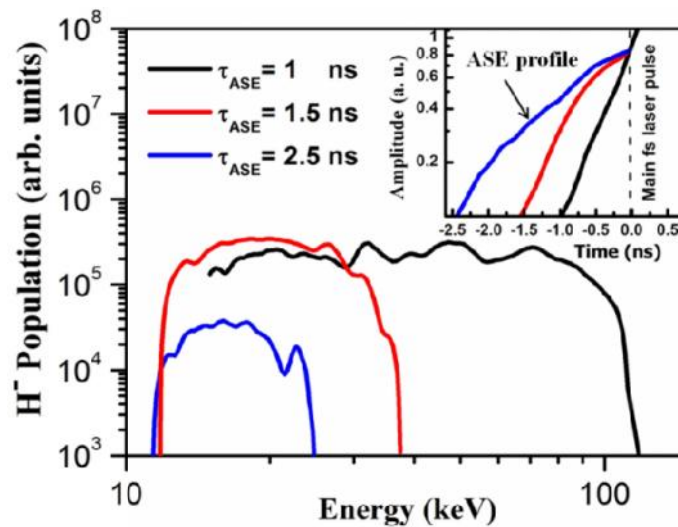


Figure 6.7: *Laser pre-pulse effect on negative ion generation.*

Discussion on observed result:

It is well known that barely 0.75 eV is required for breaking off the H^- ions and releasing the extra electron. Now the plasma formed by intense, ultra-short laser pulse has a temperature which is much higher than the set down region of plasma temperature for conventional negative ion sources. Hence the generation and survival of the H^- ions in the plasma volume formed on surface can be ruled out. The only way the negative ions can be produced is via electron capturing by the energetic protons emitted from the plasma. Therefore, a necessary condition for this to happen is the presence of donors surrounding the proton (H^+) origin. The protons are accelerated by the space charge field set up by energetic electron population at the target surface. The generated electrons and protons have velocity distribution, any overlap of the

copropagating electron and proton population in space provides the possibility of recombination during the expansion phase. Efficient Charge recombination of protons with copropagating low energy electrons during the expansion has been reported recently [140]. In addition to this it is also possible that low energy protons may also capture extra electron from the surrounding carbon and oxygen species.

The generation of H^- ions through recombination by protons is supported by the experimental observation. In other words, experimental conditions providing relatively large population of protons result in efficient H^- ion generation. For example, PMMA is enriched in hydrogen content and provides relatively large flux of protons as compared to non-hydrogen containing targets. Additionally, PMMA is a transparent material which behaves like a plasma mirror for the incident laser pulse. The ASE pre-pulse either totally passes through the target sample or forming just an underdense plasma on the PMMA target surface. The clean interaction favours the efficient proton acceleration thereby H^- generation. Normal glass target which is also transparent but contains no hydrogen produces negligibly small population of H^- . Similarly, with solid metal targets which are both opaque and also containing no hydrogen, the H^- ion flux was very low. As evident from Fig. 6.7 that even in PMMA target the increase in laser ASE pre-pulse drastically reduces the H^- ion generation. When the ASE level is raised, it is able to form the pre-plasma on the target surface which hinders the clean interaction of the main intense laser pulse with target. This in turn dilutes the sheath field thereby reducing the proton acceleration or H^+ flux and which in turns reduces H^- generation.

Target defocusing seems to be the key for efficient H^- ion generation. In case of tight focussing condition, the hot electron temperature is expected to be quite high and therefore overlap of proton and electron population in velocity space is less likely.

That's why in this case the H^- flux is very low; close to background level. When the target is defocused, the plasma electron temperature is quite low which can favour the charge recombination of protons with copropagating electron population [140], [141]. Defocusing also leads to increase in source size which means increase in overall flux of protons and electrons albeit with lower energy. The increase in proton population due to laser defocusing results in enhancement of H^- generation.

6.2 H^- acceleration from thin foil targets

During the investigation on lighter ion acceleration from thin foil targets with 10 TW, 45 fs laser system as discussed in chapter 3, we also explored the possibility of H^- ion generation from thin foils. The experimental set up is same as described in chapter 3 section 3.1. The 10 TW, 45 fs laser pulses was focused on the thin foil targets to an intensity $\sim 2-3 \times 10^{18}$ w/cm². The ion emission was recorded along rear surface normal direction. During this experiment a 40 mm size MCP was used in TPIS in off centre geometry, therefore to detect the H^- ions, the magnetic field polarity was reversed. Fig. 6.8 (a) shows the ion signal recorded from 25 μ m thick Al foil. Parabolic traces of H^- and H^+ /protons can be clearly seen. In order to increase the overall flux reaching on the MCP detector, the TPIS pin-hole is increased to 400 micron diameter. Earlier it was observed that in case of proton acceleration with 10 TW system, Al foil of 6.5 μ m thickness was the optimum thickness, giving highest proton energy and flux. But surprisingly with Al foil of 6.5 μ m thickness or less, we could not see any detectable H^- ion signal. H^- spectrum recorded using Al foils of different thicknesses is shown in Fig. 6.8 (b). Al foil with 12.5 μ m and 25 μ m thickness seems to be some sort of optimum thickness for efficient H^- generation. Maximum H^- energy around 90 keV was observed with 25 μ m Al foil. With much higher thickness, H^- signal significantly reduces. The overall H^- signal from thin foil target was found to be relatively weaker

as observed from thick PMMA target. As the foils are quite thick, therefore there should not be any pre-plasma on target rear surface. Hence there seems to be only one possibility of H^- generation which is the recombination of protons with copropagating electrons. The hot electron population form the sheath field which accelerates ions. These hot electrons are basically confined to the sheath field potential and circulate back and forth through the foil target. This causes the lateral expansion of electron population and sheath field formation on both sides of the target. It possible that for thicker foils, the expanding electrons may get sufficiently cooled so as to provide a better chance of overlap of accelerated protons and slowed down electron populations and hence for recombination. This is just a plausible explanation of H^- ion formation based on the experimental observations. However, a detailed modelling on charge recombination is required to clearly understand underlying physics behind recombination of protons and H^- formation.

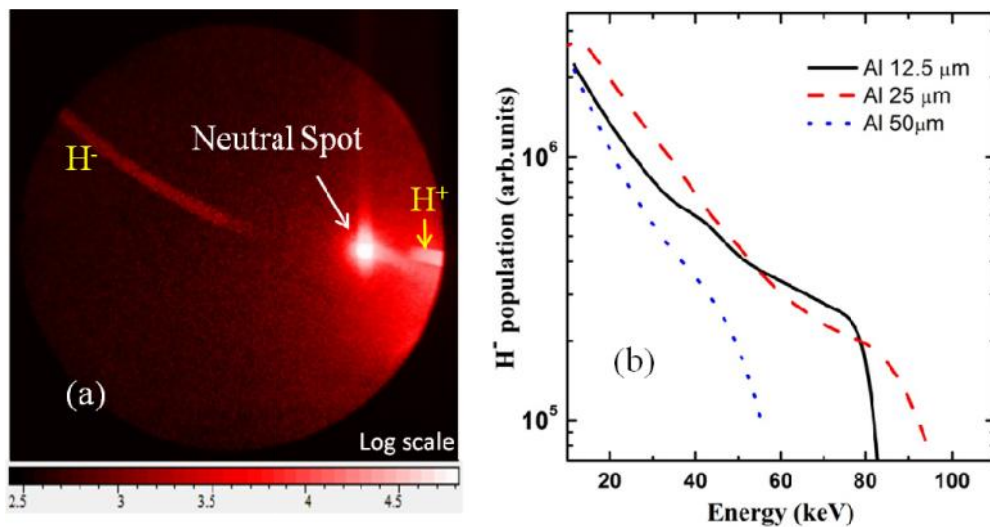


Figure 6.8: Thomson Parabola image recorded using 25 μm thick Al foil showing clear traces of H^- and H^+ . (b) H^- energy spectrum observed from Al foils of different thicknesses.

6.3 Conclusion

A new scheme on energetic (> 100 keV) H^- ion acceleration from intense, femtosecond laser pulse interaction with transparent dielectric targets have been experimentally demonstrated and explored. The method, counterintuitive to conventional H^- production mechanisms, offers low debris, high repetition rate, and consistent production of H^- ions from high density, high temperature plasma. The dependence of H^- production on the external laser focusing conditions and laser pre-pulse level indicates that H^- ions are formed due to the recombination of protons which are accelerated by the sheath field at the target surface. The accelerated H^+ while coming out of the ambient PMMA medium captures extra electrons from the co-propagating electron population to produce H^- ion. The total H^- flux estimated from CR-39 detector was found to be $\sim 10^{11}$ per shot in 4 sr. In addition H^- generation from rear surface of the thin foil was also demonstrated. The observation of H^- from thin foil targets strongly suggest that the protons (H^+) accelerated by TNSA mechanism, capture extra electrons from co-propagating electron population and become H^- .

CHAPTER 7

Applications of laser accelerated ion beam

In the recent times, there has been considerable development in high intensity laser driven ion acceleration research [3], [4]. The main motivation behind these studies is the some unparalleled characteristics owned by the laser accelerated ion beam like very low emittance [123], short pulse duration (\sim ps), and high peak current but with broad energy spectrum. The acceleration setup itself is highly compact and few 10's of MeV ion beam can be easily accelerated in few micron lengths due to very high acceleration gradient \sim few TV/m. The unique characteristics of these ion beams have been utilised in several applications like in measurement of the highly transient electric field dynamics in pico second time scale within the plasma [7] and in studies of warm dense matter [9]. Apart from this, a very important and direct practical application of laser driven ion beam could be in hadron therapy [10], [142] and in biomedical imaging applications [143]. Indeed, this has been one of the prime motivations of many laser driven ion accelerator research programmes around the globe [144]–[146].

Laser driven proton beam have been used to cause nuclear reaction in different element for producing radioisotopes [147]. Short lived radioisotopes like ^{11}C , ^{13}N and ^{18}F have important applications in medical radiography such as Positron Emission Tomography (PET) in detecting cancers. It is a non-invasive diagnostic imaging technique which measures the metabolic activity of cells in human body. Short lived positron emitting isotope is injected into the body which accumulates in tissue of interest. These isotopes produce positrons which when interacts with surrounding electrons emits characteristic 511 keV radiation which can be very precisely tracked

down or mapped. Thus it constructs the three dimensional image of the body by tracing the radioisotope that was injected in form of medicine. Conventionally, the evolution of PET produced radiation are used in conjunction with imaging techniques such as, Computer Tomography (CT) and / or Magnetic Resonance Imaging (MRI) to pinpoint the affected region. Therefore, positron emitting radio-isotopes with relatively small half-lives (typically few tens of minutes to hours) play crucial roles in this scheme. Out of these isotopes, ^{18}F is the most commonly used one with half-life of 119.7 min. However, apart from it, several other radio-isotopes have been identified for this purpose. The typical half-lives of the commonly used radio-isotopes[14], [148] and their chemical forms that are being used in clinical practice are listed in table 1 below.

Table 7.1 [149], [150]: List of isotopes used for PET application

Radioactive Nuclei	Nuclear Reaction	Half Life	Chemical Product Form
^{18}F	$^{18}\text{O}(\text{p},\text{n})^{18}\text{F}$	119.7 min	^{18}F – FDG (2-fluoro-2-deoxy-D-glucose)
^{15}O	$^{15}\text{N}(\text{p},\text{n})^{15}\text{O}$	123 sec	C^{15}O , C^{15}O_2 , H_2^{15}O
^{13}N	$^{16}\text{O}(\text{p},)^{13}\text{N}$	9.96 min	$^{13}\text{NH}_3$, ^{13}N -amino acids
^{11}C	$^{14}\text{N}(\text{p},)^{11}\text{C}$, $^{11}\text{B}(\text{p},\text{n})^{11}\text{C}$ $^{10}\text{B}(\text{d},\text{n})^{11}\text{C}$	20.34 min	^{11}CO , ^{11}C -acetate

The PET isotope have half-life few tense of minutes, therefore they need to be produced nearby the place of their use. Conventionally, ion beam from cyclotrons or linear accelerators are used to produce the PET isotope. This requires considerably large infrastructure in terms of accelerator cost and massive radiation shielding thus making it difficult to have large number of such facilities. However, in recent times with the advent of intense, ultra-short laser pulses an alternative approach has come up. The interaction of these intense, ultra-short laser pulses with thin metallic foils has been established as a routine source of MeV energy proton beams on table top [3], [4].

In this chapter, we present the experimental investigation on ^{11}C isotope production by laser accelerated proton/deuterons beam using $^{11}\text{B}(p,n)^{11}\text{C}/^{10}\text{B}(d,n)^{11}\text{C}$ reactions. Using $^{11}\text{B}(p,n)^{11}\text{C}$ reaction, an activity of 5.2 kBq per laser shot could be produced. The activity corresponds to $\sim 9 \times 10^6$ atoms of ^{11}C radioisotopes. The observed activity is the highest reported with the kind of laser system used in the present experiment. Targets containing deuterium were also used to accelerate deuterium ions to excite $^{10}\text{B}(d,n)^{11}\text{C}$ reaction. It was found that with the use of deuterium containing targets the ^{11}C isotope activity can be further enhanced.

We also discuss and present our results on proton induced fusion reaction in Boron target ($p + {}^5_1\text{B}^{11} \Rightarrow 3 \text{ }^4_2\text{He} + 8.7 \text{ MeV}$). The studies on proton-boron fusion reaction have been performed for its important application of fusion energy production [151]–[153]. The prime attraction of this fusion reaction is that the energy is released in form of α particles instead than neutrons. This scales down the problems associated with neutrons in terms of nuclear activation, radiation shielding, nuclear fuel handling and including safety. However, the conventional route namely magnetic confinement or inertial confinement fusion of achieving proton-Boron fusion is not practicable due to high plasma temperature requirement as compared to deuterium-deuterium (D-D) or deuterium-tritium (D-T) fusion reactions. In contrast, using directed energy of the proton beam the high temperature requirement for proton –boron fusion reaction can be avoided [153]. Recently, few groups have investigated this important reaction with laser accelerated proton beam using high energy and high power lasers [154], [155].

7.1 Experimental Set up

The experiment has been performed using the 150 TW (maximum power) Ti:Sa, 25 fs, laser system. For the present experiment the laser power of 85- 90 TW was used. The experimental scheme is shown in Fig. 7.1. The laser is focussed using a 30° off

axis parabolic mirror on to the target with resultant intensity $\sim 1 \times 10^{19}$ W/cm². The laser pulse duration was slightly increased to 252 fs by giving a positive chirp to enhance the accelerated ion energy as discussed in chapter 4. Aluminium (Al) 0.75 μ m, Copper (Cu) 1 μ m and Nickel (Ni) foil of 1.5 μ m thickness have been used as targets for proton acceleration. Proton/Ions are accelerated from the rear surface of thin foil which arises from hydrocarbon contaminants that are normally present at target surface. The process of ion acceleration by high intensity laser pulse is well explained by Target Normal Sheath Acceleration (TNSA) mechanism [26] and also discussed in chapter 1. For deuterium ion acceleration, the Ni 1.5 μ m target was one side coated with deuterated polyethylene CD₂. The coating thickness was around 50 nm. More than 98% enriched CD₂ foil of 8 μ m thickness was also used. Ion beams have been characterized using the developed Thomson Parabola Ion Spectrograph (TPIS). An MCP coupled with phosphor screen was used for ion detection in TPIS. An EMCCD camera is then used to capture the parabola traces forming on the phosphor screen. In this study, the CR-39 solid state nuclear track detector was also used for absolute ion flux estimation and for cross calibration of MCP-EMCCD pixel intensity counts. Radiochromic films (RCF) stacks were used to register the proton beam profile. After optimization of ion signal, a 2 mm thick, 25 \times 25 mm² size natural Boron palette with 99.9 % purity was then moved into the proton/deuteron beam path for the nuclear reaction to occur. The isotopic concentration of ¹¹B and ¹⁰B in natural Boron are 80% and 20% respectively. The generated alpha particles in p-Boron fusion reaction were detected by CR-39 detectors which were covered with Aluminium foils of varying thicknesses. The covered CR-39 sheets were kept just behind the foil target and facing the Boron palette as shown in Fig. 7.1.

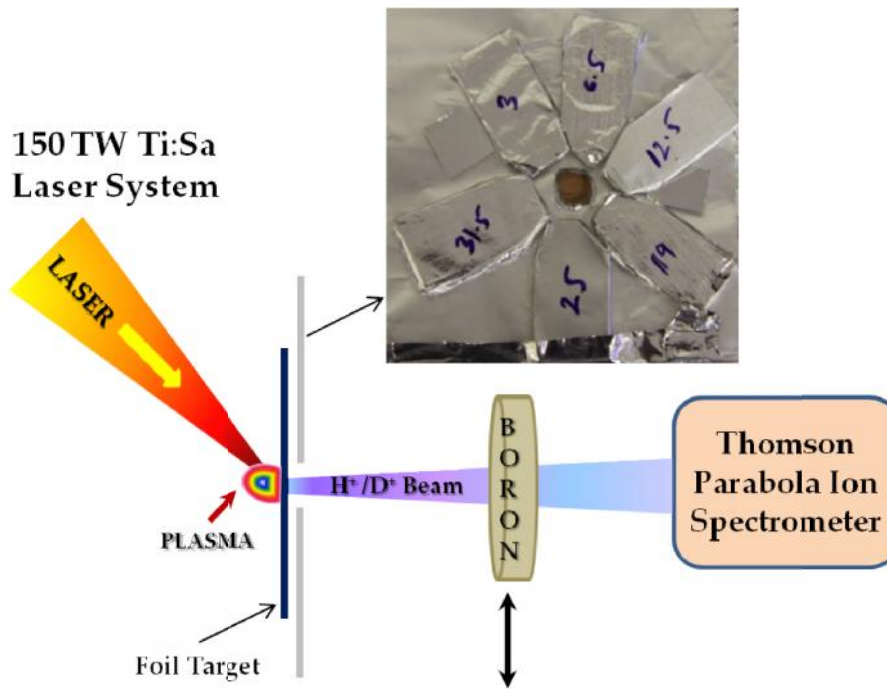


Figure 7.1: Outline of experimental set up. After optimization of ion signal the Boron pellet was moved into the beam path for the nuclear reaction to happen. A sheet of CR-39 covered with Al filters of varying thicknesses was placed for alpha particle detection is also shown.

7.2 Short lived ^{11}C PET isotope production

7.2.1 $^{11}\text{B}(p,n)^{11}\text{C}$ and $^{10}\text{B}(d,n)^{11}\text{C}$ reaction cross section

Proton and deuteron beam have been used for ^{11}C production in natural Boron target. Deuterium ions have been used mainly for the fact that energy threshold for $\text{B}(d,n)^{11}\text{C}$ reaction is low and deuterons only needs to overcome the coulomb barrier for the reaction to occur. The cross section for deuteron and proton induced reaction for ^{11}C isotope production [156], [157] is shown in Fig 7.2. The protons-Boron reaction $^{11}\text{B}(p,n)^{11}\text{C}$ has an energy threshold of about 3 MeV, which means only protons having energy higher than the threshold can induce the reaction in secondary Boron sample. However, deuterium ions with energy > 0.5 MeV are able to induce nuclear reaction in ^{10}B . In addition, the value of the reaction cross-section for $\text{B}(d,n)^{11}\text{C}$ is also higher compared to $^{11}\text{B}(p,n)^{11}\text{C}$ reaction. Hence, it is possible to efficiently utilize

the low energy deuterium ions having very high flux (due to the exponential energy profile of the TNSA accelerated ion beam) to induce nuclear reaction.

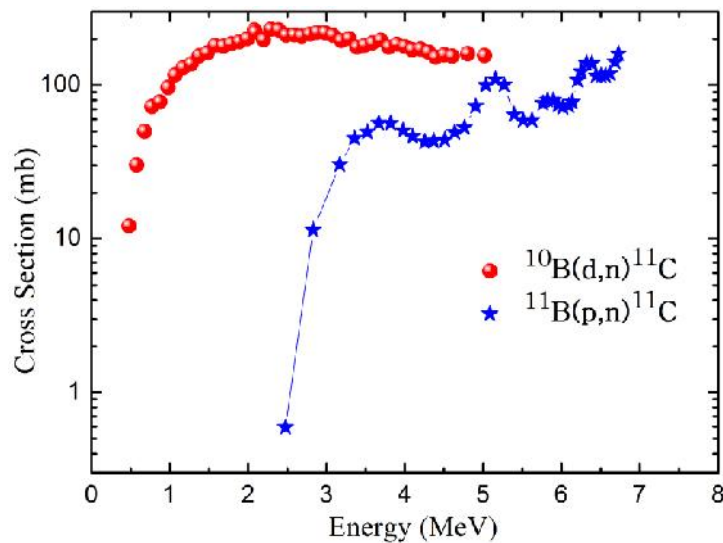


Figure 7.2: Reaction cross-section for the $^{10}\text{B}(d,n)^{11}\text{C}$ and $^{11}\text{B}(p,n)^{11}\text{C}$. taken from references [156].

7.2.2 Experimental Results on ^{11}C isotope production

Typical proton energy spectrum recorded using 1 μm thick Cu foil target is shown in Fig. 7.3 (a). The maximum proton energy observed for 0.75 μm thick Al and 1 μm thick Cu was in the range of 6-7 MeV. Proton beam profile was recorded on a stack of RCFs placed in the ion beam path at 2.5 cm distance from the foil target. The proton beam profile recorded in different layers of RCF is shown Fig. 7.3(b). The cut-off energy of every layer is also mentioned beneath the respective images. After online optimization of proton signal by observing the TPIS spectra, the Boron pellet was moved into the proton beam path. Boron pellet was placed at same distance from the foil as that for RCF i.e. at 2.5 cm. It was observed that the accelerated proton energy varies slightly on shot to shot basis, therefore for good statistics the secondary Boron target was exposed with 7-10 laser shots. The laser shot accumulation time was around 2-3 minutes. Therefore there will not be any significant reduction of ^{11}C activity during the laser shots.

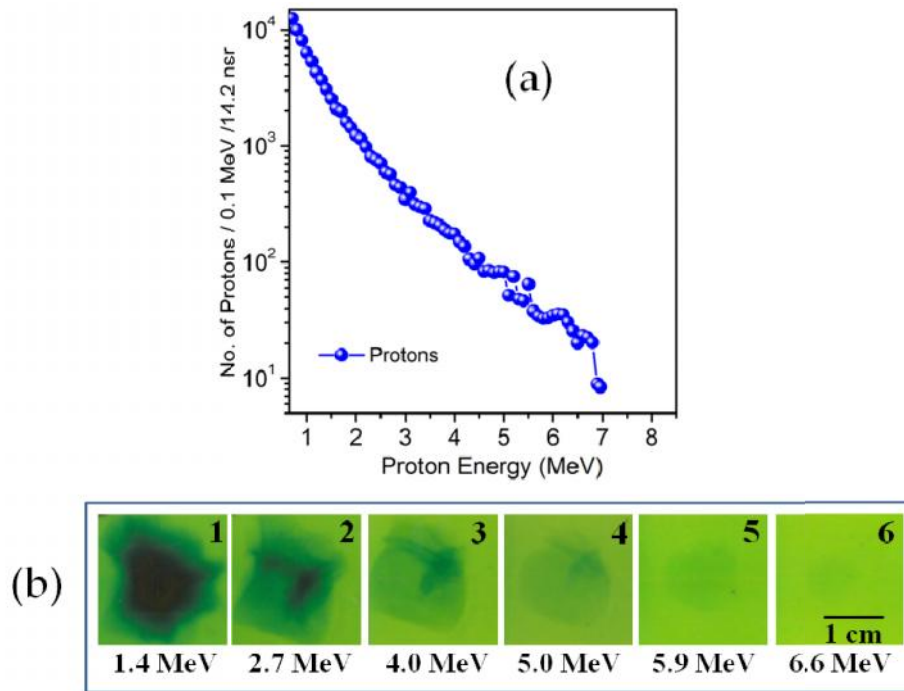


Figure 7.3 (a) Proton energy spectrum recorded using 1 μm thick Cu foil. (b) Proton beam profile recorded on different RCF layers with respective layer cut-off energies.

After irradiation with proton beam, the Boron palette was taken out from the vacuum chamber and the generated ^{11}C activity in Boron sample was measured using High Purity Germanium (HPGe) detector. The HPGe detector was pre calibrated using a standard ^{22}Na source. The decay of ^{11}C ($^{11}\text{C} \rightarrow ^{11}\text{B} + e^+ + \nu$) emits a positron (e^+) that annihilates with nearby e^- yielding two counter propagating photons each having 0.511 MeV energy. Fig. 7.4 (a) shows the photon energy spectrum recorded with HPGe detector. A pronounced peak at 511 keV energy can be easily observed which indicates significant ^{11}C isotope activity produced in the secondary Boron target. Another small peak at 1.46 MeV is attributed to decay of ^{40}K which is normally present around. To measure the half life we also recorded the ^{11}C activity at definite time intervals. The measurement is plotted in Fig. 7.4 (b). The exponential decay fit ($N=N_0 \exp^{-\lambda t}$) to the data gives the decay constant λ . The calculated half life ($T_{1/2} = 0.693 / \lambda$) was found to be 20 ± 0.4 min which is in good agreement with literature value of 20.3 min. In order to estimate the activity of ^{11}C isotope

immediately after shot accumulation; the detector's efficiency at 511 keV photon, solid angle subtended on the detector and elapsed time after the laser shots till the first measurement have to be taken into consideration. At photon energy of 511 keV, the detection efficiency of HPGe detector was measured to be 1.36%. Many experimental runs were carried out using different foil targets and the ^{11}C isotope activity was measured. The highest activity of about 5.2 kBq/shot that corresponds to $\sim 9 \times 10^6$ atoms of ^{11}C isotopes was obtained for 1 μm Cu target. Likewise for 0.75 μm Al target, the generated activity was measured to be ~ 4 kBq in a single laser shot.

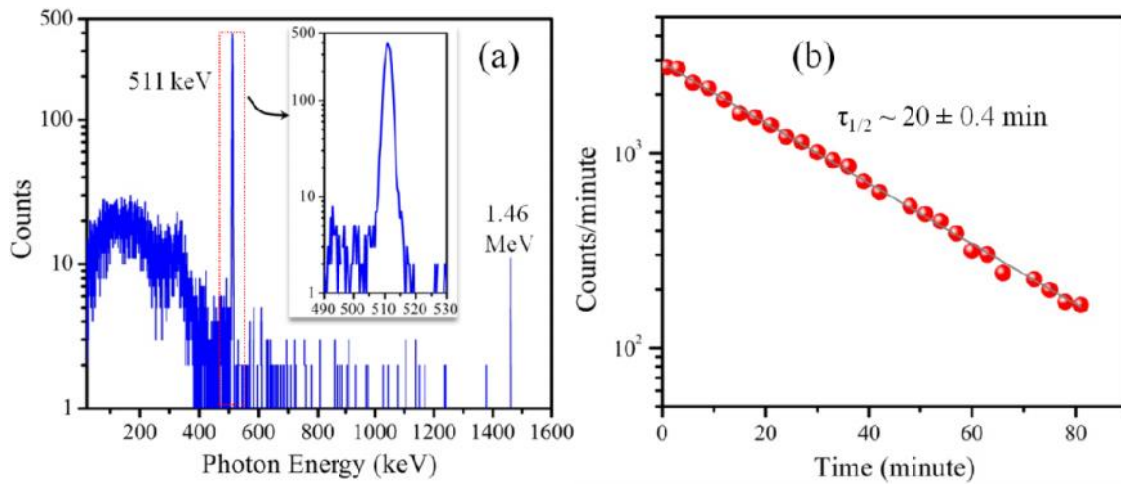


Figure 7.4: (a) Photon energy spectrum recorded with HPGe detector. The measured ^{11}C activity at definite time intervals is shown in (b). The grey line is the theoretical fit.

To study the ^{11}C isotope production using laser accelerated deuteron beam employing $^{10}\text{B}(\text{d},\text{n})^{11}\text{C}$ reaction, deuterated foil targets have been used. Fig. 7.5 (a) shows the TPIS signal recorded with 1.5 μm Ni target having CD_2 coating at its rear surface henceforth referred as 1.5 μm Ni/ CD_2 . TPIS signal recorded using plain 1.5 μm Ni target is shown in Fig. 7.5 (b). Also note that deuterium (D^+) and C^{6+} both have same charge to mass (q/m) ratio ($= 0.5$), hence they will fall on the same parabola trace. By looking at TPIS signal from 1.5 μm Ni target (Fig. 7.5 (b)), one can see that the flux of C^{6+} is quite small. At the same time, the signal from 1.5 μm Ni/ CD_2 target shows a

strong trace at $q/m = 0.5$ parabola that is primarily because to deuterons (D^+). Apart from this D^+ and C^{6+} ions can be easily distinguished in CR-39 detector by their track (pit) characteristics and hence are easily counted. The track size of D^+ is much smaller as compared to C^{6+} . Fig 7.5 (c) shows microscopical view of the $q/m = 0.5$ parabola recorded on CR-39 detector displaying tracks of C^{6+} and D^+ ions. It is evident that the C^{6+} ion flux is negligibly low as compared to D^+ ion flux. The proton (H^+) and D^+ energy spectrum recorded from 1.5 μm Ni/ CD_2 target is shown in Fig. 7.5 (d). The proton energy spectrum observed from bare 1.5 μm Ni target is also plotted in Fig. 7.5 (d). The first thing to note from the above measurement is that the proton flux observed from both Ni/ CD_2 and bare Ni targets is nearly same. The second point is that proton signal is still dominant in Ni/ CD_2 target. The Proton flux is about one order higher as compared to D^+ flux. The hydrocarbon contaminants presence on CD_2 coated surface has impeded the D^+ acceleration. This is a well known distinctive feature of TNSA. The sheath field at target rear side first accelerates the ions present in outermost contamination layer which are mostly hydrogen and D^+ acceleration gets inhibited. Once the hydrogen rich layer gets depleted, the D^+ ions in CD_2 coating layer are also quickly accelerated in the sheath field.

The generated ion beams from the 1.5 μm Ni and 1.5 μm Ni/ CD_2 targets are then impacted on secondary Boron sample containing 80% ^{11}B and 20% of ^{10}B for ^{11}C isotope production. The protons reacts with ^{11}B to generate ^{11}C via $^{11}\text{B}(p,n)^{11}\text{C}$ reaction and similarly deuterium reacts with ^{10}B to generate ^{11}C via $^{10}\text{B}(d,n)^{11}\text{C}$ reaction. In case of bare (without CD_2 coating) 1.5 μm Ni foil, the recorded ^{11}C isotope activity was 1.7 kBq/shot. The observed activity in this case is lower than that observed with 0.75 μm Al and 1 μm Cu target because of the lower protons energies. At the same time, the measured activity employing 1.5 μm Ni/ CD_2 target was found

to be 2.2 kBq which is 30% higher as compared to bare 1.5 μm Ni foil target. Since the observed proton energy spectrum is similar for both the targets, hence it is very apparent that the additional contribution in ^{11}C isotope activity is attributed to $^{10}\text{B}(\text{d},\text{n})^{11}\text{C}$ reaction.

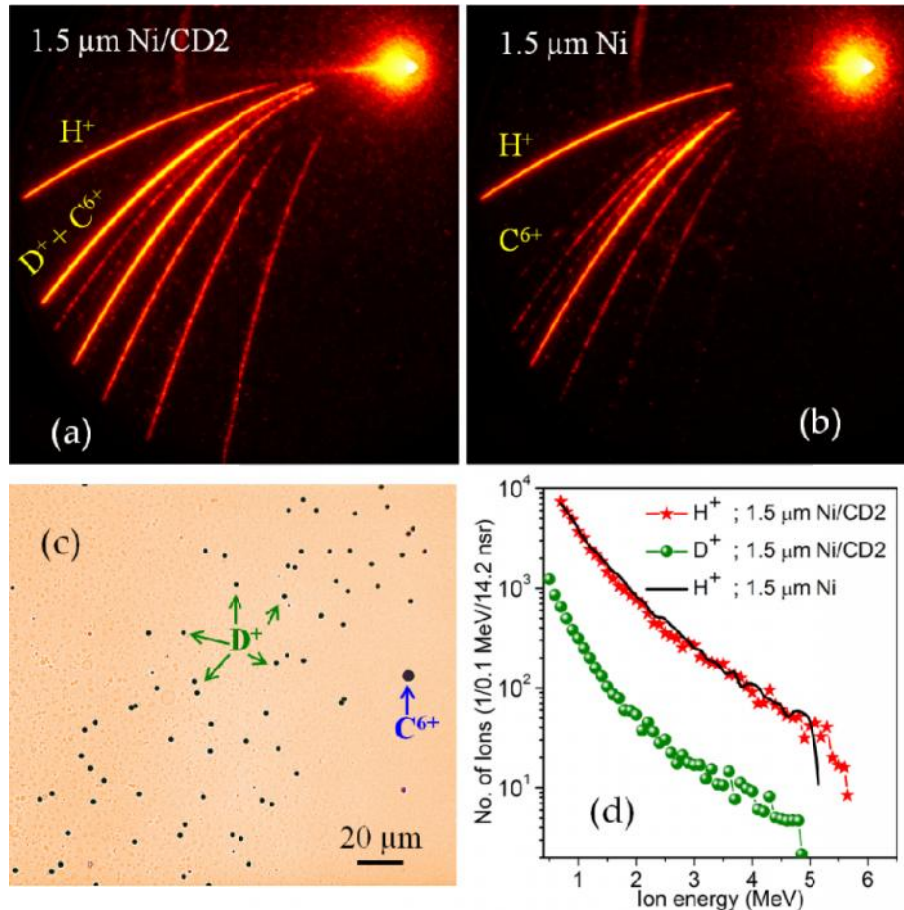


Figure 7.5: TPIS images showing ion signal recorded using (a) 1.5 μm Ni/CD₂ target and (b) from 1.5 μm Ni targets. (c) Microscope view of $q/m = 0.5$ parabola trace recorded on CR-39 detector depicting individual D⁺ and C⁶⁺ ion tracks. (d) Plotted proton (H⁺) and deuteron (D⁺) ion energy spectrum for both the targets.

Intriguing results had been observed while using 8 μm CD₂ target in respect of $^{10}\text{B}(\text{d},\text{n})^{11}\text{C}$ reaction. The ion signal recorded from 8 μm CD₂ target using TPIS detector is shown in Fig. 7.6 (a). As observed with deuterated Ni target, both proton (H⁺) and D⁺ are present. The derived proton energy spectrum is shown in Fig. 7.6 (c). It was observed that with this target the protons maximum energy cut-off was just about 3 MeV which is merely the threshold of $^{11}\text{B}(\text{p},\text{n})^{11}\text{C}$ reaction. Therefore,

primary contribution in generation of ^{11}C isotope should be from $^{10}\text{B}(\text{d},\text{n})^{11}\text{C}$ reaction. Now, we had also used 8 μm thick Mylar target to find out any possible contribution of the $^{11}\text{B}(\text{p},\text{n})^{11}\text{C}$ reaction in ^{11}C isotope generation. The typical signal captured using TPIS with 8 μm Mylar target and derived proton energy spectrum is shown in Fig. 7.6 (b) and (c) respectively.

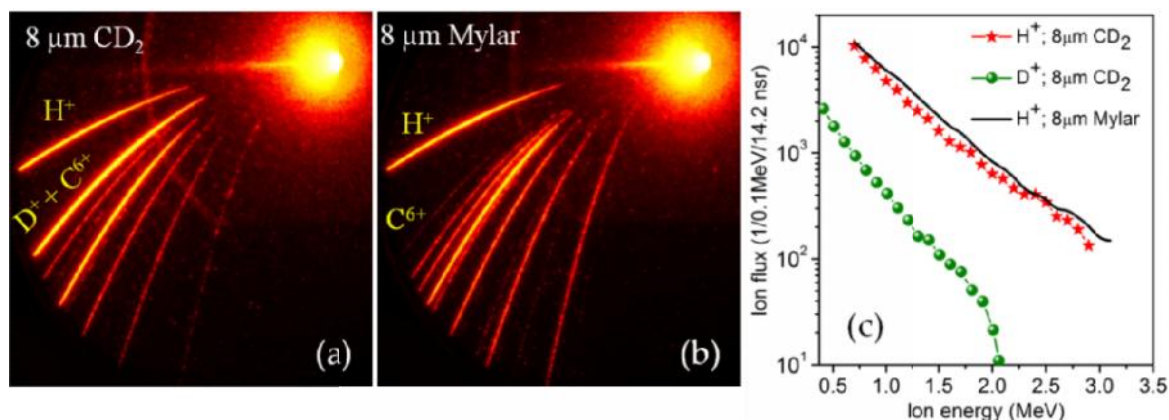


Figure 7.6: Recorded ion signal from (a) from 8 μm CD_2 and (b) 8 μm Mylar targets. Plotted proton (H^+) and deuterium (D^+) ion energy spectrum for both the targets (c).

The proton energy spectra obtained from 8 μm Mylar target 8 μm CD_2 target are almost similar. Both the targets have been used in the study of ^{11}C isotope generation. The observed ^{11}C isotope activity for 8 μm thick CD_2 and 8 μm Mylar target was 424 Bq and 37 Bq per laser shot respectively. Therefore, it is quite apparent that the major contribution in ^{11}C isotope production is because of $^{10}\text{B}(\text{d},\text{n})^{11}\text{C}$ reaction channel employing deuterium ions which is in conformity with the cross-section data. Here, it should also be noted that ^{10}B percentage abundance in natural Boron sample is only around 20%. This means use of ^{10}B enriched catcher targets could enhance the ^{11}C isotope generation by at least four times while using CD_2 target for ion generation.

7.2.3 Discussion

The present experimental investigation was motivated by previously reported works [157], [158] suggesting efficient ^{11}C isotope production employing D^+ ions. The

reasoning behind this is the low reaction threshold of the $^{10}\text{B}(\text{d},\text{n})^{11}\text{C}$ reaction as well as relatively higher flux of 0.5 MeV D^+ ions as compared to 3 MeV H^+ ions. On the present experimental investigation some important inferences can be made. In case of $^{11}\text{B}(\text{p},\text{n})^{11}\text{C}$ reaction, the targets producing higher flux of protons of more than 3 MeV (reaction threshold for $^{11}\text{B}(\text{p},\text{n})^{11}\text{C}$) generates highest isotope activity. Significant enhancement in ^{11}C isotope activity through $^{10}\text{B}(\text{d},\text{n})^{11}\text{C}$ reaction was observed while using deuterated targets. A rough estimate of ^{11}C isotope generation (N) can be made by using $N = N_i \cdot (E_i) \cdot n \cdot d_i$ formula. Where, N_i is the useful ion flux at particular energy, (E_i) is the reaction cross section, n and d_i is the density and thickness of the Boron target respectively. Target thickness is actually the range of ions (protons, deuterons) in Boron target. The density of Boron target is $n = 1.3 \times 10^{23}$ atoms per cm^3 . The total integrated proton flux with energy > 3 MeV was measured to be 7.8×10^{10} . To find out the total reactions, the integration was performed in 1 MeV energy bins and mean cross-section in that energy bin was used. The protons/deuteron range in Boron target was estimated using SRIM software [159]. Therefore as per the above described procedure, the isotopic yield of ^{11}C in $^{11}\text{B}(\text{p},\text{n})^{11}\text{C}$ reaction for 1 μm thick Cu target comes out to be 4.3×10^6 / laser shot. This corresponds to 2.4 kBq activity of ^{11}C isotope. Similarly yield estimation for $^{10}\text{B}(\text{d},\text{n})^{11}\text{C}$ reaction for 8 μm thick CD_2 target gives the ^{11}C isotope activity of 380 Bq. Here, it was assumed that deuteron beam have similar divergence as that of proton beam in calculating the total deuteron flux. The simple estimates on isotope generation both for proton and deuteron beam are in fair agreement with the experimentally observed values discussed earlier.

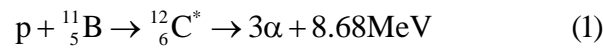
Although, the highest activity of 5.2 kBq was achieved from 1 μm thick Cu target employing $^{11}\text{B}(\text{p},\text{n})^{11}\text{C}$ reaction. It is still far less than needed value $\sim 1\text{GBq}$ for

actual PET application. Even if the current laser system is operated at maximum repetition rate of 5 Hz, the maximum generated activity could be in the range of 10^4 Bq. Hence, for actual application as a PET isotope one requires proton beam with much higher average flux. This is possible only with much higher repetition rate (100Hz – 1 kHz) as well as high power laser system. Considering the developments presently appearing in laser technology [160–162] it looks quite viable in near future. Further, employing low energy deuteron beam, the production of ^{11}C isotope can be significantly increased. This would be possible in concurrence with the use of enriched ^{10}B that is commercially available and with enhanced the deuterium ion acceleration by removing the hydrocarbon contaminants from the CD_2 foil. As described above, if we assume deuterium ion flux as that of protons ($\sim 3 \times 10^{12}$ upto 2 MeV) and ^{10}B enriched (90%) target, around 1.7×10^4 Bq activities can be produced per laser shot. Furthermore, since the demand on maximum accelerated ion energy is subdued, even the already demonstrated 9.5 TW, 23fs at 100 Hz [162] laser can give 1.7 GBq in 1000 seconds. Enhanced deuterium ion acceleration by controlling the contaminants with online deuterium deposition have been discussed in few reports [163]–[166]. Morision *et al.* [164] have shown efficient exclusive deuterium ion acceleration from the online deposited deuterium layer on the rear side of thin a foil. There is a recent report by Maksimchuk *et al.* [166], where similar acceleration technique have been used for accelerating deuterium ions and utilized them for isotope generation and neutron production. To generate the required ion beam at high repetition rate, a tape target enriched with deuterium was developed by Fujimoto *et al.* [167]. Positron emitting isotopes were produced employing deuterium ions, which were accelerated in the interaction of 33 fs, 70 TW laser pulses with deuterium loaded tape target at 10 Hz repetition rate. The generated isotope activity was quite small;

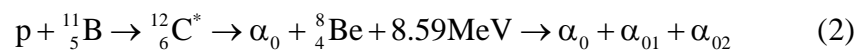
about 153 Bq in 2000 laser shots. The reason for quite low activity in their study appears to be linked with higher thickness of tape target (75 μm) in the experiment. Similar deuterated tape target but smaller thicknesses (few microns) is anticipated to be more reasonable for repetitive deuteron beam generation.

7.3 Proton-B fusion Reaction; $\text{B}^{11}(\text{p}, 3\alpha)$, (Q= 8.7 MeV)

Next, I will discuss the other aspect of the experiment i.e. study of aneutronic fusion reaction using high intensity laser accelerated proton beam. The accelerated protons from thin foil target when directed on to the secondary Boron target can also cause fusion reaction in Boron sample. In Proton-Boron fusion reaction three alpha particles are produced and several MeV energy is released in from their kinetic energy ($\text{p} + {}_5\text{B}^{11} \Rightarrow 3\alpha + 8.7 \text{ MeV}$). There are three different channels of this reaction [167], [168]. The reaction can proceed in a single step, directly emitting 3 α particles having continuous energy distribution.



The reaction can also proceed as a sequential decay via formation of ${}_4^8\text{Be}$.



The primary α particles (α_0, α_1) have well defined energies. The secondary α particles resulting from subsequent decay of ${}_4^8\text{Be}$ have continuous energy distribution. The probability for production of α_0 with ${}_4^8\text{Be}$ in ground state is very small. The dominant channel is α_1 plus excited state of ${}_4^8\text{Be}^*$ which results in α particles with energies in the range of 3-4 MeV. At proton energy of 0.67 MeV the reaction cross-section is maximum and has well pronounced peak. It is widely known that TNSA accelerated

proton beam exhibit exponential energy distribution and as a result low energy protons flux is few orders of magnitude higher as compared to proton flux near cut-off energies (Fig. 7.3 (b)). Hence, it is expected that laser accelerated proton beam can initiate large number of fusion reaction in Boron target. The alpha particles produced in p-B fusion reaction were measured using CR-39 detector. The CR-39 sheet was covered with Al foils of varying thickness (3, 6.5, 12.5, 19, 25 and 31.5 μ m) to extract the alpha particle energy spectrum. The varying filter thickness sets different cut-off energy for the alpha particles. For better statistics and to average out the shot to shot fluctuations, 20 laser shots were accumulated on CR-39 detector. The exposed CR-39 was etched in concentrated, hot NaOH solution for 4 hrs. The developed alpha tracks in CR-39 then read out in optical microscope based track analysis scanner. Alpha particles track observed in CR-39 detector is shown in Fig. 7.7. The CR-39 pieces shown in Fig. 7.7 (a) and (b) were covered with 6.5 μ m and 12.5 μ m Al filters with corresponding alpha particles cut-off energies around 2 MeV and 3.5 MeV respectively. One needs to be careful while counting the alpha particles because the accelerated ion beam while hitting the Boron target, some proton and Carbon ions may get scattered and registered on CR-39 detector. Although the Carbon ions upto 8 MeV energy would be stopped with Al filter of 6.5 μ m thickness, protons can still get across all the used filters and registered in the CR-39 detector. However, the protons track diameter are relatively small and hence are easily differentiated from alpha particles tracks as shown in Fig. 7.7. We estimated the alpha particle yield (having energy > 2 MeV) to be $\sim 1.7 \times 10^7$ in single laser shot in 4 ns by the observed tracks on CR-39 detector. Similar rough estimate as made earlier for isotope yield can also be made for p-B fusion yield using the relation $N = N_p \cdot (E_i) \cdot n \cdot d$ and employing the cross section data available in literature (inset Fig.7.8 (b)). Here d is the range of

protons in secondary Boron target and was estimated with SRIM [159] software. The total fusion yield in single laser shot is calculated to be $\sim 4 \times 10^8$ in 4 sr. This simple estimate comes out to be one order higher than observed experimentally. The reason behind this large deviation is primarily because of the small range of alpha particles in Boron target in comparison to protons as given in Table 2. Hence, particles which are produced beyond a certain depth inside the solid Boron sample cannot come out.

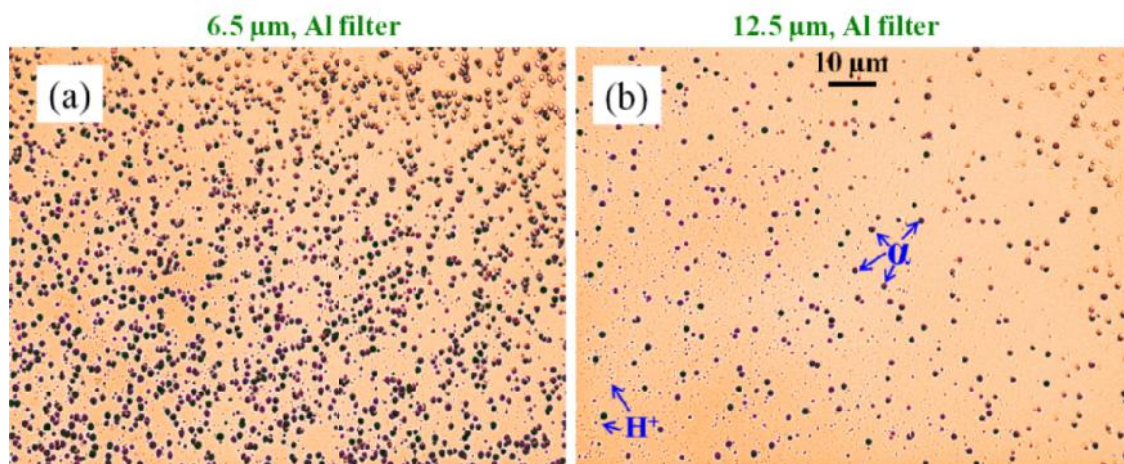


Figure 7.7: Alpha particles track observed on CR-39 detector covered with (a) 6.5 μm Al filter and (b) 12.5 μm Al filter. Very small tracks are due to scattered protons

Table 7.2: Range of protons and alpha particles (in microns) in solid Boron.

Energy	0.5MeV	1MeV	2MeV	3MeV	4MeV	5MeV	6MeV	7MeV
Proton	4.39	12.58	38.70	76.32	124.72	183.43	252.16	330.63
α particle	1.34	2.40	5.02	8.46	12.73	17.83	23.75	30.48

The energy spectrum of α -particles extracted using Al filters of different cut-off energy is plotted in Fig. 7.8. The error bars in Fig. 7.8 are due to the energy bin dictated by two successive energy filters and typical observed error in track counting respectively. The alpha energy spectrum shows a peak around 3 MeV. The observed α -particle spectrum grossly agrees with p-Boron fusion spectrum reported in literature [164]. The energy distribution of α -particles can have multiple peaks depending on the reaction channel as described above. Peak at 3-4 MeV range is attributed to the

formation of excited nucleus ${}^8\text{Be}^*$ in intermediate step and its consequent decay into two α particles (${}^8\text{Be}^* \rightarrow 2\alpha$). As majority of p-B fusion reaction is taking place within the Boron sample, therefore α particles energy spectrum is likely to be altered due to their stopping in the target.

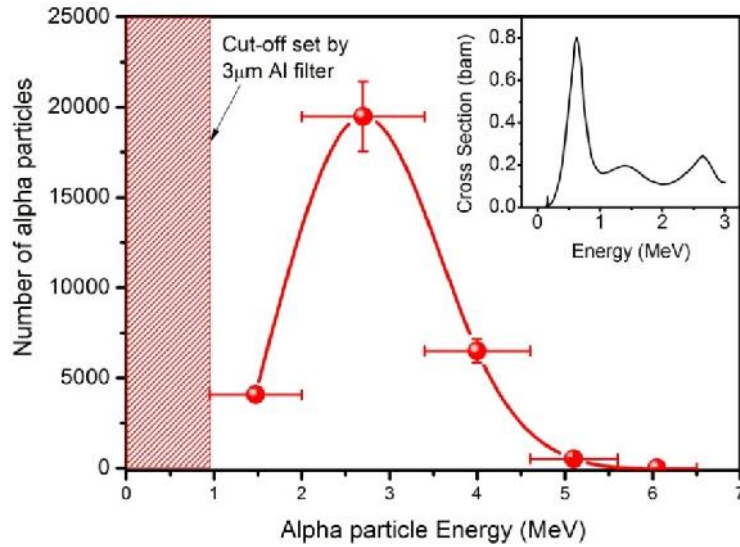


Figure 7.8: Extracted alpha particle energy spectrum (alpha particles count are given for a scan area of 1mm^2 on CR-39). Inset shows fusion cross section data [156].

7.4 Conclusion

Experimental investigations on nuclear reactions using intense, ultra-short laser accelerated proton and deuteron beam with a potential for societal benefits have been performed. The ${}^{11}\text{C}$ radio-isotope generation utilizing laser produced deuteron and protons beams was studied via ${}^{10}\text{B}(d, n){}^{11}\text{C}$ and ${}^{11}\text{B}(p, n){}^{11}\text{C}$ reactions respectively. We observed maximum activity of 5.2 kBq of ${}^{11}\text{C}$ in single laser shot employing ${}^{11}\text{B}(p, n){}^{11}\text{C}$ reaction that corresponds to $\sim 9 \times 10^6$ atoms of radioactive isotopes. It was also established that foil targets loaded with deuterium can increase the radio isotope production. In this regards around 30% increase in ${}^{11}\text{C}$ production was demonstrated employing $1.5\ \mu\text{m}$ Ni/ CD_2 target as compared to bare $1.5\ \mu\text{m}$ Ni target. It was argued that because of the relatively low deuteron energy threshold for ${}^{10}\text{B}(d, n){}^{11}\text{C}$ reaction, even the low energy part of the accelerated deuterons of the exponential spectrum can

be used for efficient ^{11}C production. Next, it was also found that exclusive deuterium ion acceleration in laser foil interaction have brighter prospect for producing practicable amount of ^{11}C isotope. It is estimated that with the kind laser developed by R. Clady et. al. [161] which is operating at 100 Hz with 9.5 TW peak power at 23 fs, the generated isotope activity can reach to GBq range in ~ 15 minutes. This looks possible once the laser systems with high repetition rate and high peak power become commercially available. The α -particles produced in fusion reaction involving proton and boron were also characterized. More than 10^7 particles in single laser shot have been observed. The present work shows that laser driven proton beam can be useful in studying many important reactions such as p-B fusion reaction which is quite promising for futuristic power generation [153].

REFERENCES:

- [1] “Reviews of Accelerator Science and Technology” edited by A. W. Chao and W. Chou, *World Scientific, Singapore*, **2009**
- [2] “Industrial Accelerators and Their Applications”, edited by R. W. Hamm and M. E. Hamm, *World Scientific Singapore*, **2012**
- [3] “Ion acceleration by superintense laser-plasma interaction,” A. Macchi, M. Borghesi, and M. Passoni, *Rev. Mod. Phys.*, **2013**, *85*, 751–793.
- [4] “Review of laser-driven ion sources and their applications,” H. Daido, M. Nishiuchi, and A. S. Pirozhkov, *Rep. Prog. Phys.*, **2012**, *75*, 056401.
- [5] “Proton Radiography of a Laser-Driven Implosion,” A. J. Mackinnon, P. K. Patel, M. Borghesi, R. C. Clarke, R. R. Freeman, H. Habara, S. P. Hatchett, D. Hey, D. G. Hicks, S. Kar, M. H. Key, J. A. King, K. Lancaster, D. Neely, A. Nikkro, P. A. Norreys, M. M. Notley, T. W. Phillips, L. Romagnani, R. A. Snavely, R. B. Stephens, and R. P. J. Town, *Phys. Rev. Lett.*, **2006**, *97*, 045001.
- [6] “Using high-intensity laser-generated energetic protons to radiograph directly driven implosions,” A. B. Zylstra, C. K. Li, H. G. Rinderknecht, F. H. Séguin, R. D. Petrasso, C. Stoeckl, D. D. Meyerhofer, P. Nilson, T. C. Sangster, S. Le Pape, A. Mackinnon, and P. Patel, *Review of Scientific Instruments*, **2012**, *83*, 013511.
- [7] “Measurement of highly transient electrical charging following high-intensity laser–solid interaction,” M. Borghesi, L. Romagnani, A. Schiavi, D. H. Campbell, M. G. Haines, O. Willi, A. J. Mackinnon, M. Galimberti, L. Gizzi, R. J. Clarke, and S. Hawkes, *Applied Physics Letters*, **2003**, *82*, 1529.
- [8] “Proton radiography as an electromagnetic field and density perturbation diagnostic (invited),” A. J. Mackinnon, P. K. Patel, R. P. Town, M. J. Edwards, T. Phillips, S. C. Lerner, D. W. Price, D. Hicks, M. H. Key, S. Hatchett, S. C. Wilks, M. Borghesi, L. Romagnani, S. Kar, T. Toncian, G. Pretzler, O. Willi, M. Koenig, E. Martinolli, S. Lepape, A. Benuzzi-Mounaix, P. Audebert, J. C. Gauthier, J. King, R. Snavely, R. R. Freeman, and T. Boehlly, *Review of Scientific Instruments*, **2004**, *75*, 3531–3536.
- [9] “Isochoric Heating of Solid-Density Matter with an Ultrafast Proton Beam,” P. K. Patel, A. J. Mackinnon, M. H. Key, T. E. Cowan, M. E. Ford, M. Allen, D. F. Price, H. Ruhl, P. T. Springer, and R. Stephens, *Phys. Rev. Lett.*, **2003**, *91*, 125004.

- [10] “Towards ion beam therapy based on laser plasma accelerators,” L. Karsch, E. Beyreuther, W. Enghardt, M. Gotz, U. Masood, U. Schramm, K. Zeil, and J. Pawelke, *Acta Oncologica*, **2017**, *56*, 1359–1366.
- [11] “Development of a laser-driven proton accelerator for cancer therapy,” C.-M. Ma, I. Veltchev, E. Fourkal, J. S. Li, W. Luo, J. Fan, T. Lin, and A. Pollack, *Laser Phys.*, **2006**, *16*, 639–646.
- [12] “What will it take for laser driven proton accelerators to be applied to tumor therapy?,” U. Linz and J. Alonso, *Phys. Rev. ST Accel. Beams*, **2007**, *10*, 094801.
- [13] “Practicability of protontherapy using compact laser systems,” V. Malka, S. Fritzler, E. Lefebvre, E. d’Humières, R. Ferrand, G. Grillon, C. Albaret, S. Meyroneinc, J.-P. Chambaret, A. Antonetti, and D. Hulin, *Medical Physics*, **2004**, *31*, 1587–1592.
- [14] “High-Power Laser Production of PET Isotopes,” in *Lasers and Nuclei: Applications of Ultrahigh Intensity Lasers in Nuclear Science*, H. Schwoerer, B. Beleites, and J. MagillEds., Berlin, Heidelberg: Springer Berlin Heidelberg, 2006, 191–203.
- [15] “Fast Ignition by Intense Laser-Accelerated Proton Beams,” M. Roth, T. E. Cowan, M. H. Key, S. P. Hatchett, C. Brown, W. Fountain, J. Johnson, D. M. Pennington, R. A. Snavely, S. C. Wilks, K. Yasuike, H. Ruhl, F. Pegoraro, S. V. Bulanov, E. M. Campbell, M. D. Perry, and H. Powell, *Phys. Rev. Lett.*, **2001**, *86*, 436–439.
- [16] “A first analysis of fast ignition of precompressed ICF fuel by laser-accelerated protons,” S. Atzeni, M. Temporal, and J. J. Honrubia, *Nucl. Fusion*, **2002**, *42*, L1–L4.
- [17] “High-Energy Ion Expansion in Laser-Plasma Interactions,” R. Decoste and B. H. Ripin, *Phys. Rev. Lett.*, **1978**, *40*, 34–37.
- [18] “60-fsec pulse generation from a self-mode-locked Ti:sapphire laser,” D. E. Spence, P. N. Kean, and W. Sibbett, *Opt. Lett.*, *OL*, **1991**, *16*, 42–44.
- [19] “Compression of amplified chirped optical pulses,” D. Strickland and G. Mourou, *Optics Communications*, **1985**, *56*, 219–221.
- [20] “Energetic Heavy-Ion and Proton Generation from Ultraintense Laser-Plasma Interactions with Solids,” E. L. Clark, K. Krushelnick, M. Zepf, F. N. Beg, M. Tatarakis, A. Machacek, M. I. K. Santala, I. Watts, P. A. Norreys, and A. E. Dangor, *Phys. Rev. Lett.*, **2000**, *85*, 1654–1657.
- [21] “Multi-MeV Ion Production from High-Intensity Laser Interactions with Underdense Plasmas,” K. Krushelnick, E. L. Clark, Z. Najmudin, M. Salvati, M. I. K. Santala, M. Tatarakis, A. E. Dangor, V. Malka, D. Neely, R. Allott, and C. Danson, *Phys. Rev. Lett.*, **1999**, *83*, 737–740.

- [22] “High-energy ions produced in explosions of superheated atomic clusters,” T. Ditmire, J. W. G. Tisch, E. Springate, M. B. Mason, N. Hay, R. A. Smith, J. Marangos, and M. H. R. Hutchinson, *Nature*, **1997**, 386, 54.
- [23] “Intense High-Energy Proton Beams from Petawatt-Laser Irradiation of Solids,” R. A. Snavely, M. H. Key, S. P. Hatchett, T. E. Cowan, M. Roth, T. W. Phillips, M. A. Stoyer, E. A. Henry, T. C. Sangster, M. S. Singh, S. C. Wilks, A. MacKinnon, A. Offenberger, D. M. Pennington, K. Yasuike, A. B. Langdon, B. F. Lasinski, J. Johnson, M. D. Perry, and E. M. Campbell, *Phys. Rev. Lett.*, **2000**, 85, 2945–2948.
- [24] “Forward Ion Acceleration in Thin Films Driven by a High-Intensity Laser,” A. Maksimchuk, S. Gu, K. Flippo, D. Umstadter, and V. Yu. Bychenkov, *Phys. Rev. Lett.*, **2000**, 84, 4108–4111.
- [25] “Measurements of Energetic Proton Transport through Magnetized Plasma from Intense Laser Interactions with Solids,” E. L. Clark, K. Krushelnick, J. R. Davies, M. Zepf, M. Tatarakis, F. N. Beg, A. Machacek, P. A. Norreys, M. I. K. Santala, I. Watts, and A. E. Dangor, *Phys. Rev. Lett.*, **2000**, 84, 670–673.
- [26] “Energetic proton generation in ultra-intense laser–solid interactions,” S. C. Wilks, A. B. Langdon, T. E. Cowan, M. Roth, M. Singh, S. Hatchett, M. H. Key, D. Pennington, A. MacKinnon, and R. A. Snavely, *Physics of Plasmas*, **2001**, 8, 542–549.
- [27] “Laser-plasma acceleration of quasi-monoenergetic protons from microstructured targets,” H. Schworer, S. Pfoth, O. Jäckel, K.-U. Amthor, B. Liesfeld, W. Ziegler, R. Sauerbrey, K. W. D. Ledingham, and T. Esirkepov, *Nature*, **2006**, 439, 445.
- [28] “Laser acceleration of quasi-monoenergetic MeV ion beams,” B. M. Hegelich, B. J. Albright, J. Cobble, K. Flippo, S. Letzring, M. Paffett, H. Ruhl, J. Schreiber, R. K. Schulze, and J. C. Fernández, *Nature*, **2006**, 439, 441.
- [29] “Maximum Proton Energy above 85 MeV from the Relativistic Interaction of Laser Pulses with Micrometer Thick CH₂ Targets,” F. Wagner, O. Deppert, C. Brabetz, P. Fiala, A. Kleinschmidt, P. Poth, V. A. Schanz, A. Tebartz, B. Zielbauer, M. Roth, T. Stöhlker, and V. Bagnoud, *Phys. Rev. Lett.*, **2016**, 116, 205002.
- [30] “Highly Efficient Relativistic-Ion Generation in the Laser-Piston Regime,” T. Esirkepov, M. Borghesi, S. V. Bulanov, G. Mourou, and T. Tajima, *Phys. Rev. Lett.*, **2004**, 92, 175003.
- [31] ““Light Sail” Acceleration Reexamined,” A. Macchi, S. Veghini, and F. Pegoraro, *Phys. Rev. Lett.*, **2009**, 103, 085003.

- [32] “Proton Shock Acceleration in Laser-Plasma Interactions,” L. O. Silva, M. Marti, J. R. Davies, R. A. Fonseca, C. Ren, F. S. Tsung, and W. B. Mori, *Phys. Rev. Lett.*, **2004**, 92, 015002.
- [33] “Collisionless shocks in laser-produced plasma generate monoenergetic high-energy proton beams,” D. Haberberger, S. Tochitsky, F. Fiuza, C. Gong, R. A. Fonseca, L. O. Silva, W. B. Mori, and C. Joshi, *Nature Physics*, **2012**, 8, 95–99.
- [34] “Monoenergetic and GeV ion acceleration from the laser breakout afterburner using ultrathin targets,” L. Yin, B. J. Albright, B. M. Hegelich, K. J. Bowers, K. A. Flippo, T. J. T. Kwan, and J. C. Fernández, *Physics of Plasmas*, **2007**, 14, 056706.
- [35] “*The Interaction of High-Power Lasers with Plasmas*”, Shalom Elizer, *Institute of Physics Publishing*, **2002**.
- [36] “The Physics Of Laser Plasma Interactions”, William L. Kruer, *CRC Press*, **2019**
- [37] “Short Pulse Laser Interactions with Matter.”, Paul Gibbon, *Imperial College Press*, **2005**
- [38] “Absorption of ultrashort, ultra-intense laser light by solids and overdense plasmas,” S. C. Wilks and W. L. Kruer, *IEEE Journal of Quantum Electronics*, **1997**, 33, 1954–1968.
- [39] “Not-so-resonant, resonant absorption,” F. Brunel, *Phys. Rev. Lett.*, **1987**, 59, 52–55.
- [40] “Wave breaking and absorption efficiency for short pulse p-polarized laser light in a very steep density gradient,” S. Kato, B. Bhattacharyya, A. Nishiguchi, and K. Mima, *Physics of Fluids B: Plasma Physics*, **1993**, 5, 564–570.
- [41] “Electron Acceleration in Cavitated Channels Formed by a Petawatt Laser in Low-Density Plasma,” S. P. D. Mangles, B. R. Walton, M. Tzoufras, Z. Najmudin, R. J. Clarke, A. E. Dangor, R. G. Evans, S. Fritzler, A. Gopal, C. Hernandez-Gomez, W. B. Mori, W. Rozmus, M. Tatarakis, A. G. R. Thomas, F. S. Tsung, M. S. Wei, and K. Krushelnick, *Phys. Rev. Lett.*, **2005**, 94, 245001.
- [42] “Particle acceleration in relativistic laser channels,” A. Pukhov, Z.-M. Sheng, and J. Meyer-ter-Vehn, *Phys. Plasmas*, **1999**, 6, 2847–2854.
- [43] “Multi-MeV Electron Beam Generation by Direct Laser Acceleration in High-Density Plasma Channels,” C. Gahn, G. D. Tsakiris, A. Pukhov, J. Meyer-ter-Vehn, G. Pretzler, P. Thirolf, D. Habs, and K. J. Witte, *Phys. Rev. Lett.*, **1999**, 83, 4772–4775.
- [44] “Beyond the ponderomotive limit: Direct laser acceleration of relativistic electrons in sub-critical plasmas,” A. V. Arefiev, V. N. Khudik, A. P. L. Robinson, G. Shvets, L. Willingale, and M. Schollmeier, *Phys. Plasmas*, **2016**, 23, 056704.

- [45] “Acceleration of heavy Ions to MeV/nucleon Energies by Ultrahigh-Intensity Lasers,” B. M. Hegelich, *PhD Thesis*, Ludwig-Maximilians-Universität München, 2002.
- [46] “Fast ions and hot electrons in the laser–plasma interaction,” S. J. Gitomer, R. D. Jones, F. Begay, A. W. Ehler, J. F. Kephart, and R. Kristal, *The Physics of Fluids*, **1986**, *29*, 2679–2688.
- [47] “A study of picosecond laser–solid interactions up to 10^{19} W cm⁻²,” F. N. Beg, A. R. Bell, A. E. Dangor, C. N. Danson, A. P. Fews, M. E. Glinsky, B. A. Hammel, P. Lee, P. A. Norreys, and M. Tatarakis, *Physics of Plasmas*, **1997**, *4*, 447–457.
- [48] “Nuclear fusion from explosions of femtosecond laser-heated deuterium clusters,” T. Ditmire, J. Zweiback, V. P. Yanovsky, T. E. Cowan, G. Hays, and K. B. Wharton, *Nature*, **1999**, *398*, 489.
- [49] “SELF-SIMILAR MOTION OF RAREFIED PLASMA,” A. V. Gurevich, L. V. Pariiskaya, and L. P. Pitaevskii, *6*.
- [50] “Plasma Expansion into a Vacuum,” M. Widner, I. Alexeff, and W. D. Jones, *The Physics of Fluids*, **1971**, *14*, 795–796.
- [51] “The expansion of a plasma into a vacuum,” J. E. Crow, P. L. Auer, and J. E. Allen, *Journal of Plasma Physics*, **1975**, *14*, 65–76.
- [52] “Proton Acceleration with High-Intensity Ultrahigh-Contrast Laser Pulses,” T. Ceccotti, A. Lévy, H. Popescu, F. Réau, P. D’Oliveira, P. Monot, J. P. Geindre, E. Lefebvre, and Ph. Martin, *Phys. Rev. Lett.*, **2007**, *99*, 185002.
- [53] “Plasma Expansion into a Vacuum,” P. Mora, *Phys. Rev. Lett.*, **2003**, *90*, 185002.
- [54] “All-optical measurement of the hot electron sheath driving laser ion acceleration from thin foils,” O. Jäckel, J. Polz, S. M. Pfotenhauer, H.-P. Schlenvoigt, H. Schworer, and M. C. Kaluza, *New J. Phys.*, **2010**, *12*, 103027.
- [55] “Laser-driven proton scaling laws and new paths towards energy increase,” J. Fuchs, P. Antici, E. d’Humières, E. Lefebvre, M. Borghesi, E. Brambrink, C. A. Cecchetti, M. Kaluza, V. Malka, M. Manclossi, S. Meyroneinc, P. Mora, J. Schreiber, T. Toncian, H. Pépin, and P. Audebert, *Nature Physics*, **2006**, *2*, 48.
- [56] “Influence of the Laser Prepulse on Proton Acceleration in Thin-Foil Experiments,” M. Kaluza, J. Schreiber, M. I. K. Santala, G. D. Tsakiris, K. Eidmann, J. Meyer-ter-Vehn, and K. J. Witte, *Phys. Rev. Lett.*, **2004**, *93*, 045003.
- [57] “Stable GeV Ion-Beam Acceleration from Thin Foils by Circularly Polarized Laser Pulses,” B. Qiao, M. Zepf, M. Borghesi, and M. Geissler, *Phys. Rev. Lett.*, **2009**, *102*, 145002.

- [58] “Interstellar Vehicle Propelled By Terrestrial Laser Beam,” G. Marx, *Nature*, **1966**, *211*, 22.
- [59] “Laser Acceleration of Ion Bunches at the Front Surface of Overdense Plasmas,” A. Macchi, F. Cattani, T. V. Liseykina, and F. Cornolti, *Phys. Rev. Lett.*, **2005**, *94*, 165003.
- [60] “Radiation pressure acceleration of thin foils with circularly polarized laser pulses,” A. P. L. Robinson, M. Zepf, S. Kar, R. G. Evans, and C. Bellei, *New J. Phys.*, **2008**, *10*, 013021.
- [61] “Ion Acceleration in Multispecies Targets Driven by Intense Laser Radiation Pressure,” S. Kar, K. F. Kakolee, B. Qiao, A. Macchi, M. Cerchez, D. Doria, M. Geissler, P. McKenna, D. Neely, J. Osterholz, R. Prasad, K. Quinn, B. Ramakrishna, G. Sarri, O. Willi, X. Y. Yuan, M. Zepf, and M. Borghesi, *Phys. Rev. Lett.*, **2012**, *109*, 185006.
- [62] “Radiation-Pressure Acceleration of Ion Beams Driven by Circularly Polarized Laser Pulses,” A. Henig, S. Steinke, M. Schnürer, T. Sokollik, R. Hörlein, D. Kiefer, D. Jung, J. Schreiber, B. M. Hegelich, X. Q. Yan, J. Meyer-ter-Vehn, T. Tajima, P. V. Nickles, W. Sandner, and D. Habs, *Phys. Rev. Lett.*, **2009**, *103*, 245003.
- [63] “Radiation pressure acceleration of protons to 93 MeV with circularly polarized petawatt laser pulses,” I. J. Kim, K. H. Pae, I. W. Choi, C.-L. Lee, H. T. Kim, H. Singhal, J. H. Sung, S. K. Lee, H. W. Lee, P. V. Nickles, T. M. Jeong, C. M. Kim, and C. H. Nam, *Physics of Plasmas*, **2016**, *23*, 070701.
- [64] “Three-Dimensional Dynamics of Breakout Afterburner Ion Acceleration Using High-Contrast Short-Pulse Laser and Nanoscale Targets,” L. Yin, B. J. Albright, K. J. Bowers, D. Jung, J. C. Fernández, and B. M. Hegelich, *Phys. Rev. Lett.*, **2011**, *107*, 045003.
- [65] “Laser-driven ion acceleration from relativistically transparent nanotargets,” B. M. Hegelich, I. Pomerantz, L. Yin, H. C. Wu, D. Jung, B. J. Albright, D. C. Gautier, S. Letzring, S. Palaniyappan, R. Shah, K. Allinger, R. Hörlein, J. Schreiber, D. Habs, J. Blakeney, G. Dyer, L. Fuller, E. Gaul, E. Mccary, A. R. Meadows, C. Wang, T. Ditmire, and J. C. Fernandez, *New J. Phys.*, **2013**, *15*, 085015.
- [66] “Laser-driven 1 GeV carbon ions from preheated diamond targets in the break-out afterburner regime,” D. Jung, L. Yin, D. C. Gautier, H.-C. Wu, S. Letzring, B. Dromey, R. Shah, S. Palaniyappan, T. Shimada, R. P. Johnson, J. Schreiber, D. Habs,

- J. C. Fernández, B. M. Hegelich, and B. J. Albright, *Physics of Plasmas*, **2013**, *20*, 083103.
- [67] “Bright Laser-Driven Neutron Source Based on the Relativistic Transparency of Solids,” M. Roth, D. Jung, K. Falk, N. Guler, O. Deppert, M. Devlin, A. Favalli, J. Fernandez, D. Gautier, M. Geissel, R. Haight, C. E. Hamilton, B. M. Hegelich, R. P. Johnson, F. Merrill, G. Schaumann, K. Schoenberg, M. Schollmeier, T. Shimada, T. Taddeucci, J. L. Tybo, F. Wagner, S. A. Wender, C. H. Wilde, and G. A. Wurden, *Phys. Rev. Lett.*, **2013**, *110*, 044802.
- [68] “Role of target material in proton acceleration from thin foils irradiated by ultrashort laser pulses,” M. Tayyab, S. Bagchi, B. Ramakrishna, T. Mandal, A. Upadhyay, R. Ramis, J. A. Chakera, P. A. Naik, and P. D. Gupta, *Phys. Rev. E*, **2014**, *90*, 023103.
- [69] “Filamentation control and collimation of laser accelerated MeV protons,” B. Ramakrishna, M. Tayyab, S. Bagchi, T. Mandal, A. Upadhyay, S. M. Weng, M. Murakami, T. E. Cowan, J. A. Chakera, P. A. Naik, and P. D. Gupta, *Plasma Phys. Control. Fusion*, **2015**, *57*, 125013.
- [70] “Micrometer-sized negative-ion accelerator based on ultrashort laser pulse interaction with transparent solids,” S. Bagchi, M. Tayyab, B. Ramakrishna, A. Upadhyay, T. Mandal, J. A. Chakera, P. A. Naik, and P. D. Gupta, *Phys. Rev. E*, **2015**, *92*, 051103.
- [71] “Mono-energetic heavy ion acceleration from laser plasma based composite nano-accelerator,” M. Tayyab, S. Bagchi, J. A. Chakera, D. K. Avasthi, R. Ramis, A. Upadhyay, B. Ramakrishna, T. Mandal, and P. A. Naik, *Physics of Plasmas*, **2018**, *25*, 123102.
- [72] “Aberration-free stretcher design for ultrashort-pulse amplification,” G. Cheriaux, P. Rousseau, F. Salin, J. P. Chambaret, B. Walker, and L. F. Dimauro, *Opt. Lett.*, **1996**, *21*, 414–416.
- [73] “A second-order autocorrelator for single-shot measurement of femtosecond laser pulse durations,” M. Raghuramaiah, A. K. Sharma, P. A. Naik, P. D. Gupta, and R. A. Ganeev, *Sadhana*, **2001**, *26*, 603–611.
- [74] “Full characterization of the amplified spontaneous emission from a diode-pumped high-power laser system,” S. Keppler, M. Hornung, R. Bödefeld, A. Sävert, H. Liebetrau, J. Hein, and M. C. Kaluza, *Opt. Express*, 2014, *22*, 11228–11235
- [75] “A modified Thomson parabola spectrometer for high resolution multi-MeV ion measurements—Application to laser-driven ion acceleration,” D. C. Carroll, P. Brummitt, D. Neely, F. Lindau, O. Lundh, C.-G. Wahlström, and P. McKenna,

Nuclear Instruments and Methods in Physics Research Section A: Accelerators, Spectrometers, Detectors and Associated Equipment, **2010**, 620, 23–27.

- [76] “Design of and data reduction from compact Thomson parabola spectrometers,” J. T. Morrison, C. Willis, R. R. Freeman, and L. Van Woerkom, *Review of Scientific Instruments*, **2011**, 82, 033506.
- [77] “A Thomson parabola ion imaging spectrometer designed to probe relativistic intensity ionization dynamics of nanoclusters,” R. Rajeev, K. P. M. Rishad, T. M. Trivikram, V. Narayanan, and M. Krishnamurthy, *Review of Scientific Instruments*, **2011**, 82, 083303.
- [78] “Development of a high resolution and high dispersion Thomson parabola,” D. Jung, R. Hörlein, D. Kiefer, S. Letzring, D. C. Gautier, U. Schramm, C. Hübsch, R. Öhm, B. J. Albright, J. C. Fernandez, D. Habs, and B. M. Hegelich, *Review of Scientific Instruments*, **2011**, 82, 013306.
- [79] “High-resolution Thomson parabola for ion analysis,” J. A. Cobble, K. A. Flippo, D. T. Offermann, F. E. Lopez, J. A. Oertel, D. Mastro Simone, S. A. Letzring, and N. Sinenian, *Review of Scientific Instruments*, **2011**, 82, 113504.
- [80] “Improved technique for preparation of deuterated-polyethylene targets,” M. Febbraro, D. Walter, S. C. Shadrack, S. D. Pain, K. A. Chipps, C. Thornsberry, and E. Lesser, *Nuclear Instruments and Methods in Physics Research Section B: Beam Interactions with Materials and Atoms*, **2017**, 410, 53–59.
- [81] “Preparation of Thin Film Deuterated Polyethylene Targets,” G. E. Tripart and B. L. White, *Review of Scientific Instruments*, **1967**, 38, 435–436.
- [82] “Effects of laser prepulses on laser-induced proton generation,” D. Batani, R. Jafer, M. Veltcheva, R. Dezulian, O. Lundh, F. Lindau, A. Persson, K. Osvay, C.-G. Wahlström, D. C. Carroll, P. McKenna, A. Flacco, and V. Malka, *New J. Phys.*, **2010**, 12, 045018.
- [83] “Enhanced proton beams from ultrathin targets driven by high contrast laser pulses,” D. Neely, P. Foster, A. Robinson, F. Lindau, O. Lundh, A. Persson, C.-G. Wahlström, and P. McKenna, *Appl. Phys. Lett.*, **2006**, 89, 021502.
- [84] “High-Current, Relativistic Electron-Beam Transport in Metals and the Role of Magnetic Collimation,” M. Storm, A. A. Solodov, J. F. Myatt, D. D. Meyerhofer, C. Stoeckl, C. Mileham, R. Betti, P. M. Nilson, T. C. Sangster, W. Theobald, and C. Guo, *Phys. Rev. Lett.*, **2009**, 102, 235004.

- [85] “MULTI — A computer code for one-dimensional multigroup radiation hydrodynamics,” R. Ramis, R. Schmalz, and J. Meyer-Ter-Vehn, *Computer Physics Communications*, **1988**, *49*, 475–505.
- [86] “Density effect on proton acceleration from carbon-containing high-density thin foils irradiated by high-intensity laser pulses,” C. T. Zhou, M. Y. Yu, and X. T. He, *Journal of Applied Physics*, **2007**, *101*, 103302.
- [87] “Investigation of laser-driven proton acceleration using ultra-short, ultra-intense laser pulses,” S. Fourmaux, S. Buffechoux, B. Albertazzi, D. Capelli, A. Lévy, S. Gnedyuk, L. Lecherbourg, P. Lassonde, S. Payeur, P. Antici, H. Pépin, R. S. Marjoribanks, J. Fuchs, and J. C. Kieffer, *Physics of Plasmas*, **2013**, *20*, 013110.
- [88] “Dependence on pulse duration and foil thickness in high-contrast-laser proton acceleration,” A. Flacco, F. Sylla, M. Veltcheva, M. Carrié, R. Nuter, E. Lefebvre, D. Batani, and V. Malka, *Phys. Rev. E*, **2010**, *81*, 036405.
- [89] “Hard x-ray emission in high intensity femtosecond laser–target interaction,” J. Yu, Z. Jiang, J. C. Kieffer, and A. Krol, *Physics of Plasmas*, **1999**, *6*, 1318–1322.
- [90] “Study of fast electron transport in thin foil targets irradiated by ultrashort intense laser pulses,” T. Mandal, V. Arora, M. Tayyab, S. Bagchi, R. Rathore, B. Ramakrishna, C. Mukharjee, J. A. Chakera, P. A. Naik, and P. D. Gupta, *Appl. Phys. B*, **2015**, *119*, 281–286.
- [91] “Ultra-intense laser pulse propagation in plasmas: from classic hole-boring to incomplete hole-boring with relativistic transparency,” S. M. Weng, M. Murakami, P. Mulser, and Z. M. Sheng, *New J. Phys.*, **2012**, *14*, 063026.
- [92] “Laser-Driven Proton Acceleration Enhancement by Nanostructured Foils,” D. Margarone, O. Klimo, I. J. Kim, J. Prokúpek, J. Limpouch, T. M. Jeong, T. Mocek, J. Pšikal, H. T. Kim, J. Proška, K. H. Nam, L. Štolcová, I. W. Choi, S. K. Lee, J. H. Sung, T. J. Yu, and G. Korn, *Phys. Rev. Lett.*, **2012**, *109*, 234801.
- [93] “Hot Electrons Transverse Refluxing in Ultraintense Laser-Solid Interactions,” S. Buffechoux *et al.*, *Phys. Rev. Lett.*, **2010**, *105*, 015005.
- [94] “Toward high-energy laser-driven ion beams: Nanostructured double-layer targets,” M. Passoni, A. Sgattoni, I. Prencipe, L. Fedeli, D. Dellasega, L. Cialfi, I. W. Choi, I. J. Kim, K. A. Janulewicz, H. W. Lee, J. H. Sung, S. K. Lee, and C. H. Nam, *Phys. Rev. Accel. Beams*, **2016**, *19*, 061301.
- [95] “Micro-sphere layered targets efficiency in laser driven proton acceleration,” V. Floquet, O. Klimo, J. Psikal, A. Velyhan, J. Limpouch, J. Proška, F. Novotny, L.

- Stolcova, A. Macchi, A. Sgattoni, L. Vassura, L. Labate, F. Baffigi, L. A. Gizzi, Ph. Martin, and T. Ceccotti, *Journal of Applied Physics*, **2013**, *114*, 083305.
- [96] “Electron-Yield Enhancement in a Laser-Wakefield Accelerator Driven by Asymmetric Laser Pulses,” W. P. Leemans, P. Catravas, E. Esarey, C. G. R. Geddes, C. Toth, R. Trines, C. B. Schroeder, B. A. Shadwick, J. van Tilborg, and J. Faure, *Phys. Rev. Lett.*, **2002**, *89*, 174802.
- [97] “Study of X-Ray Emission Enhancement via a High-Contrast Femtosecond Laser Interacting with a Solid Foil,” L. M. Chen, M. Kando, M. H. Xu, Y. T. Li, J. Koga, M. Chen, H. Xu, X. H. Yuan, Q. L. Dong, Z. M. Sheng, S. V. Bulanov, Y. Kato, J. Zhang, and T. Tajima, *Phys. Rev. Lett.*, **2008**, *100*, 045004.
- [98] “2.1 Ultrafast solid-state lasers,” in *Laser Systems, Part 1*, 11, G. Herziger, H. Weber, and R. Poprawe Eds., Berlin, Heidelberg: Springer Berlin Heidelberg, 2007, 33–167.
- [99] “Temporal characterization of chirped femtosecond laser pulses,” K.-H. Hong, J. H. Sung, Y. S. Lee, and C. H. Nam, *Optics Communications*, **2002**, *213*, 193–200.
- [100] “Influence of subpicosecond laser pulse duration on proton acceleration,” M. Carrié, E. Lefebvre, A. Flacco, and V. Malka, *Physics of Plasmas*, **2009**, *16*, 053105.
- [101] “Enhancement of Proton Acceleration by Hot-Electron Recirculation in Thin Foils Irradiated by Ultraintense Laser Pulses,” A. J. Mackinnon, Y. Sentoku, P. K. Patel, D. W. Price, S. Hatchett, M. H. Key, C. Andersen, R. Snavely, and R. R. Freeman, *Phys. Rev. Lett.*, **2002**, *88*, 215006.
- [102] “Effects of chirp and pulse shape on high harmonic generation and absorption in overdense plasmas,” X. Lavocat-Dubuis, F. Vidal, J.-P. Matte, C. Popovici, T. Ozaki, and J.-C. Kieffer, *Laser and Particle Beams*, **2011**, *29*, 95–104.
- [103] “Generation and propagation of hot electrons in laser-plasmas,” J. Zhang, Y. T. Li, Z. M. Sheng, Z. Y. Wei, Q. L. Dong, and X. Lu, *Appl. Phys. B*, **2005**, *80*, 957–971.
- [104] “Effect of a laser prepulse on fast ion generation in the interaction of ultra-short intense laser pulses with a limited-mass foil target,” A. A. Andreev, R. Sonobe, S. Kawata, S. Miyazaki, K. Sakai, K. Miyauchi, T. Kikuchi, K. Platonov, and K. Nemoto, *Plasma Phys. Control. Fusion*, **2006**, *48*, 1605–1619.
- [105] “Influence of a preplasma on electron heating and proton acceleration in ultraintense laser-foil interaction,” R. Nuter, L. Gremillet, P. Combis, M. Drouin, E. Lefebvre, A. Flacco, and V. Malka, *Journal of Applied Physics*, **2008**, *104*, 103307.
- [106] “Absorption of ultra-intense laser pulses,” S. C. Wilks, W. L. Kruer, M. Tabak, and A. B. Langdon, *Phys. Rev. Lett.*, **1992**, *69*, 1383–1386.

- [107] “Nonlinear electron heating in ultrahigh-intensity-laser--plasma interaction,” E. Lefebvre and G. Bonnaud, *Phys. Rev. E*, **1997**, *55*, 1011–1014.
- [108] “Hot-Electron Temperature and Laser-Light Absorption in Fast Ignition,” M. G. Haines, M. S. Wei, F. N. Beg, and R. B. Stephens, *Phys. Rev. Lett.*, **2009**, *102*, 045008.
- [109] “*Laser-Plasma Interactions and Applications*”, edited by Paul McKenna David Neely Robert Bingham Dino Jaroszynski, Springer International Publishing, **2013**.
- [110] “Nonlinear absorption of a short intense laser pulse in a nonuniform plasma,” A. A. Andreev, K. Yu. Platonov, T. Okada, and S. Toraya, *Physics of Plasmas*, **2002**, *10*, 220–226.
- [111] “Ultrafast Laser-Driven Microlens to Focus and Energy-Select Mega-Electron Volt Protons,” T. Toncian, M. Borghesi, J. Fuchs, E. d’Humières, P. Antici, P. Audebert, E. Brambrink, C. A. Cecchetti, A. Pipahl, L. Romagnani, and O. Willi, *Science*, **2006**, *312*, 410–413.
- [112] “Collisionless shock acceleration of narrow energy spread ion beams from mixed species plasmas using 1 μm lasers,” A. Pak, S. Kerr, N. Lemos, A. Link, P. Patel, F. Albert, L. Divol, B. B. Pollock, D. Haberberger, D. Froula, M. Gauthier, S. H. Glenzer, A. Longman, L. Manzoor, R. Fedosejevs, S. Tochitsky, C. Joshi, and F. Fiuza, *Phys. Rev. Accel. Beams*, **2018**, *21*, 103401.
- [113] “Collisionless shocks driven by 800 nm laser pulses generate high-energy carbon ions,” H. Zhang, B. F. Shen, W. P. Wang, Y. Xu, Y. Q. Liu, X. Y. Liang, Y. X. Leng, R. X. Li, X. Q. Yan, J. E. Chen, and Z. Z. Xu, *Physics of Plasmas*, **2015**, *22*, 013113.
- [114] “Laser-Driven Shock Acceleration of Monoenergetic Ion Beams,” F. Fiuza, A. Stockem, E. Boella, R. A. Fonseca, L. O. Silva, D. Haberberger, S. Tochitsky, C. Gong, W. B. Mori, and C. Joshi, *Phys. Rev. Lett.*, **2012**, *109*, 215001.
- [115] “Ion acceleration from laser-driven electrostatic shocks,” F. Fiuza, A. Stockem, E. Boella, R. A. Fonseca, L. O. Silva, D. Haberberger, S. Tochitsky, W. B. Mori, and C. Joshi, *Physics of Plasmas*, **2013**, *20*, 056304.
- [116] “Combined proton acceleration from foil targets by ultraintense short laser pulses,” Y. Fang, T. Yu, X. Ge, S. Yang, W. Wei, T. Yuan, F. Liu, M. Chen, J. Liu, Y. Li, X. Yuan, Z. Sheng, and J. Zhang, *Plasma Phys. Control. Fusion*, **2016**, *58*, 045025.
- [117] “Proton acceleration mechanisms in high-intensity laser interaction with thin foils,” E. d’Humières, E. Lefebvre, L. Gremillet, and V. Malka, *Physics of Plasmas*, **2005**, *12*, 062704.

- [118] “Collisionless electrostatic shock generation and ion acceleration by ultraintense laser pulses in overdense plasmas,” M. Chen, Z.-M. Sheng, Q.-L. Dong, M.-Q. He, Y.-T. Li, M. A. Bari, and J. Zhang, *Physics of Plasmas*, **2007**, *14*, 053102.
- [119] “Acceleration dynamics of ions in shocks and solitary waves driven by intense laser pulses,” M.-Q. He, Q.-L. Dong, Z.-M. Sheng, S.-M. Weng, M. Chen, H.-C. Wu, and J. Zhang, *Phys. Rev. E*, **2007**, *76*, 035402.
- [120] “Shaping laser accelerated ions for future applications – The LIGHT collaboration,” S. Busold *et al.*, *Nuclear Instruments and Methods in Physics Research Section A: Accelerators, Spectrometers, Detectors and Associated Equipment*, **2014**, *740*, 94–98.
- [121] “Dose-dependent biological damage of tumour cells by laser-accelerated proton beams,” S. D. Kraft, C. Richter, K. Zeil, M. Baumann, E. Beyreuther, S. Bock, M. Bussmann, T. E. Cowan, Y. Dammene, W. Enghardt, U. Helbig, L. Karsch, T. Kluge, L. Laschinsky, E. Lessmann, J. Metzkes, D. Naumburger, R. Sauerbrey, M. Schürer, M. Sobiella, J. Woithe, U. Schramm, and J. Pawelke, *New J. Phys.*, **2010**, *12*, 085003.
- [122] “Electric field detection in laser-plasma interaction experiments via the proton imaging technique,” M. Borghesi, D. H. Campbell, A. Schiavi, M. G. Haines, O. Willi, A. J. MacKinnon, P. Patel, L. A. Gizzi, M. Galimberti, R. J. Clarke, F. Pegoraro, H. Ruhl, and S. Bulanov, *Physics of Plasmas*, **2002**, *9*, 2214–2220.
- [123] “Ultralow Emittance, Multi-MeV Proton Beams from a Laser Virtual-Cathode Plasma Accelerator,” T. E. Cowan, J. Fuchs, H. Ruhl, A. Kemp, P. Audebert, M. Roth, R. Stephens, I. Barton, A. Blazevic, E. Brambrink, J. Cobble, J. Fernández, J.-C. Gauthier, M. Geissel, M. Hegelich, J. Kaae, S. Karsch, G. P. Le Sage, S. Letzring, M. Manclossi, S. Meyroneinc, A. Newkirk, H. Pépin, and N. Renard-LeGalloudec, *Phys. Rev. Lett.*, **2004**, *92*, 204801.
- [124] “Radiation pressure-assisted acceleration of ions using multi-component foils in high-intensity laser–matter interactions,” B. Aurand, S. Kuschel, O. Jäckel, C. Rödel, H. Y. Zhao, S. Herzer, A. E. Paz, J. Bierbach, J. Polz, B. Elkin, G. G. Paulus, A. Karmakar, P. Gibbon, T. Kuehl, and M. C. Kaluza, *New J. Phys.*, **2013**, *15*, 033031.
- [125] “Synthesis of metal–polymer nanocomposite for optical applications,” D. K. Avasthi, Y. K. Mishra, D. Kabiraj, N. P. Lalla, and J. C. Pivin, *Nanotechnology*, **2007**, *18*, 125604.
- [126] “Blue-Shifted SPR of Au Nanoparticles with Ordering of Carbon by Dense Ionization and Thermal Treatment,” R. Singhal, D. Kabiraj, P. K. Kulriya, J. C. Pivin, R. Chandra, and D. K. Avasthi, *Plasmonics*, **2013**, *8*, 295–305.

- [127] “Effect of Plasma Scale Length on Multi-MeV Proton Production by Intense Laser Pulses,” A. J. Mackinnon, M. Borghesi, S. Hatchett, M. H. Key, P. K. Patel, H. Campbell, A. Schiavi, R. Snavely, S. C. Wilks, and O. Willi, *Phys. Rev. Lett.*, **2001**, *86*, 1769–1772.
- [128] “Spatially resolved analysis of K- α x-ray emission from plasmas induced by a femtosecond weakly relativistic laser pulse at various polarizations,” G. Cristoforetti, M. P. Anania, A. Ya. Faenov, A. Giulietti, D. Giulietti, S. B. Hansen, P. Koester, L. Labate, T. Levato, T. A. Pikuz, and L. A. Gizzi, *Phys. Rev. E*, **2013**, *87*, 023103.
- [129] “Present status of the negative ion based NBI system for long pulse operation on JT-60U,” Y. Ikeda, N. Umeda, N. Akino, N. Ebisawa, L. Grisham, M. Hanada, A. Honda, T. Inoue, M. Kawai, M. Kazawa, K. Kikuchi, M. Komata, K. Mogaki, K. Noto, F. Okano, T. Ohga, K. Oshima, T. Takenouchi, Y. Tanai, K. Usui, H. Yamazaki, and T. Yamamoto, *Nucl. Fusion*, **2006**, *46*, S211–S219.
- [130] “Synchrotrons and accumulators for high-intensity proton beams,” J. Wei, *Rev. Mod. Phys.*, **2003**, *75*, 1383–1432.
- [131] “Use of hydrogen negative ions in particle accelerators,” G. I. Dimov, *Review of Scientific Instruments*, **1996**, *67*, 3393–3404.
- [132] “Negative hydrogen ion production in fusion dedicated ion sources,” M. Bacal, *Chemical Physics*, **2012**, *398*, 3–6.
- [133] “Ultimate Top-down Etching Processes for Future Nanoscale Devices: Advanced Neutral-Beam Etching,” S. Samukawa, *Jpn. J. Appl. Phys.*, **2006**, *45*, 2395.
- [134] “Negative hydrogen ion production mechanisms,” M. Bacal and M. Wada, *Applied Physics Reviews*, **2015**, *2*, 021305.
- [135] “MeV negative ion generation from ultra-intense laser interaction with a water spray,” S. Ter-Avetisyan, B. Ramakrishna, M. Borghesi, D. Doria, M. Zepf, G. Sarri, L. Ehrentraut, A. Andreev, P. V. Nickles, S. Steinke, W. Sandner, M. Schnürer, and V. Tikhonchuk, *Appl. Phys. Lett.*, **2011**, *99*, 051501.
- [136] “Energetic beams of negative and neutral hydrogen from intense laser plasma interaction,” F. Abicht, R. Prasad, M. Borghesi, G. Priebe, J. Braenzel, A. Andreev, P. V. Nickles, M. Schnürer, S. Jequier, G. Revet, V. Tikhonchuk, and S. Ter-Avetisyan, *Appl. Phys. Lett.*, **2013**, *103*, 253501.
- [137] “A compact laser-driven plasma accelerator for megaelectronvolt-energy neutral atoms,” R. Rajeev, T. Madhu Trivikram, K. P. M. Rishad, V. Narayanan, E. Krishnakumar, and M. Krishnamurthy, *Nature Physics*, **2013**, *9*, 185–190.

- [138] “New source of MeV negative ion and neutral atom beams,” S. Ter-Avetisyan, J. Braenzel, M. Schnürer, R. Prasad, M. Borghesi, S. Jequier, and V. Tikhonchuk, *Review of Scientific Instruments*, **2015**, 92, 02B134.
- [139] “Generation of energetic negative ions from clusters using intense laser fields,” R. Rajeev, T. M. Trivikram, K. P. M. Rishad, V. Narayanan, and M. Krishnamurthy, *New J. Phys.*, **2013**, 15, 043036.
- [140] “Recombination of Protons Accelerated by a High Intensity High Contrast Laser,” S. Tata, A. Mondal, S. Sarkar, J. Jha, Y. Ved, A. D. Lad, J. Colgan, J. Pasley, and M. Krishnamurthy, *Phys. Rev. Lett.*, **2018**, 121, 134801.
- [141] “Compact acceleration of energetic neutral atoms using high intensity laser-solid interaction,” M. Dalui, T. M. Trivikram, J. Colgan, J. Pasley, and M. Krishnamurthy, *Scientific Reports*, **2017**, 7, 3921.
- [142] “A compact solution for ion beam therapy with laser accelerated protons,” U. Masood, M. Bussmann, T. E. Cowan, W. Enghardt, L. Karsch, F. Kroll, U. Schramm, and J. Pawelke, *Appl. Phys. B*, **2014**, 117, 41–52.
- [143] “Proton beams generated with high-intensity lasers: Applications to medical isotope production,” S. Fritzler, V. Malka, G. Grillon, J. P. Rousseau, F. Burgy, E. Lefebvre, E. d’Humières, P. McKenna, and K. W. D. Ledingham, *Appl. Phys. Lett.*, **2003**, 83, 3039–3041.
- [144] “Laser-driven ion acceleration: methods, challenges and prospects,” J. Badziak, *J. Phys.: Conf. Ser.*, **2018**, 959, 012001.
- [145] “ELIMAIA: A Laser-Driven Ion Accelerator for Multidisciplinary Applications,” D. Margarone *et al.*, *Quantum Beam Science*, **2018**, 2, 8.
- [146] “Performance demonstration of the PEnELOPE main amplifier HEPA I using broadband nanosecond pulses,” D. Albach, M. Loeser, M. Siebold, and U. Schramm, *High Power Laser Science and Engineering*, **2019**, 7.
- [147] “Laser Induced Nuclear Physics and Applications,” K. W. D. Ledingham, *Nuclear Physics A*, **2005**, 752, 633–684.
- [148] “High purity materials as targets for radioisotope production: Needs and challenges,” V. Shivarudrappa and K. V. Vimalnath, *Bull Mater Sci*, **2005**, 28, 325–330.
- [149] “Radiopharmaceuticals in PET Imaging,” K. Duncan, *J. Nucl. Med. Technol.*, **1998**, 26, 228–234.
- [150] “Unconventional Nuclides for Radiopharmaceuticals,” J. P. Holland, M. J. Williamson, and J. S. Lewis, *Mol Imaging*, **2010**, 9, 1–20.

- [151] “Potentiality of the proton-boron fuel for controlled thermonuclear fusion,” D. C. Moreau, *Nucl. Fusion*, **1977**, *17*, 13–20.
- [152] “Colliding Beam Fusion Reactor,” N. Rostoker, M. W. Binderbauer, and H. J. Monkhorst, *Science*, **1997**, *278*, 1419–1422.
- [153] “Fusion energy using avalanche increased boron reactions for block-ignition by ultrahigh power picosecond laser pulses,” H. Hora, G. Korn, L. Giuffrida, D. Margarone, A. Picciotto, J. Krasa, K. Jungwirth, J. Ullschmied, P. Lalouis, S. Eliezer, G. H. Miley, S. Moustazis, and G. Mourou, *Laser and Particle Beams*, **2015**, *33*, 607–619.
- [154] “Boron-Proton Nuclear-Fusion Enhancement Induced in Boron-Doped Silicon Targets by Low-Contrast Pulsed Laser,” A. Picciotto, D. Margarone, A. Velyhan, P. Bellutti, J. Krasa, A. Szydlowsky, G. Bertuccio, Y. Shi, A. Mangione, J. Prokupek, A. Malinowska, E. Krousky, J. Ullschmied, L. Laska, M. Kucharik, and G. Korn, *Phys. Rev. X*, **2014**, *4*, 031030.
- [155] “Fusion reactions initiated by laser-accelerated particle beams in a laser-produced plasma,” C. Labaune, C. Baccou, S. Depierreux, C. Goyon, G. Loisel, V. Yahia, and J. Rafelski, *Nature Communications*, **2013**, *4*, 2506.
- [156] Michelmann R W, Krauskopf J, Meyer J D and Bethge K 1990 Excitation functions for the reactions $^{10}\text{B}(d, n)^{11}\text{C}$ and $^{12}\text{C}(d, n)^{13}\text{N}$ for charged particle activation analysis *Nucl. Instrum. Methods Phys. Res. Sect. B Beam Interact. Mater. At.* **51** 1–4. and “B-11(p,3a) reaction”, Hale G M 1979, Priv. Comm. Data taken from EXFOR database, file EXFOR D0017, EXFOR D0095002 and EXFOR F0507002.
- [157] “Deuteron-induced reactions generated by intense lasers for PET isotope production,” S. Kimura and A. Bonasera, *Nuclear Instruments and Methods in Physics Research Section A: Accelerators, Spectrometers, Detectors and Associated Equipment*, **2011**, *637*, 164–170.
- [158] “Possible PET isotope production using linear deuteron accelerators,” P. Volkovitsky and D. M. Gilliam, *Nuclear Instruments and Methods in Physics Research Section A: Accelerators, Spectrometers, Detectors and Associated Equipment*, **2005**, *548*, 571–573.
- [159] “SRIM & TRIM”, James Ziegler - <http://www.srim.org>, 2013:
- [160] “New Generation of Ultra-High Peak and Average Power Laser Systems,” V. Chvykov, *High Power Laser Systems*, **2017**.

- [161] “22 W average power multiterawatt femtosecond laser chain enabling 10¹⁹ W/cm² at 100 Hz,” R. Clady, Y. Azamoum, L. Charmasson, A. Ferré, O. Utéza, and M. Sentis, *Appl. Phys. B*, **2018**, *124*, 89.
- [162] “High peak and average power Ti:sapphire thin disk amplifier with extraction during pumping,” V. Chvykov, H. Cao, R. Nagymihaly, M. P. Kalashnikov, N. Khodakovskiy, R. Glassock, L. Ehrentraut, M. Schnuerer, and K. Osvay, *Opt. Lett.*, *OL*, **2016**, *41*, 3017–3020.
- [163] “Laser-ion acceleration through controlled surface contamination,” B. Hou, J. A. Nees, Z. He, G. Petrov, J. Davis, J. H. Easter, A. G. R. Thomas, and K. M. Krushelnick, *Physics of Plasmas*, **2011**, *18*, 040702.
- [164] “Selective deuteron production using target normal sheath acceleration,” J. T. Morrison, M. Storm, E. Chowdhury, K. U. Akli, S. Feldman, C. Willis, R. L. Daskalova, T. Growden, P. Berger, T. Ditmire, L. Van Woerkom, and R. R. Freeman, *Physics of Plasmas*, **2012**, *19*, 030707.
- [165] “Selective deuterium ion acceleration using the Vulcan petawatt laser,” A. G. Krygier, J. T. Morrison, S. Kar, H. Ahmed, A. Alejo, R. Clarke, J. Fuchs, A. Green, D. Jung, A. Kleinschmidt, Z. Najmudin, H. Nakamura, P. Norreys, M. Notley, M. Oliver, M. Roth, L. Vassura, M. Zepf, M. Borghesi, and R. R. Freeman, *Physics of Plasmas*, **2015**, *22*, 053102.
- [166] “Dominant deuteron acceleration with a high-intensity laser for isotope production and neutron generation,” A. Maksimchuk, A. Raymond, F. Yu, G. M. Petrov, F. Dollar, L. Willingale, C. Zulick, J. Davis, and K. Krushelnick, *Appl. Phys. Lett.*, **2013**, *102*, 191117.
- [167] “Repetitive production of positron emitters using deuterons accelerated by multiterawatt laser pulses,” M. Fujimoto, K. Matsukado, H. Takahashi, Y. Kawada, S. Ohsuka, and S.-I. Aoshima, *Review of Scientific Instruments*, **2009**, *80*, 113301.
- [168] “Low-energy cross sections for ¹¹B(p, 3α),” H. W. Becker, C. Rolfs, and H. P. Trautvetter, *Z. Physik A - Atomic Nuclei*, **1987**, *327*, 341–355.
- [169] “Observation of neutronless fusion reactions in picosecond laser plasmas,” V. S. Belyaev, *Phys. Rev. E*, **2005**, *72*.

Thesis Highlight

Name of the Student: MOHAMMAD TAYYAB

Name of the CI/OCC: RRCAT, INDORE

Enrolment No.: PHYS03201404003

Thesis Title: *Studies on ion acceleration in ultrashort ultra-high intensity laser matter interaction*

Discipline: Physical Sciences

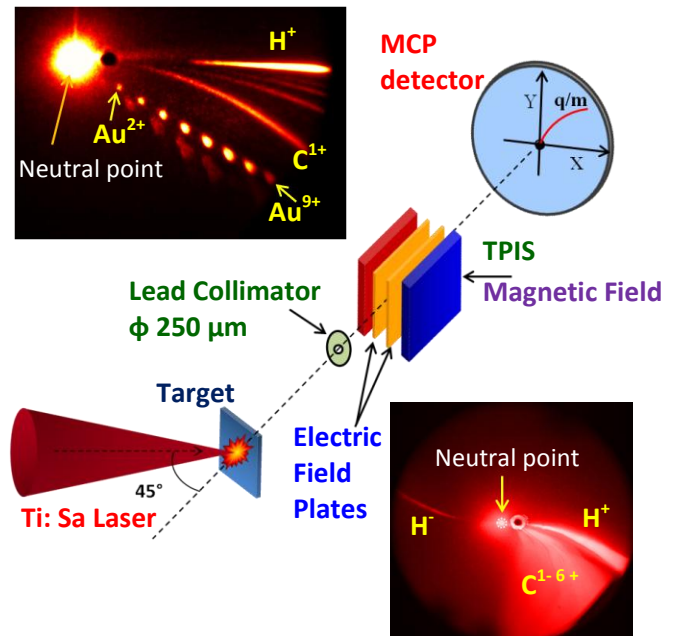
Sub-Area of Discipline: Plasma Physics

Date of viva voce: 27-07-2020

The present thesis work primarily deals with proton/ion acceleration from solids, thin foils and specialized nano structured targets using 10 TW, 45 fs and 150 TW, 25 fs Ti:Sapphire laser systems at RRCAT. The major findings of the thesis include the acceleration of quasi monoenergetic heavy ions which have been demonstrated for the first time. The dependence of lighter ion (H^+ and C^{1-6+}) acceleration on various laser and target parameters have been investigated. The important roles played by foil material and laser temporal shape on proton acceleration are identified. By controlling the laser irradiation parameters, generation of negative H^- ion from solid targets have been demonstrated. Application of laser accelerated proton and deuteron beam in short lived positron emitting radioisotope isotope production and proton-boron fusion studies are demonstrated.

Initial ion acceleration studies were started on 10 TW Ti: Sapphire laser system to optimize the experimental parameters related to laser-foil interaction. Foils of different materials and thicknesses have been used to achieve higher H^+ /proton energy. In particular, it was also found that an appropriate selection of foil material or atomic number-Z can improve the proton acceleration efficiency, for a given laser parameter on laser prepulse thereby increasing the accelerated proton/ion energy. Later the ion acceleration studies were carried out at higher laser intensities using 150 TW laser. Maximum H^+ ion energy was 10-11 MeV while C^{5+} ion yielded a maximum energy of 14.5 MeV. Effect of laser intensity, pulse contrast and pulse duration/ laser chirp have been studied in details. In particular, significant enhancement of ion energy from thin foil targets was observed by adjusting the laser temporal characteristics. Next, by using transparent CH solid target, H^- (negative ion) acceleration is also demonstrated. The flux of the H^- ions was observed to be very high ($> 10^{10}$ /shot). In a typical laser ion acceleration, protons (H^+) are the most dominant species having broad energy distribution. Contrary to this, acceleration of quasi

mono-energetic gold (heavy) ions to sub MeV energies have been demonstrated for the first time from gold-carbon nano-composite and multilayer targets irradiated at moderate laser intensities of 10^{18} - 10^{19} W/cm². Next, applications of laser driven proton beam towards (p,B) fusion reaction was carried out. The resultant alpha particle flux and energy distribution is characterized. Further, generation of ¹¹C (positron emitter) radioisotope by proton and D⁺ beam induced ¹¹B(p,n)¹¹C and ¹⁰B(d,n)¹¹C reactions have also been studied. About 5.2 kBq activity of ¹¹C radio-isotope was produced in a single laser shot through ¹¹B(p, n)¹¹C reaction. This represents $\sim 9 \times 10^6$ atoms of ¹¹C radio-isotopes. Higher yield is demonstrated by exploiting both deuteron and proton beam which is generated using CD₂ target in producing ¹¹C radio-isotope.



Laser driven ion acceleration schematic. The ultrahigh intensity laser is focused on thin foil target and ions are accelerated at the target rear. The ions are analysed using Thomson parabola ion spectrometer (TPIS). Typical ion signal recorded from Au-C nano composite target showing quasi mono-energetic Au ions (top left) and negative ions from PMMA target (bottom right).